THE UNIVERSITY *of* EDINBURGH

Analysis of PS-converted wave seismic data in the presence of azimuthal anisotropy

Weining Liu

Thesis submitted for the degree of

Doctor of Philosophy

School of Geoscience

University of Edinburgh

2014

Declaration

I declare that this thesis has been composes solely by myself and that is has not been submitted, either in whole or in part, in any previous application for a degree. Except where otherwise acknowledged, the work presented is entirely my own.

Weining Liu

April 2014

Abstract

Shear-wave splitting and azimuthal variations of seismic attributes are two major anisotropic effects induced by vertically-aligned fractures. They both have influences on seismic data processing and interpretation, and provide information on fracture properties. Azimuthal variations in P-wave data have been intensively studied to improve imaging and obtain fracture parameters. However, azimuthal variations in PS-converted wave seismic data, particularly the velocity variation in PS-converted wave data, have not been well studied. Shear-wave splitting has been frequently used to estimate fracture directions and densities. However, its influence on the azimuthal variations of PS-converted wave data has also lacked a proper analysis. In this thesis, I analyse the anisotropic behaviour of PS-converted wave seismic data in the presence of azimuthal anisotropy, which includes the azimuthal variation of the PS-converted wave and PS-converted wave splitting.

First, I demonstrate the robustness of PS-converted wave splitting for fracture characterisation. PS-converted wave seismic data is also influenced by the splitting effect due to its upgoing shear-wave leg. This important feature enables the application of shear-wave splitting analysis to PS-converted wave seismic data. I use synthetic data to show the necessity for separation of the split PS-converted waves. Then I apply the PS-converted wave splitting analysis to Sanhu 3D3C land seismic data. By separation of the fast and slow PS-converted waves and compensation for the time delays, the imaging quality has been improved. Dominant fracture properties obtained from the splitting analysis show a good correlation with the stress-field data. However, this work is accomplished by assuming only one set of vertical fractures in processing a given time window. In future work a specific layer-stripping algorithm could be constructed and applied. .

Second, I study azimuthal variations of velocities in PS-converted wave seismic data. It involves two major parts: analysing azimuthal variations of NMO velocities to improve imaging, and examining the sensitivity of azimuthal variations to different fluid saturations. For a layer with HTI anisotropy induced by a set of vertical

fractures, seismologists usually analyse the azimuthal behaviour exhibited on the radial and transverse components, on which PS-converted wave data are recorded. However, PS-converted waves also undergo shear-wave splitting, which complicates the azimuthal variations of PS-converted wave data. I demonstrate that it is essential to separate the fast P-SV1 wave from the slow P-SV2 wave, before applying any azimuthal analysis. I derive an equation describing the azimuthal variation in PS-converted wave NMO velocities, which shows the variation can be approximated into an ellipse. Based on this theory, I build a workflow to analyse the azimuthal variations of velocities in PS-converted wave data and apply this workflow to synthetic data. The imaging quality can be improved by using this workflow.

Different fluid saturations in fractures have different influences on the azimuthal variations of both P-wave and PS-converted wave data. I perform a numerical study to understand how dry or water-saturated fractures control the azimuthal variations. Through theoretical and synthetic studies, I find that the azimuthal variation of velocities in PS-converted wave data is sensitive to different fluid saturations. By analysing the azimuthal variation, the fracture properties can also be estimated, but results are not as robust as those from PS-converted wave splitting analysis. I find that azimuthal variations of fast P-SV1 and slow P-SV2 waves show in-phase characteristics in dry fractures, but exhibit out-of-phase characteristics in water-saturated fractures. This important feature could open a new application for using PS-converted wave seismic data to distinguish oil-filled fractures from gas-filled fractures. In cases where multiple HTI layers are involved, I have developed a specific layer-stripping method to analyse both azimuthal variations and splitting effects of PS-converted waves. By applying this method to synthetic data, the fracture properties of each HTI layer can be estimated.

The analysis of azimuthal variations in PS-converted wave velocities is applied to Daqing 3D3C land data. By using azimuthal velocity models in the PS-converted wave seismic data processing, the imaging quality is improved, especially in the anticline area where intensive fractures are likely to be developed. Furthermore, all fracture information obtained from analysis of azimuthal variations and splitting

effects is compared with the stress-field data. The results from splitting analysis show a better correlation with the stress-field study.

Finally, it is important to conclude that the analysis of PS-converted wave splitting is a robust method to estimate fracture directions and densities. However, it is not sensitive to different fluid saturations, which limits its application to fractured reservoir characterisation. Azimuthal variations of PS-converted wave seismic data can be analysed to improve imaging quality. Moreover their sensitivity to fluid saturations may provide a new way to discriminate between oil-filled and gas-filled fractures. However, the analysis of azimuthal variations is not as robust as the analysis of splitting effects, and it may require appropriate calibration with other fracture characterisation methods.

Acknowledgements

It would not have been possible to write this thesis without help and support of the kind people around me, to only some of whom it is possible to give particular mention here.

Above all, I would like thank my wife Nan Wang for encouraging me in all of my pursuits and inspiring me to follow my dreams. I am grateful to my parents Xiao Liu and Yuping Wang, and my parents-in-law Xing Wang and Tao Qi. They always believe in me and want the best for me, which are invaluable treasures in my life.

I must thank my principle supervisor Professor Xiangyang Li for his academic instruction and guidance throughout my PhD study. He and his wife also provide all kinds of assistances in these years, which helps me concentrate on my research.

I would like to thank Dr Hengchang Dai for providing advices particularly in seismic data processing and computer programming. I want to express my attitudes to Dr Mark Chapman, who are always nice to everybody and giving academic advices to me. I am also grateful to my supervisor in School of Geosciences Andrew Curtis for his good suggestions during this period.

Special thanks to David Booth for helping me improve my academic writing through these years and proofreading every paragraph of this thesis.

I want to thanks Dr Zhongping Qian and his colleagues in BGP (Bureau of Geophysical Prospecting) for sponsoring my intern in 2013 and valuable suggestions on my research area.

I would like to thank all staff in British Geological Survey, especially Love Steve, Jane Broughton and Jane Roberson for providing a great work environment.

It has been my pleasure to work with so many nice lab mates, Yungui Xu, Martin, Zhiqi Guo, Song Hou, Yingrui Ren, Feng, zhang, Shuangquan, Chen and Li Yang. I would like to thank all my friends in Edinburgh, with whom I had countless enjoyable days in those years.

Finally, I would like to thank all sponsors of EAP (Edinburgh Anisotropy Project) for sponsoring my PhD study.

To my family

Contents

List of Figures

List of Tables

Notations and conventions

All mathematical variables and other abbreviations used in this thesis are explained here. They are arranged by chapters in the order of their appearance.

Chapter 1

VTI	transverse isotropy with a vertical symmetry axis
HTI	transverse isotropy with a horizontal symmetry axis
P-wave	compression seismic wave
NMO	normal moveout correction
3D	three-dimension
3C	three-component

Chapter 2

AVO	Amplitude versus offset
qP	quasi-P wave
qS1	fast quasi-S wave
qS2	slow quasi-S wave
x_i	Cartesian coordinates
σ_{ji}	stress tensors
u, v, w	displacement vectors
ε_{ij}	strain tensors
C_{ijkl}	elastic stiffness tensors
s_{ijkl}	elastic compliance tensors
ρ	density
λ , μ	Lamé's constants
TTI	transverse isotropy with a tilted symmetry axis
v_{p0}	P-wave vertical velocity
v_{s0}	shear-wave vertical velocity
ε , δ and γ	three non-dimensional Thomsen's anisotropic parameters
qP	quasi-P wave
qSV	quasi-SV wave
qSH	quasi-SH wave
σ , η and ζ	anisotropy parameters based on Thomsen's parameters
C^{eff}	stiffness tensors of the effective medium
C^0	stiffness tensors of the isotropic background medium
C^1, C^2	1st order and 2nd order stiffness tensor corrections
e	fracture density
a	crack radius

α	aspect ratio
ϕ	porosity
S^{eff}	compliance tensors of the effective medium
S^0	compliance tensors of the isotropic background medium
S^1	compliance tensors of included fractures
S_N, S_T	normal and tangential compliance tensors
R and T	radial and transverse components
S1 and S2	fast S1-wave and slow S2-wave
$v_2(\theta)$	azimuthal nmo velocity of seismic waves
θ	azimuth angle
v_{2-0^0}	NMO velocity along the fracture direction
v_{2-90^0}	NMO velocity along the fracture normal direction
t	two-way traveltime of seismic waves
M_{pp}	P-wave reflection coefficient
φ	incident angle
A	AVO intercept
B	AVO gradient
D	AVO curvature
B_0	conventional isotropic AVO gradient
B_1	anisotropic AVO gradient
9C	nine components seismic
4C	four components seismic
SV-wave	shear-wave polarised in the vertical plane
SH-wave	Shear-wave polarised in the horizontal plane
P-SV1 (PSV1)	fast PS-converted wave
P-SV2 (PSV2)	slow PS-converted wave
SV-P	SV-P converted wave
P-SV	P-SV converted wave
OBC	ocean-bottom cable
OBS	ocean-bottom sensor
CMP	common-middle-point
CCP	common-conversion-point
ACP	asymptotic common-conversion-point
Z	reflector depth
t_{ps}	two-way ps-converted wave traveltime
v_p	P-wave velocity
v_s	shear-wave velocity
x	source-receiver offset
v_{ps}	PS-wave velocity
t_{ps0}	two-way PS-converted wave vertical traveltime
R	velocity ratio ($R = V_p / V_s$)

A_4 and A_5	non-hyperbolic coefficients
x_c	conversion point offset
t_{p0}	two way P-wave vertical traveltimes
t_{s0}	two way shear-wave vertical traveltimes
R_0	vertical velocity ratio ($R_0 = V_{p0} / V_{s0}$)
R_{eff}	effective velocity ratio
v_{ps2}	PS-converted wave NMO velocity
χ_{eff}	PS-converted wave anisotropy parameter
κ_{eff} and m_4	Non-hyperbolic terms for the PS-converted wave

Chapter 3

X-Y coordinates	inline and crossline components
β	fracture direction

Chapter 4

CRG	common receiver gather
SN	signal-to-noise ratio
β	fracture direction
NE	northeast
W-E	west-east
N-S	north-south
NNE	north-northeast

Chapter 5

β	fracture direction
v_{p2}	P-wave NMO velocity
v_{p2-0^o}	P-wave NMO velocity along the fracture direction
v_{p2-90^o}	P-wave NMO velocity along the fracture normal direction
$v_{S_1 2}$	S1-wave NMO velocity
$v_{S_2 2}$	S2-wave NMO velocity
$v_{S_1 2-0^o}$	S1-wave NMO velocity along the fracture direction
$v_{S_1 2-90^o}$	S1-wave NMO velocity along the fracture normal direction
$v_{S_2 2-0^o}$	S2-wave NMO velocity along the fracture direction
$v_{S_2 2-90^o}$	S2-wave NMO velocity along the fracture normal direction
$v_{psv_1 2}$	P-SV1 wave NMO velocity

$v_{psv_2 2}$	P-SV2 wave NMO velocity
$v_{psv_1 2-0^O}$	P-SV1 wave NMO velocity along the fracture direction
$v_{psv_1 2-90^O}$	P-SV1 wave NMO velocity along the fracture normal direction
$v_{psv_2 2-0^O}$	P-SV2 wave NMO velocity along the fracture direction
$v_{psv_2 2-90^O}$	P-SV2 wave NMO velocity along the fracture normal direction
$t_{S_1 0}$	one-way S1-wave vertical traveltime
$t_{S_2 0}$	one-way S2-wave vertical traveltime
t_{psv_1}	two-way P-SV1 wave traveltime
t_{psv_1}	two-way P-SV2 wave traveltime
$t_{psv_1 0}$	two-way P-SV1 wave vertical traveltime
$t_{psv_2 0}$	two-way P-SV2 wave vertical traveltime
v_p	P-wave base velocity
Δ_p	P-wave velocity perturbation
v_{S_1}	S1-wave base velocity
Δ_{S_1}	S1-wave velocity perturbation
v_{S_2}	S2-wave base velocity
Δ_{S_2}	S2-wave velocity perturbation
ω	velocity ratio ($\omega = v^2_{2-0^o} / v^2_{2-90^o}$)
v_{psv_1}	P-SV1 wave base velocity
Δ_{psv_1}	P-SV1 wave velocity perturbation
v_{psv_2}	P-SV2 wave base velocity
Δ_{psv_2}	P-SV2 wave velocity perturbation

Chapter 7

X/Z	offset-to-depth ratio
Δt	azimuthal moveout difference
ΔT	time delay between split PS-converted waves

Chapter 8

SEG-Y	data format of the Society of Exploration Geophysicists
SU	Seismic Unix
UTM	Universal Transverse Mercator
ESE	east-southeast
WNW	west-northwest
SSW	south-southwest
ENE	east-northeast

Chapter 1 Introduction

1.1 Seismic anisotropy

Seismic anisotropy usually refers to the phenomenon in which seismic velocities vary with the direction of propagation of seismic waves in rocks. Seismological studies on anisotropy began in the late 19th century and went through slow advancement until the 1980s. Following the advent of wide-azimuth seismic acquisition, the application of seismic anisotropy in the hydrocarbon industry has gained wide acceptance in the last three decades (e.g. Crampin, 1984; Helbig, 1983; Thomsen, 1986). Much work has been done on two major applications of seismic anisotropy. The first one is the use of seismic anisotropy in seismic data processing for improved imaging (e.g. Alkhalifah and Tsvankin, 1995; Li and Yuan, 2003). The second is using anisotropic parameters to interpret subsurface structures and rock properties (e.g. Bakulin et al., 2000; Chapman, 2003). There are two common types of anisotropy in sedimentary basins where seismic exploration is carried out: transverse isotropy with a vertical symmetry axis, usually referred to as vertical transverse isotropy (VTI), and transverse isotropy with a horizontal symmetry axis, or horizontal transverse isotropy (HTI). VTI can be induced by a stack of horizontal thin layers, such as sedimentary sequences, shales, etc., whilst HTI can be caused by a set of vertical fractures. The combination of VTI and HTI gives rise to orthorhombic anisotropy, such as induced vertical fractures in horizontally layered shales, or two orthogonal sets of vertical fractures. Both HTI and orthogonal anisotropy can cause azimuthal variations in seismic attributes, e.g., seismic velocity,

amplitude, etc, which is referred to as azimuthal anisotropy. This thesis will focus on the azimuthal anisotropy induced by HTI.

1.2 Multicomponent Seismics

Seismic reflection surveys using compressional P-waves have been performed in hydrocarbon exploration for many years. P-wave data are widely available and of high quality, which makes the use of P-wave technology dominant in seismic exploration (Sheriff and Geldart, 1982). However shear-wave information can be needed when P-wave data fails to provide satisfactory results, such as in the context of seismic imaging through gas clouds, fracture characterization, etc. Shear-wave data can provide additional information because shear-waves and P-waves have different polarisation directions and react to Earth's properties in different ways (Shearer, 2009). Moreover, shear-waves are found to be more sensitive to seismic anisotropy. However, pure shear-wave data are not widely available due to the higher cost of acquisition and lower data quality, compared to P-waves(Garotta, 1999).

Alternatively, obtaining shear-wave information from PS-converted wave data has proved to be a more efficient method. PS-converted waves normally refer to mode conversion from a downgoing P-wave leg to an upgoing shear-wave leg, occurring at layer interfaces. PS-converted wave data are acquired by using conventional P-wave sources and three-component receivers, which is much easier than shear-wave surveys using pure shear-wave sources. The PS-converted wave, due to its shear-wave content, is more sensitive to the internal structure of media than the P-wave (Crampin, 1993). Pure shear-waves data are more affected by the attenuative near surface and phase changes at relatively short offsets(Guevara, 2000; Stewart et al., 2002). Therefore, PS-converted wave seismic data is usually of better quality than pure shear-wave seismic data. Moreover, PS-converted waves are more sensitive to seismic anisotropy due to its upgoing shear-wave leg (Thomsen, 1988, 2001). Analysing anisotropic effects shown on PS-converted wave data can provide more beneficial information on rock properties than the analysis of P-wave anisotropy alone.

PS-converted wave data acquisition has been successfully implemented both on land and in the marine environment for many years (Garotta, 1999). Due to the

asymmetric raypath, processing PS-converted wave data is more complicated than P-wave data and this has attracted interests in processing PS-converted wave seismic data. These include the use of PS-converted wave data to improve subsurface imaging by using the shear-wave capacity of travelling through gas cloud (e.g. Olofsson et al., 2003), lithology discrimination by taking advantage of the P-to-S velocity ratio(e.g. Hardage et al., 2006; Qian et al., 2007b), and fracture detection by analysing shear-wave splitting (e.g. Dai et al., 2011; Li, 1997; Mattocks et al., 2005).

As seismic acquisition technology advances, more wide-azimuth P and PS-wave seismic data are becoming available, which is beneficial to more accurate imaging of the sub-surface and more accurate characterisation of subsurface fractures. This thesis focuses on the analysis of wide-azimuth PS-converted wave seismic data.

1.3 Azimuthal anisotropy and fracture detection

Fractures can affect porosity and permeability of hydrocarbon reservoirs. Therefore Fracture detection and the estimation of fracture properties are important for reservoir characterisation and hydrocarbon production (Nelson, 2001). Effective medium theories are often used to model wave propagation in fractured media and to recover fracture parameters from seismic attributes. According to these effective medium theories (Hudson, 1980; Schoenberg, 1980), fractures often give rise to azimuthal anisotropy, which is usually observed in wide-azimuth seismic data and used to estimate fracture orientations and densities through the analysis of azimuthal variations of P-wave attributes and shear-wave splitting.

The analysis of the azimuthal variations of P-wave attributes has been well studied and been frequently used to detect fractures. Azimuthal P-wave NMO velocity ellipses are important representations of fracture properties (e.g. Li et al., 2003; Tsvankin, 1997b). P-wave azimuthal moveout analysis has also been successfully applied in many exploration regions (e.g. Corrigan et al., 1996; Li, 1999; Lynn et al., 1999b), as well as azimuthal variations of P-wave reflectivity (e.g. Rüger, 1998; Rüger and Tsvankin, 1997). Shear-wave splitting is another important anisotropic feature induced by vertically aligned fractures. The splitting effect has been observed

in many laboratory experiments and is directly related to fracture properties (Tillotson et al., 2012; Xu and King, 1989). Using Alford rotation (Alford, 1986) , or linear transform techniques (Li and Crampin, 1993), fracture direction and density can be estimated. Wide-azimuth PS-converted wave data are also beneficial for the analysis of azimuthal anisotropy and fracture characterisation. Due to the upgoing shear-wave leg, PS-converted waves also undergo the splitting effect.

Current studies of PS-converted waves for fracture detection mainly focus on PS-converted wave splitting (e.g. Jianming et al., 2009; Li, 1998; Simmons Jr, 2008; Yue et al., 2013). There is a lack of studies on the analysis of azimuthal variations of PS converted-wave attributes for fracture detection (e.g. Dai and Li, 2010; Mattocks et al., 2005), and this thesis addresses this issue.

1.4 Motivations and objectives

I have five major objectives:

1. I demonstrate the robustness of shear-wave splitting for fracture characterisation. PS-converted wave splitting has been frequently studied to obtain fracture directions and densities (e.g. Cheng et al., 2009; Horne, 2003; Yue et al., 2013). I use synthetic data to introduce basic methods required for the splitting analysis. I also apply the splitting analysis to Sanhu 3D3C seismic data to obtain fracture properties.
2. I study the azimuthal variation of the NMO velocity in PS-converted waves. As mentioned previously, P-wave azimuthal variations have been intensively studied and widely used to obtain fracture properties and to improve imaging (e.g. Li, 1999; Rüger, 1998; Tsvankin, 1997b). The azimuthal variations of P-wave NMO velocity, moveout and AVO response are all frequently applied in fractured reservoir characterisation (e.g. Hall and Kendall, 2003; Ikelle, 1997; Li et al., 2003; Tod et al., 2007; Wang and Li, 2006). However, in comparison, PS-converted wave azimuthal variations are not well studied. The theory of PS-converted wave velocity variation is not fully established (Qian et al., 2007a; Thomsen, 1999), although anisotropic processing of PS-converted waves has attracted intensive interest (Yuan, 2001). In this thesis, I fill this gap by developing theory to describe the azimuthal variation of PS-converted wave

moveout and velocity, and evaluate their accuracy and sensitivity for parameter inversion.

3. I build a processing workflow to use the velocity ellipse to improve imaging. In the past, the processing and analysis of PS-converted-waves are mainly focused on the horizontal radial component, and the horizontal transverse component is often ignored (e.g. Dai and Li, 2010). In fact, the azimuthal variations of PS-converted wave data are also complicated by the splitting effect (e.g. Simmons Jr, 2008), and analysis of the variations using the radial component alone can give misleading results. Therefore, there is a need to build an appropriate workflow for compensating for the azimuthal variation. Considering this, I develop a practical workflow to compensate for the azimuthal variations of PS-converted waves. Specific methods are introduced to complete the compensation procedure. The separation of split PS-converted waves is necessary before applying appropriate azimuthal analysis. Considering processing efficiency and the signal-to-noise ratio, azimuth binning is also critical for the application of azimuthal analysis of PS-converted waves, and a least-square method is developed to obtain elliptical velocity models from azimuthal velocity analysis.
4. I compare the PS-converted wave splitting effects with azimuthal variations of NMO velocities, and evaluate their merits in terms of fracture characterisation. Although azimuthal variations of both PP and PS-converted waves have been used to characterise fractured reservoirs (e.g. Mattocks et al., 2005; Olofsson et al., 2003), PS-converted wave splitting analysis is still regarded as a better method to predict fracture properties. However, there is still a lack of comparative studies in the use of P- and PS converted-wave azimuthal attributes, and PS-converted wave splitting for fracture detection. In this thesis, I fill this gap through full-wave modelling studies to compare and evaluate the merits of azimuthal variations of PP and PS attributes as well as PS-converted wave splitting for fracture detection. I compare their abilities for distinguishing fracture saturations. Moreover, in the case of multiple HTI layers, I develop a specific layer-stripping method to analyse both the azimuthal variations and the splitting effect of PS-converted waves.

5. I apply all methods to real data for characterising fractured reservoirs using wide-

azimuth PS-converted wave data. Daqing 3D3C seismic data are studied in these applications.

1.5 Outline of the thesis

This thesis contains eight chapters. Following Chapter 1, which is the general introduction to this thesis, the other chapters, with short descriptions, are:

Chapter 2 I review PS-converted wave exploration in anisotropic media. Fundamental theories of seismic anisotropy and PS-converted waves are reviewed. Effective medium theory and its applications to fracture characterisation are introduced as well, forming the essential theoretical basis of this thesis.

Chapter 3 I introduce basic methods to process PS-converted wave seismic data in the presence of HTI anisotropy. Separation of split PS-converted waves is essential to PS-converted wave seismic data processing and interpretation.

Chapter 4 I demonstrate the robustness of shear-wave splitting for fracture characterisation by studying Sanhu 3D3C data. I also provide the geological background of the Sanhu field and show how PS-converted wave data is influenced by the splitting effect. A practical workflow is developed to compensate for PS-converted wave splitting. Finally the parameters acquired from splitting analysis are related to fracture properties.

Chapter 5 I study the anisotropic parameters for HTI media. The azimuthal variations of P- and shear-waves are both studied. I derive elliptical equations used to describe azimuthal variations in PS-converted wave velocities and moveouts in HTI media. The accuracy of the velocity ellipses of PS-converted waves is also tested. Using synthetic data, I study the application of using PS-converted wave azimuthal variations for fracture detection.

Chapter 6 I discuss essential methods used in data processing to analyse the azimuthal variations of PS-converted waves. Practical issues associated with these processing methods are also studied. Finally, a synthetic study is performed to show how the analysis is performed and imaging quality is improved.

Chapter 7 I compare azimuthal variations with the PS-converted wave splitting effect, in terms of fracture characterisation. Influences of different fluid saturations on azimuthal variations are also discussed. A specific layer-stripping algorithm is also developed to deal with models containing multiple HTI layers.

Chapter 8 I apply the methods developed in previous chapters to Daqing 3D3C data. The general geological background is firstly provided and data evaluation is then performed. Azimuthal analysis and splitting analysis are both applied to this dataset. While the imaging quality is improved by the analysis of azimuthal variations, fracture properties are also obtained in carrying out fracture characterisation.

Chapter 9 I give my conclusions on the results and findings from previous chapters. I also discuss some remaining questions relevant to this PhD study and give some recommendations for future work.

1.6 Datasets used in thesis

Both synthetic and field datasets are analysed in this thesis. Several synthetic datasets were simulated by considering dry and water-saturated fractures, with different fracture densities. Two sets of field data are studied in this PhD study. Both datasets are 3D3C datasets that have been pre-processed by experienced data processors.

To clearly demonstrate the azimuthal variation induced by vertical fractures, the synthetic data is based on a three-layer model. The first and bottom layers are both isotropic. The second layer is a HTI layer induced by vertically aligned fractures. Those synthetic datasets are used to perform analysis of azimuthal variations and PS-converted wave splitting. A synthetic model containing multiple HTI layers is also created, to demonstrate the application of the layer-stripping algorithm. All synthetic data are acquired with intensive azimuthal coverage, which provides sufficient accuracy to perform azimuthal analysis.

Two sets of field data are analysed in this thesis. The first dataset is Sanhu 3D3C dataset. It is acquired in Sanhu depression, which is located in Qaidam basin, northwest China. This field is famous for its natural gas storage, which has significant influence on P-wave data. This 3D3C dataset is acquired for using PS-

converted wave seismic data to detect fractures and improve imaging quality. The application of splitting analysis to the Sanhu 3D3C data is accomplished in Chapter 4. The second dataset is Daqing 3D3C seismic data, which is acquired in Daqing Oilfield, northeast China. Daqing Oilfield is one of the most productive oil fields in China. This 3D3C dataset is acquired for the use of wide-azimuth PS-converted wave seismic data to improve fractured reservoir characterisation. The Daqing 3D3C data study is provided in Chapter 8.

1.7 Software used in this thesis

Several software packages including 'ANISEIS', 'Seismic Unix', 'CxTools', 'MatLab' are used to complete this thesis. All synthetic datasets in this thesis are created by 'ANISEIS' software. 'ANISEIS' is a flexible computer modelling system for calculating synthetic seismograms from point sources in plane-layered anisotropic and cracked models (Taylor, 1990). A more detailed introduction to ANISEIS is provided in Appendix A. Vertical seismic profiles, surface to surface reflections and cross-hole shooting are some of the model geometries that can be accommodated. Isotropic modelling is available as a by-product. Four component output is available for sea-floor models. The methods used in ANISEIS are based on plane-wave analysis and involve the reflectivity method and accumulation of plane-waves for different horizontal slownesses and horizontal azimuths. For models with a vertical axis of symmetry, including the isotropic case, analytic integration over azimuth simplifies the calculation. This also provides an inexpensive approximation for more complicated models.

'Seismic Unix' is a famous open-source seismic processing package developed by Center for Wave Phenomena (CWP) at the Colorado School of Mines. It provides basic tools for seismic data processing with considerations of anisotropic effects. In 'Seismic Unix', routines can be connected by the pipeline facility to perform complicated jobs. It also supports efficient data visualisation in LINUX or UNIX systems. Besides, its libraries allow me to develop the specific algorithms used in this thesis.

'CxTools' is a processing package designed for multi-component seismic data. It has been developed by students and staff of Edinburgh Anisotropy Project (EAP) and is

now maintained by Dr Hengchang Dai. ‘CxTools’ is built in the ‘Seismic Unix’ platform, which makes it easy to switch processing tools between these two packages. ‘CxTools’ also provide GUI (Graphic User Interface) tools for parameter estimation and parallel prestack migration on a PC cluster.

‘MatLab’ is a famous high performance interactive software package for scientific and engineering computations. It provides a massive package of computation functions, which greatly facilitate data analysis carried out in this PhD study. It also provides well-designed plotting facilities, which enables a number of figures shown in this thesis to be efficiently generated.

Chapter 2

Basic concepts of anisotropy in PS-converted wave seismic waves

2.1 Introduction

In this chapter, I review basic concepts of seismic anisotropy including parameterization and classification, which form the theoretical basis of this PhD study. I also review anisotropy produced by fractures, and applications of fracture characterisation using seismic methods. Finally, I give a review of theories and applications of PS-converted wave seismic data including acquisition and processing.

2.2 Anisotropy and elastic tensor

For most of the last century, seismic exploration theories and applications assumed that seismic waves propagate equally fast in all directions. This assumption of isotropy was made for mathematical and computational convenience. Actually, the rocks which are dealt with in hydrocarbon exploration are usually anisotropic. Anisotropy can be caused by dominant alignments of minerals, cracks and fractures, and geological formations with sedimentary layers. When these effects are

considered at a scale smaller than the length of seismic waves, this introduces the concept of seismic anisotropy.

Seismic anisotropy

Seismic anisotropy is recognised as the variation of seismic attributes with the direction of seismic wave propagation. Commonly studied seismic attributes include seismic velocity, moveout, amplitude, attenuation and AVO (Amplitude Versus Offset) response. Those directional variations of seismic attributes certainly affect seismic data acquisition, processing and interpretation. Consideration and analysis of anisotropic effects are critically important in providing better results in hydrocarbon exploration and production.

It is important to recognise that seismic wave propagation is affected by anisotropy. In anisotropic media, polarisations of body waves are not necessarily normal or parallel to the wave propagation directions (Winterstein, 1990). The expressions 'quasi-compressional' wave (qP-wave) and 'quasi-shear' wave (qS1-and qS2-wave) are usually used to refer P-wave and shear-waves in anisotropic media.

Elastic tensors

Seismic anisotropy can be explained by the classic Hooke's law, in which the stress and strain tensors are related by stiffness or compliance tensors (Sheriff and Geldart, 1982).

Stress is defined as force per unit area. If a cube of material is taken into consideration, the stress upon each of the six faces of the material can be measured in various directions, as shown in Figure 2- 1. Subscripts 1, 2 and 3 denote the X_1, X_2 and X_3 axis, respectively. When the force is perpendicular to an area, the stress is defined as normal stress (σ_{ii}, i=1, 2 and 3). When the force is tangential to an element area, the stress is defined as shearing stress (σ_{ij}, $i \neq j$). For example, σ_{12} represents the stress parallel to the axis X_2 acting upon the X_2-X_3 plane. It can be seen that any stress on a material can be decomposed into normal and shearing stresses. Moreover, considering static equilibrium, which requires that the summation of moments with

respect to an arbitrary point is zero, the stress tensors are symmetric. In general the relation $\sigma_{ij}= \sigma_{ji}$ ($i \neq j$) can be assumed.

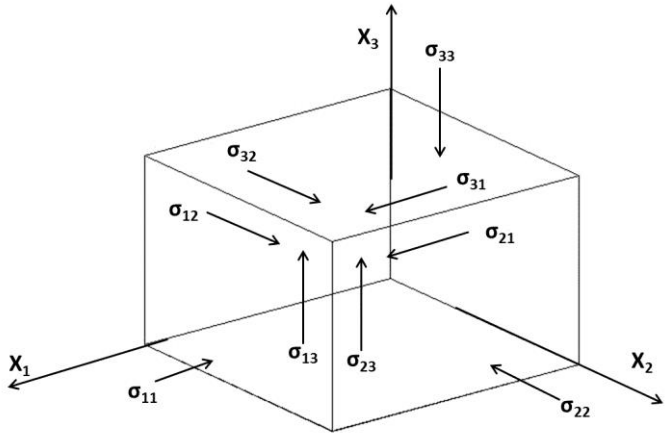

Figure 2- 1: Components of stress tensors on a cube of material

Strain is defined as the relative change in the position of points within a body that has undergone deformation. A two dimensional example is shown in Figure 2- 2, which is used to explain strain tensors. In this example, a rectangle indicated by ABCD is moved and deformed into A ' B ' C ' D '. $u(x_1, x_2)$ and $v(x_1, x_2)$ are displacement vectors of point A along X_1 and X_2 axis, respectively. Displacements of point A and C can be defined as:

$$\left.\begin{aligned} A: u &= u(x_1, x_2) + \frac{\partial u}{\partial x_2} dx_2, \quad v = v(x_1, x_2) + \frac{\partial v}{\partial x_2} dx_2 \\ B: u &= u(x_1, x_2) + \frac{\partial u}{\partial x_1} dx_1, \quad v = v(x_1, x_2) + \frac{\partial v}{\partial x_1} dx_1 \end{aligned}\right\} \qquad (2\text{- }1)$$

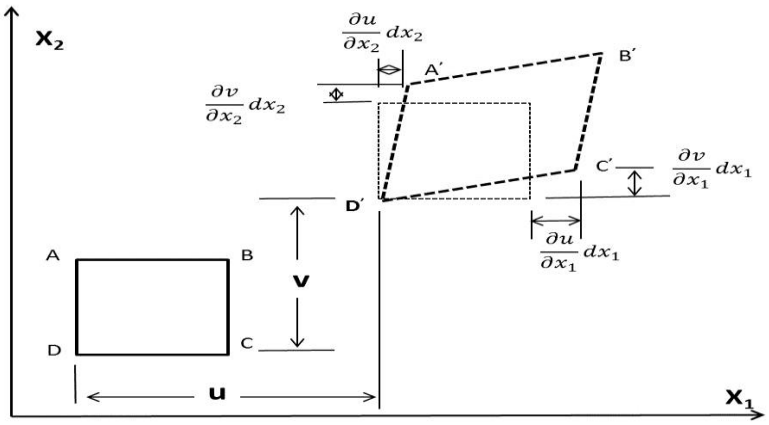

Figure 2- 2: Analysis of two-dimensional strain

According to the definition of strain tensor:

$$\left.\begin{aligned}\varepsilon_{11} &= \frac{\partial u}{\partial x_1}\\ \varepsilon_{22} &= \frac{\partial v}{\partial x_2}\\ \varepsilon_{12} &= \frac{\partial v}{\partial x_1} + \frac{\partial u}{\partial x_2}\end{aligned}\right\} \tag{2- 2}$$

ε_{11} and ε_{22} are relative changes along the X_1 and X_2 axis, which are defined as normal strains. ε_{12} is the measurement of shape changes in the X_1-X_2 plane, which are defined as shearing strains. Extending the analysis into three dimensions, the displacement vector w along the X_3 axis is introduced. Then the strain tensors in three dimensions are:

$$\left.\begin{aligned}\varepsilon_{11} &= \frac{\partial u}{\partial x_1}\\ \varepsilon_{22} &= \frac{\partial v}{\partial x_2}\\ \varepsilon_{33} &= \frac{\partial w}{\partial x_3}\\ \varepsilon_{12} &= \frac{\partial v}{\partial x_1} + \frac{\partial u}{\partial x_2}\\ \varepsilon_{23} &= \frac{\partial w}{\partial x_2} + \frac{\partial v}{\partial x_3}\\ \varepsilon_{31} &= \frac{\partial u}{\partial x_3} + \frac{\partial w}{\partial x_1}\end{aligned}\right\} \tag{2- 3}$$

where the similar symmetry ε_{ij} and ε_{ji} ($i \neq j$) can also be established.

The relationship between stress and stain tensors of a material can be built by Hooke's law, which is given by:

$$\sigma_{ij} = C_{ijkl}\varepsilon_{kl} \quad (i,j,k,l=1,2,3) \tag{2- 4}$$

where σ_{ij} are the strain tensors and ε_{kl} are the stress tensors. C_{ijkl} are the stiffness tensors. C_{ijkl} is a fourth-order tensor that has 81 constants. Considering the symmetry of strain and stress tensors, the symmetric relation $C_{ijkl} = C_{jikl} = C_{jilk} = C_{ijkl}$ can be obtained. Then 81 ($81=3^4$) constants are reduced to 36 independent constants. The

Voigt notation is usually used to simplify the denotation of those constants by the following convention:

ij(kl)	***11***	***22***	***33***	***23,32***	***13,31***	***12,21***
M(N)	***1***	***2***	***3***	***4***	***5***	***6***

Table 2- 1: Voigt notations of stiffness tensors

Four subscripts are replaced by two subscripts and the stiffness can be represented as:

$$\begin{pmatrix} C_{11} & C_{12} & C_{13} & C_{14} & C_{15} & C_{16} \\ C_{21} & C_{22} & C_{23} & C_{24} & C_{25} & C_{26} \\ C_{31} & C_{32} & C_{33} & C_{34} & C_{35} & C_{36} \\ C_{41} & C_{42} & C_{43} & C_{44} & C_{45} & C_{46} \\ C_{51} & C_{52} & C_{53} & C_{54} & C_{55} & C_{56} \\ C_{61} & C_{62} & C_{63} & C_{64} & C_{65} & C_{66} \end{pmatrix} \quad (2\text{- }5)$$

If the symmetry $C_{MN} = C_{NM}$ (*N,M=1,2,3,4,5,6*) is introduced, the number of independent constants is further reduced to 21. In other words, 21 constants are required for the most complicated material or the material with the lowest symmetry.

Alternatively, the relationship between strain and stress tensors can be described by a different form of Hooke's law:

$$\varepsilon_{kl} = S_{ijkl}\sigma_{ij} \text{ (i,j,k,l=1,2,3)} \quad (2\text{- }6)$$

where s_{ijkl} are called compliance tensors. s_{ijkl} is similar to C_{ijkl} and also has 21 independent constants. In this thesis, C_{ijkl} is used to describe different types of anisotropic media.

2.3 Common types of anisotropy and their origin

A variety of rocks and geological formations can be involved in seismic exploration. Different cases result in different anisotropic models, which also enable geophysicists to develop specific theories and methods to study anisotropic effects on seismic data. Usually, the complexity of a given material is determined by the number of independent constants contained in the stiffness tensors C_{ijkl}. Therefore,

different types of anisotropy can be defined. The most complicated anisotropic medium requires 21 independent constants. It is extremely difficult to study this type of anisotropic model because too many parameters are involved. In practice, some symmetric features of certain rocks and geological formations can be introduced to reduce the number of independent constants.

Depending on the different numbers of independent constants, eight symmetry systems are usually used to describe anisotropic media (Mavko et al., 2009). There are Isotropic, Cubic, Hexagonal, Tetragonal, Trigonal, Orthorhombic, Monoclinic and Triclinic systems. The number of independent constants for each type of anisotropy is provided in Table 2- 2. However in the context of geophysical applications, only Isotropic, Hexagonal, Orthorhombic, Monoclinic and Triclinic systems are studied.

Type of anisotropy	Number of independent constants
Isotropy	2
Cubic	3
Hexagonal	5
Tetragonal	6
Trigonal	6
Orthorhombic	9
Monoclinic	13
Triclinic	21

Table 2- 2: Number of independent constants for different anisotropic media

Isotropy

Isotropy has the highest symmetry, and is the simplest type of elastic medium. In an isotropic medium, seismic properties are not dependent on any direction. It forms the basis of study for any anisotropic media, although it is not a valid representation of the Earth. Only two independent constants are required to describe this special type of elastic medium. The stiffness tensor can be written as:

$$\begin{pmatrix} C_{11} & C_{11}-2C_{44} & C_{11}-2C_{44} & 0 & 0 & 0 \\ C_{11}-2C_{44} & C_{11} & C_{11}-2C_{44} & 0 & 0 & 0 \\ C_{11}-2C_{44} & C_{11}-2C_{44} & C_{11} & 0 & 0 & 0 \\ 0 & 0 & 0 & C_{44} & 0 & 0 \\ 0 & 0 & 0 & 0 & C_{44} & 0 \\ 0 & 0 & 0 & 0 & 0 & C_{44} \end{pmatrix} \quad (2\text{-}7)$$

The stiffness tensor is frequently replaced by Lamé's constants λ and μ for convenience:

$$C_{11} = \lambda + 2\mu \qquad C_{44} = \mu \quad (2\text{-}8)$$

Hexagonal anisotropy

The hexagonal anisotropy is often named as transverse isotropy with a single symmetry axis. This type of anisotropy is more realistic than isotropy. The seismic properties are determined by the angle between the seismic wave propagation direction and the symmetry axis. Specifically, seismic properties do not have directional variations in the plane perpendicular to the symmetry axis. Five independent constants are required to describe the hexagonal anisotropy

Two most realistic models are VTI (transverse isotropy with a vertical symmetry axis) and HTI (transverse isotropy with a horizontal symmetry axis). They are individually described below.

VTI model anisotropy possesses a vertical symmetry axis, and is displayed in Figure 2- 3(a). The VTI stiffness tensors are:

$$\begin{pmatrix} C_{11} & C_{12} & C_{13} & 0 & 0 & 0 \\ C_{12} & C_{11} & C_{13} & 0 & 0 & 0 \\ C_{13} & C_{13} & C_{33} & 0 & 0 & 0 \\ 0 & 0 & 0 & C_{44} & 0 & 0 \\ 0 & 0 & 0 & 0 & C_{44} & 0 \\ 0 & 0 & 0 & 0 & 0 & \frac{1}{2}(C_{11}-C_{12}) \end{pmatrix} \quad (2\text{-}9)$$

This model is usually considered as approximation of formations containing thin horizontal layers. Horizontally aligned microstructures, which are commonly found in shales, also give rise to a VTI model. Therefore the VTI model is an important

type of anisotropy, which is also relatively simple to implement in seismic exploration.

If the symmetry axis is horizontal, as shown in Figure 2- 3(b), the type of hexagonal anisotropy is specifically referred to as the HTI model. The HTI stiffness tensors are:

$$\begin{pmatrix} C_{11} & C_{13} & C_{13} & 0 & 0 & 0 \\ C_{13} & C_{11} & C_{33}-2C_{44} & 0 & 0 & 0 \\ C_{13} & C_{33}-2C_{44} & C_{33} & 0 & 0 & 0 \\ 0 & 0 & 0 & C_{44} & 0 & 0 \\ 0 & 0 & 0 & 0 & C_{55} & 0 \\ 0 & 0 & 0 & 0 & 0 & C_{55} \end{pmatrix} \quad (2\text{- }10)$$

This type of anisotropy is often induced by vertically aligned fractures, which is usually called azimuthal anisotropy. Shear-wave splitting often results from shear-wave propagation through a medium with HTI anisotropy, and this can be used to determine fracture properties. Knowledge of fracture orientations and densities are very important requirements in drilling programs. Therefore, the study of the HTI model is also important in seismic exploration.

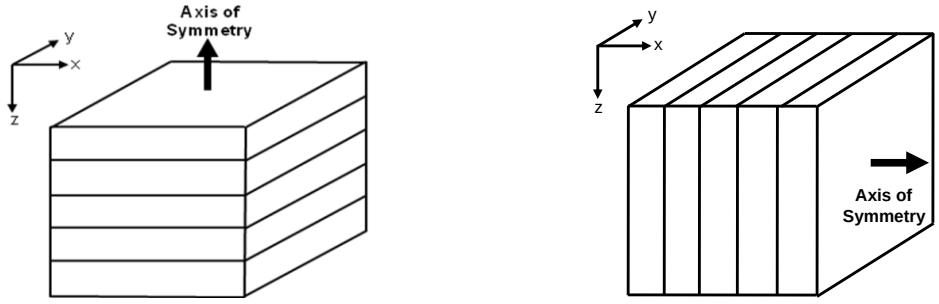

(a) (b)

Figure 2- 3: VTI model (a) and HTI model (b)

There is another type of hexagonal anisotropy, Tilted Transverse Isotropy (TTI) which contains a tilted symmetry axis. The symmetry axis is neither vertical nor horizontal, and one example consists of dipping thin layers. The TTI model is more complicated than the VTI and HTI models and is less frequently implemented in seismic exploration.

Orthorhombic anisotropy

This type of anisotropy is more complex than hexagonal anisotropy, and requires nine independent constants. The stiffness tensors have the form:

$$C = \begin{pmatrix} C_{11} & C_{12} & C_{13} & 0 & 0 & 0 \\ C_{12} & C_{22} & C_{23} & 0 & 0 & 0 \\ C_{13} & C_{23} & C_{33} & 0 & 0 & 0 \\ 0 & 0 & 0 & C_{44} & 0 & 0 \\ 0 & 0 & 0 & 0 & C_{55} & 0 \\ 0 & 0 & 0 & 0 & 0 & C_{66} \end{pmatrix} \tag{2- 11}$$

One typical cause of orthorhombic anisotropy is the incorporation of vertical fractures in thin horizontal layers (Wild and Crampin, 1991). Two or more orthogonal fracture systems, or two identical systems of fractures making an arbitrary angle with each other also result in orthorhombic anisotropy (Tsvankin, 1997a). Orthorhombic anisotropy is more difficult to work with than hexagonal anisotropy because more independent constants are involved.

Monoclinic anisotropy

Monoclinic anisotropy is described by 13 independent constants:

$$C = \begin{pmatrix} C_{11} & C_{12} & C_{13} & 0 & C_{15} & 0 \\ C_{12} & C_{22} & C_{23} & 0 & C_{25} & 0 \\ C_{13} & C_{23} & C_{33} & 0 & C_{35} & 0 \\ 0 & 0 & 0 & C_{44} & 0 & C_{46} \\ C_{15} & C_{25} & C_{35} & 0 & C_{55} & 0 \\ 0 & 0 & 0 & C_{46} & 0 & C_{66} \end{pmatrix} \tag{2- 12}$$

If multiple sets of fractures systems are encountered, it often gives rise to monoclinic anisotropy (Schoenberg and Sayers, 1995). A set of vertical fractures included in a background medium without a horizontal plane of symmetry also results in monoclinic anisotropy (Grechka et al., 2000). This type of anisotropy is more realistic but difficult to apply due to the large number of independent constants in the stiffness tensors.

Triclinic Anisotropy

The most complicated case is triclinic anisotropy, which has 21 independent constants:

$$C = \begin{pmatrix} C_{11} & C_{12} & C_{13} & C_{14} & C_{15} & C_{16} \\ C_{12} & C_{22} & C_{23} & C_{24} & C_{25} & C_{26} \\ C_{13} & C_{23} & C_{33} & C_{34} & C_{35} & C_{36} \\ C_{14} & C_{24} & C_{34} & C_{44} & C_{45} & C_{46} \\ C_{15} & C_{25} & C_{35} & C_{45} & C_{55} & C_{56} \\ C_{16} & C_{26} & C_{36} & C_{46} & C_{56} & C_{66} \end{pmatrix} \quad (2\text{- }13)$$

Although elastic wave propagation in triclinic media has been theoretically studied (Musgrave, 1970), estimation of anisotropic parameters in the context of seismic exploration is still very difficult due to the large number of independent constants.

2.4 Anisotropic parameters

Independent constants in stiffness tensors define different anisotropy systems, which can be used to describe seismic wave velocities along different directions (Rudzki, 1911). However, this type of description is not efficient, and a convenient parameterization is required to facilitate analysis of seismic anisotropy.

Specifically, a weak VTI medium can be considered as a deviation from an isotropic medium. So the isotropic medium may be considered as the reference for the definition of the new parameters. Mathematically and physically, the purest reference is the isotropic average over all directions, since that approach shows no *a priori* preference over any particular direction. However, in geophysics, we recognize that the vertical is a special direction (because the acquisition surface tends to be normal to it). It has therefore been found especially useful to define anisotropy in terms of the deviation from vertical velocity. The new parameters are defined as the combinations of the tensor elements and the density of the medium, which are frequently referred as Thomsen's parameters (Thomsen, 1986):

$$\left.\begin{aligned} v_{p0} &= \sqrt{\frac{C_{33}}{\rho}} \\ v_{s0} &= \sqrt{\frac{C_{44}}{\rho}} \\ \varepsilon &= \frac{C_{11}-C_{33}}{2C_{33}} \\ \gamma &= \frac{C_{66}-C_{44}}{2C_{44}} \\ \delta &= \frac{(C_{13}+C_{44})^2-(C_{33}-C_{44})^2}{2C_{33}(C_{33}-C_{44})} \approx \frac{C_{13}+2C_{44}-C_{33}}{C_{33}} \end{aligned}\right\} \quad (2\text{- }14)$$

where v_{p0} and v_{s0} are the vertical velocities of the P-wave and S-wave, and ε, δ, γ are three non-dimensional combinations which reduce to zero in the case of isotropy, and are called anisotropy parameters. ε and γ are measurements of P-wave anisotropy and shear-wave anisotropy, respectively. δ is more complicated, and it is related to wavefront ellipticity. In a medium with weak anisotropy, $\varepsilon \ll 1$, $\gamma \ll 1$, $\delta \ll 1$. Elliptical anisotropy is defined when $\varepsilon = \delta$.

Based on Thomsen's parameters, the phase velocities of the P-wave, SV-wave and SH-wave in a VTI medium, which represent the qP-wave, qSv-wave and qSH-wave, respectively, can be expressed as:

$$\left.\begin{aligned} v_p(\theta) &\approx v_{p0}[1+\delta\sin^2\theta\cos^2\theta+\varepsilon\sin^4\theta] \\ v_{sv}(\theta) &\approx v_{s0}[1+(\frac{v_{p0}}{v_{s0}})^2(\varepsilon-\delta)\sin^2\theta\cos^2\theta] \\ v_{sh}(\theta) &= v_{s0}[1+\gamma\sin^2\theta] \end{aligned}\right\} \quad (2\text{- }15)$$

where θ is the angle between wave vector and the symmetry axis (the symmetry is vertical in VTI model).

Another parameter σ is introduced to facilitate analysis of seismic anisotropy (Tsvankin and Thomsen, 1994):

$$\sigma = \frac{v_{p0}^2}{v_{s0}^2}(\varepsilon-\delta) \quad (2\text{- }16)$$

σ is used to simplify the description of SV-wave velocity. It can be seen that the it reduces to zero when elliptical anisotropy ($\varepsilon-\delta$) is assumed.

Considering non-hyperbolic effects in moveout, two more anisotropic parameters are introduced (Alkhalifah and Tsvankin, 1995; Tsvankin and Thomsen, 1994):

$$\left.\begin{aligned}\eta &= \frac{\varepsilon-\delta}{(1+2\delta)^2}\left(1+\frac{2\delta}{1-v_{s0}^2/v_{p0}^2}\right)\\ \zeta &= \frac{\sigma}{(1+2\sigma)^2}\left(1+\frac{2\delta}{1-v_{s0}^2/v_{p0}^2}\right)\end{aligned}\right\} \qquad (2\text{-}17)$$

Parameters η and ζ are introduced to control the anisotropic behaviour in long-spread P-wave reflection moveout, and the anisotropic behaviour in intermediate–spread S-wave moveout, respectively,

Similarly, Thomsen's parameters can be extended to a HTI model. In the HTI model, the symmetry axis is horizontal, which can be regarded as a 90-degree-rotation of the VTI model. The results of analysis for VTI media can be extended to the vertical plane that contains the symmetry axis of a HTI medium (the "symmetry-axis plane") by using an "equivalence" between VTI and HTI media (Tsvankin, 1997b). Assuming fracture normal (x_1), strike (x_2), and vertical axis (x_3), Thomsen's anisotropic parameters in a HTI medium can be expressed as (Li, 1999):

$$\left.\begin{aligned}v_{p0} &= \sqrt{\frac{C_{33}}{\rho}}\\ v_{s0} &= \sqrt{\frac{C_{44}}{\rho}}\\ \varepsilon &= \frac{C_{33}-C_{11}}{2C_{11}}\\ \gamma &= \frac{C_{44}-C_{55}}{2C_{55}}\\ \delta &= \frac{(c_{13}+c_{55})^2-(c_{11}-c_{55})^2}{2c_{11}(c_{11}-c_{55})} \approx \frac{c_{13}+2c_{55}-c_{11}}{c_{11}}\end{aligned}\right\} \qquad (2\text{-}18)$$

With Thomsen's parameters for a HTI model, the analysis of azimuthal variations of seismic attributes can be efficiently performed.

2.5 Fracture-induced anisotropy and equivalent medium theory

Fractures of different scales are commonly found in the Earth (Figure 2- 4), which must influence permeability and fluid movement (Nelson, 2001). Specifically, fractures can provide pathways for hydrocarbons, and fluid storage in hydrocarbon reservoirs. Therefore, fractures are critically important to the exploration and development of hydrocarbon reservoirs.

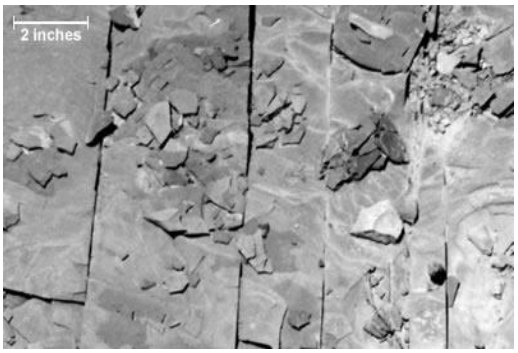

Figure 2- 4: Example of highly fractured shales (Milici and Swezey, 2006)

Different methods can be deployed to obtain fracture information contained in hydrocarbon reservoirs. Core samples, borehole data and log data are capable of providing fracture information but at a small scale (centimeter-scale) in reservoirs. A complete image of fracture information cannot be delivered by this type ofapplication. Discontinuities displayed on seismic images resulting from conventional data processing are often studied by seismic data interpreters to identify large-scale fracture systems (kilometer-scale). This approach is always subject to uncertainties and is not efficient in providing detailed fracture properties. A geostatistic method is another type of method that statistically interpolates data to obtain fracture information. Different results may be produced by different geostatistical methods and rock discontinuities and mineralisation always reduce the accuracy of the data interpolations (Merks, 1992).

It is generally accepted that vertically aligned fractures often give rise to azimuthal anisotropy. Therefore taking azimuthal anisotropy into account in seismic data processing and inversion can bring a direct benefit to fracture characterisation. However this could not be achieved without an equivalent medium theory to describe

the seismic responses in media containing fractures. Based on equivalent medium theory, several different models have been built (Chapman, 2003; Hudson, 1980, 1981; Liu et al., 2000; Schoenberg, 1980; Schoenberg and Sayers, 1995; Thomsen, 1995). Two major equivalent medium theories, and the use of fracture-induced anisotropy to detect fractures, are reviewed below.

Equivalent medium theory has been developed to estimate the effective elastic properties of fractured media, given some fracture parameters. Provided that cracks have idealized shapes and the scale length of fractures is much smaller than the wavelength of seismic waves, a heterogeneous medium containing fractures or cracks can be regarded as an equivalent homogeneous medium(Schoenberg and Sayers, 1995). This equivalent medium has the same overall anisotropic properties as the actual fractured medium. Then the relationship between fracture properties and anisotropic parameters for the equivalent medium can be constructed, which enables description of the anisotropic behaviour of seismic attributes, in order to deduce or invert for fracture information.

Two major equivalent medium theories are widely-used in the study of fractured media. The first one is the Hudson model that is established by incorporating thin, penny-shaped ellipsoidal cracks or inclusions into an isotropic volume, and uses scattering theory (Hudson, 1980, 1981). The stiffness tensors of the effective medium can be given as:

$$C^{eff} = C^0 + C^1 + C^2 \tag{2- 19}$$

where C^0 are stiffness tensors of the isotropic background medium. C^1 and C^2 are the first- and second-order corrections, respectively. C^1 and C^2 are introduced to describe the overall effect as a result of the cracks, and are dependent on crack properties (crack density, crack orientation and crack aspect ratio).

The fracture density *e* is defined as:

$$e = \frac{N}{V} a^3 \tag{2- 20}$$

where a is crack radius, *N/V* is the number of cracks per unit volume. Therefore, the fracture density is linked to anisotropic parameters, which is beneficial for fracture detection and analysis using seismic data.

Hudson model is an effective model, in which crack density can be directly calculated and fluid substitution can be applied. It can be extended to incorporate more complex fracture systems. However, it is only valid for penny-shaped cracks with small crack density and small aspect ratio.

The other theory is the linear slip model introduced by Schoenberg (1980). This model is based on a linear relationship between the discontinuity of particle velocity and applied traction. The effective compliance tensors influenced by fractures can be written as:

$$S^{eff} = S^0 + S^1 \tag{2- 21}$$

where S^0 are compliance tensors of the isotropic background medium, and S^1 are the compliance tensors of included fractures, which have two independent elements:

$$S^1 = \begin{bmatrix} S_N & 0 \\ 0 & S_T \end{bmatrix} \tag{2- 22}$$

S_N are the normal compliance tensors and S_T are the tangential compliance tensors.

Unlike the Hudson model, the Schoenberg model is not limited in terms of crack shape and small crack density. However, it does not provide a direct link to the microstructure properties of fractured media. It is important to note that the corresponding stiffness tensors can be calculated if the compliance tensors are known ($C^{eff} = (S^{eff})^{-1}$). The inverted stiffness matrix has the same structure as the result of the Hudson model. They become identical if specific fracture weakness conditions are satisfied (Schoenberg and Douma, 1988).

With equivalent medium theory, a relation between fracture properties and anisotropic parameters can be built, which enables geophysicists to detect and analyse fractures using seismic data.

2.6 Shear-wave splitting

Shear-wave splitting, or shear-wave birefringence, is an important phenomenon which occurs when shear-waves propagate through anisotropic media. The incident shear-wave splits into two shear-waves which have different polarisation directions and propagation velocities (Figure 2- 5).

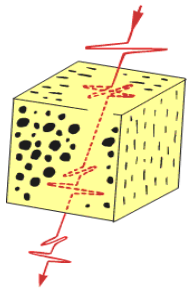

Figure 2- 5: Shear-wave splitting in an anisotropic medium (after Crampin, 1994)

In practice, shear-wave splitting induced by vertical fractures always attracts great interest because such fractures are important to hydrocarbon exploration and production. When the incident shear wave propagates through a set of vertical fractures and is not polarised in either the plane of isotropy, or a symmetry plane, as shown in Figure 2- 6, it splits into two orthogonally-polarized shear-waves with different velocities. The fast S1-wave is polarised in the isotropy plane while the slow S2-wave is polarised in the symmetry plane. The velocity differences cause a time delay between the fast S1-wave and slow S2-wave arrivals.

Shear-wave splitting, which has been successfully observed and measured in several laboratory studies, is related to the physical properties of anisotropic media. Usually, it is regarded as an efficient tool to characterise vertical fractures. The polarisation direction of the fast S1-wave corresponds to the fracture orientation. However, the shear-wave window and near-surface effects complicate the polarisation features, which can cause analysis of the polarisation of fast S1-wave to be inaccurate (Booth and Crampin, 1985; Garotta, 1999). The time delay is related to the anisotropic parameters of the fractured medium, and can be used to determine the fracture density.

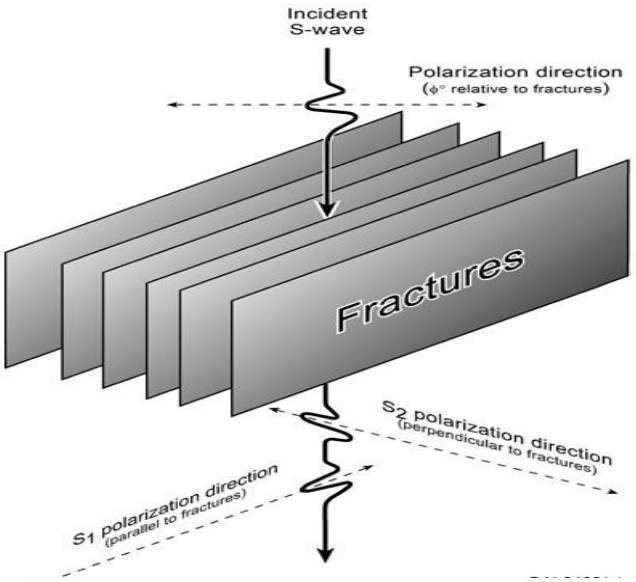

Figure 2- 6: Shear-wave splitting in a set of vertical fractures

In shear-wave data acquisition, if the horizontal receivers do not align with the isotropy plane direction and the symmetry axis direction, both the fast S1-wave and slow S2-wave are projected into the radial and transverse components. As illustrated in Figure 2- 7, the recorded R (radial) and T (transverse) components can be transformed into fast S1 and slow S2 components:

$$[R(t) \quad T(t)] = [S1(t) \quad S2(t)] \begin{bmatrix} \cos\theta & \sin\theta \\ \sin\theta & -\cos\theta \end{bmatrix} \tag{2- 23}$$

where θ is the angle between radial direction and fracture direction. When the radial direction is along the fracture direction, θ is equal to zero and only the fast S1 component is recorded on the radial component. Meanwhile, only the slow S2 component is recorded on the transverse component. It is not difficult to find that radial and transverse components only contain the slow S2 and fast S1 component, respectively when θ is equal to 90^o. Conversely, the fast S1 and slow S2 components can be transformed into radial and transverse components as well:

$$[S1(t) \quad S2(t)] = [R(t) \quad T(t)] \begin{bmatrix} \cos\theta & \sin\theta \\ \sin\theta & -\cos\theta \end{bmatrix} \tag{2- 24}$$

Based on this relationship, Alford rotation is commonly used to rotate the radial and transverse components into the fast S1 and slow S2 components (Alford, 1986).

Then the time delay between fast S1 and S2 components can be obtained and used to estimate fracture density. The analysis of shear-wave splitting is often performed on VSP data because it is easier to analyse shear-wave data for a near vertical raypath (e.g. Lynn et al., 1999a; MacBeth, 2002).

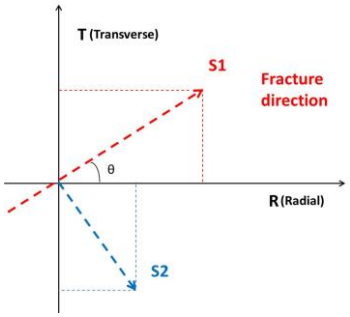

Figure 2- 7: Relation between R-T coordinate system and S1-S2 coordinate system.

Direct acquisition of pure shear-wave seismic data is not widely used due to the high cost and low data quality. Using a conventional P-wave source, PS-converted wave data is usually studied instead of pure shear-wave data. The PS-converted wave also suffers shear-wave splitting due to the upgoing shear-wave leg, as illustrated in Figure 2- 8.

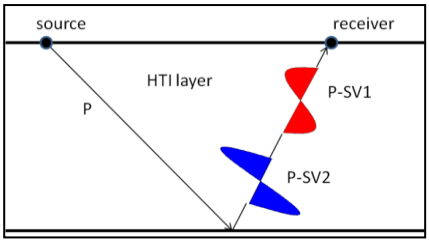

Figure 2- 8: PS-converted wave splitting phenomenon. (P-SV1 and P-SV2 represent split fast and slow PS-converted waves, respectively)

In a fractured medium, the PS-converted wave is also split into a fast P-SV1 wave and a slow P-SV1 wave. In a wide-azimuth PS-converted wave survey in fractured media, as shown in Figure 2- 9, both fast P-SV1 and slow P-SV2 waves are projected into radial and transverse components. It can be seen that only the fast P-SV1 wave is observed along the fracture direction. In the direction perpendicular to the fracture direction, only the slow P-SV2 wave is observed. More importantly, the polarisation of the transverse component reverses across the symmetry planes and isotropy planes.

This is another important feature, which can be used to determine fracture direction (e.g. Li, 1998; Mattocks et al., 2005). The Alford rotation can be similarly applied to PS-converted waves to rotate radial and transverse components into fast P-SV1 and slow P-SV2 waves. This analysis of splitting parameters is frequently used to estimate fracture orientations and densities (e.g. Simmons Jr, 2008; Yue et al., 2013). Specifically, in the case where multiple fractured layers are involved, a layer-stripping method can be used to uncover fracture properties of individual fracture layers (e.g. Cheng et al., 2009; MacBeth, 2002).

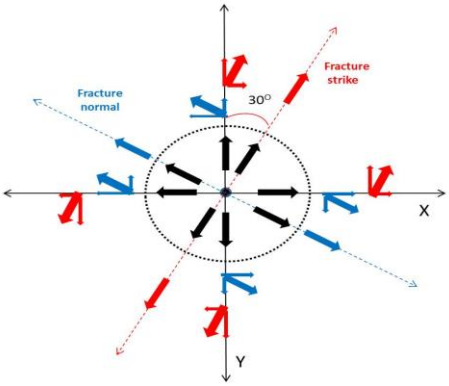

Figure 2- 9: Converted wave survey in HTI media. (red dotted line: fracture direction; blue dotted line: the direction normal to the fracture direction; Black arrows: incident P-waves; Red arrows: fast P-SV1 waves; blue arrows: slow P-SV2 waves)

2.7 Azimuthal P-wave seismic response

Vertically aligned fractures often give rise to azimuthal anisotropy. Then azimuthal variations of seismic attributes are usually analysed to characterise fractures. Specifically, P-wave data is easier to acquire than shear-waves and simpler than mode-converted waves. The azimuthal variation of P-wave attributes has been intensively studied to facilitate fracture characterisation. Current studies usually focus on azimuthal variations of P-wave NMO velocities and AVO responses (e.g. Hall and Kendall, 2003; MacBeth, 1999; Mallick et al., 1997).

In a HTI medium induced by vertically aligned fractures, the P-wave NMO velocity can be approximated as an ellipse in the horizontal plane (Tsvankin, 1997b):

$$v_2^2(\theta) = \frac{v_{2-0^0}^2 v_{2-90^0}^2}{v_{2-0^0}^2 \sin^2\theta + v_{2-90^0}^2 \cos^2\theta} \tag{2- 25}$$

where θ is the azimuth angle between the vertical plane and the symmetry axis plane. v_{2-0^0} is P-wave NMO velocity along the fracture direction and v_{2-90^0} is P-wave NMO velocity along the fracture normal direction. This velocity ellipse is illustrated in Figure 2- 10. The fracture direction is 0^o in the horizontal plane. P-wave NMO velocity along the fracture direction is larger than along the fracture normal direction. From this elliptical equation, knowledge of NMO velocities along directions parallel and perpendicular to the fracture direction can deliver NMO velocity at any other azimuth angle. More importantly, measurement of NMO velocities at different azimuth angles, and application of ellipse fitting, can estimate fracture direction. The velocity difference between the fracture direction and fracture normal direction can be used to estimate fracture densities. This elliptical equation is valid for all pure-mode waves in a HTI model, which is an efficient tool for fracture characterisation.

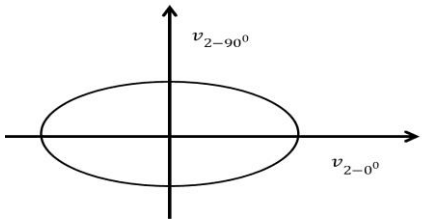

Figure 2- 10: Examples of P-wave velocity ellipse. (The fracture direction is 0^o)

Based on the elliptical equation of P-wave NMO velocity, the traveltime can also be approximated as (Li, 1999):

$$t^2(\theta) = t_{\max}^2 \cos^2(\theta - \theta_0 + \frac{\pi}{2}) + t_{\min}^2 \sin^2(\theta - \theta_0 + \frac{\pi}{2}) \tag{2- 26}$$

where θ is the azimuth angle and θ_0 denotes the fracture direction. $t_{\max}$ and $t_{\min}$ are the maximum and minimum traveltimes, respectively. This equation provides a way to determine fracture information from travel-times in P-wave seismic data.

Another important application is associated with P-wave amplitudes. Seismic reflection and transmission coefficients are dependent on the incidence angle. This fact introduces the important study of AVO-amplitude variation with offset. AVO analysis is an important tool to invert for medium properties, which is beneficial for reservoir characterisation. In fracture-induced HTI media, reflection coefficients are not only dependent on the incidence angle but also the azimuth angle. The P-wave reflection coefficient M_{pp} can be expressed as (e.g. Rüger, 2001; Thomsen, 2002):

$$M_{pp}(\phi,\theta) = A + B(\theta)\sin^2(\varphi) + D(\theta)\sin^2(\varphi)\tan^2(\varphi) \tag{2- 27}$$

where θ is the azimuth angle in the horizontal plane and φ is the incidence angle. A is called AVO intercept and B is the AVO gradient. D is the AVO curvature. For small to moderate offsets, the high-order curvature term can be ignored:

$$M_{pp}(\varphi,\theta) = A + B(\theta)\sin^2(\varphi) \tag{2- 28}$$

where the AVO gradient $B(\theta)$ can be written as:

$$B(\theta) = B_0 + B_1\cos^2(\theta - \theta_0) \tag{2- 29}$$

where B_0 is the conventional isotropic AVO gradient and B_1 is the anisotropic AVO gradient. Based on these trigonometric functions, Equation (2- 29) can be reformed as:

$$B(\theta) = \frac{B_1 + 2B_0}{2} + \frac{B_1}{2}\cos[2(\theta - \theta_0)] \tag{2- 30}$$

$B(\theta)$ is a function of azimuth angle θ.Then for a fixed incidence angle ϕ_0 , Equation (2- 28) can be reformed as:

$$\left.\begin{aligned} M_{pp}(\phi_0,\theta) &= E + F\cos[2(\theta - \theta_0)] \\ E &= A + \frac{(B_1 + 2B_0)}{2}\sin^2(\varphi_0) \\ F &= B_1\sin^2(\varphi_0) \end{aligned}\right\} \tag{2- 31}$$

where E and F are also constants. $M_{pp}(\varphi_0,\theta)$ is a function of azimuth angle θ. From both Equation (2- 30) and (2- 31), the reflection coefficient and AVO gradient both

vary with azimuth angle, and are both elliptical in the azimuthal plane. Therefore, analysis of azimuthal variations of reflection coefficients and AVO gradients can be performed for seismic fracture characterisation. An example of P-wave amplitude variation is shown in Figure 2- 11. The amplitude is measured on a reflector formed by an upper HTI layer and lower isotropic layer. The fracture direction in this example is 120^{o}. For a given incidence angle or a given offset, the azimuthal variation of P-wave amplitudes are consistent with a $\cos[2(\theta-\theta_0)]$ function. This azimuthal feature is very useful to determine fracture orientations.

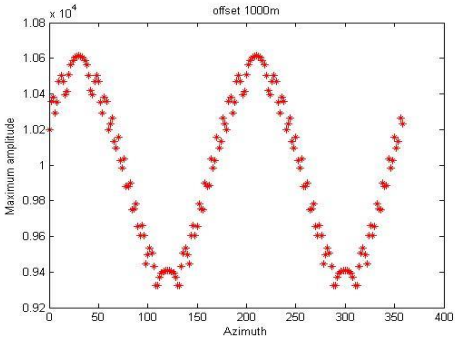

Figure 2- 11: Example of P-wave amplitude azimuthal variation in HTI media.

2.8 Overview of PS-converted wave exploration

Shear wave information has been thought to be effective in enhancing the seismic resolution because the shear-wave velocity is lower than the P-wave velocity and the shear wave wavelength is smaller than the P-wave wavelength. Also, shear-waves are found to be beneficial for improving imaging quality because they are hardly affected by fluid (Garotta, 1999; Probert et al., 2000). Many efforts have been made to apply pure-mode shear wave exploration, following the development of the horizontal vibrator in the 1960s and 1970s. Due to low quality and high cost, shear-wave surveys are not widely used in the hydrocarbon industry. However, acquisition of shear-wave information is still in great demand because some advantages of shear wave exploration have been recognised. Thus PS-converted wave exploration has been regarded as an effective way to acquire shear-wave information.

Increasing demand for better delineation of hydrocarbon reservoirs, advanced seismic survey instruments and designations, as well as highly-developed processing and interpretation techniques have caused multicomponent technology to be widely used in recent years, although the fundamental concepts of multicomponent seismic exploration were developed more than twenty years ago (Hardage et al., 2011).

Generally speaking, the term "converted-wave exploration" in many cases simply refers to PS-converted exploration. The PS-converted wave propagation is illustrated in Figure 2- 12: the downgoing P-wave converts into an upgoing shear wave at its conversion point. Other mode-conversions are present but are not usually considered. The reason is that the magnitude of other mode-conversions is generally lower than the magnitude of P-to-S conversion (Rodriguez, 2002).

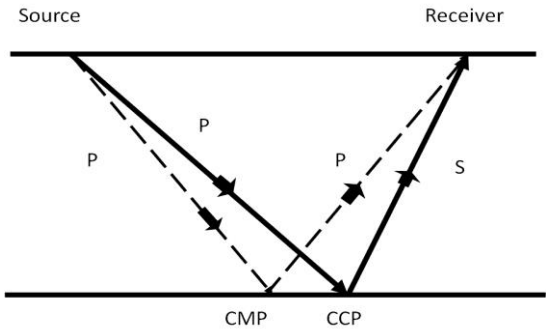

Figure 2- 12: PS-converted wave reflection. CMP represents the common mid-point for P-P reflection. CCP represents the common reflection point for P-S converted wave reflection.

Both onshore and offshore converted-wave acquisitions have been successfully applied in many areas but different types of sources, receivers and survey designs are deployed for different purposes(Stewart et al., 2002). Important additional information and some critical issues have been provided to geophysicists(e.g. Garotta, 1999; Kristiansen, 2000; Lynn et al., 2001). The processing and interpretation of PS-converted wave seismic data are usually different from conventional P-wave seismic data processing and interpretation, and usually require special algorithms and methods. PS-converted wave seismic data acquisition and processing as well as major applications are reviewed below.

2.9 PS-converted wave seismic data acquisition

In the context of isotropic media, the P-wave and two modes of shear wave, SV and SH shear waves are three major types of elastic wave considered in seismic exploration. They are polarized in three orthogonal directions and have different velocities (Figure 2- 13). The velocities of SV- and SH-waves are little different but are both much less than P-wave velocity. These three wave modes have been acquired and analysed for different purposes. However, when a P-wave hits an interface, it can be reflected as an SV-wave that can be recorded as another mode of effective shear wave. That wave is called a P-SV converted wave or simply PS-converted wave.

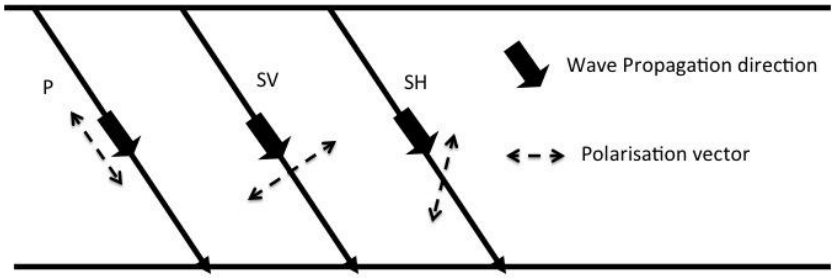

Figure 2- 13: The propagation of three different mode waves: P-, SV- and SH-waves. The P-wave and SV-wave polarization vectors are both confined to the incident plane but are parallel and perpendicular to the wave propagation direction, respectively. The polarization vector of the SH-wave is perpendicular to the incident plane and orthogonal to the wave propagation direction.

The behaviour of shear-waves (SV- and SH-waves) is more complicated in anisotropic media. A shear wave splits into two modes of shear wave with two orthogonal polarizations and different velocities, as discussed above. Thus it is clear to understand what nine-component (9C) and three-component (3C) seismic data acquisition represent. 9C seismic data is obtained by a source generating three orthogonal displacement vectors and the sensor receiving displacements in three orthogonal directions. 3C seismic data is obtained by using a conventional P-wave source and a three-orthogonal-component receiver. 4C seismic data is similar to 3C seismic data, and is mainly acquired in marine seismic exploration. The difference is that it has the extra 4^{th} component. This is acquired by hydrophones to record the

pressure change in the water. Different modes of wave can be created and recorded in 9C, 3C and 4C data acquisition. Different modes of converted-waves are also indicated in Table 2- 3. 9C seismic data is more expensive than 3C although it contains more types of converted-waves (P-SV1, P-SV2, SV1-P and SV2-P). 3C or 4C seismic data is cost-effective and normally provides the necessary information.

Acquisition	Modes (Isotropic)	Modes (Anisotropy)
9C	P-P, P-SV, SV-SV, SV-P, SH-SH	P-P, P-SV1, P-SV2, SV1-SV1, SV2-SV2 SV1-P, SV2-P, SH1-SH1, SH2-SH2
3C	P-P, P-SV	P-P, P-SV1, P-SV2
4C	P-P, P-SV	P-P, P-SV1, P-SV2

Table 2- 3: Different modes of waves recorded by different types of multicomponent acquisition in both isotropic and anisotropic cases. The number 1 denotes the fast shear wave mode and the number 2 denotes the slow shear wave mode.

The conventional P-wave source is used in PS-converted wave seismic data acquisition. However the source power should be adjusted to compensate for amplitude loss in PS-converted wave data (Garotta and Granger, 2003). Specifically, the air-gun source used in marine seismic acquisition generates only P-wave energy, which determines that the recorded wave modes are P-P and P-SV reflections. If 9C seismic data is needed in the marine environment, the 3C source should be located on the seafloor. The reason is that shear waves cannot propagate in water, where the shear modulus is zero. There are many issues associated with installation of a source on the seafloor. Thus it is used less frequently than the air-gun source in seismic exploration.

Receivers containing only one horizontal vector sensor were used in some field studies to provide shear wave information and even PS converted wave information (e.g. Sutton and Duennebier, 1987). However, P-wave data is still important to the processing and interpretation of PS –converted wave seismic data. Moreover one single horizontal component is not sufficient to record all information involved in three-dimensional seismic exploration. Thus the receivers used in PS-converted wave

survey should contain three orthogonal vector sensors: one vertical and two horizontals.

Regardless of the seismic sensors used in seafloor seismic data acquisition, there are two major types of receivers deployed in PS-converted wave seismic data acquisition. The first one is the analogue 3C geophone, which has been used for many years. It was simply assembled from a vertical-vector sensor and two horizontal-vector sensors in the early stage. From the late 1980s, manufacturers were able to produce a single geophone that contained three orthogonal vector sensors. It is based on coils that capture the particle-displacement. The second type is the digital 3C accelerometer, which is based on the MEMS (Micro Electro Mechanical System) technology and is designed to measure the acceleration. Also, a new type of seismic sensor has been developed in recent years – that is, the fiber-optic seismic sensor that is expected to improve acquisition efficiency and data quality. However, more tests and studies must be accomplished to confirm its validity before it becomes widely used in the industry.

The output of the analogue 3C geophone is the analogue signal, which needs to be digitalised before data processing. The digital signal directly delivered by MEMS accelerometers avoids noise contamination during analogue-to-digital transmission (Mougenot and Thorburn, 2004). Compared with 3C geophones, accelerometers have broadband responses and low distortions, which can improve the vector fidelity. Moreover accelerometer deployment does not require the many connectors and strict geophone orientation which traditional geophone deployment does. A comparison between accelerometers and geophones has been performed in many field studies (e.g. Gibson et al., 2005; Hons et al., 2008; Mougenot and Thorburn, 2004; Ronen et al., 2005; Stotter et al., 2008). Many cases suggest that the data quality is not always improved by replacing geophones with accelerometers. In practice a careful analysis and comparison test between geophones and accelerometers should be made before any choice is made.

Multicomponent receivers should be used on the seafloor when marine acquisition is needed, because shear waves cannot propagate in water. Accelerometers and a hydrophone are used to set up the 4C receiver specifically designed for offshore

acquisition. There are two types of seafloor 4C receivers: OBC (Ocean-Bottom Cable) and OBS (Ocean-Bottom Sensor). The OBC technology illustrated in Figure 2- 14 is usually used when the water depth is within about 1000 meters (Johnstad, 2008). The heavy sensors and cables are towed by one or several cable boats. The equipment can be conveniently reused in a new place in a later survey. When the water depth exceeds 1000 meters, the OBS recording system, which is illustrated in Figure 2- 15 should be selected. The OBS requires more demanding operation of sensor positioning and data collection but provides better coupling (Hardage et al., 2011).

PS-converted wave and P-wave data can be acquired at the same time by three component (3C) seismic survey. However replacing 1C receivers with 3C receivers is not the only task to deal with. A PS-converted wave survey should consider features of both the P-wave and PS-converted wave because P-wave data is important to the processing and interpretation of PS-converted wave data. Conversion at the interface, different reflection coefficients between P-waves and S-waves, and different Q-factors between P-waves and S-waves all have influences on the quality of PS-converted wave seismic data and should be carefully studied. Therefore the final survey design should be an optimisation selection determined by trials.

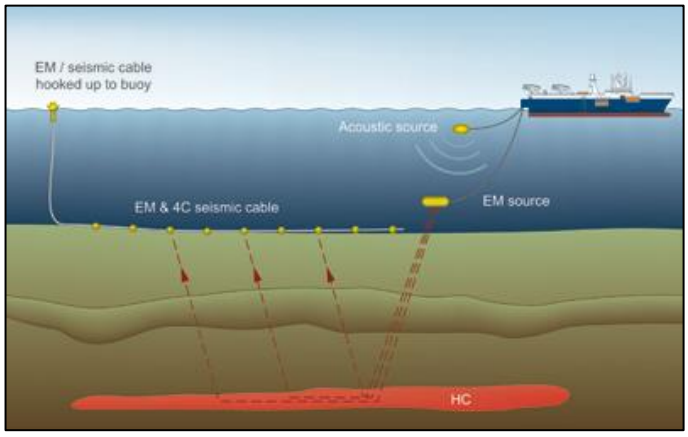

Figure 2- 14: Ocean Bottom Cable technology

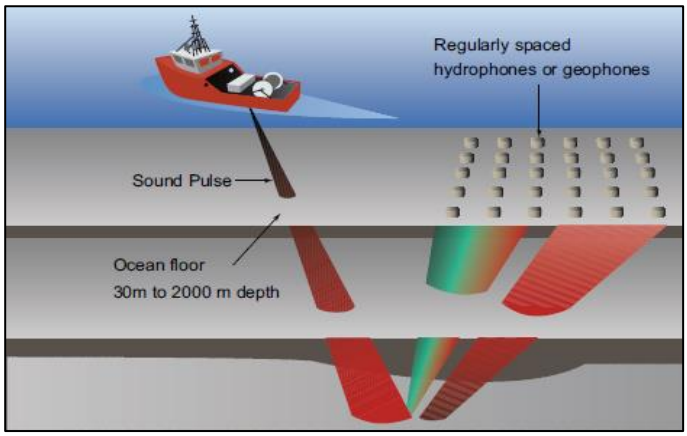

Figure 2- 15: Ocean Bottom Sensor technology

Specifically, the source energy and number of folds can be increased to compensate for the different absorption effect between P-waves and S-waves (Garotta and Granger, 2003). The PS-converted wave requires CCP (common conversion point) stacking, which is different from the CMP (common mid-point) stacking used in P-wave surveys. A P-SV-stacking chart and binning periodicity can be used to obtain an optimized survey design (Eaton and Lawton, 1992). Moreover 3D seismic survey is now a common practice and has brought some specific issues to PS-converted data acquisition (Vermeer and Beasley, 2002). Those issues are important for the PS-converted wave amplitude, polarization and the analysis of azimuthal effects. The P-wave to S-wave velocity ratio is needed to determine the CCP coordinate. Many more recording channels are involved in PS-converted wave data acquisition. The traveltime of PS-converted waves is longer than the traveltime of P-waves, which requires the recording time to be increased. The 3C receiver should be carefully planted so that the two horizontal vector sensors are aligned with the inline and crossline directions respectively. Those issues mentioned above cause extra work and cost, which should be considered before PS-converted wave data acquisition is performed.

2.10 PS-converted wave seismic data processing

PS-converted wave seismic data processing is more complex than P-wave seismic data processing, which causes extra cost and time. Specific concepts and techniques related to later analysis and discussion are reviewed here.

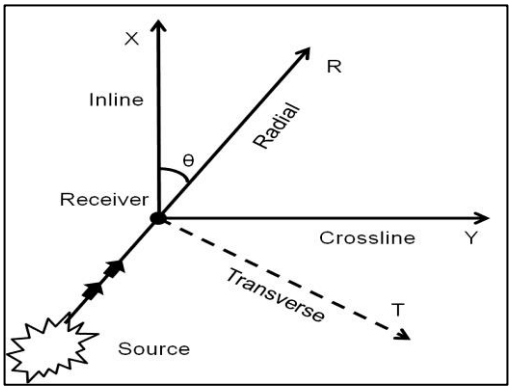

Figure 2- 16: Geometry relation between inline-crossline coordinates and radial-transverse coordinates. R is the radial component and T is the transverse component. X and Y represent inline and crossline directions. θ denotes the angle between the inline and radial directions.

The geometrical relation between the inline-crossline coordinate and the radial-transverse coordinate in PS-converted wave data acquisition is shown in Figure 2- 16. The X component is in the inline direction while the Y component is in the crossline direction. The radial and transverse components are parallel and perpendicular to the source-receiver direction, respectively. As illustrated in Figure 2- 13, the P-SV converted wave energy should be confined in the radial component and weak SH-wave energy may be recorded in the transverse component. Therefore the P-SV converted wave could be projected into both X (inline) and Y (crossline) components. In order to obtain the more significant P-SV converted wave energy, the X and Y components should be rotated into R (radial) and T (transverse) components by the angle θ. The angle θ can be found by scanning different angle values. The accepted angle value delivers the maximum energy ratio of the R component to the T component. A data example, displayed in Figure 2- 17, is used to show the improved P-SV converted wave energy on the radial component after horizontal rotation.

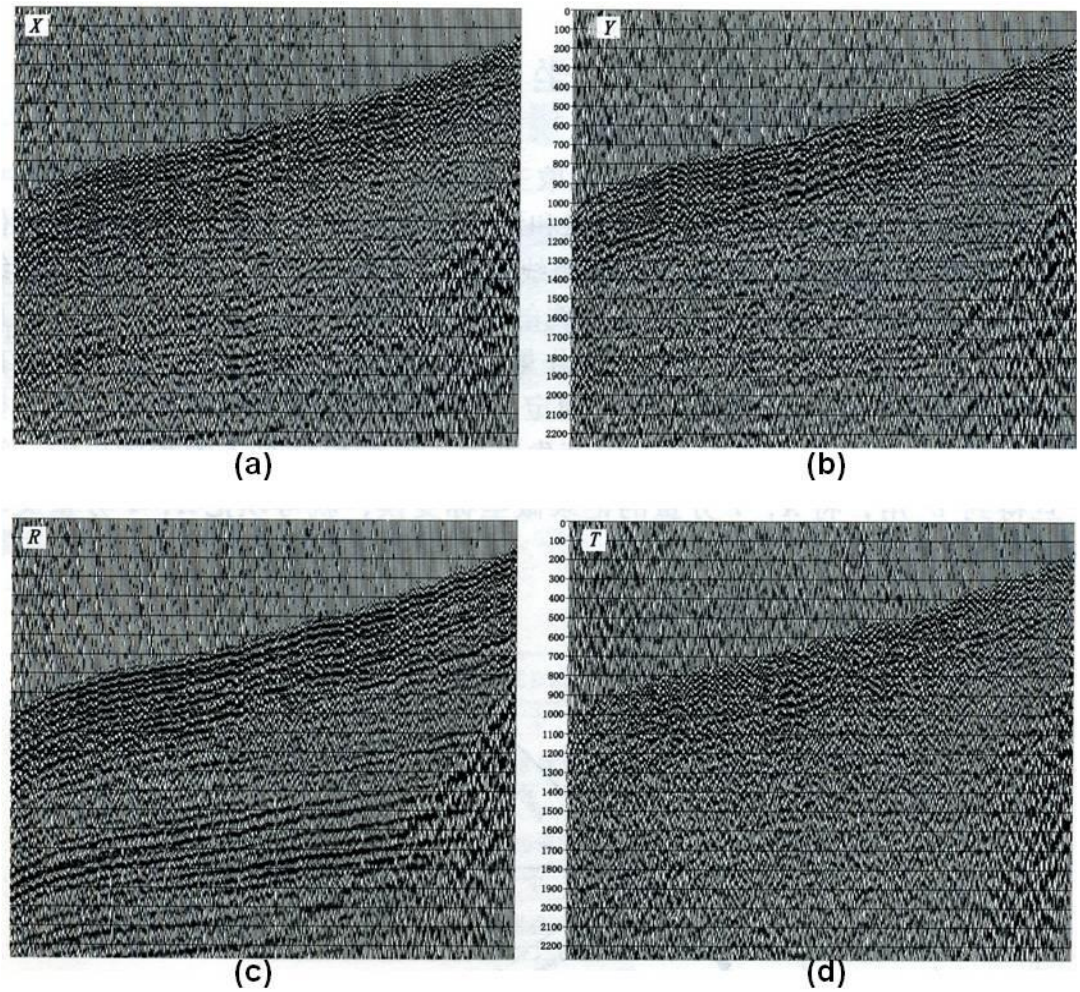

Figure 2- 17: Improvement by rotating X and Y components into R and T components in a single shot gather. (a): X (inline) component; (b): Y (crossline) component; (c) R (radial) component; (d) T (transverse) component. (The data set is from an oilfield in the northwest of China)

The asymmetric ray path of PS-converted waves causes the failure of the CMP (common midpoint) assumption (Figure 2- 18). The conversion point no longer locates at the midpoint between a pair of sources and receivers and varies with the reflector depth. Applying CMP stacking to P-SV converted wave seismic data would bring negative effects to lateral continuity, especially for dipping reflectors (Frasier and Winterstein, 1990; Schafer, 1992). Then the CCP and ACP binning methods were developed to improve the accuracy and efficiency of PS-converted wave seismic data processing (Tessmer and Behle, 1988; Tessmer et al., 1990). ACP (asymptotic conversion point) binning is illustrated in Figure 2- 18 and is a good

approximation of CCP binning for deep reflectors. Depth-variant CCP binning was proposed to deal with the disadvantages of ACP binning, which maps each sample point to its true conversion point (Eaton et al., 1990). It is more accurate than ACP binning but requires more computation time to accomplish. The above theories are all based on the assumption of flat reflectors, which are untrue in the real situation. Then dip moveout (DMO) was introduced to compensate for the effect of dipping reflectors, which is also more accurate than ACP binning (Harrison, 1992). However it is time-consuming because it is applied to the original dataset.

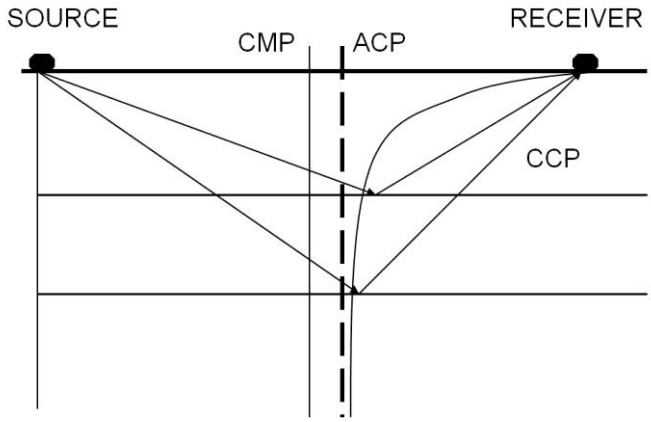

Figure 2- 18: Illustration of P-SV converted wave raypath. The conversion point is closer to the receiver as the reflector depth decreases. CMP represents the common midpoint binning; CCP represents the common conversion point binning and ACP represents the asymptotic conversion point binning

The traveltime equation for a PS converted wave forms the basis of velocity analysis, NMO correction and imaging. With the assumption of an isotropic layer, it is given for the illustration of Figure 2- 19 as:

$$t_{ps} = \frac{Z}{v_p \cos\beta_p} + \frac{Z}{v_s \cos\beta_s} \qquad (2\text{- }32)$$

where t_{ps} is the two-way traveltime of PS-converted wave. Z is the reflector depth. v_p and v_s are the P-wave velocity and S-wave velocity, respectively. β_p is the incidence angle of the downgoing P-wave while β_s is the reflected angle of the converted upgoing SV-wave. Taylor series expansion is usually used to approximate the exact equation into some simplified forms to facilitate data processing. The

hyperbolic assumption has been commonly used to perform velocity analysis, although it is only valid for short spread data (Taner and Koehler, 1969). It is actually the first order of the Taylor expansion of Equation (2- 32) (Tessmer and Behle, 1988):

$$t_{ps}^2 = t_{ps0}^2 + \frac{x^2}{v_{ps}^2} \tag{2- 33}$$

where v_{ps} is the NMO (normal moveout) velocity of PS-converted waves, which can be calculated as:

$$v_{ps}^2 = v_p v_s \tag{2- 34}$$

t_{ps0} is the two-way vertical traveltime of PS-converted waves and x is the offset. v_p and v_s are P-wave and shear-wave NMO velocities, respectively.

If the velocity ratio R is introduced, the PS-converted wave NMO velocity can also be simplified into:

$$v_{ps}^2 = v_p^2 / R \quad (R = v_p / v_s) \tag{2- 35}$$

However the hyperbolic approximation is only valid when the offset-to-depth ratio is smaller than 1.0 (Yuan, 2001). Thus a three-term Taylor expansion is derived to consider the non-hyperbolic effect of the traveltime equation (Thomsen, 1999):

$$\left.\begin{aligned} t_{ps}^2 &= t_{ps0}^2 + \frac{x^2}{v_{ps}^2} + \frac{A_4 x^4}{1 + A_5 x^2} \\ A_4 &= \frac{-(R-1)^2}{4(1+R)t_{ps0}^2 v_{ps}^4} \\ A_5 &= \frac{-A_4 v_{ps}^2}{1 - v_{ps}^2 / v_p^2} \end{aligned}\right\} \tag{2- 36}$$

This three-term equation has been proved to be valid when the offset-to depth ratio is up to 2.0, which is beneficial for processing seismic data with large offsets (Li and Yuan, 2003).

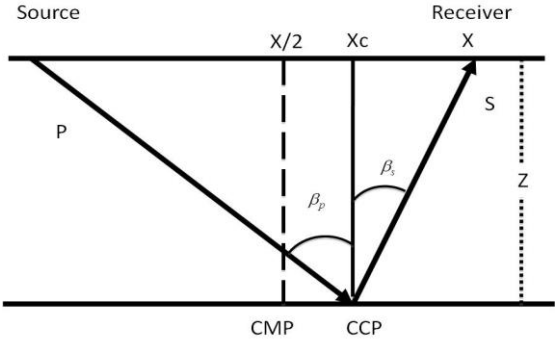

Figure 2- 19: PS-converted wave propagation in an isotropic layer. CCP and CMP represent the common conversion point and common midpoint, respectively. x is the offset, which is the distance between the source and the receiver. x_c is the distance between the source and the conversion point. Z is the reflector depth.

The above discussion is based on isotropic assumption. In a VTI medium, the approximated moveout equation for the P-wave and the SV-wave are (Tsvankin and Thomsen, 1994):

$$t_p^2 = t_{p0}^2 + \frac{x^2}{v_{p2}^2} - 2\eta \frac{x^4}{V_{p2}^2[t_{p0}^2 v_{p2}^2 + (1+2\eta)x^2]} \tag{2- 37}$$

$$t_s^2 = t_{s0}^2 + \frac{x^2}{v_{s2}^2} - 2\zeta \frac{x^4}{v_{s2}^2[t_{s0}^2 v_{s2}^2 + x^2]} \tag{2- 38}$$

where t_{p0} and t_{s0} are two way vertical traveltimes of P- and SV-waves, respectively. Anisotropic parameters η and ζ are defined in Equation (2- 17). These equations can be used to improve pure-mode wave data analysis in VTI medium.

Based on pure-mode waves, corresponding parameters of PS-converted waves can be defined as (Li and Yuan, 2003):

$$\left.\begin{aligned} R_0 &= \frac{v_{p0}}{v_{s0}} \\ v_{ps2}^2 &= \frac{1}{1+R_0} v_{P2}^2 + \frac{R_0}{1+R_0} v_{S2}^2 \\ R_2 &= \frac{v_{p2}}{v_{s2}} \\ R_{eff} &= \frac{R_2^2}{R_0} \\ \chi_{eff} &= R_0 R_{eff}^2 \eta - \zeta \end{aligned}\right\} \quad (2\text{- }39)$$

Here v_{ps2} is the velocity of the PS converted wave, R_0 is the vertical velocity ratio, R_{eff} is the effective velocity ratio and χ_{eff} is the anisotropy parameter for PS-converted waves. For a single VTI layer, ζ can be approximates as: $\zeta = R_{eff}^2 \eta$.

Based on above parameters, the moveout of the PS-converted wave is written as:

$$\left.\begin{aligned} t_{ps}^2 &= t_{ps0}^2 + \frac{x^2}{v_{ps2}^2} - \frac{2\kappa_{eff} x^4}{v_{ps}^2 [t_{ps0}^2 v_{ps2}^2 + m_4 \cdot x^2]} \\ \kappa_{eff} &= \frac{(R_0 R_{eff} - 1)^2 + 8\chi_{eff}(1+R_0)}{8R_0(1+R_{eff})^2} \\ m_4 &= 2\kappa_{eff} \frac{(1+R_0)[(R_0-1)R_{eff}{}^2 + 2\chi_{eff}]}{(R_0-1)R_{eff}(R_0 R_{eff} - 1) + 2(1+R_0)\chi_{eff}} \end{aligned}\right\} \quad (2\text{- }40)$$

The above discussion can be extended to multi-layer VTI media. Interval Thomsen's parameters (v_{p0i}, ε_i, v_{s0i}, δ_i, and z_i, $i = 1,2,3,\ldots,n$) are required for each layer (Figure 2- 20).

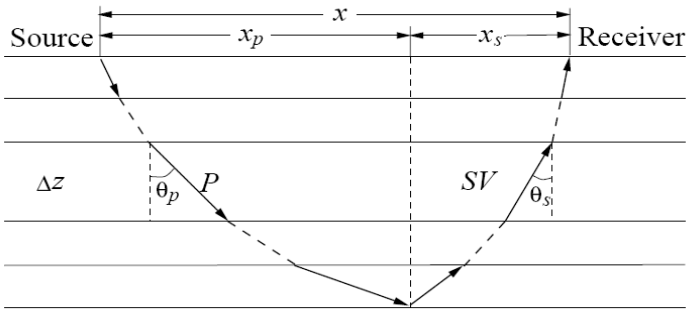

Figure 2- 20: Multi-layer VTI media

Then PS-converted wave moveout equation in multi-layer VTI media can be written as:

$$\left.\begin{aligned} t_{ps}^2 &= t_{ps0}^2 + \frac{(2h)^2}{v_{ps}^2} - \frac{2\kappa_{eff}(2h)^4}{v_{ps}^2[t_{ps0}^2 v_{ps}^2 + m_4 \cdot (2h)^2]} \\ \kappa_{eff} &= \frac{(R_0 R_{eff} - 1)^2 + 8\chi_{eff}(1+R_0)}{8R_0(1+R_{eff})^2} \\ m_4 &= 2\kappa_{eff}\frac{(1+R_0)[(R_0-1){R_{eff}}^2 + 2\chi_{eff}]}{(R_0-1)R_{eff}(R_0 R_{eff}-1) + 2(1+R_0)\chi_{eff}} \end{aligned}\right\} \quad (2\text{- }41)$$

where h is the half offset and

$$\left.\begin{aligned} V_{ps2}^2 &= \frac{1}{t_{ps0}}[\sum_{i=1}^{n} v_{p2i}^2 t_{p0i} + \sum_{i=1}^{n} v_{s2i}^2 t_{s0i}] \\ R_{eff} &= [(1+R_0)\frac{v_{ps2}^2}{v_{p2}^2} - 1]^{-1} \end{aligned}\right\} \quad (2\text{- }42)$$

2.11 PS-converted wave applications

PS-converted wave seismic data retains both characteristics of P-waves and shear-waves, which provide additional information to P-wave seismic data. Therefore PS-converted wave seismic data is applied in several operations for the improvement of seismic exploration.

Improve imaging

Conventional P-waves can fail to provide satisfactory results, although P-wave seismic data remains dominant in seismic exploration. P-wave data is significantly degraded when travelling through gas-charged sediments. Typically, P-wave reflections are delayed and attenuated due to the gas saturation. Poor results are usually obtained in the gas-saturated area in the image of subsurface structures. The term ‘P-wave wipeout zone’ arises from this feature, which is usually used as an important indicator of gas reservoirs. Unlike P-wave data, shear-waves are insensitive to the gas-saturation. Therefore PS-converted wave seismic data could be used to improve imaging of gas-saturated reservoirs. This method has been applied to

many fields, including North Sea (e.g. Granli et al., 1999; Li et al., 2001), Gulf of Mexico (e.g. Barkved et al., 2004; Hardage et al., 2008) and other places (Ensley, 1984; Li et al., 2007; Xiyuan et al., 2009). A field data example from south China is illustrated in Figure 2- 21. Visual inspection of Figure 2- 21(a) shows that the P-wave imaging is poor. Reliable interpretation results cannot be obtained from the P-wave data. In contrast, PS-converted wave data provides improved images, which is beneficial for structure mapping.

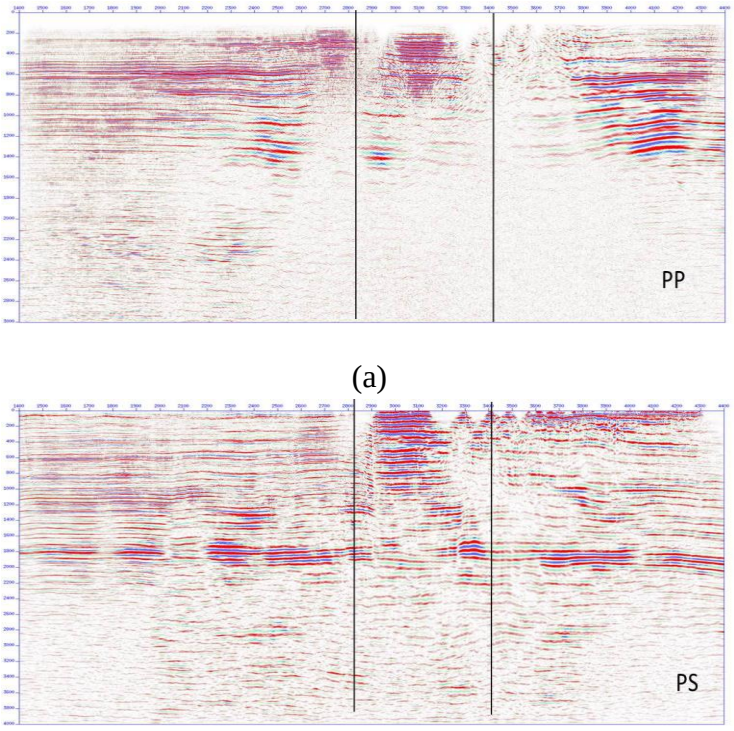

(a)

(b)

Figure 2- 21: Comparison of P-wave and PS-converted wave images of gas-saturated reservoirs

PS-converted wave data is also applied to the improvement of imaging by taking advantage of high shear-wave velocity contrasts. In certain cases, the P-wave velocity contrast is low but the shear-wave velocity contrast is relatively higher. Therefore, the shear-wave reflectivity is higher than the P-wave reflectivity. Thus PS-converted waves can be used to improve imaging in certain areas (e.g. MacLeod et al., 1999). In the case of complicated structures and sub-salts, PS-converted wave seismic data are used to improve the delineation of reservoirs. Examples from the

Gulf of Mexico show that PS-wave converted wave seismic data provides better imaging of faults and salt intrusions (e.g. Cary and Couzens; Kendall et al., 1998).

Obtain lithology information

P-wave data may provide limited lithology information on rocks and fluids. Additional lithology information can be obtained by combined analysis of PS- and P-wave seismic data. Specifically, v_p / v_s ratio, which is related to Poisson's ratio, is an efficient tool for determining lithological information. Limestones, sands and shales are separated in the v_p / v_s domain but overlap in the v_p domain (Garotta, 1999). For instance, many PS-converted wave experiments were performed in the Blackfoot oil field to identify reservoir facies using the v_p / v_s ratio, which is found to be well correlated with oil production (e.g. Dufour et al., 2002; Stewart et al., 1996). Besides, the v_p / v_s ratio can also be used to determine the porosity trend in carbonates. An example provided by Garotta (1985) shows that the high-porosity zones are successfully identified in carbonate reservoirs. Another application concerns the different responses of P-wave data and shear-wave data to fluid changes. P-wave data is more sensitive to fluid changes in reservoirs. When a P-wave reflection is observed but a PS-converted wave refection is not, the P-wave reflection is likely associated with fluid-contact boundaries (e.g. MacLeod et al., 1999).

Characterising fractured reservoirs

Due to the sensitivity of shear-waves to seismic anisotropy, PS-converted wave seismic data is often used to obtain fracture properties, which are important to reservoir characterization. PS-converted wave splitting analysis, which is based on pure shear-wave splitting, is frequently applied to improve fractured reservoir characterisation (e.g. Bale et al., 2009; Cheng et al., 2009; Yue et al., 2013). The fracture orientation corresponds to the fast P-SV1 wave polarization direction and the fracture density can be inverted from the time delays between the fast P-SV1 and slow P-SV2 components. Azimuthal variations shown on common-azimuth stack radial and transverse components can be used to determine fracture properties (e.g. Dai et al., 2011; Li, 1998; Vetri et al., 2003).

2.12 Summary

In this chapter, I have given a review of the basic concepts of seismic anisotropy and PS-converted wave seismics. Based on Hooke's law, stiffness tensors, which relate stress and strain tensors, are used to describe seismic anisotropy. Different rocks and geological formations produce different types of seismic anisotropy and simplified anisotropy parameters are introduced to improve seismic data analysis. Specifically, fractured-induced anisotropy is important to reservoir characterisation and production. Using equivalent medium theory, a relationship between fracture properties and anisotropic analysis can be constructed. Then several methods are developed to detect fractures including shear-wave splitting and azimuthal variations. PS-converted wave data, as a compromise for pure shear-wave data, is often acquired on land and at sea to improve seismic exploration. PS-converted wave data processing creates several practical issues, which make it more difficult than single-mode data processing. However, PS-converted wave seismic data is still frequently studied to improve imaging, obtain lithological information and characterize fractured reservoirs.

Chapter 3

Processing methods for PS-converted wave splitting analysis

3.1 Introduction

In this chapter, I introduce basic processing methods for the analysis of PS-converted wave splitting. To obtain the radial component containing most PS-converted wave energy, the acquisition coordinate system needs to be rotated into the radial-transverse component. In the presence of vertically aligned fractures, PS-converted wave also undergoes shear-wave splitting due to its upgoing shear-wave leg. Separation between fast P-SV1 and slow P-SV2 waves is also an important processing method to obtain the individual split PS-converted waves.

3.2 Coordinate transform

Unlike P-wave data which is mainly captured by the vertical components of 3C receivers, shear-wave information including PS-converted wave data is captured by the two orthogonal horizontal components. Horizontal rotation is often necessary for PS-converted wave data processing. This horizontal rotation converts the acquisition coordinate system (X-Y) into the processing coordinate system (Radial-Transverse).

In the Radial-Transverse (R-T) coordinate system, most PS-converted wave energy is contained in the radial component. This horizontal rotation is explained by Figure 3- , in which θ is the rotation angle between the X-Y and R-T coordinate systems.

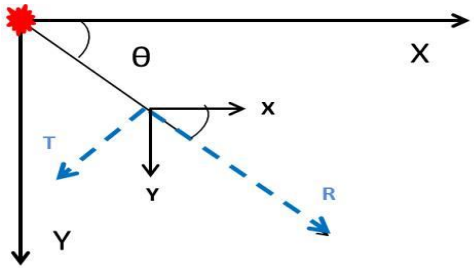

Figure 3- 1: Transformation between X-Y coordinate system and R-T coordinate system

Here, a synthetic dataset is created to show the improvement of this coordinate transformation. The model parameters are shown in Figure 3- 2. It is a simple three-layer model. The first layer is an isotropic layer. The second layer is a VTI layer specified by Thomsen parameters (ε=0.11, δ=0.09, γ=0.165). The third layer is an isotropic halfspace. A single-shot acquisition is applied to this synthetic study, which is described in Figure 3- 1. The rotation angle θ is equal to 45^{o} in the azimuthal plane.

Shot gathers for both X and Y components are shown in Figure 3- 3. The horizontal axis is the offset and the vertical axis is the time. Two reflection events are both indicated by red arrows in Figure 3- 3. It can be noticed that both PS-converted reflectors are observed on both X and Y components, which is attributed to the azimuthal angle θ. The radial and transverse components are obtained by horizontal rotation, and are shown in Figure 3- 4. After horizontal rotation, most PS-converted wave energy is moved into the radial component. This improvement is true for both reflectors. There is less energy remaining in the transverse component. Therefore, this proves that the transformation to the radial-transverse component is essential for PS-converted wave data processing.

Vp=1100 m/s Vs=520 m/s ρ=1.45 g/cm³ ΔZ=700m
Vp=2074 m/s Vs=869 m/s ρ=2.25 g/cm³ ΔZ=300m (ε=0.11, δ=0.09, ϒ=0.165)
Vp=2800 m/s Vs=1350 m/s ρ=2.6 g/cm³

Figure 3- 2: Model parameters

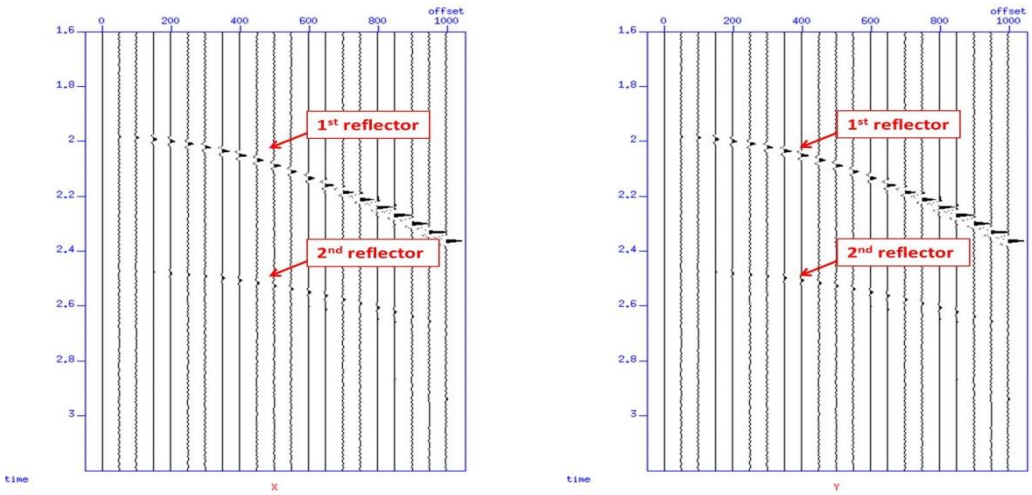

(a) (b)

Figure 3- 3: Shot gathers of X (a) and Y (b) components

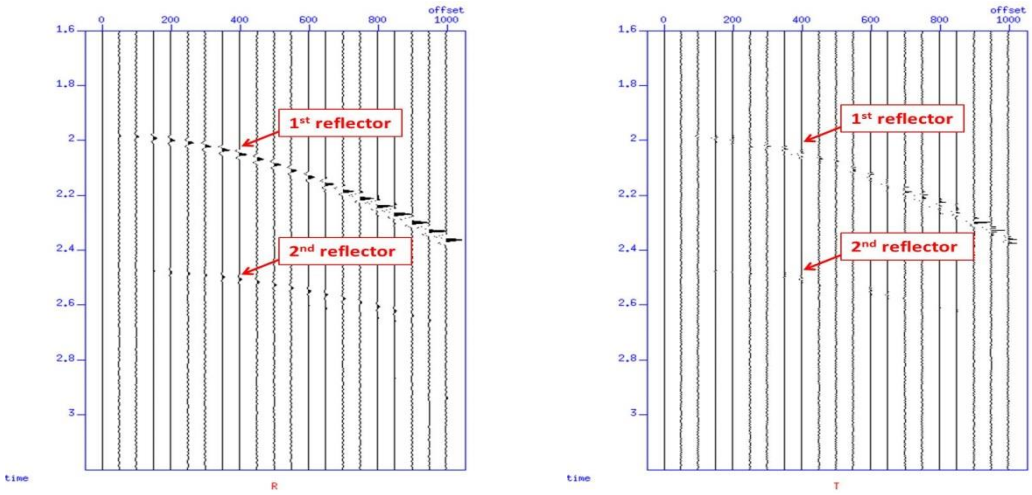

(a) (b)

Figure 3- 4: Shot gathers of radial (a) and transverse (b) components

3.3 Separation of split PS-converted waves

As the discussion in Chapter 2 suggests, PS-converted waves also suffer from the shear-wave splitting effect in the presence of vertical fractures. Both fast P-SV1 and slow P-SV2 components are projected into radial and transverse components. Therefore, compensation for the azimuthal variation of PS-converted waves is complicated by converted-wave splitting. The azimuthal variations of P-SV1 and P-SV2 components may be different from each other, which introduces difficulties in compensating for the azimuthal variation. The inverted anisotropic parameters might not be reliable representations of fracture properties. Therefore it is essential to separate the fast P-SV1 wave from the P-SV2 wave before compensating for the azimuthal variation.

The converted wave splitting caused by vertically aligned fractures can be described by Figure 3- 5. Black dotted lines represent a set of vertical fractures. The angle between the X-Y and R-T coordinate systems is θ and the angle between the fracture direction and X component is β. The fast P-SV1 component is polarised in the fracture direction and the slow P-SV2 component is polarised in the direction perpendicular to the fracture direction. Therefore the angle between the fracture direction and the radial component is ($\beta - \theta$). If the term ($\beta - \theta$) is non-zero, then the radial and transverse components contain both split PS-converted waves. In order to reveal the real behaviour of both P-SV1 and P-SV2 components, separation of the split PS converted waves is necessary.

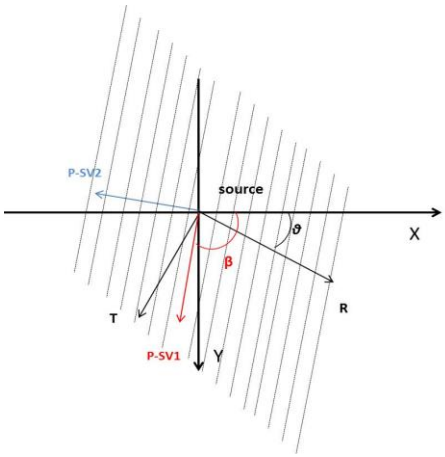

Figure 3- 5: Converted-wave splitting in the presence of vertical fractures

Separation of the P-SV1 wave from the P-SV2 wave can be achieved by Alford rotation (Alford, 1986), which is introduced in Chapter 2. Using the geometry displayed in Figure 3- 5 as an example, the horizontal rotation can be expressed by the following equation:

$$\begin{pmatrix} PSV1(\beta) \\ PSV2(\beta) \end{pmatrix} = \begin{pmatrix} \cos(\beta-\theta) & \sin(\beta-\theta) \\ \sin(\beta-\theta) & -\cos(\beta-\theta) \end{pmatrix} \begin{pmatrix} R \\ T \end{pmatrix} \qquad (3\text{- }1)$$

R and T represent radial and transverse components, respectively. Term ($\beta-\theta$) specifies the rotation angle used to separate the P-SV1 component (PSV1) from the P-SV2 component (PSV2).

Single-shot synthetic data is introduced here to show the separation of the P-SV1 component from the P-SV2 component. This model is similar to the previous one used to describe rotation to the radial-transverse coordinate system. The second layer is a HTI layer induced by vertical fractures, which is based on Hudson theory (Hudson, 1980, 1981). The required parameters include crack radius (*a*), crack density (*e*), aspect ratio (α) and the isotropic content of the cracks (ρ, λ and μ). ρ, λ and μ are defined to be 0,0,0 for dry (empty) fractures and 1,2.25,0 for water saturation, respectively. In limited conditions, dry fractures can be used to model gas-saturated fractures. This approximation simplifies the modelling work. More details of Hudson's model and dry fracture modelling can be found in Appendix B. The dominant frequency should be specified as well to determine the viscosity of the liquid content of cracks, which is 25Hz for this study. In this example, the crack radius *a* is 0.001 meters, aspect ratio α is 0.01 and fracture density *e* is 0.08. Gas saturation is used to obtain the synthetic dataset in this study. The gas is methane and its isotropic contents are calculated at atmosphere pressure and room temperature. The detailed model parameters are shown in Figure 3- 6(a). The acquisition geometry is displayed in Figure 3- 6(b). Black dotted lines represent vertically aligned fractures. The angle between the fracture direction and source-receiver direction is 45^{o}. Radial and transverse components are indicated by black arrows. The P-SV1 and P-SV2 components are indicated by red and blue arrows, respectively.

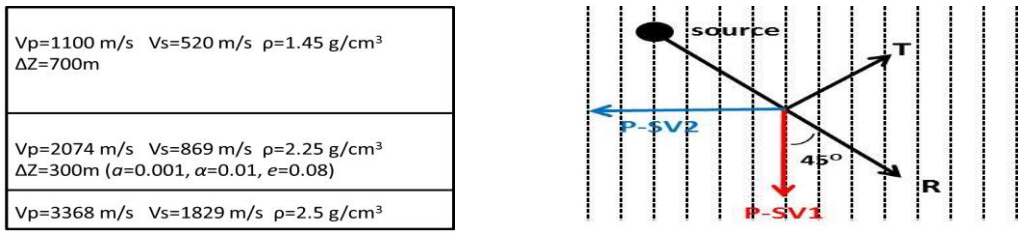

(a) (b)

Figure 3- 6: Description of the synthetic study. (a): Model parameters; (b): Acquisition geometry

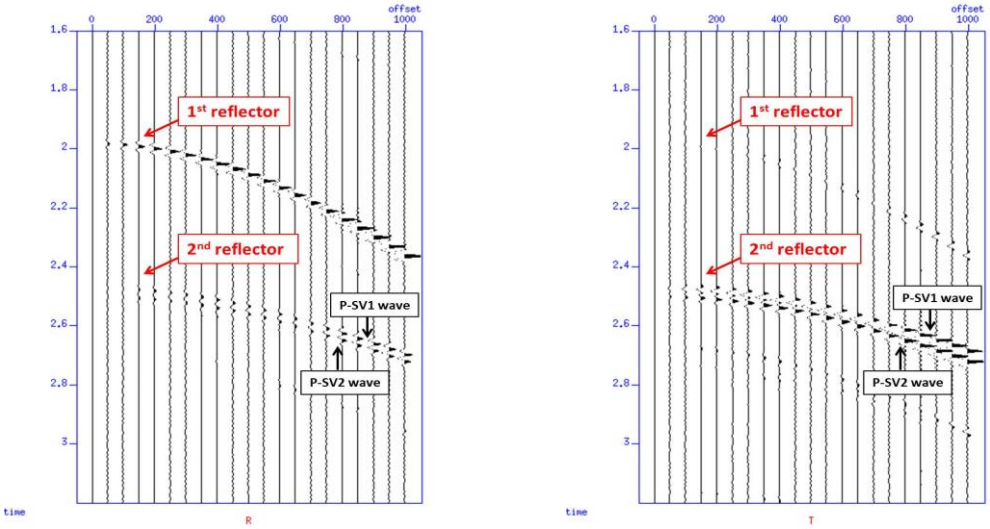

(a) (b)

Figure 3- 7: Shot gathers of radial (a) and transverse (b) components

The shot gathers for the radial and transverse components are displayed in Figure 3-7. The horizontal axis is the offset and the vertical axis is the time. The two reflectors can be observed on the radial component, which are indicated by red arrows. Due to the HTI effect, the second reflector is influenced by shear-wave splitting. The down black arrow represents the fast P-SV1 wave and the up arrow represents the slow P-SV2 wave. It can be seen that the P-SV1 and P-SV2 waves have similar waveforms. The time delay between the split converted waves can also be observed, which is caused by the different propagation velocities of the P-SV1 and P-SV2 waves. Due to the transformation to the radial-transverse component, the energy of the first reflector, only propagating in the first isotropic layer, has been rotated into the radial component, and little energy is seen in the transverse component. However, the

converted-splitting effect is still retained for the second reflector. P-SV1 and P-SV2 waves with a time delay can be found on the transverse component. It proves again that the PS-converted waves are also influenced by shear-wave splitting in the presence of fractures, and this should be compensated for.

By applying the horizontal rotation described by Equation (3- 1), the P-SV1 wave can be separated from the P-SV2 wave. The individual P-SV1 and P-SV2 components are shown in Figure 3- 8. It can be seen that the first reflector is clearly displayed in both P-SV1 and P-SV2 components with similar magnitudes. For the second reflector, the splitting effect has been removed. The P-SV1 component only contains the P-SV1 wave reflection and the P-SV2 component only contains the P-SV2 wave reflection. A red solid line is drawn in Figure 3- 8. It is used to identify the time delay between the P-SV1 and P-SV2 waves. This short red line corresponds to the first arrival of the P-SV1 wave, which is shown in Figure 3- 8(a). In Figure 3- 8(b), the first arrival of the P-SV2 wave is later than the time indicated by the red line. Therefore it is much easier to observe that the P-SV2 wave is travelling with a lower velocity than the P-SV1 wave. Moreover, the separated P-SV1 and P-SV2 waves can be used to study the azimuthal variation induced by vertical fractures. Because the P-SV1 wave and P-SV2 wave are polarised in different directions, they may display different responses to the subsurface rocks and structures. They can be also individually processed and studied, which is beneficial for seismic inversion and interpretation.

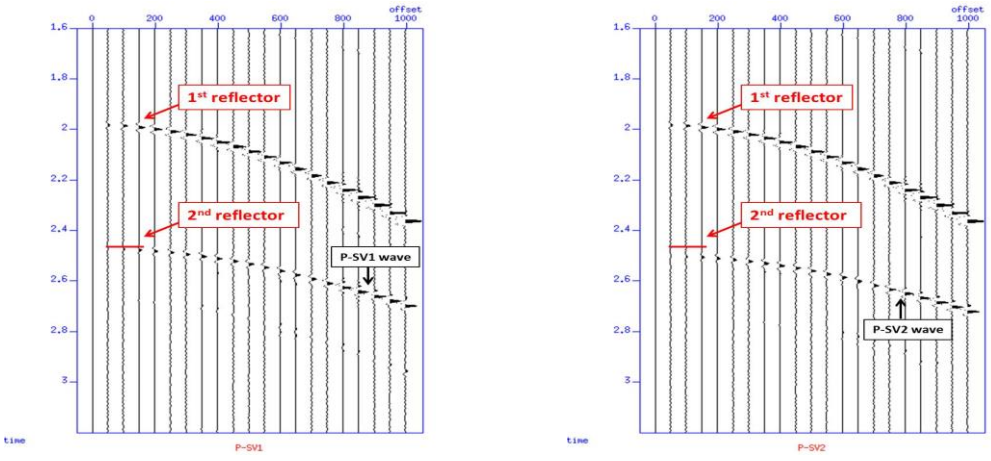

(a) (b)

Figure 3- 8: Shot gathers of P-SV1 (a) and P-SV2 (b) components

Chapter 4

Analysis of the PS-converted wave splitting in Sanhu 3D3C data

4.1 Introduction

A case study of a land 3D3C seismic dataset is performed in this chapter. This 3D3C seismic data is acquired in Sanhu, which is in the northwest of China. The main objective of this field data study is to compensate for the converted-wave splitting effect. As converted wave splitting is more significant than azimuthal variations, this chapter focuses on shear-wave splitting analysis. The estimated splitting parameters are related to the dominant fracture directions and fracture densities.

The workflow for this study is shown in Figure 4- 1. The seismic dataset is converted into an internal data format. Noise elimination, static correction and other preprocessing methods are applied to improve the data quality. The velocity analysis and NMO correction are both accomplished by the contractor. In order to provide wide azimuthal coverage, experienced data processors suggested that it is better that the dataset is sorted into common receiver gathers (CRG). Therefore, the following work is performed in individual CRGs and throughout different receiver lines.

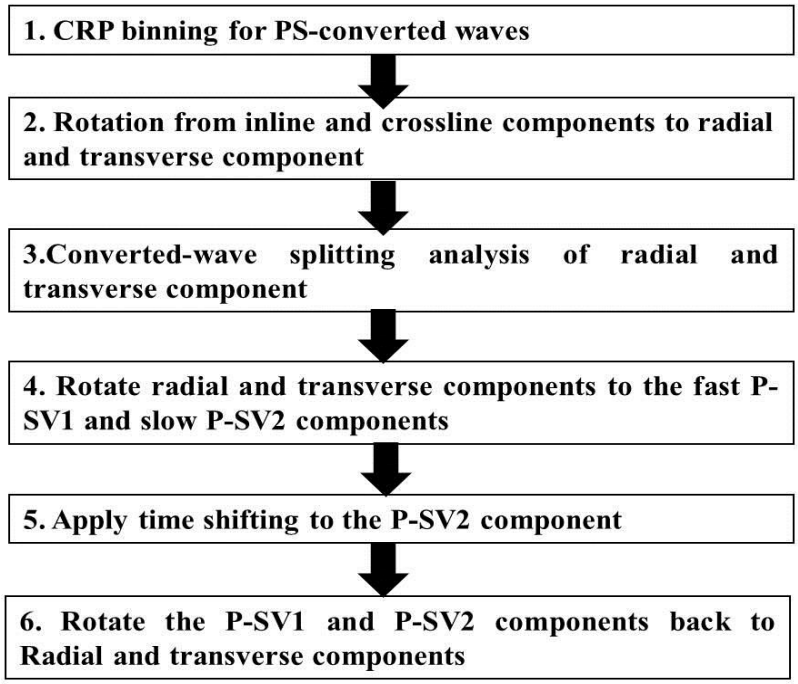

Figure 4- 1: Work flow of the Sanhu seismic data processing

The inline and crossline components are converted to radial and transverse components to better display the splitting effect on azimuthal gathers. A correlation function is used to acquire the relevant splitting parameters, which are representations of fracture properties including the fracture direction and fracture density. Then the radial and transverse components can be rotated into the fast P-SV1 and slow P-SV2 components accordingly. The major focus of this study is compensation for the converted-wave splitting effect. Therefore the azimuthal variation is not considered in this work. The fracture characterisation is mainly dependent on analysis of the converted-wave splitting. Applying a time shift to the P-SV2 component can compensate for the time delay between the P-SV1 and P-SV2 components. Finally, the updated P-SV2 and P-SV1 components can be rotated back to the radial and transverse components to improve the imaging. The fracture directions and time delays are also studied to provide an understanding of fracture properties in the survey area.

4.2 3D3C seismic survey in Sanhu Depression

Sanhu 3D3C seismic data is acquired from the Sanhu depression, which is located in Qaidam Basin. Qaidam Basin, which is the main exploration area of Qinghai Oilfield, occupies the northwestern part of Qinghai province, western China Figure 4- 2. The Sanhu depression, which is the largest biogenic gas production region, is in the central depression of Qaidam basin (Shuai et al., 2010). The gas reservoir in the Sanhu depression has been explored since 1956. The total area of the gas reservoir is about 128.8 km^2 and there is a proven deposit of 1958.06×10^8 cubic meters of natural gas. 2D multi-component seismic exploration had been applied before and a new 3D3C seismic acquisition was applied in 2009. The conventional P-wave seismic data is suffering from serious attenuation due to the gas saturation. Therefore this new acquisition project aims to use PS-converted wave seismic data to characterise the fractured reservoirs and predict the lithology. Previous and future seismic survey designs are shown in Figure 4- 3. The 3D3C seismic survey in Sanhu depression is displayed in the lower left corner of Figure 4- 3. The geometry of the Sanhu data acquisition is shown in Figure 4- 4. Blue lines displayed in Figure 4- 4 represent different receiver lines, which are all in the N-S direction. The following processing and analysis are based on this geometry. Therefore, it is not necessary to make conversions of azimuth angles between different coordinate systems. Notice that the azimuth 0° represents North and azimuth 90^o represents East in this geometry. The interpretation of dominant fracture directions and correlation with other types of data can be simplified by this simple directional representation. The fold-of-coverage map shown in Figure 4- 5indicates that the central area coloured green has high coverage. The highest coverage is seen in the left side of the survey area, coloured blue. The survey parameters can be found in Table 4- 1.

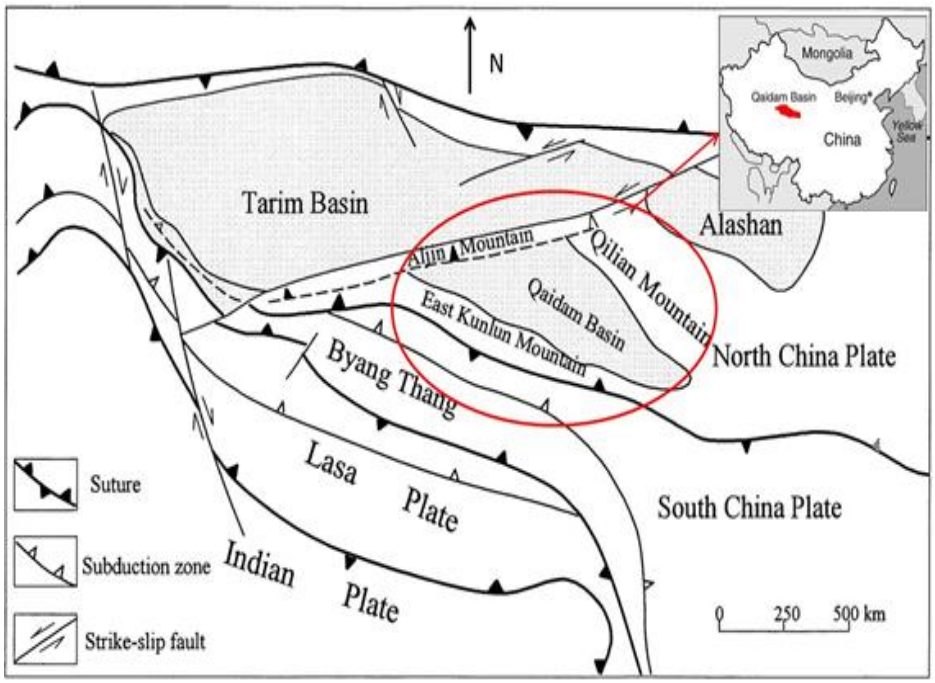

Figure 4- 2: Qaidam basin map in the northwest of China

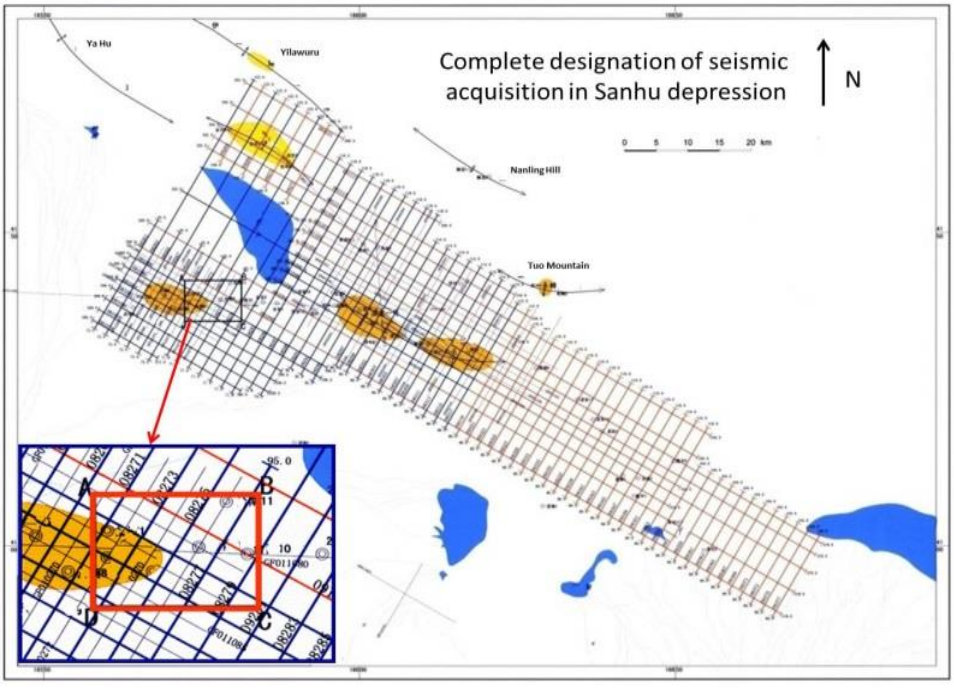

Figure 4- 3: The designation of previous and future seismic surveys in Sanhu depression. The 3D3C data is acquired in the area indicated by the red rectangle in the lower left corner.

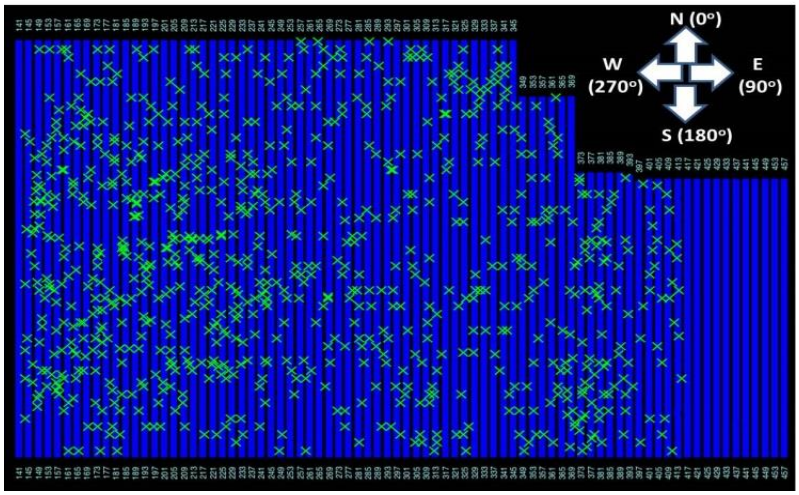

Figure 4- 4: The geometry of Sanhu data acquisition. (Green crosses are sources and blue points are receivers)

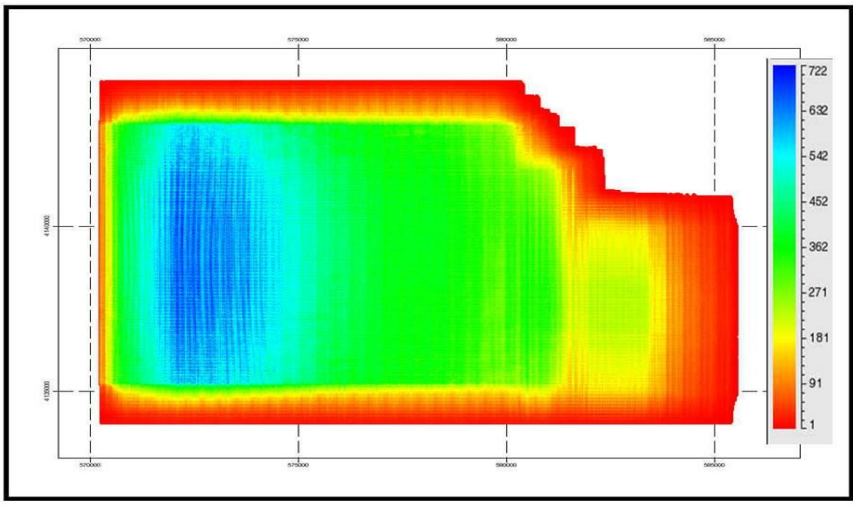

Figure 4- 5: Fold-of-coverage map in the 3D3C seismic survey

Sanhu 3D3C seismic acquisition parameters	
Source type	Dynamite
Source line interval	50m
Receiver line interval	200m
Short interval	200m
Receiver interval	50m
Number of swaths	28
Maximum offset	10682.547m
Minimum offset	15.355m
Number of shots	11648
Survey area	59.668 km^2
Sampling interval	4ms
Record length	10s

Table 4- 1: Acquisition parameters of the Sanhu 3D3C seismic survey

4.3 Geological background of Sanhu Depression

From the Mesozoic era to the Quaternary period, the Sanhu depression has undergone a similar tectonic development to the Qaidam basin, but it has its own features. The whole development procedure can be divided into three stages (Burchfiel and Wang, 2008):

I. Faulting depression stage（M_E～K）-The northern boundary of Sanhu depression suffered strong faulting. This not only controlled the Jurassic and Cretaceous sediments, but also created slight upfolds on the south margin of the north boundary faults. Some secondary small faults were also created on the upfold.

II. Depression stage （ E_{1+2} ～ N_2^2 ）-The whole Qaidam basin was descending and the amount of sedimentation increased during the Paleocene and Eocene series. The sedimentation was more significant in the west and north than in the east and south. At the end of the Eocene series, the Tibetan Plateau was rising due to the collision between the Indian and Eurasian Plates. The rise of Kunlun Mountain caused the large subsidence in the west of the basin. Lacustrine mudstones with a thickness of over several thousand metres were deposited in this period. The western margin of Sanhu depression is in the slope area of the western subsidence of Qaidam basin, and some lacustrine mudstones are expected to be deposited in this area as well. During the continuous rising of the Tibetan Plateau, the depression centre moved towards the east of the basin.

III. Folding inversion stage （N_2^3～Q）-The movement of the depression centre to the east of Qaidam basin at the end of the Pliocene series and Pleistocene resulted in the significantly thick Quaternary sediments in the east of the basin. At the same time, Sanhu area was still in the depression stage, which made the Sanhu depression, which provides the most important gas source rocks in the basin. Then the west of the basin was going through a folding inversion. The whole basin was uplifted by new

tectonic activities at the end of the Holocene series, ending the depositional history of Qaidam Basin.

4.4 Data evaluation

After the dataset has been sorted into common receiver gathers, the azimuthal coverage of the data can be evaluated. Here the receiver line 277, which is located in the middle of the survey area, is selected to show the azimuthal coverage. Receiver line 277 is highlighted in Figure 4- 6. Due to its central position, receiver line 277 is expected to contain a large range of azimuth angles and offset values, which are beneficial for the analysis of converted-wave splitting. Receiver line 277 includes a number of common receiver gathers (CRGs) ranging from 114514 to 115319. The number of traces contained in each CRG is displayed in Figure 4- 7. It is found that CRG 114680 and 114916 contain less than 3000 traces, which is much fewer than the traces in other CRGs. Apart from CRGs 114680 and 114916, other CRGs generally contain more than 4500 traces in each gather.

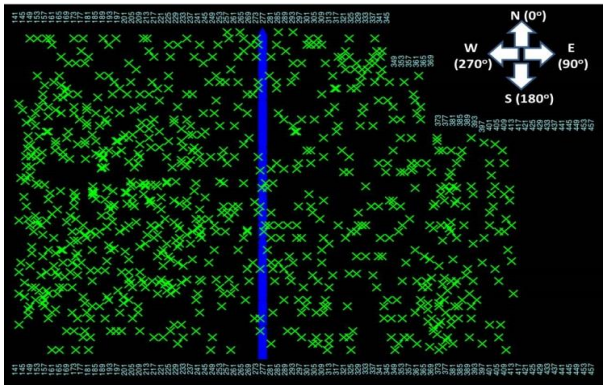

Figure 4- 6: Receiver line 277 (Blue line) in the data acquisition geometry.

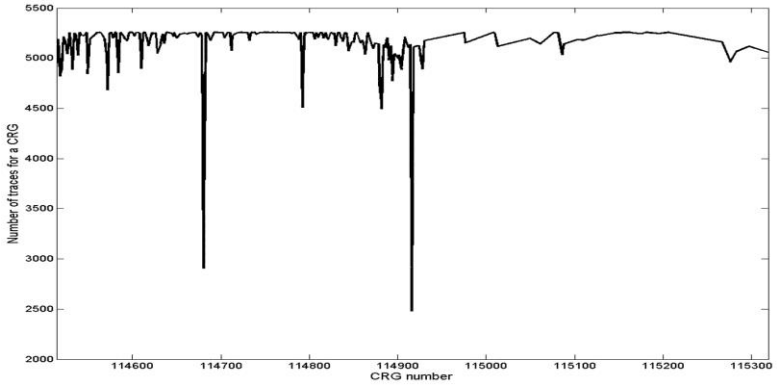

Figure 4- 7: Number of traces in each common receiver gather (CRG)

The first and last CRGs in receiver line 277 are CRG 114514 and 115319, respectively. CRG 114514 is the southernmost gather and CRG 115319 is the northernmost gather. Therefore, those gathers might have relatively narrow azimuth coverage, for which it could be difficult to perform reliable splitting analysis. The azimuth-versus-offset maps of those two gathers are displayed in Figure 4- 8. CRG 114830 is in the middle of receiver line 277 and its azimuth-versus-offset map is also displayed in Figure 4- 9 for comparison. For CRG 114514, the azimuth angles approximately range from 0^o to 90^o and from 270^o to 360^o. The azimuth coverage also includes a large range of offset values, from 176m to over 10000m. It is not difficult to understand this specific azimuth coverage by observing Figure 4- 6. Since CRG 114514 is at the bottom boundary of the survey and all sources are located above it, there is no available reflection data coming from the south of receiver 114514. Therefore the azimuth angles ranging from 90^o to 270^o are missing. CRG 115319 suffers from a similar limitation. However, reflection data coming from the north of receiver 115319 is not totally unavailable. There are a few azimuth angles ranging from 0^o to 90^o and from 270^o to 360^o at near offsets in CRG 115319. The azimuthal coverage of CRG 114830 is much clearer. Due to its central position in receiver line 277, CRG 114830 includes nearly all azimuth angles. It is not difficult to conclude that when the receiver is close to the central position, wider azimuth data becomes available. As the receiver is close to the survey boundary, nearly half of the azimuth angles are missing. However, due to the symmetry of the Cartesian coordinate system, azimuth angles covering two quadrants are still enough to provide acceptable results.

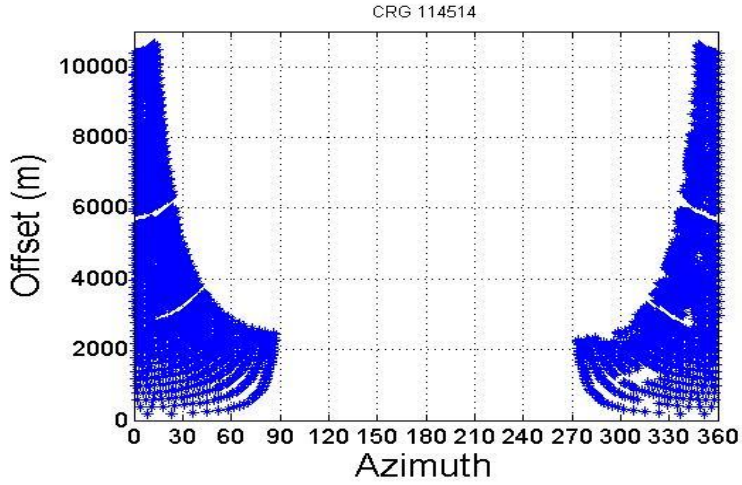

(a)

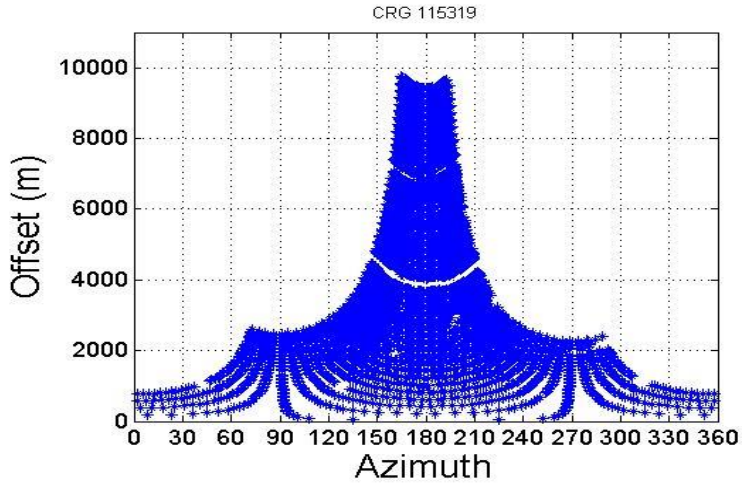

(b)

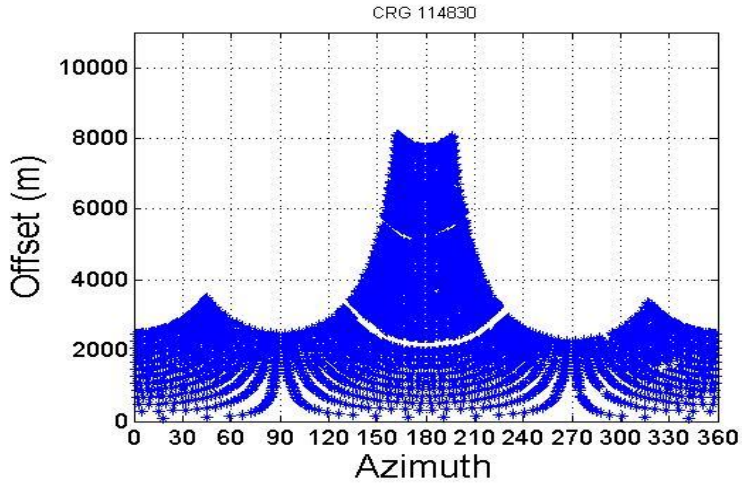

(c)

Figure 4- 8: Azimuth-versus-offset maps of CRG 114514 (a), 115319 (b) and 114830 (c)

The azimuth-versus-offset maps of CRG 114680 and 114916 are also displayed in Figure 4- 9. These two receivers all have a small number of traces. For receiver 114680, almost all azimuth angles are included but the largest offset is only about 6600m. A few azimuth angles are missing around 90^o. Therefore, azimuthal analysis of this CRG will not be significantly influenced by the azimuthal coverage. It is seen that the major azimuth coverage of CRG 114916 is from 180^o to 270^o. There are only a few traces at small offsets covering the azimuth angles ranging from 270^o to 360^o. Some azimuth angles are obviously missing in this azimuth range. The azimuthal coverage between 0^o and 180^o is even poorer. Azimuth angles from 90^o to 180^o are almost unavailable, although there are a number of traces with azimuth angles close to 90^o. Therefore, CRG 114916 suffers from a narrow azimuthal coverage, which could make it difficult to apply azimuthal analysis to obtain reliable splitting parameters and fracture properties.

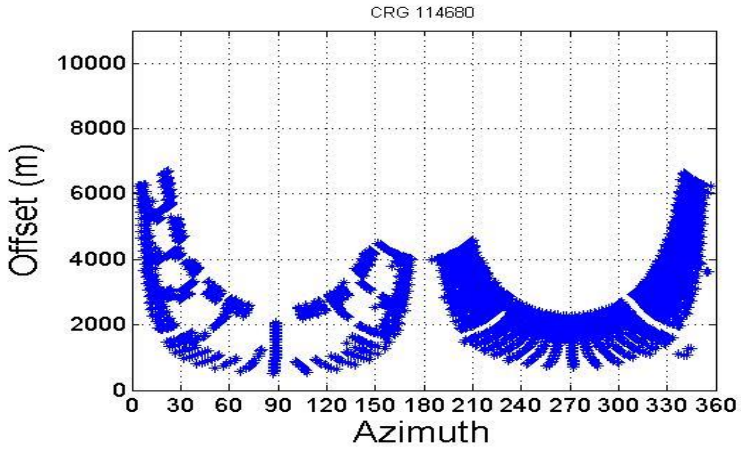

(a)

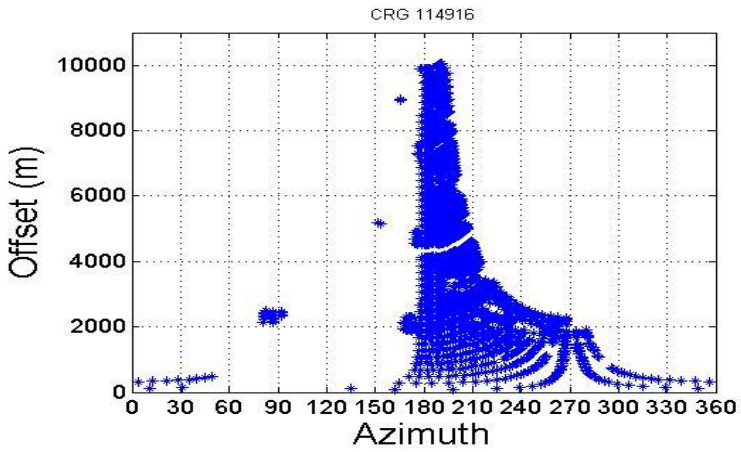

(b)

Figure 4- 9: Azimuth-versus-offset maps of CRG 114680 (a), 114916 (b).

A stack section of receiver line 277 can be obtained after the NMO correction has been applied to the dataset. The image of the stack result of receiver line 277 is displayed in Figure 4- 10. The horizontal axis is the receiver number along receiver line 277. Numbers are from 114514 to 115319, specifying the N-S direction. The area emphasised by a red rectangle is enlarged in Figure 4- 11. Anticline structures can be found in the stack section along receiver line 277. The fold axis of the anticline structures is generally aligned along the N-S direction. It can be seen that receivers ranging from approximately 11480 to 11500 have a poor imaging quality above 1s. It is suggested that those receivers might suffer from serious energy attenuation caused by gas saturation. These weak-energy positions are also located in the arched region of anticline structures, where large fracture densities are expected. Therefore, intensive fractures around this special area could provide significant space for gas saturation. As a result, the wave propagation through this area is significantly affected and poor imaging is obtained. In Figure 4- 11, some events, emphasised by red ellipses, look like "double-fold eyes". This strange feature shown in the stack section is a typical result of the shear-wave splitting effect. Fast and slow PS converted waves, travelling with different velocities, are dealt with as a single type of wave in the radial component. Separation of the fast P-SV1 component from the P-SV2 component is not applied, so both components are contained in the radial component. Therefore the direct processing and analysis of the radial components can reduce the seismic resolution and degrade the image quality. It could also cause ambiguities since it might create fake geological structures. Therefore, it is essential to compensate for the shear-wave splitting effect for PS-converted wave seismic data before applying any other processing methods. Besides, splitting parameters from the converted-wave splitting analysis can be used to facilitate fracture characterisation.

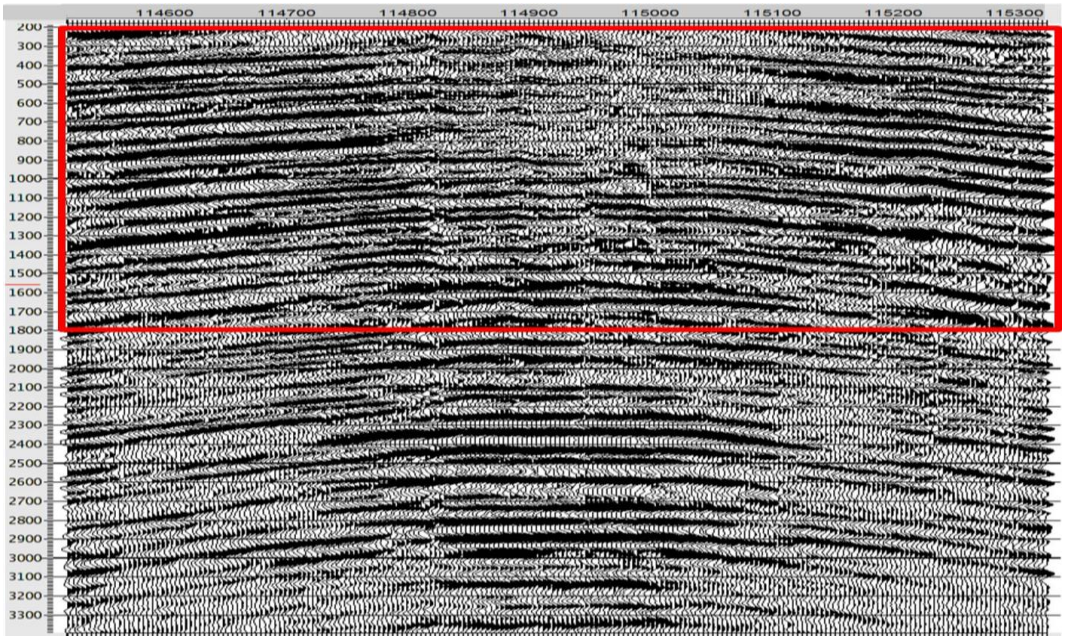

Figure 4- 10: Stack results of the radial components along receiver line 277. (The area emphasised by a red rectangle is enlarged in Figure 4-).

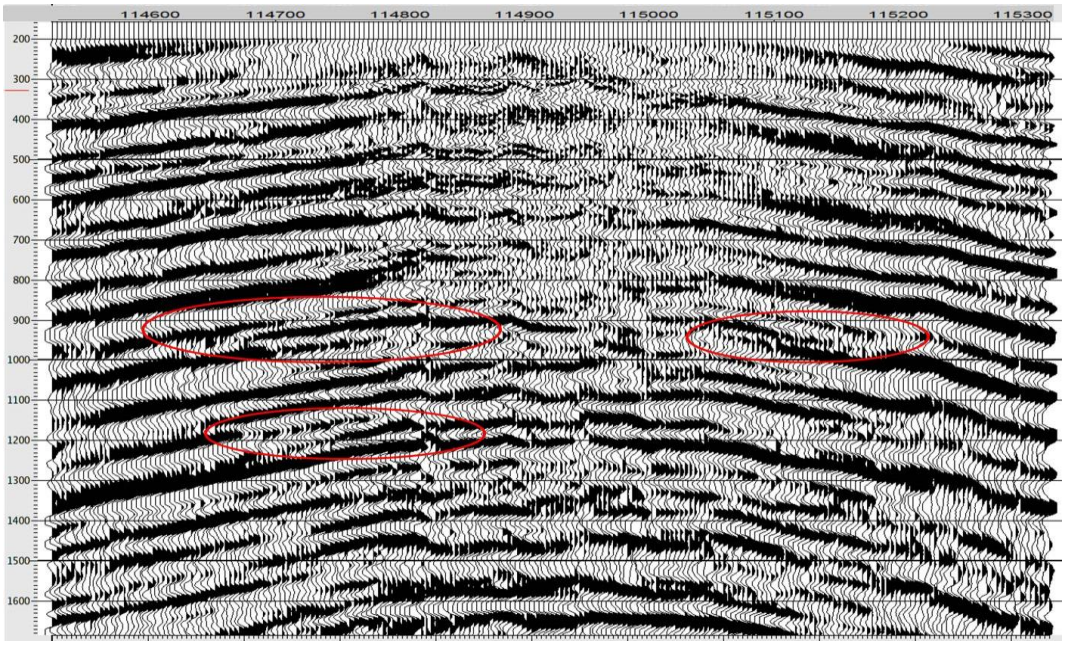

Figure 4- 11: Enlarged image of the red rectangle in Figure 4- 10.

4.5 Compensation for the PS-converted wave splitting effect

Due to the shear-wave splitting, the fast P-SV1 and P-SV2 waves are both projected into radial and transverse components. Therefore compensation for the converted-wave splitting must be based on analysis of both radial and transverse components. CRG 114830 is selected here to perform the analysis of splitting effects contained in

the radial and transverse components. CRG 114830 is in the middle position of receiver line 277 and has a wide azimuth coverage (Figure 4- (c)).

The common azimuth-stack gathers of both radial and transverse components are displayed in Figure 4- . The time windows indicated by red rectangles in both radial and transverse components are enlarged in Figure 4- . In order to provide better resolution and ease the processing time, the azimuth bin size is selected to cover 5^o. Consequently, the final results for the azimuth angles are actually azimuth ranges, in which five consecutive azimuth angles are all valid. This 5-degree-deviation of the fracture direction is acceptable in the context of seismic inversion and interpretation.

Fast P-SV1 and slow P-SV2 waves, caused by shear-wave splitting, can be observed in Figure 4- . On the azimuth-stack gather of the radial component, the splitting effect at about 0.75s and 0.85s is much clearer than the effect at other time positions. It is not difficult to notice the time delay between fast P-SV1 and slow P-SV2 components. Both fast and slow components occupy certain azimuth ranges, which causes sinusoidal azimuthal variations on the radial component. This effect complicates the processing and analysis of radial components, in which the major PS-converted wave energy is normally contained. Some experienced data processors usually simplify this problem by regarding it as a single type of azimuthal variation. Then the azimuthal processing methods and algorithms of P-wave data are directly applied to the PS-converted wave data. However, as discussed before, the azimuthal variation is complicated by shear-wave splitting. The separation of the fast P-SV1 component from the slow P-SV2 component is essential for subsequent data processing. Therefore, direct processing of the radial component can fail to improve the image quality. In the transverse component, the seismic resolution is not as high as the resolution of the radial component. The typical polarization reversals at every 90^o can be found on the transverse component, which are indicated by blue arrows in Figure 4- (b). This is an important effect caused by shear-wave splitting, which has been intensively studied in order to invert for fracture properties. It proves again that the transverse component is as important as the radial component in terms of improving the processing of PS-converted wave seismic data and estimating fracture parameters. Besides, it is difficult to observe azimuthal variations on the transverse

component. This implies that the azimuthal variation is less significant than the converted-wave splitting.

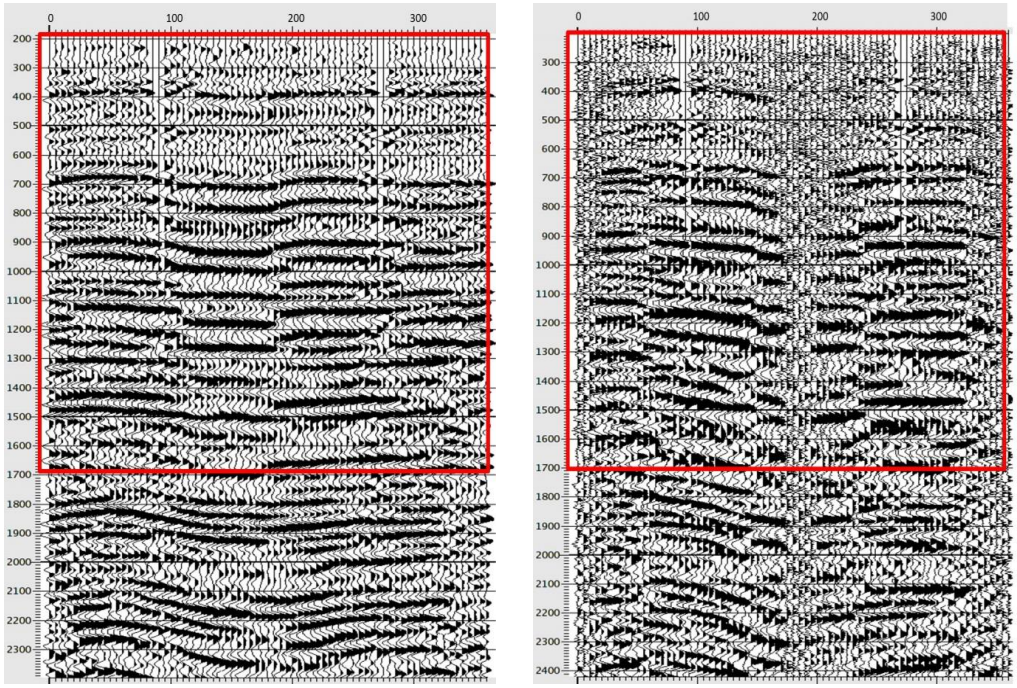

(a) (b)

Figure 4- 12: Azimuth-stack gathers of radial (a) and transverse (b) components of CRG 114830.

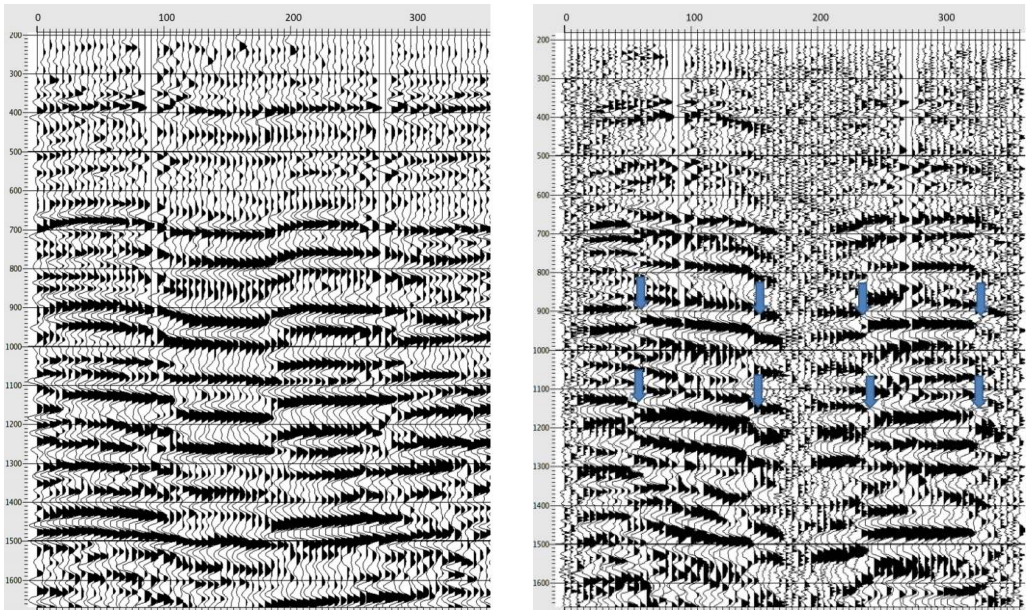

(a) (b)

Figure 4- 13: Enlargements of red rectangles of both radial (a) and transverse (b) components in Figure 4- .

The following analysis will be mainly focused on the splitting effect. The radial and transverse components are both studied to obtain the fracture direction and time delays between the P-SV1 and P-SV2 components. Assuming the fast P-SV1 and slow P-SV2 waves have similar waveforms with only a time delay, an objective function, which measures the similarity of the two waveforms, can be defined (Macbeth and Crampin, 1991):

$$F(\theta,\Delta T)=\sum_{t=win1}^{win2} PSV1(\theta,t)PSV2(\theta,t-\Delta T) \qquad (4\text{- }1)$$

where θ is the azimuth angle and ΔT is the time delay between the P-SV1 (*PSV1*) and P-SV2 (*PSV2*) components. *win1* and *win2* are the start time and end time of the analysis window. By scanning the horizontal rotation of the radial and transverse components, the fracture direction and time delay value will deliver a maximum value for function F. Then the two corresponding horizontal components will be the fast P-SV1 and slow P-SV2 components.

The P-SV1 component and P-SV2 component are considered to have similar waveforms. The only difference is the time delay between the two components. After calculation, the azimuth angle representing the fracture direction is 55^o in the azimuthal plane. It actually delivers an azimuth range, in which 55^o, 56^o, 57^o, 58^o and 59^o are all possible fracture directions. The calculated time delay between the fast P-SV1 and slow P-SV2 component is 44ms. The time delay is a representation of the fracture density. Large time delays are related to large fracture densities. Then the radial and transverse components can be rotated into the fast P-SV1 and slow P-SV2 components. The azimuth-stack gathers of the fast P-SV1 and slow P-SV2 components are shown in Figure 4- 14. The time windows indicated by red rectangles are enlarged in Figure 4- 15. It can be noticed that individual P-SV1 and P-SV2 components are obtained by horizontal rotation. The seismic resolution has been improved for both P-SV1 and P-SV2 components. The azimuthal behaviour of both components are similar. Moreover, it is difficult to find sinusoidal variation on both P-SV1 and P-SV2 components, indicating that the azimuthal variation is not significant.

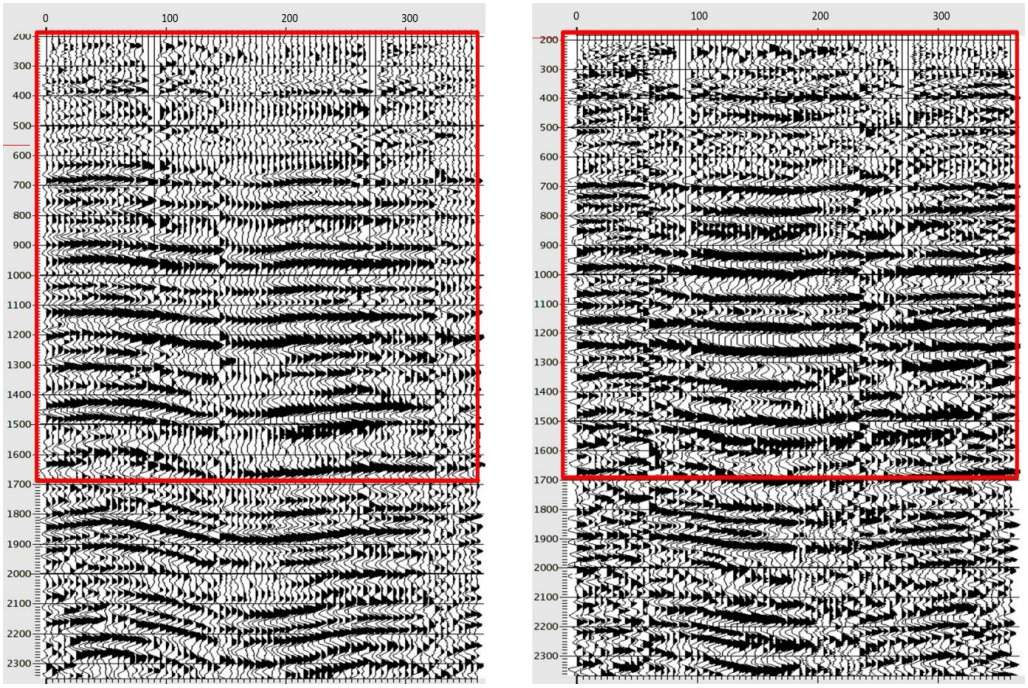

(a) (b)

Figure 4- 14: Azimuth-stack gathers of P-SV1 (a) and P-SV2 (b) components of CRG 114830.

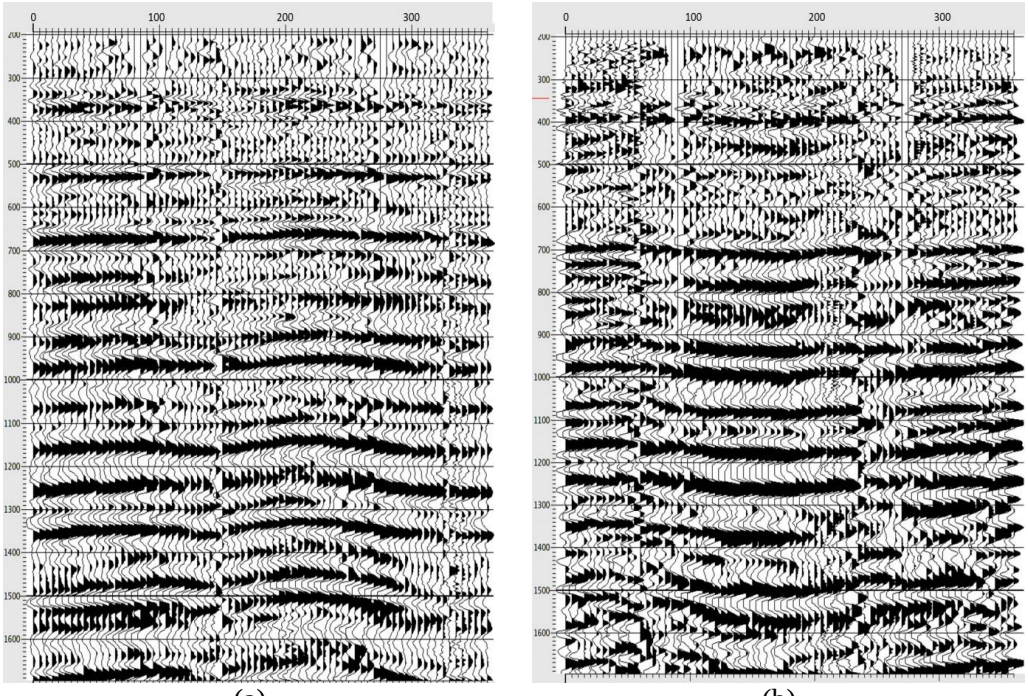

(a) (b)

Figure 4- 15: Enlargements of red rectangles of both P-SV1 (a) and P-SV2 (b) components in Figure 4- 14.

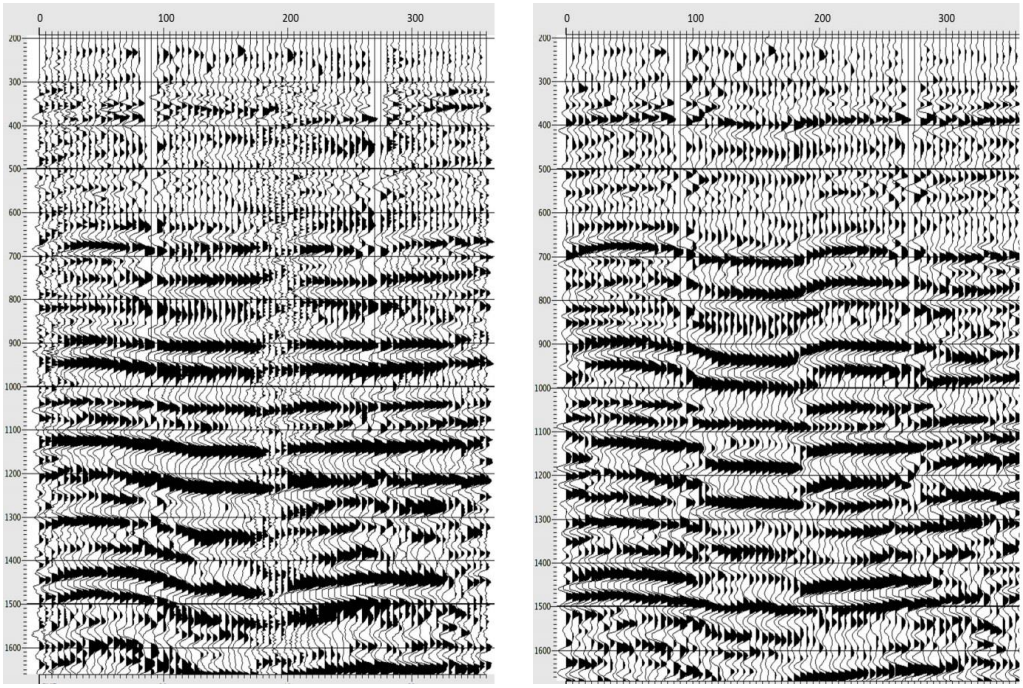

(a) (b)

Figure 4- 16: Azimuth-stack gathers of radial components of CRG 114830 with (a) and without (b) compensation for the converted-wave splitting.

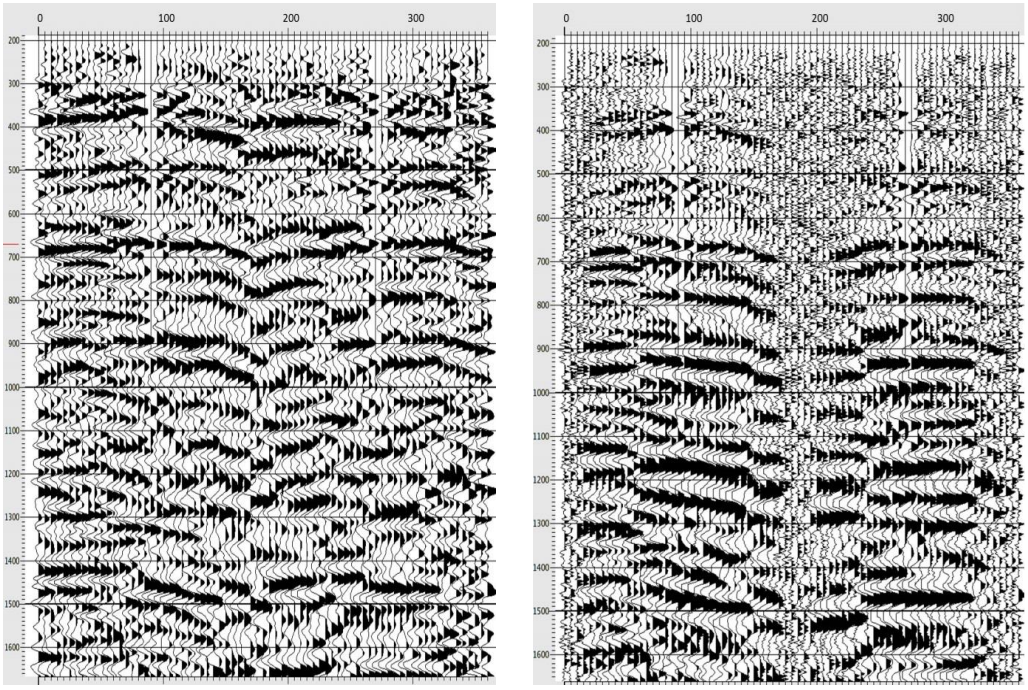

(a) (b)

Figure 4- 17: Azimuth-stack gathers of transverse components of CRG 114830 with (a) and without (b) compensation for the converted-wave splitting.

The time shift is then applied to the P-SV2 component to compensate for the time delay between the P-SV1 and P-SV2 components. The P-SV1 component and shifted P-SV2 component can be rotated back to the radial and transverse components. The updated radial and transverse components are displayed in Figure 4- 16 and Figure 4-17, respectively. After compensation for converted-wave splitting, the sinusoidal effect on the azimuth-stack gathers of the radial component has been removed and events are better focused, especially in the time window between 0.6s and 1s. This improvement surely enhances imaging quality. However, the events between 1.4s and 1.5s exhibit more significant sinusoidal azimuthal variation after the compensation for the splitting is applied. This indicates a potential need to apply an appropriate layer-stripping algorithm in future work. It can be seen that the transverse component contains less effective reflection energy after the compensation for the PS-converted wave splitting. The polarization reversal effect is also removed by the compensation. It implies that the interference of the P-SV1 and P-SV2 waves on both radial and transverse components has been eliminated. Moreover, most of the important information has been rotated back to the updated radial component. Therefore, the updated radial component is more effective for subsequent processing and analysis of PS-converted wave seismic data. Compared with the original radial component, the updated radial component shall be mainly used and analysed in the following processing and interpretation.

Similar analysis and processing are applied to other common receiver gathers along receiver 277. CRG 114698 is introduced here as a special example because it has a low signal-to-noise ratio. The azimuth-stack gathers of radial and transverse components of CRG 114698 are displayed in Figure 4- 18. Due to the low signal-to-noise ratio, it is very difficult to observe the typical sinusoidal variation on the radial component, although some events representing effective reflections can be identified. In this situation, it is even more difficult to directly analyse the azimuthal variation on the radial component. It will not bring reliable fracture parameters and fail to enhance the imaging quality. For the transverse component, the low signal-to-noise ratio also causes difficulties in observing converted-splitting effects. The seismic resolution of the transverse component is even poorer than the seismic resolution of the radial component. The uniform polarisation reversals at every $90°$ are

complicated by noise, and are very hard to identify. However, careful observation finds polarisation reversals on the events between 1s and 1.3s.

Using the similar objective function, the fracture direction and time delay parameters can be calculated. The fracture direction is also 55^o, which indicates a range from 55^o to 59^o. This fracture direction range is in accordance with the fracture direction range of CRG 114830. The time delay between the fast P-SV1 component and slow P-SV2 component of CRG 114698 is 40ms, which is slightly smaller than the time delay parameter of CRG 114830. Compared with CRG 114830, CRG 114698 provides a nearly equal fracture density. After horizontal rotation, the radial and transverse components are rotated into individual P-SV1 and P-SV2 components, which are shown in Figure 4- 19. It can be seen that both P-SV1 and P-SV2 components are still influenced by a low signal-to-noise ratio. However, the resolution of both P-SV1 and P-SV2 components is slightly higher than the resolution of either the radial or transverse components. More events representing effective reflections can be identified. The time delay between P-SV1 and P-SV2 components can also be seen by careful observation, although the signal-to-noise ratio is low.

Applying the similar time shifting to the P-SV2 component, the time delay between the P-SV1 and P-SV2 component can be compensated for. A horizontal rotation is applied to obtain the updated radial and transverse components, which are displayed in Figure 4- 20 and Figure 4- 21. The imaging improvement for the radial component is limited. The seismic resolution is slightly enhanced, especially between 1.3s and 1.6s. These improvements are certainly beneficial to imaging quality but in a less significant manner. Comparing the transverse components with and without compensation for the splitting effect, the polarisation reversals are also removed. Moreover, the overall effective reflection energy on the updated transverse becomes weaker. This also indicates that useful information on the original transverse component has been moved into the updated radial component.

It can be seen that the splitting effect is also influenced by low signal-to-noise ratio, although it is more robust than the azimuthal anisotropy. When the signal-to-noise ratio is low, the improvement is difficult to identify on the radial component although the PS-converted wave splitting is carefully compensated for. However, the

fracture direction and time-delay parameters are still useful for fracture characterization.

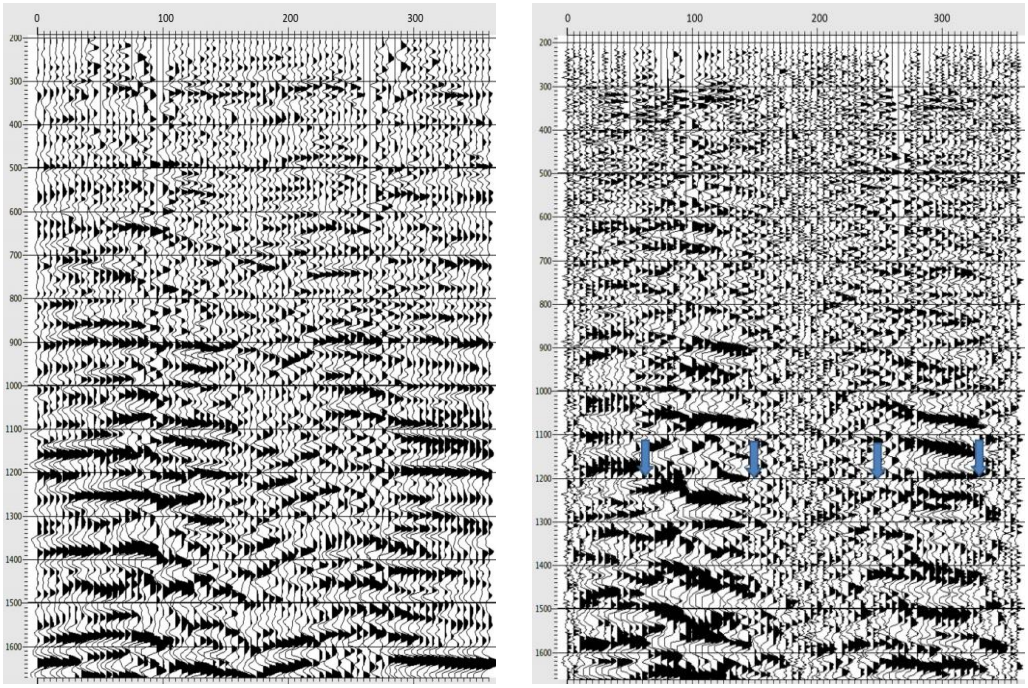

(a) (b)

Figure 4- 18: Azimuth-stack gathers of radial (a) and transverse (b) components of CRG 114698.

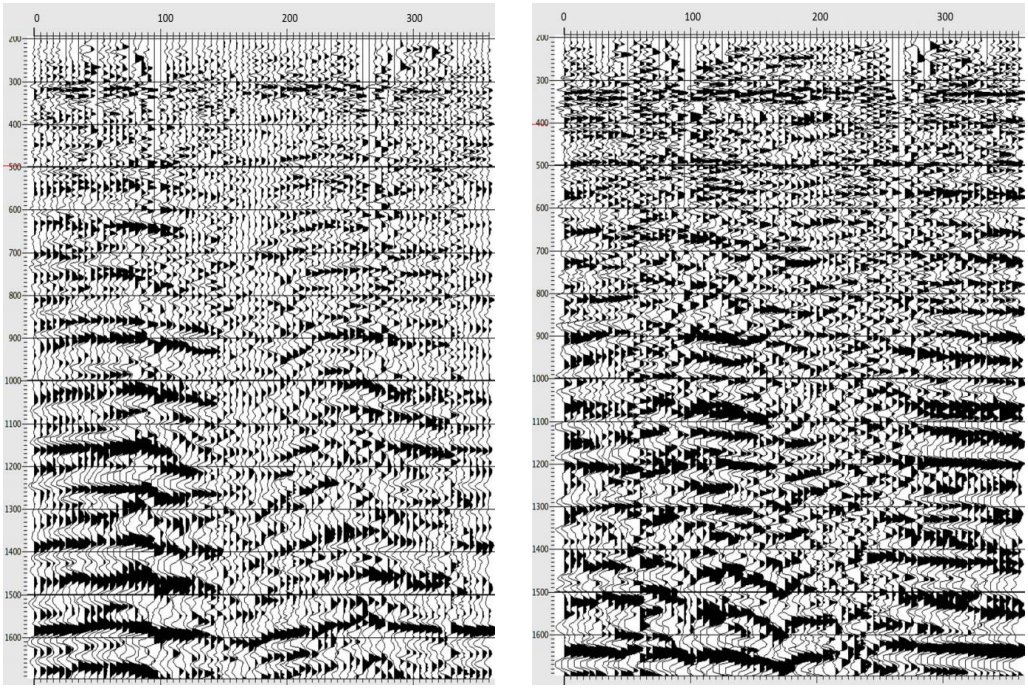

(a) (b)

Figure 4- 19: Azimuth-stack gathers of P-SV1 (a) and P-SV2 (b) components of CRG 114698.

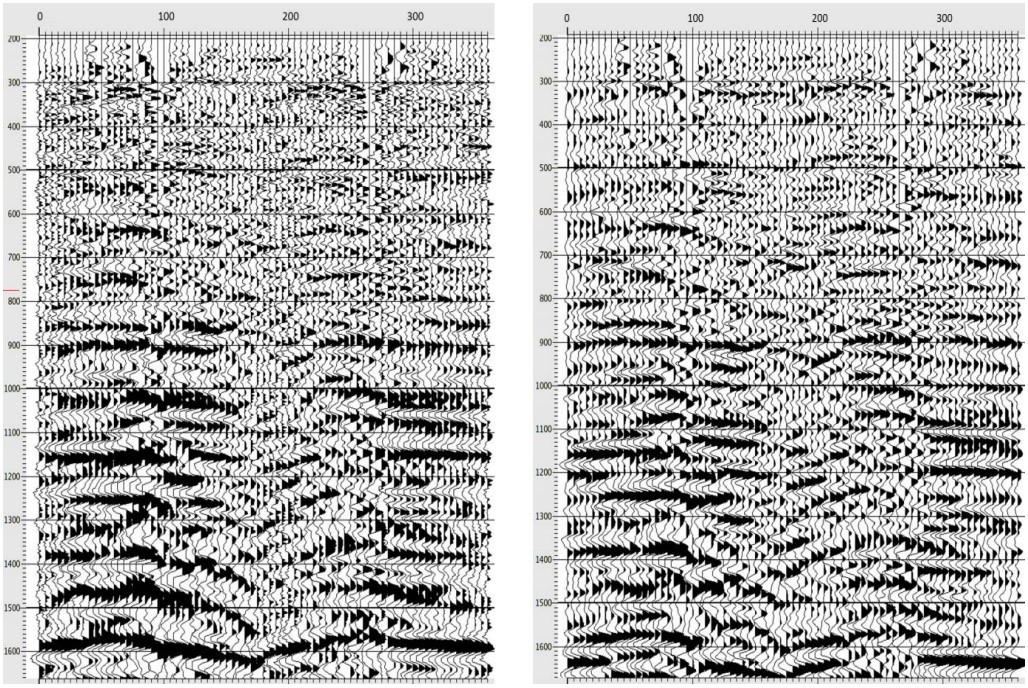

(a) (b)

Figure 4- 20: Azimuth-stack gathers of radial components of CRG 114698 with (a) and without (b) compensation for the converted-wave splitting.

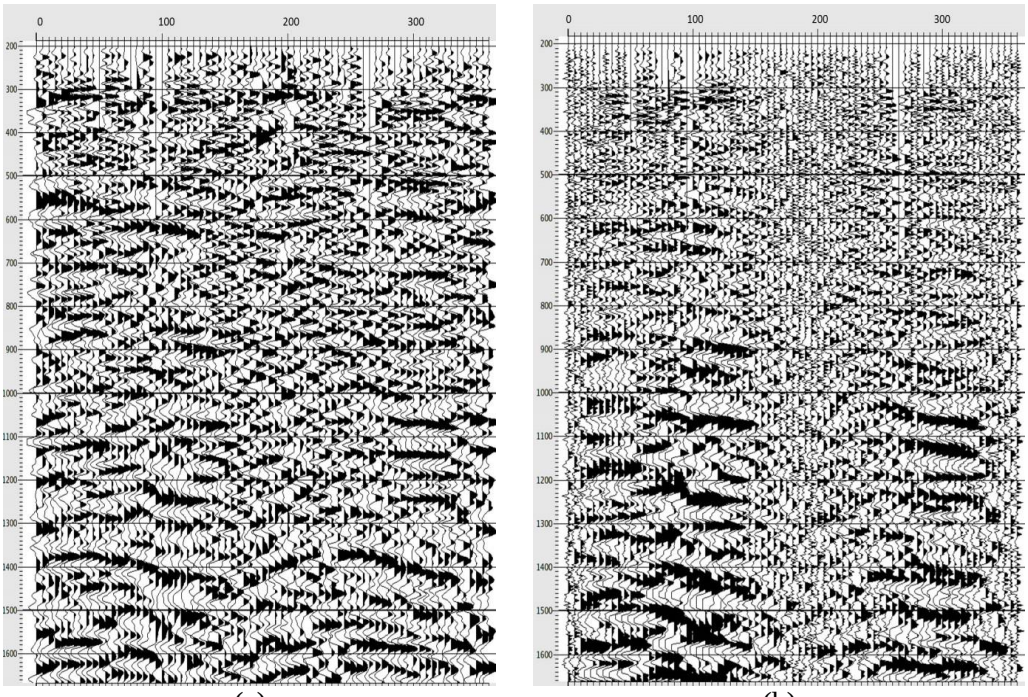

(a) (b)

Figure 4- 21: Azimuth-stack gathers of transverse components of CRG 114698 with (a) and without (b) compensation for the converted-wave splitting.

After the compensation for the converted-wave splitting is performed for all common receiver gathers along receiver line 277, P-SV1 and P-SV2 components of all receiver gathers can be obtained. Then common receiver gathers can be stacked to form the stack section along receiver line 277. The stack sections of the fast P-SV1 and slow P-SV2 components along receiver line 277 are shown in Figure 4- 22. Both P-SV1 and P-SV2 components exhibit anticline structures in their stack sections. The "double-fold eyes" feature shown on the original radial component is hard to find on either P-SV1 or P-SV2 components. This implies that the image quality of both P-SV1 and P-SV2 components is higher than the image quality of the original radial component. A time delay between the two sections can be observed, which is attributed to the PS-converted wave splitting. For both P-SV1 and P-SV2 components, the area above 1s and in the receiver range from 114800 and 115100 is poorly imaged. This observation is in accordance with the stack section of the original radial component. The analysis of the radial component suggests that this could be caused by intensive fractures, in which gas is saturated. Moreover, some events indicated by red arrows are well imaged in the P-SV2 component but are poorly imaged in the P-SV1 component. Some events indicated by yellow arrows are poorly imaged in the P-SV1 component but are well imaged in the P-SV2 component. This is related to the increase in fracture density in this special area, which affects the reflector reflectivity.

It has been proved in laboratory studies that the velocity of the slow S2 wave decreases as the fracture density increases (Hardage et al., 2011). However, the velocity of the fast S1 wave changes slightly as the fracture density increases. This variation has an influence on the reflectivity of the P-SV2 component. As the P-SV2 velocity in a fractured layer decreases, the velocity difference between the fractured layer and its lower layer becomes larger. Consequently, the reflectivity of the bottom reflector also becomes larger, which could create certain points of stronger energy and better focusing on the stack section. However, the decrease of the P-SV2 velocity in a fractured layer makes it closer to the velocity of its upper layer. Therefore, the reflectivity of the upper reflector decreases and the amplitude of the P-SV2 component could also decrease.

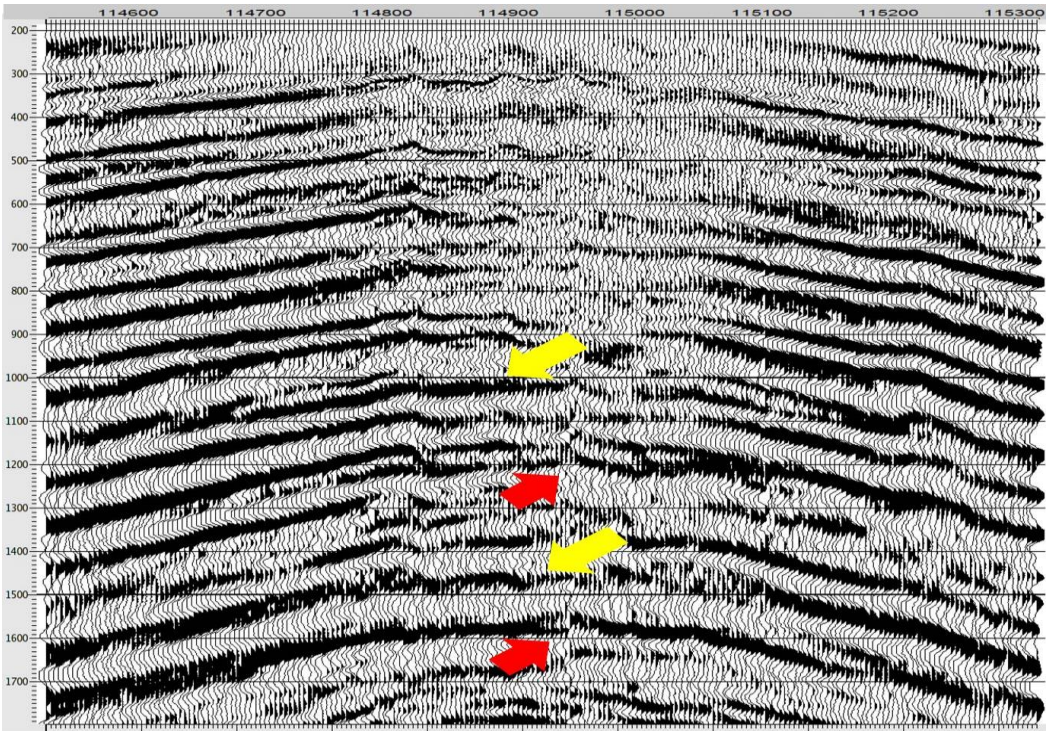

(a)

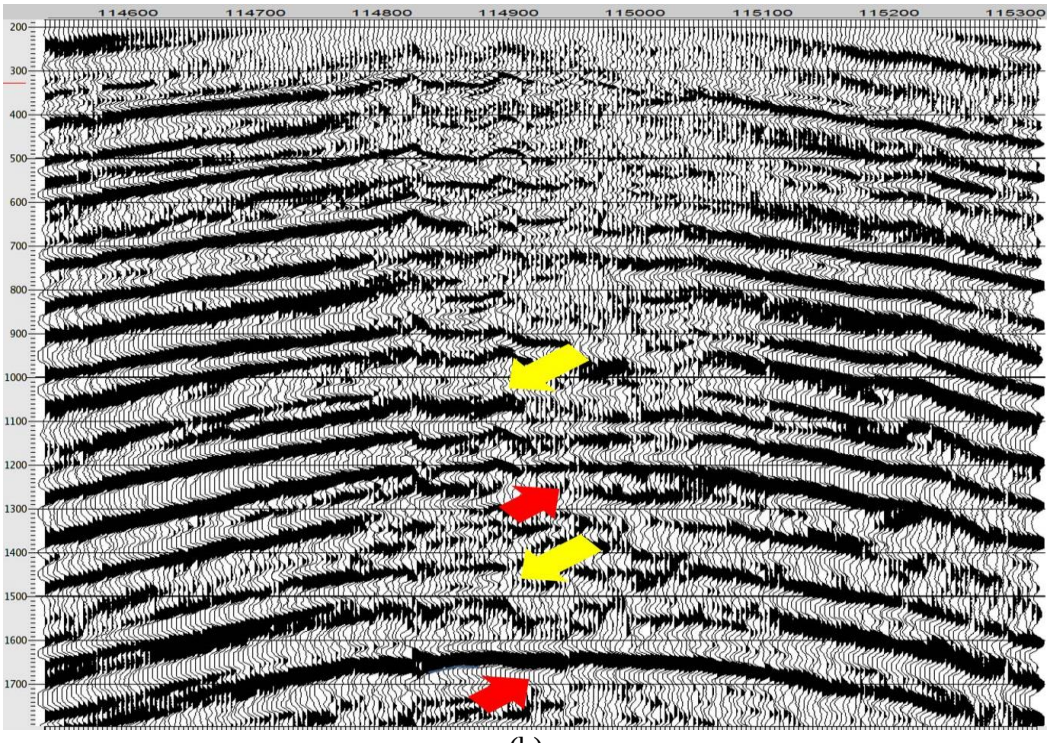

(b)

Figure 4- 22: Stack sections of the P-SV1 (a) and P-SV2 (b) component of receiver line 277.

The differences between the reflection magnitudes of both P-SV1 and P-SV2 components can be observed by comparisons of their individual stack sections. In Figure 4- 22, the red arrow at about 1.7s indicates the area, where the energy of P-SV2 components is higher than the energy of P-SV1 components. This is caused by the increase of reflectivity of this reflector. However, the upper reflector, indicated by the yellow arrow at about 1.45s, has lower energy on the P-SV2 component than on the P-SV1 component. This is attributed to the decrease of the upper reflectivity. A similar phenomenon can be found between 1s and 1.3s, indicated by another pair of red and yellow arrows. These differences in the stack sections imply that the fracture density in this area is relatively larger than in other locations, which is also consistent with the previous conclusion.

Therefore, it is not wise to make a simple judgment that the P-SV1 component has either a higher or lower imaging quality than the P-SV2 component. For this dataset, it is more reasonable to study both P-SV1 and P-SV2 components for inversion and interpretation, rather than only focusing on one single component.

With individual P-SV1 and P-SV2 components available, the time delay between two components can be compensated for and the updated radial component can be obtained. Finally the stack section of the updated radial component along receiver 277 is displayed in Figure 4- 23(a). The stack section of the original radial component along receiver 277 is shown in Figure 4- 23(b) for comparison. The events looking like “double-fold eyes” are removed in the updated radial component. Some of them are indicated by red ellipses in both Figure 4- 23(a) and Figure 4- 23 (b) to show the improvement. Compared with events on the original radial component, the events on the updated radial component are better focused. Seismic resolution of the updated radial component is enhanced by those improvements, which is beneficial to seismic data interpretation.

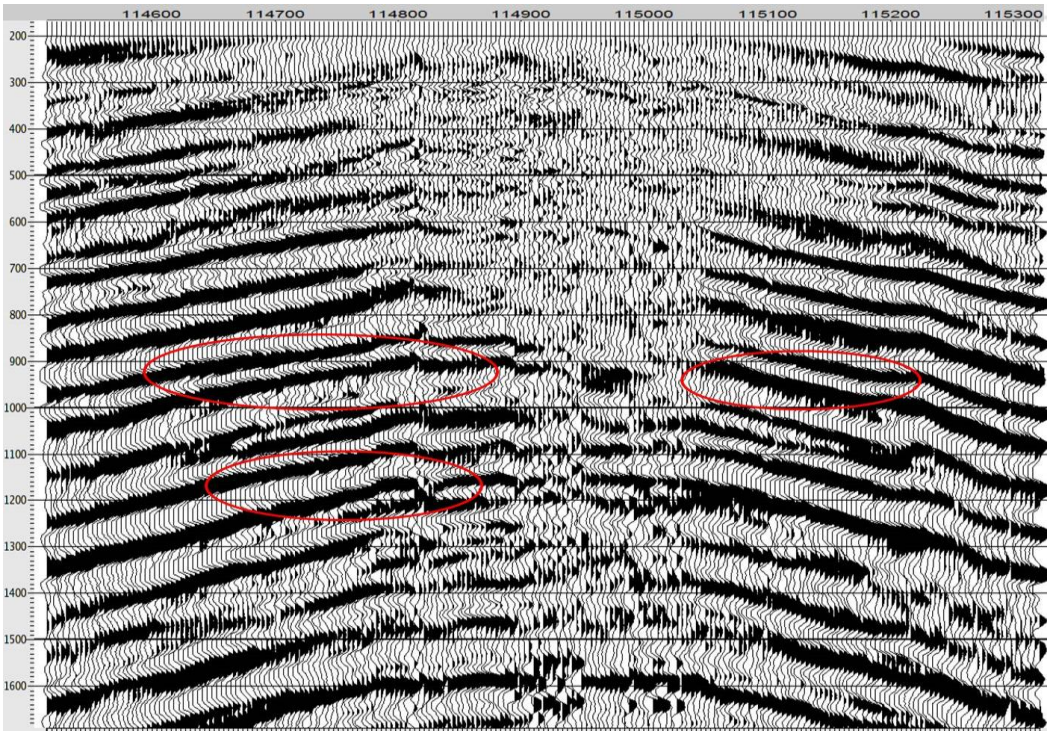

(a)

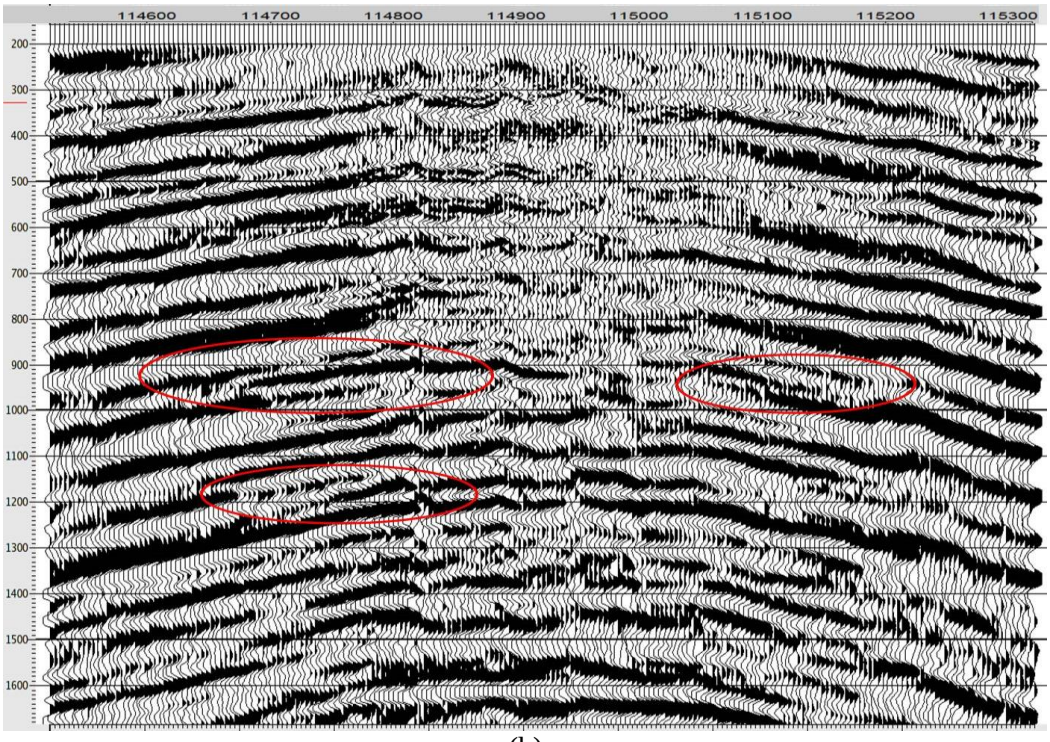

(b)

Figure 4- 23: Stack sections of the radial component of receiver line 277 (a) with, and (b) without, compensation for the converted-wave splitting.

Careful inspection finds that significant imaging improvements are mainly located on the two sides of the anticline area. The image quality on the two sides for both P-SV1 and P-SV2 components is higher than in the centre arched area. Therefore the two sides on the radial component retain high image quality after the compensation for time delay between P-SV1 and P-SV2 components.

The improvement in the centre arched area is limited. This area is likely to be subject to gas saturation in intensive fractures. Firstly, the significant attenuation caused by gas saturation decreases image quality in this area. Secondly, the behaviour in this area differs for stack sections of P-SV1 and P-SV2 components. As previous observations suggests, some events are better focused on the P-SV1 component and some events are better focused on the P-SV2 component. Therefore, image quality of this area on the radial component is a compromise resulting from horizontal rotation of both the P-SV1 component and P-SV2 component.

When compensation for the PS-converted wave splitting of each common receiver gather has been accomplished, the fracture direction and time delay can be obtained. A similar procedure is applied to the common receiver gathers of other receiver lines. The distribution of fracture direction and time-delay parameters for the whole survey is displayed in Figure 4- 24. The horizontal axis represents the X-coordinate of receivers and the vertical axis represents the Y-coordinate of receivers. The numbers on the color bar are time delays in ms. Black arrows in Figure 4- 24 represent fracture directions of individual common receiver gathers.

It is seen that all fracture directions are in the range between 0^o and 90^o. Most of them are generally aligned in the NE direction. Moreover, the distribution of fracture directions is uniform in this survey area, suggesting consistency among neighboring receiver gathers. The time delays are in the range between approximately 14ms and 45ms. The area of large time delays is specified by receivers with X-coordinates approximately from 18000 to 45000 and with Y-coordinates approximately from 25000 to 31000. The coverage is wide in the W-E direction and relatively narrow in the N-S direction. The time delays at the southern, northern and western boundaries are much smaller than time delays in the central area. Large time delays are normally associated with large fracture densities. As stack sections of receiver line 277

indicate, such a fractured area with large fracture densities is usually found in the arched area of anticline structures, where a large compressive stress is expected. The spread of this area of interest is generally aligned in the W-E direction. Therefore, the distribution of large fracture densities could be helpful for locating anticline structures. Moreover, this wide distribution of intensive fractures might provide suitable storage for natural gas, which is important in gas exploration and extraction.

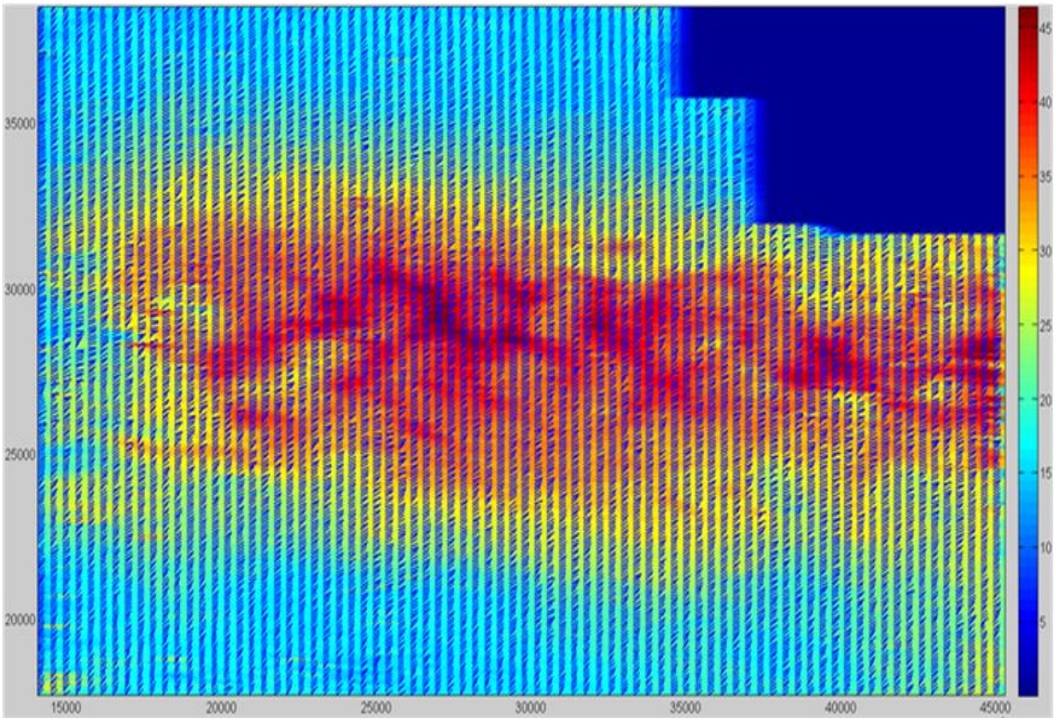

Figure 4- 24: Map of fracture orientation and time-delay of the survey area.

My result for fracture characterisation, as concluded from seismic data, is also compared with the stress-field map of China. The maximum stress directions in China, which are derived from earthquake focal mechanisms, are shown in Figure 4-25. The Qaidam basin, where Sanhu seismic data acquisition is performed, is highlighted in the orange circle. The maximum stress directions approximately follow the NNE-NE direction. This provides a good correlation between the fracture directions and the maximum stress directions. It gives increased confidence in the methods used to analyse the PS-converted wave splitting. Moreover, Sanhu depression is famous for its gas production. This also provides support to the fact that intensive fractures have been developed there in a large region, suitable for gas

storage. However, other types of data are still necessary for a fully integrated study of fracture characterization, which is critically important for exploration of, and production from, fractured reservoir.

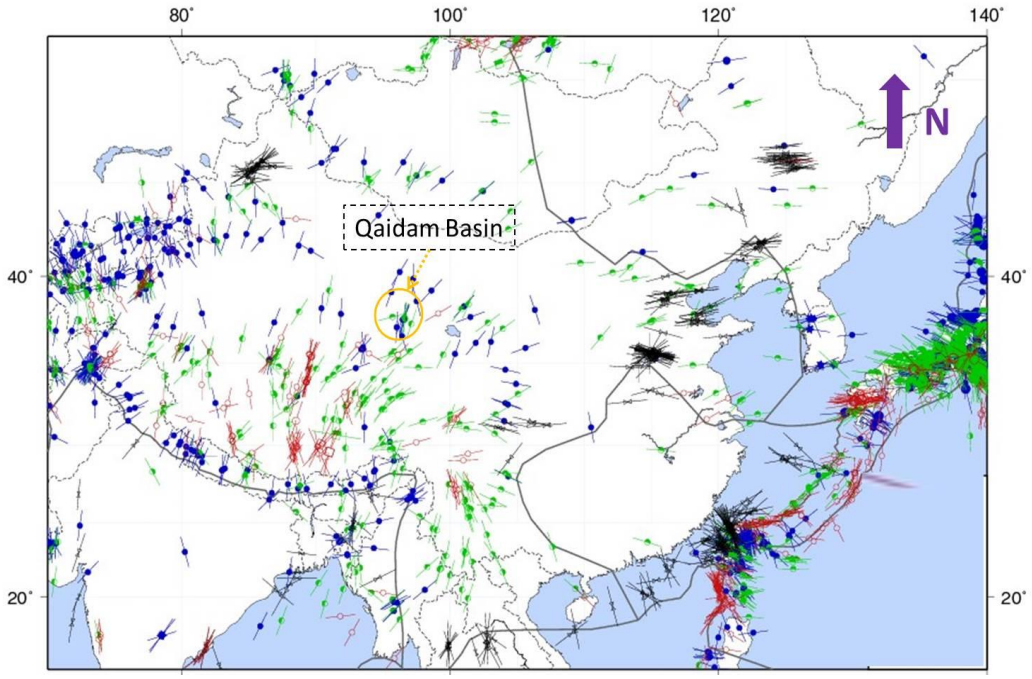

Figure 4- 25: Map of maximum stress directions in China. The image is modified from the work by Heidbach et al (2008) and the Qaidam basin is highlighted in the orange circle. Blue, red, green and black indicators represent NF (normal faulting), SS (strike-slip), TF (thrust faulting) and U (unknown) tectonic stress regime, accordingly.

4.6 Summary

The PS-converted wave seismic data acquired in Sanhu has been studied in this chapter. The dataset was sorted into common receiver gathers to obtain wider azimuth coverage. PS-converted wave splitting can be observed on azimuth-stack gathers of both radial and transverse components. Radial and transverse components are scanned to find the fracture direction and the time delay between the P-SV1 and P-SV2 component. Then horizontal rotation is applied to obtain the fast P-SV1 and slower P-SV2 component and the time delay is compensated for. Finally, the P-SV1 and time-shifted P-SV2 component can be rotated back to radial and transverse components. Events which look like “double-fold eyes” on the radial component, and

are caused by the splitting, are removed by this procedure and less effective reflections remain on the transverse component. However, this analysis algorithm is influenced by the signal-to-noise ratio. The image quality cannot be greatly enhanced if the signal-to-noise ratio is low.

This procedure is applied to all receiver gathers in the survey. The stack section of a single receiver line is studied to show the improvement. Stack sections of both P-SV1 and P-SV2 are better imaged than the stack section of the original radial component. The "double-fold eyes" are removed, and events are better focused. These improvements are mainly found on the two sides of anticline structures. In the arched area of anticline structures, where significant gas saturation is expected, the signal-to-noise ratio is low and the improvement is not significant. Besides, in the arched area, some events are poorly imaged on the P-SV1 component but are well imaged on the P-SV2 component. Some events of low image quality on the P-SV2 component are found to be of good image quality on the P-SV1 component. This result is attributed to increased fracture densities in this special area. The updated radial component also has higher image quality than the original radial component. However, in the arched area, the imaging of the updated radial component is a compromise of both the P-SV1 and P-SV2 component.

Fracture directions and time delays obtained during the compensation for converted-wave splitting are mapped into the survey area. Dominant fracture directions are approximately aligned in the NE direction. This result is close to the maximum stress direction in Qaidam basin, which is along the NNE-NE direction. The area, where large time delays are found, has a wide range along the W-E direction. It is likely to be associated with the arched area of anticline structures, where intensive fractures are likely to be developed. This intensively fractured area will be beneficial for the storage and migration of natural gas, and this should be carefully considered with the assistance of other types of data.

Chapter 5

Azimuthal variations of moveout and velocity of PS converted waves in HTI media

5.1 Introduction

Velocities and moveouts of seismic waves have been regarded as typical indicators of azimuthal anisotropy. The pure-mode NMO velocities have an elliptical variation with azimuth in a HTI medium (Tsvankin, 1997b). The P-wave NMO velocity and moveout azimuthal variations have been widely used to compensate for the azimuthal anisotropy and estimate fracture properties. However, the PS-converted waves in HTI media is not well studied and less widely used. Some applications (e.g. Dai and Li, 2010; Mattocks et al., 2005) assume that the azimuthal variation of the PS-converted wave velocity is an ellipse. This is mainly based on moveout measurements from PS-converted wave seismic data, and not supported by theory. In this chapter, formulas for the azimuthal variation of the fast P-SV1 and slow P-SV2 wave NMO velocities are derived, and can be approximated into ellipses. Incorporating the elliptical equations into PS-converted wave moveout equations, the moveouts of P-SV1 and P-SV2 waves are also close to ellipses, which enable the analysis of PS-converted moveouts to detect azimuthal variations in HTI media. The

analysis is also extended into multi-layered media and an accuracy test is performed. The azimuthal moveout equation is more accurate than the hyperbolic moveout equation when the fracture density (fracture density is defined in Equation 2-20) is as large as 0.1 and the offset-to-depth ratio is as large as 1.5.

5.2 Interval parameters of a HTI medium

A HTI medium has a symmetry axis aligned in a fixed direction in the horizontal plane. In a HTI medium induced by vertical fracturing, the fracture strike is perpendicular to the symmetry axis. In anisotropic medium, particle motion is neither purely longitudinal (P-waves) or purely transverse (S-waves), which is different from the particle motion in isotropic medium (Pilant, 2012). For this reason, shear waves in anisotropy medium are referred as qS1 (quasi S1-wave) and qS2 (quasi S2-wave). For shear waves, the fracture strike is the direction in which the fast shear wave (qS1) is polarised and the symmetry axis direction is the direction in which the slow shear wave (qS2) is polarised. For other directions, the S-wave is the combination of qS1- and qS2-waves. In the following discussion, qS1 and qS2 will be replaced by S1 and S2 for simplicity.

The P-wave NMO velocity in HTI medium can be approximated into an ellipse and can be written as (Tsvankin, 1997b):

$$v_{p2}^2(\theta) = \frac{v_{p2-0^o}^2 v_{p2-90^o}^2}{v_{p2-0^o}^2 \sin^2(\theta-\beta) + v_{p2-90^o}^2 \cos^2(\theta-\beta)} \tag{5- 1}$$

where θ is the azimuth angle. β represents the isotropy plane direction, which is fracture direction. v_{p2} is the P-wave NMO velocity, which is a function of azimuth angle θ. v_{p2-0^o} and v_{p2-90^o} are the P-wave NMO velocities in the direction parallel and perpendicular to the fracture direction, respectively.

In the isotropy plane, the P-wave NMO velocity v_{p2} is defined to be equal to the vertical velocity (the fracture direction is represented by 0^o in the azimuthal plane):

$$v_{p2-0^o} = v_{p0} \equiv \sqrt{\frac{c_{33}}{\rho}} \tag{5- 2}$$

while in the symmetry axis direction, the P-wave NMO velocity is defined as:

$$v_{p2-90^O} = v_{p0}\sqrt{1+2\delta} \tag{5- 3}$$

It can be seen that the anisotropic parameter δ controls the NMO velocity differences along directions parallel and perpendicular to the fracture direction. If the sign of δ is negative, the P-wave NMO velocity is larger along the fracture direction than along the symmetry axis direction. If the sign of δ is positive, the P-wave NMO velocity is smaller along the fracture direction than along the symmetry axis direction. Considering weak seismic anisotropy, $|\delta| \ll 1$, the velocity difference between these two orthogonal directions is also small.

Shear-waves are more complicated than P-waves due to the splitting effect. However, NMO velocities of both shear-waves can also be described as ellipses:

$$v^2_{S_1 2}(\theta) = \frac{v^2_{S_1 2-0^o} v^2_{S_1 2-90^o}}{v^2_{S_1 2-0^o}\sin^2(\theta-\beta) + v^2_{S_1 2-90^o}\cos^2(\theta-\beta)} \tag{5- 4}$$

$$v^2_{S_2 2}(\theta) = \frac{v^2_{S_2 2-0^o} v^2_{S_2 2-90^o}}{v^2_{S_2 2-0^o}\sin^2(\theta-\beta) + v^2_{S_2 2-90^o}\cos^2(\theta-\beta)} \tag{5- 5}$$

The fast S1-wave is polarised in the isotropy plane while the slow S2-wave is polarised in the symmetry axis plane. The NMO velocities of the fast S1-wave and slow S2-wave along the isotropy plane are defined as:

$$v_{s_1 2-0^0} = v_{s_1 0} \equiv \sqrt{\frac{c_{44}}{\rho}} \tag{5- 6}$$

$$v_{s_2 2-0^o} = v_{s_2 0} \equiv \sqrt{\frac{c_{55}}{\rho}} \tag{5- 7}$$

while their NMO velocities along the symmetry plane are also defined as:

$$v_{s_1 2-90^o} = v_{s_1 0}\sqrt{1+2\gamma} \tag{5- 8}$$

$$\left.\begin{aligned} v_{s_2 2-90^o} &= v_{s_2 0}\sqrt{1+2\sigma} \\ \sigma &= \frac{v_{p0}^2}{v_{s_2 0}^2}(\varepsilon-\delta) \end{aligned}\right\} \tag{5- 9}$$

Similar to P-wave NMO velocities, the S1-wave NMO velocity along the symmetry plane is determined by an anisotropic parameter, which is γ. If the sign of γ is negative, the S1-wave NMO velocity is larger along the fracture direction than along the symmetry axis direction. If the sign of γ is positive, the S1-wave NMO velocity is smaller along the fracture direction than along the symmetry axis direction. The velocity difference between the two directions is also small due to the weak seismic anisotropy.

The S2-wave is more complex than either the P-wave or the S1-wave. The NMO velocity difference of S2-waves is determined by the term $(\varepsilon-\delta)$. If the sign of $(\varepsilon-\delta)$is negative, the S2-wave NMO velocity is larger along the fracture direction than along the symmetry axis direction. If the sign of $(\varepsilon-\delta)$is positive, the S2-wave NMO velocity is smaller along the fracture direction than along the symmetry axis direction. Moreover, if the term $(\varepsilon-\delta)$ is zero, which gives arise to elliptical anisotropy, the S2-wave NMO velocities along directions parallel and perpendicular to the fracture direction are the same.

Considering the splitting analysis, the internal anisotropy parameters of the P- and S-waves can be defined, and are based on (2- 17):

$$\eta_{S_1} = \frac{\varepsilon-\delta}{(1+2\delta)^2}\left(1+\frac{2\delta}{1-v_{S_1 0}^2/v_{p0}^2}\right) \tag{5- 10}$$

$$\eta_{S_2} = \frac{\varepsilon-\delta}{(1+2\delta)^2}\left(1+\frac{2\delta}{1-v_{S_2 0}^2/v_{p0}^2}\right) \tag{5- 11}$$

$$\zeta_{S_1} = \frac{\sigma}{(1+2\sigma)^2}\left(1+\frac{2\delta}{1-v_{S_1 0}^2/v_{p0}^2}\right) \tag{5- 12}$$

$$\zeta_{S_2} = \frac{\sigma}{(1+2\sigma)^2}\left(1+\frac{2\delta}{1-v_{S_2 0}^2/v_{p0}^2}\right) \tag{5- 13}$$

The PS-converted wave is usually regarded as a combination of a downgoing P-wave leg and an upgoing S-wave leg and can inherit both characteristics. Actually, the PS-converted wave also splits into a fast P-SV1 and slow P-SV2 wave in a HTI medium. Based on the definition of PS-converted velocity (Equation (2- 39)), Their NMO velocities along the fracture direction can be defined as:

$$v^2_{psv_1 2-0^o} = \frac{1}{1+R_0} v^2_{P2-0^o} + \frac{R_0}{1+R_0} v^2_{S_1 2-0^o} \tag{5- 14}$$

$$v^2_{psv_2 2-0^o} = \frac{1}{1+R_0} v^2_{P2-0^o} + \frac{R_0}{1+R_0} v^2_{S_2 2-0^o} \tag{5- 15}$$

while their NMO velocities along the symmetry axis direction can also be defined as:

$$v^2_{psv_1 2-90^o} = \frac{1}{1+R_0} v^2_{P2-90^o} + \frac{R_0}{1+R_0} v^2_{S_1 2-90^o} \tag{5- 16}$$

$$v^2_{psv_2 2-90^o} = \frac{1}{1+R_0} v^2_{P2-90^o} + \frac{R_0}{1+R_0} v^2_{S_2 2-90^o} \tag{5- 17}$$

It can be seen that the P-SV1 NMO velocity is determined by both the P-wave NMO velocity and fast S1-wave NMO velocity. Similarly, the P-SV2 NMO velocity is dependent on both the P-wave NMO velocity and slow S2-wave NMO velocity. They are more complex than pure-mode wave NMO velocities, and will be discussed later in this chapter.

Similarly, the anisotropy parameters of PS-converted waves can be defined (Li and Yuan, 2003):

$$\left.\begin{aligned} \chi_{ps_1 eff} &= R_{S_1 0} R^2_{S_1 eff} \eta_{S_1} - \zeta_{S_1} \\ \chi_{ps_2 eff} &= R_{S_2 0} R^2_{S_2 eff} \eta_{S_2} - \zeta_{S_2} \end{aligned}\right\} \tag{5- 18}$$

$\chi_{ps_1 eff}$ and $\chi_{ps_2 eff}$ are anisotropic parameters for P-SV1 and P-SV2 waves, respectively. Definition of $R_{S_1 0}$, $R_{S_1 eff}$, $R_{S_2 0}$ and $R_{S_1 eff}$ can be found between Equations (5- 32) and (5- 35) Based on the PS-converted wave moveout equation in a VTI

medium, shown in Equation (2- 41), the PS-converted wave moveout equation along the fracture direction and symmetry direction of a HTI medium can be obtained:

$$t^2_{psv_1-0^o} = t^2_{psv_1 0} + \frac{x^2}{v^2_{psv_1 2-0^o}} - \frac{2\kappa_{eff} x^4}{v^2_{psv_1-0^o}[t^2_{psv_1 0} v^2_{psv_1 2-0^o} + m_4 \cdot x^2]} \quad (5\text{- }19)$$

$$t^2_{psv_2-0^o} = t^2_{psv_2 0} + \frac{x^2}{v^2_{psv_2 2-0^o}} - \frac{2\kappa_{eff} x^4}{v^2_{psv_2-0^o}[t^2_{psv_2 0} v^2_{psv_2 2-0^o} + m_4 \cdot x^2]} \quad (5\text{- }20)$$

$$t^2_{psv_1-90^o} = t^2_{psv_1 0} + \frac{x^2}{v^2_{psv_1 2-90^o}} - \frac{2\kappa_{eff} x^4}{v^2_{psv_1-90^o}[t^2_{psv_1 0} v^2_{psv_1 2-0^o} + m_4 \cdot x^2]} \quad (5\text{- }21)$$

$$t^2_{psv_2-90^o} = t^2_{psv_2 0} + \frac{x^2}{v^2_{psv_2 2-90^o}} - \frac{2\kappa_{eff} x^4}{v^2_{psv_2-90^o}[t^2_{psv_2 0} v^2_{psv_2 2-0^o} + m_4 \cdot x^2]} \quad (5\text{- }22)$$

where

$$\kappa_{ps_1 eff} = \frac{(R_{S_1 0} R_{S_1 eff} - 1)^2 + 8\chi_{ps_1 eff}(1 + R_{S_1 0})}{8R_{S_1 0}(1 + R_{S_1 eff})^2} \quad (5\text{- }23)$$

$$m_{ps_1 4} = 2\kappa_{ps_1 eff} \frac{(1 + R_{S_1 0})[(R_{S_1 0} - 1)R_{S_1 eff}{}^2 + 2\chi_{ps_1 eff}]}{(R_{S_1 0} - 1)R_{S_1 eff}(R_{S_1 0} R_{S_1 eff} - 1) + 2(1 + R_{S_1 0})\chi_{ps_1 eff}} \quad (5\text{- }24)$$

$$\kappa_{ps_2 eff} = \frac{(R_{S_2 0} R_{S_2 eff} - 1)^2 + 8\chi_{ps_2 eff}(1 + R_{S_2 0})}{8R_{S_2 0}(1 + R_{S_2 eff})^2} \quad (5\text{- }25)$$

$$m_{ps_2 4} = 2\kappa_{ps_2 eff} \frac{(1 + R_{S_2 0})[(R_{S_2 0} - 1)R_{S_2 eff}{}^2 + 2\chi_{ps_2 eff}]}{(R_{S_2 0} - 1)R_{S_2 eff}(R_{S_2 0} R_{S_2 eff} - 1) + 2(1 + R_{S_2 0})\chi_{ps_2 eff}} \quad (5\text{- }26)$$

It is found that the PS-converted moveouts are also complex, and the azimuthal behavior is also more complicated than pure-mode waves.

5.3 Effective parameters of the stratified HTI medium

The above parameters are based on a single layer. Effective parameters are needed if multiple layers are involved. As Figure 5- 1 illustrates, for each layer, interval Thomsen's parameters (t_{p0i}, $t_{s_1 0i}$, $t_{s_2 0i}$, ε_i, δ_i, γ_i and z_i, $i = 1,2,3,\ldots n$) are required. t_{p0i}, $t_{s_1 0i}$ and $t_{s_2 0i}$ are vertical one-way travel-times in the *i*-th layer. ε_i, δ_i and γ_i are anisotropy parameters in the *i*-th layer. z_i is the thickness of the *i*-th layer.

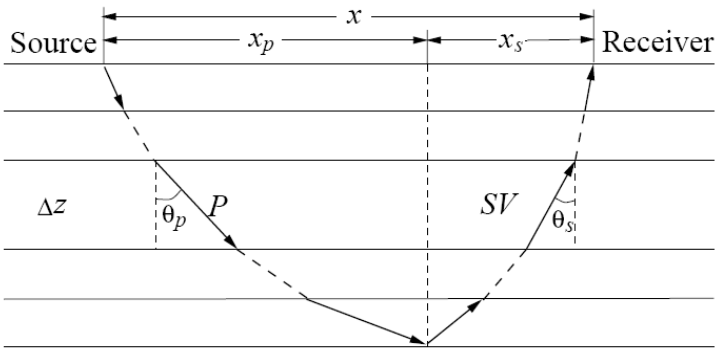

Figure 5- 1: Illustration of multi-layer medium.

For PS-converted waves, the following effective parameters can be defined:

$$t_{p0} = \sum_{i=1}^{n} t_{p0i} \tag{5- 27}$$

$$t_{S_1 0} = \sum_{i=1}^{n} t_{S_1 0i} \tag{5- 28}$$

$$t_{S_2 0} = \sum_{i=1}^{n} t_{S_2 0i} \tag{5- 29}$$

$$t_{psv_1 0} = \sum_{i=1}^{n} t_{p0i} + \sum_{i=1}^{n} t_{s_1 0i} = t_{p0} + t_{s_1 0} \tag{5- 30}$$

$$t_{psv_2 0} = \sum_{i=1}^{n} t_{p0i} + \sum_{i=1}^{n} t_{s_2 0i} = t_{p0} + t_{s_2 0} \tag{5- 31}$$

where t_{p0}, $t_{S_1 0}$, $t_{S_2 0}$ are effective one-way vertical traveltimes of P-, S1- and S2-waves, respectively. $t_{psv_1 0}$ and $t_{psv_2 0}$ are effective two-way vertical traveltimes of P-SV1 and P-SV2 waves, respectively.

Parameters for velocity ratios can be defined as:

$$R_{S_1 0} = \frac{t_{S_1 0}}{t_{p0}} \tag{5- 32}$$

$$R_{S_2 0} = \frac{t_{S_1 0}}{t_{p0}} \tag{5- 33}$$

$$R_{S_1 eff} = [(1+\gamma_{S_1 0})\frac{v_{psv_1 2}^2}{v_{p2}^2} - 1]^{-1} \tag{5- 34}$$

$$R_{S_2 eff} = [(1+\gamma_{S_2 0})\frac{v_{psv_2 2}^2}{v_{p2}^2} - 1]^{-1} \tag{5- 35}$$

And the effective NMO velocities for P-, S- and PS-converted waves are defined accordingly:

$$v_{p2}^2 = \frac{1}{t_{p0}}\sum_{i=1}^{n} v_{p2i}^2 t_{p0i} \tag{5- 36}$$

$$v_{S_1 2}^2 = \frac{1}{t_{S_1 0}}\sum_{i=1}^{n} v_{S_1 2i}^2 t_{S_1 0i} \tag{5- 37}$$

$$v_{S_2 2}^2 = \frac{1}{t_{S_2 0}}\sum_{i=1}^{n} v_{S_2 2i}^2 t_{S_2 0i} \tag{5- 38}$$

$$v_{psv_1 2}^2 = \frac{1}{t_{psv_1 0}}[\sum_{i=1}^{n} v_{p2i}^2 t_{p0i} + \sum_{i=1}^{n} v_{S_1 2i}^2 t_{S_1 0i}] \tag{5- 39}$$

$$v_{psv_2 2}^2 = \frac{1}{t_{psv_2 0}}[\sum_{i=1}^{n} v_{p2i}^2 t_{p0i} + \sum_{i=1}^{n} v_{S_2 2i}^2 t_{S_2 0i}] \tag{5- 40}$$

Effective anisotropy parameters for P-, S- and PS-converted waves can be similarly defined:

$$\eta_{S_1 eff} = \frac{1}{8t_{p0}v_{p2}^4}[\sum_{i=1}^{n} v_{p2i}^4 (1+8\eta_{S_1 i}) t_{p0i} - t_{p0} v_{p2}^4] \tag{5- 41}$$

$$\eta_{S_2 eff} = \frac{1}{8t_{p0}v_{p2}^4}[\sum_{i=1}^{n} v_{p2i}^4 (1+8\eta_{S_2 i}) t_{p0i} - t_{p0} v_{p2}^4] \tag{5- 42}$$

$$\zeta_{S_1 eff} = -\frac{1}{8t_{S_1 0} v_{S_1 2}^4}[\sum_{i=1}^{n} v_{S_1 2i}^4 (1-8\zeta_i) t_{S_1 0i} - t_{S_1 0} v_{S_1 2}^4] \quad (5\text{- }43)$$

$$\zeta_{S_2 eff} = -\frac{1}{8t_{S_2 0} v_{S_2 2}^4}[\sum_{i=1}^{n} v_{S_2 2i}^4 (1-8\zeta_i) t_{S_2 0i} - t_{S_2 0} v_{S_2 2}^4] \quad (5\text{- }44)$$

$$\chi_{psv_1 eff} = R_{S_1 0} R_{S_1 eff}^2 \eta_{eff} + \zeta_{S_1 eff} \quad (5\text{- }45)$$

$$\chi_{psv_2 eff} = R_{S_2 0} R_{S_2 eff}^2 \eta_{eff} + \zeta_{S_2 eff} \quad (5\text{- }46)$$

With these effective parameters, it is possible to extend the analysis in single layer to a multi-layer model, which is important for real seismic data processing.

5.4 Azimuthal variations of velocity and moveout of P-waves

NMO velocities of pure-mode waves have an elliptical variation in a HTI medium (Tsvankin, 1997b). The elliptical Equation (2- 25) can be used to compensate for azimuthal variations and determine fracture direction.

As Equation (5- 1) suggest, the NMO velocity variation of P-waves in a HTI medium is an ellipse. This equation can be used to analyse the azimuthal variation of P-wave NMO velocities in the HTI medium. By acquiring velocity models for different azimuth bins, the fracture direction and fracture density can be deduced.

However, the exact elliptical equation is not efficient in the azimuthal analysis of NMO velocities. In order to simplify the analysis process, Equation (5- 1) can be approximated into:

$$\left.\begin{aligned} v_{p2}^2(\theta) &\approx v_p^2 + \Delta_p^2 \cos 2(\theta - \beta) \\ v_p^2 &= \frac{v_{p2-0^0}^2 + v_{p2-90^0}^2}{2} \\ \Delta_p^2 &= \frac{v_{p2-0^0}^2 - v_{p2-90^0}^2}{2} \end{aligned}\right\} \quad (5\text{- }47)$$

v_p is the base velocity, which is a measurement of the average velocity. Δ_p is the velocity perturbation, which represents the velocity difference between two orthogonal directions. It can be seen that the major axis of the velocity ellipse is determined by Δ_p. The detailed derivation can be found in Appendix C.

In order to replace the exact elliptical equation by this simplified cosine function, a numerical study is performed to test the accuracy of this cosine function. This numerical study is illustrated in Figure 5- 2. In this study, the P-wave NMO velocity at $\theta = 0^o$ is fixed at 2000 m/s. At $\theta = 90^o$, the P-wave NMO velocity is set to be 1800, 1600, 1400 and 1200 m/s, respectively. In each figure, the solid curves are the velocity variations of P-waves calculated by Equation (5- 1), which is the exact elliptical expression. The dotted curve is calculated using Equation (5- 47). In Figure 5- 2(a), the ellipse calculated by Equation (5- 47) is almost identical to the ellipse calculated by Equation (5- 1). Therefore Equation (5-) is proved to be accurate enough to replace Equation (5- 1), when the ratio Δ^2 / v^2 is up to 0.11. When $\Delta^2 / v^2 = 0.22$ in Figure 5- 2(b), a difference between the two equations can be seen but it is very small. Therefore the accuracy of Equation (5- 1) is still acceptable when $\Delta^2 / v^2 = 0.22$. When $\Delta^2 / v^2 = 0.34$ in Figure 5- 2(c), the difference between the two equations is much larger. Accuracy is significantly disturbed when $\Delta^2 / v^2 = 0.47$ in Figure 5- 2(d). Therefore, when $\Delta^2 / v^2 \le 0.22$ the elliptical Equation (5- 1) can be replaced by the simplified Equation (5- 47).

Substituting Equation (5- 47) to P-wave moveout equation (Equation (2- 37)) and ignoring the anisotropic term for weak VTI anisotropy, the azimuthal variation of P-wave moveout can be expressed as:

$$t_p^2(\theta) \approx t_{p0}^2 + x^2\left[\frac{\sin^2(\theta-\beta)}{v_{p2-90^0}^2} + \frac{\cos^2(\theta-\beta)}{v_{p2-0^0}^2}\right] \tag{5- 48}$$

Reform it as:

$$\frac{t_p^2(\theta) - t_{ps0}^2}{x^2} \approx \frac{\sin^2(\theta-\beta)}{v_{p2-90^0}^2} + \frac{\cos^2(\theta-\beta)}{v_{p2-0^0}^2} \tag{5- 49}$$

Equation (5- 49) is also an ellipse which is similar to the velocity ellipse. This equation shows that the azimuthal moveout measurements make it possible to recover the NMO velocity in the symmetry plane and its orientation.

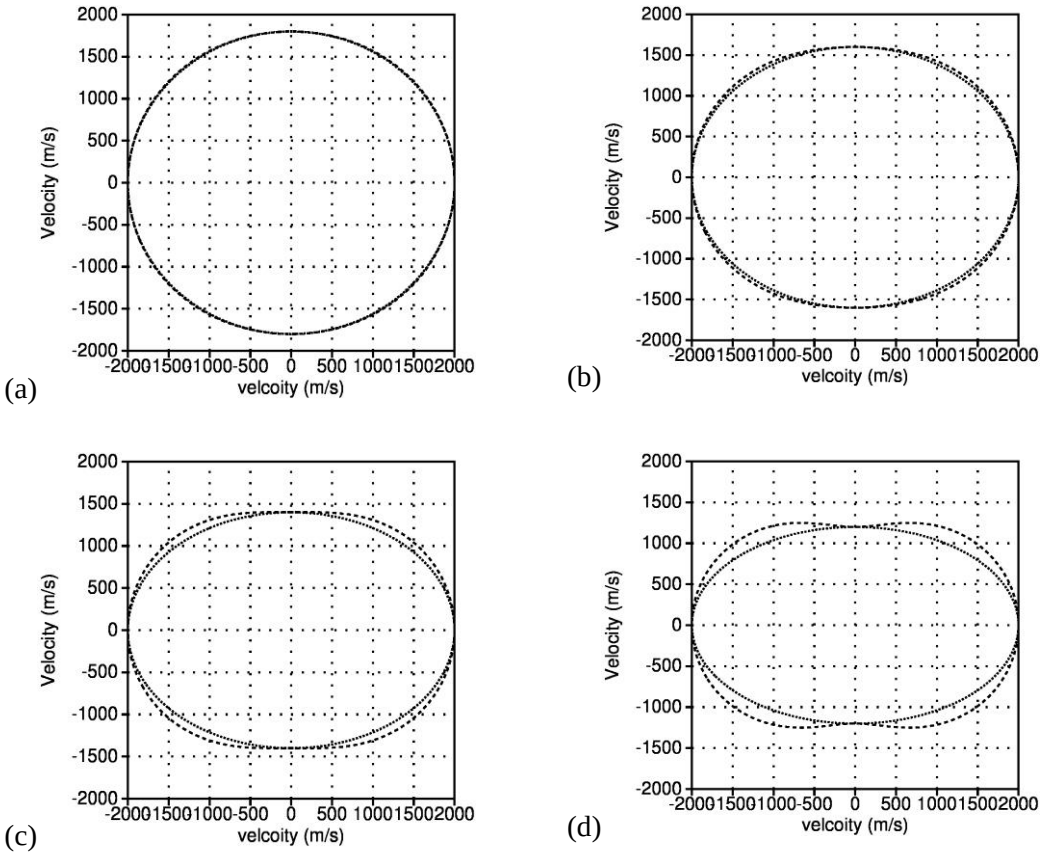

Figure 5- 2: The azimuthal variation of P-wave NMO velocity ($v_{p2-0^o} = 2000m/s$). (a) $v_{p2-90^o} = 1800m/s\,(\Delta^2/v^2 = 0.11)$, (b) $v_{p2-90^o} = 1600m/s\ (\Delta^2/v^2 = 0.22)$ and (c) $v_{p2-90^o} = 1400m/s\ (\Delta^2/v^2 = 0.34)$. (d) $v_{p2-90^o} = 1200m/s\ (\Delta^2/v^2 = 0.47)$.

5.5 Azimuthal variations of velocity and moveout of shear-waves

The shear-wave splits into a fast S1-wave and slow S2-wave in a HTI medium. But the fast S1-wave and slow S2-wave are all pure-mode waves, which are similar to P-waves. Therefore, the above azimuthal analysis for P-waves can be directly applied to shear-waves in a HTI medium.

NMO velocities of the S1-wave and S2-wave in HTI medium are also elliptical and can be simplified into a similar cosine equation:

$$\left.\begin{aligned} v_{s_1 2}^2(\theta) &\approx v_{s_1}^2 + \Delta_{s_1}^2 \cos 2(\theta-\beta) \\ v_{S_1}^2 &= \frac{v_{s_1 2-0^0}^2 + v_{s_1 2-90^0}^2}{2} \\ \Delta_{S_1}^2{}^2 &= \frac{v_{s_1 2-0^0}^2 - v_{s_1 2-90^0}^2}{2} \end{aligned}\right\} \quad (5\text{- }50)$$

$$\left.\begin{aligned} v_{s_2 2}^2(\theta) &\approx v_{s_2}^2 + \Delta_{s_2}^2 \cos 2(\theta-\beta) \\ v_{S_2}^2 &= \frac{v_{s_2 2-0^0}^2 + v_{s_2 2-90^0}^2}{2} \\ \Delta_{S_2}^2 &= \frac{v_{s_2 2-0^0}^2 - v_{s_2 2-90^0}^2}{2} \end{aligned}\right\} \quad (5\text{- }51)$$

Note that the validity of the cosine function is similar to the P-wave cosine equation. When $\Delta^2/v^2 \le 0.22$, the simplified cosine equation can replace the exact elliptical equation.

Similarly, the moveout equation of S1-wave and S2-wave can also be approximated into ellipse:

$$\frac{t_{S_1}^2(\theta) - t_{S_1 0}^2}{x^2} \approx \frac{\sin^2(\theta-\beta)}{v_{S_1 2-90^0}^2} + \frac{\cos^2(\theta-\beta)}{v_{S_1 2-0^0}^2} \quad (5\text{- }52)$$

$$\frac{t_{S_2}^2(\theta) - t_{S_2 0}^2}{x^2} \approx \frac{\sin^2(\theta-\beta)}{v_{S_2 2-90^0}^2} + \frac{\cos^2(\theta-\beta)}{v_{S_2 2-0^0}^2} \quad (5\text{- }53)$$

5.6 Azimuthal variations of moveout and velocity of PS-converted waves

The PS-converted wave is usually regarded as a combination of a downgoing P-wave leg and an upgoing S-wave leg and can inherit both wave behaviours. The upgoing shear-wave leg discussed here could be either a fast S1-wave or slow S2-wave. Then the azimuthal variation of PS-converted NMO velocity is determined by the azimuthal variations of NMO velocities of P- and S-waves.

Substituting the elliptical equations (Equation (2- 25)) of P- and shear-waves into the equation of PS-converted wave NMO velocity (Equation (2- 39):

$$v^2_{psv_1 2}(\theta)=\frac{1}{1+R_0}\frac{v^2_{p2-0^0}v^2_{p2-90^0}}{v^2_{p2-0^0}\sin^2(\theta-\beta)+v^2_{p2-90^0}\cos^2(\theta-\beta)}+\frac{R_0}{1+R_0}\frac{v^2_{s_1 2-0^0}v^2_{s_1 2-90^0}}{v^2_{s_1 2-0^0}\sin^2(\theta-\beta)+v^2_{s_1 2-90^0}\cos^2(\theta-\beta)} \quad (5\text{- }54)$$

$$v^2_{psv_2 2}(\theta)=\frac{1}{1+R_0}\frac{v^2_{p2-0^0}v^2_{p2-90^0}}{v^2_{p2-0^0}\sin^2(\theta-\beta)+v^2_{p2-90^0}\cos^2(\theta-\beta)}+\frac{R_0}{1+R_0}\frac{v^2_{s_2 2-0^0}v^2_{s_2 2-90^0}}{v^2_{s_2 2-0^0}\sin^2(\theta-\beta)+v^2_{s_2 2-90^0}\cos^2(\theta-\beta)} \quad (5\text{- }55)$$

It can be seen that Equation (5- 54) and (5- 55) are very complex. Select the fast P-SV1 wave as an example, if $(\theta-\beta)=0^o$, $v^2_{psv_1 2}(\beta)=\frac{1}{1+R_0}v^2_{p2-0^0}+\frac{R_0}{1+R_0}v^2_{s_1 2-0^0}$, which is the square of P-SV1 wave NMO velocity in the vertical plane parallel to the fracture direction if the angle β represents the fracture direction. For $(\theta-\beta)=90^o$, $v^2_{psv_1 2}(\beta+90^o)=\frac{1}{1+R_0}v^2_{p2-90^0}+\frac{R_0}{1+R_0}v^2_{s_1 2-90^0}$ is the square of P-SV1 wave NMO velocity in the vertical plane perpendicular to the fracture direction. For other azimuthal angles, the azimuthal variation is not simple. The P-SV2 wave is similar to the P-SV1 wave, which have complicated terms in the equation. However, inspection of a special case for the P-SV1 can be performed to study the azimuthal variation. Firstly, a simple case is considered in which the ratio between $v^2_{p2-0^0}$ and $v^2_{p2-90^0}$ and the ratio between $v^2_{s_1 2-0^0}$ and $v^2_{s_1 2-90^0}$ are the same, e.g. $\frac{v^2_{p2-0^0}}{v^2_{p2-90^0}}=\frac{v^2_{s_1 2-0^0}}{v^2_{s_1 2-90^0}}=\omega$. Then Equation (5- 54) can be reformed as:

$$v^2_{psv_1 2}(\theta)=(\frac{1}{1+R_0}v^2_{p2-0^0}+\frac{R_0}{1+R_0}v^2_{s_1 2-0^0})\frac{1}{\omega\sin^2(\theta-\beta)+\cos^2(\theta-\beta)} \quad (5\text{- }56)$$

It is not difficult to observe that Equation (5- 56) is mathematically elliptical. So in this special case, the P-SV1 wave NMO velocity can be described as an ellipse in the horizontal plane. This analysis can be applied to the P-SV2 wave as well and it is found that the P-SV2 wave NMO velocity is also an ellipse for this special case.

For a more general and complicated case, in which ω_p ($\omega_p = \frac{v^2_{p2-0^0}}{v^2_{p2-90^0}}$) is not equal to ω_{s_1} ($\omega_{s_1} = \frac{v^2_{s_1 2-0^0}}{v^2_{s_1 2-90^0}}$), Equation (5- 54) can be written as:

$$v^2_{psv_1 2}(\theta) = \frac{1}{1+R_0}\frac{v^2_{p2-0^0}}{\omega_p \sin^2(\theta-\beta)+\cos^2(\theta-\beta)} + \frac{R_0}{1+R_0}\frac{v^2_{s_1 2-0^0}}{\omega_{s_1} \sin^2(\theta-\beta)+\cos^2(\theta-\beta)} \quad (5\text{- }57)$$

Mathematically, Equation (5- 57) is not an elliptical equation. Moreover, it is difficult to analyse the azimuthal variation through this complex form.

Using the simplified cosine equation, analysis of the azimuthal variation of PS-converted-wave NMO velocities can be simplified. Substituting Equations (5- 47), (5- 50) and (5- 51) into Equation (2- 39), the PS-converted wave NMO velocity can be written as:

$$\left.\begin{aligned} v^2_{psv_1 2}(\theta) &\approx v^2_{psv_1} + \Delta^2_{psv_1}\cos 2(\theta-\beta) \\ v^2_{psv_1} &= \left(\frac{1}{1+R_0}v^2_p + \frac{R_0}{1+R_0}v^2_{s_1}\right) \\ \Delta^2_{psv_1} &= \left(\frac{1}{1+R_0}\Delta^2_p + \frac{R_0}{1+R_0}\Delta^2_{s_1}\right) \end{aligned}\right\} \quad (5\text{- }58)$$

$$\left.\begin{aligned} v^2_{psv_2 2}(\theta-\beta) &\approx v^2_{psv_2} + \Delta^2_{psv_2}\cos 2(\theta-\beta) \\ v^2_{psv_2} &= \left(\frac{1}{1+R_0}v^2_p + \frac{R_0}{1+R_0}v^2_{s_2}\right) \\ \Delta^2_{psv_2} &= \left(\frac{1}{1+R_0}\Delta^2_p + \frac{R_0}{1+R_0}\Delta^2_{s_2}\right) \end{aligned}\right\} \quad (5\text{- }59)$$

The full derivation of the cosine equations for the PS-converted wave can be found in Appendix D.

Similar to Equations (5- 1), (5- 50) and (5- 51), Equations (5- 58) and (5- 59) can also be approximated into velocity ellipses if the weak anisotropy condition $\Delta^2 << v^2$

is satisfied. If Equations (5- 58) and (5- 59) are close to ellipses, they could be written in the exact elliptical form:

$$\left.\begin{aligned} v^2_{psv_1 2}(\theta) &= \frac{v^2_{psv_1 2-0^0} v^2_{psv_1 2-90^0}}{v^2_{psv_1 2-0^0}\sin^2(\theta-\beta)+v^2_{psv_1 2-90^0}\cos^2(\theta-\beta)} \\ v^2_{psv_1 2-0^o} &= \frac{1}{1+R_0}v^2_{p2-0^0}+\frac{R_0}{1+R_0}v^2_{s_1 2-0^0} \\ v^2_{psv_1 2-90^o} &= \frac{1}{1+R_0}v^2_{p2-90^0}+\frac{R_0}{1+R_0}v^2_{s_1 2-90^0} \end{aligned}\right\} \quad (5\text{- }60)$$

$$\left.\begin{aligned} v^2_{psv_2 2}(\theta) &= \frac{v^2_{psv_2 2-0^0} v^2_{psv_2 2-90^0}}{v^2_{psv_2 2-0^0}\sin^2(\theta-\beta)+v^2_{psv_2 2-90^0}\cos^2(\theta-\beta)} \\ v^2_{psv_2 2-0^o} &= \frac{1}{1+R_0}v^2_{p2-0^0}+\frac{R_0}{1+R_0}v^2_{s_2 2-0^0} \\ v^2_{psv_2 2-90^o} &= \frac{1}{1+R_0}v^2_{p2-90^0}+\frac{R_0}{1+R_0}v^2_{s_2 2-90^0} \end{aligned}\right\} \quad (5\text{- }61)$$

In order to verify the azimuthal variation of PS-converted waves, a numerical study is applied to the P-SV1 wave and the accuracy of Equation (5- 58) and (5- 60) is tested. The analysis of the P-SV1 wave can be similarly applied to the P-SV2 wave. In this numerical analysis, the velocity at the fracture strike (β) is fixed: $v_{p2-0^o}=2000m/s$ and $v_{s_1 2-0^o}=1000m/s$. The vertical velocity ratio is 2.2. The velocities in the direction of the symmetry axis vary. NMO velocity variations of the P-SV1 wave are shown in Figure 5- 3.

Each figure has three curves. The solid curve is calculated by Equation (5- 54), which is the exact velocity equation of the P-SV1 wave. The dotted curve is calculated by Equation (5- 58), and the dashed curve is calculated by Equation (5- 60), which is mathematically an exact ellipse. In Figure 5- 3, Equation (5- 60) is very close to Equation (5- 54) even if Δ_p / v_p and Δ_{s_1} / v_{s_1} are relatively large. For example, in Figure 5- 3(d), where $\Delta_p / v_p = 0.9$ and $\Delta_{s_1} / v_{s_1} = 0.8$, Equation (5- 60) is still close to Equation (5- 54). However, Equation (5- 58) significantly deviates from

Equation (5- 54) in Figure 5- 3(c) and Figure 5- 3(d). This means that the simplified Equation (5- 54) is only valid when Δ_p/v_p and Δ_{s_1}/v_{s_1} are small. The above synthetic can also be applied to the analysis of the NMO velocity variation of the P-SV2 wave, which proves that the P-SV2 NMO velocity can be approximated as an ellipse as well.

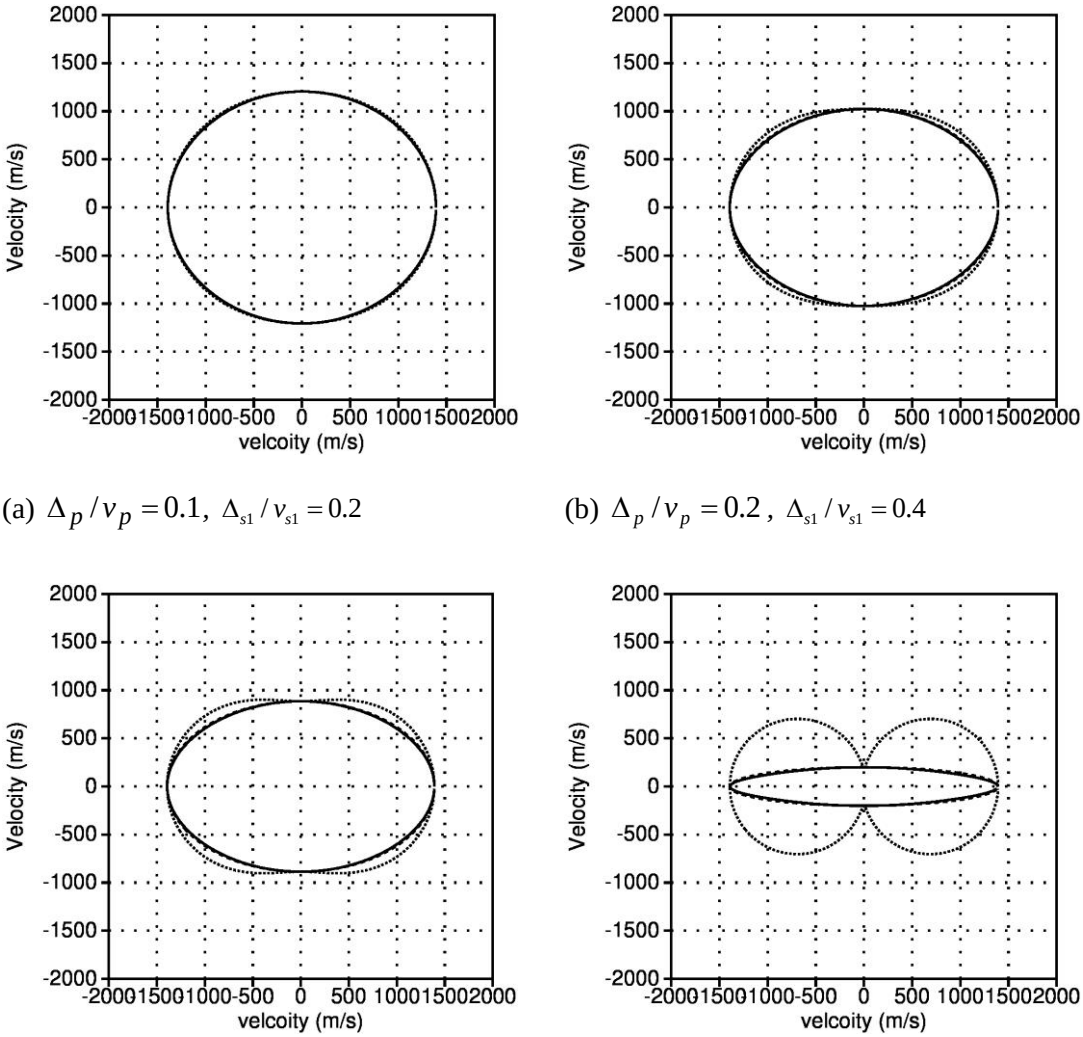

(a) $\Delta_p/v_p = 0.1$, $\Delta_{s1}/v_{s1} = 0.2$ (b) $\Delta_p/v_p = 0.2$, $\Delta_{s1}/v_{s1} = 0.4$

(c) $\Delta_p/v_p = 0.3$, $\Delta_{s1}/v_{s1} = 0.5$ (d) $\Delta_p/v_p = 0.9$, $\Delta_{s1}/v_{s1} = 0.8$

Figure 5- 3: Azimuthal velocities of PS converted wave calculated by Equation (5-54) (solid curve), Equation (5- 58) (dotted curve) and Equation (5- 60) (dashed curve).

From Equations (5- 60) and (5- 61), the elliptical variation of NMO velocities of P-SV1 and P-SV2 waves are determined by $\Delta^2_{psv_1}$ and $\Delta^2_{psv_2}$, respectively. Taking the P-SV1 wave as an example, the $\Delta^2_{psv_1}$ is a combination of Δ^2_p and $\Delta^2_{s_1}$ (Equation (5-60)). Mathematically, if $\Delta^2_{psv_1}$ is zero, the velocity ellipse becomes a velocity circle. In this special case, there is no azimuthal variation. If $\Delta^2_{psv_1}$ is either positive or negative, the azimuthal variations of P-SV1 NMO velocities can be approximated as ellipses. Moreover, the signs of $\Delta^2_{psv_1}$ and $\Delta^2_{psv_2}$ could be the same or different. If the sign of $\Delta^2_{psv_1}$ is as same as $\Delta^2_{psv_2}$, azimuthal variations of P-SV1 and P-SV2 waves are in phase. In other words, the major axes of their velocity ellipses are in the same direction. However, if $\Delta^2_{psv_1}$ and $\Delta^2_{psv_2}$ have different signs, the azimuthal variations of P-SV1 and P-SV2 waves are out-of-phase. The major axis of P-SV1 NMO velocity ellipse is perpendicular to the major axis of P-SV2 NMO velocity ellipse. For this special case, direct analysis of either radial or transverse components is not accurate.

Similarly, the derived NMO elliptical equations of the P-SV1 and P-SV2 wave make it possible to study their azimuthal variations of moveouts. Substituting Equations (5-60) and (5- 61) into Equation (2- 41) and ignoring the anisotropy term for weak anisotropy:

$$\frac{t^2_{psv_1}(\theta)-t^2_{psv_1 0}}{x^2} \approx \frac{\sin^2(\theta-\beta)}{v^2_{psv_1 2-90^0}} + \frac{\cos^2(\theta-\beta)}{v^2_{psv_1 2-0^0}} \qquad \text{(5- 62)}$$

$$\frac{t^2_{psv_2}(\theta)-t^2_{psv_2 0}}{x^2} \approx \frac{\sin^2(\theta-\beta)}{v^2_{psv_2 2-90^0}} + \frac{\cos^2(\theta-\beta)}{v^2_{psv_2 2-0^0}} \qquad \text{(5- 63)}$$

Equations (5- 62) and (5- 63) are also elliptical equations. These equations show that the azimuthal moveout measurements make it possible to recover the NMO velocity in the symmetry plane and its orientation.

5.7 Extension into multi-layer media

With the above effective parameters available, the moveout equations of PS-converted waves in multi-layered media can be defined. Based on Equation (2- 41)

and effective parameters, I derive the azimuthal movetout equations of P-SV1 and P-SV2 waves converted at the N-th layer, respectively:

$$\left.\begin{aligned} t^2_{psv_1}(\theta) &= t^2_{psv_1 0} + \frac{(2h)^2}{v^2_{psv_1 2}(\theta)} - \frac{2\kappa_{psv_1 eff}(\theta)(2h)^4}{V^2_{psv_1 2}(\theta)[t^2_{psv_1 0} v^2_{psv_1 2}(\theta) + m_{psv_1 4}(\theta)\cdot(2h)^2]} \\ \kappa_{psv_1 eff}(\theta) &= \frac{(R_{S_1 0}R_{S_1 eff}(\theta)-1)^2 + 8\chi_{psv_1 eff}(\theta)(1+R_{S_1 0})}{8R_{S_1 0}(1+R_{S_1 eff}(\theta))^2} \\ m_{psv_1 4}(\theta) &= 2\kappa_{psv_1 eff}(\theta)\frac{(1+R_{S_1 0})[(R_{S_1 0}-1)R^2{}_{S_1 eff}(\theta) + 2\chi_{psv_1 eff}(\theta)]}{(R_{S_1 0}-1)R_{S_1 eff}(\theta)(R_{S_1 0}R_{S_1 eff}(\theta)-1) + 2(1+R_{S_1 0})\chi_{psv_1 eff}(\theta)} \end{aligned}\right\} \quad (5\text{- }64)$$

$$\left.\begin{aligned} t^2_{psv_2}(\theta) &= t^2_{psv_2 0} + \frac{(2h)^2}{v^2_{psv_2 2}(\theta)} - \frac{2\kappa_{psv_2 eff}(\theta)(2h)^4}{V^2_{psv_2 2}(\theta)[t^2_{psv_2 0} v^2_{psv_2 2}(\theta) + m_{psv_2 4}(\theta)\cdot(2h)^2]} \\ \kappa_{psv_2 eff}(\theta) &= \frac{(R_{S_2 0}R_{S_2 eff}(\theta)-1)^2 + 8\chi_{psv_2 eff}(\theta)(1+R_{S_2 0})}{8R_{S_2 0}(1+R_{S_2 eff}(\theta))^2} \\ m_{psv_2 4}(\theta) &= 2\kappa_{psv_2 eff}(\theta)\frac{(1+R_{S_1 0})[(R_{S_1 0}-1)R^2{}_{S_1 eff}(\theta) + 2\chi_{psv_2 eff}(\theta)]}{(R_{S_1 0}-1)R_{S_1 eff}(\theta)(R_{S_1 0}R_{S_1 eff}(\theta)-1) + 2(1+R_{S_1 0})\chi_{psv_2 eff}(\theta)} \end{aligned}\right\} \quad (5\text{- }65)$$

As discussed above, moveouts of P-SV1 and P-SV2 waves can be approximated as ellipses. A synthetic study is performed to test the accuracy of those azimuthal moveout equations.

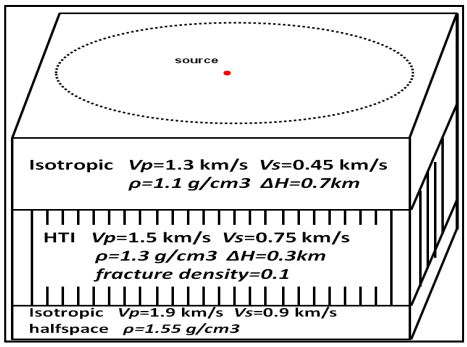

Figure 5- 4: Model used to test the accuracy of azimuthal moveout equations.

The model and its parameters are shown in Figure 5- 4. It is a three-layer model, in which the second layer is a HTI layer induced by vertical fractures. The first layer is an isotropic layer and the third layer is an isotropic halfspace. The azimuthal moveout on the second reflector is measured at every 2^o in the azimuthal plane. The

largest moveout difference at a certain azimuth angle is calculated. Different offset-to-depth (X/Z) ratios and different fracture densities are tested. For comparison, the azimuthal moveouts based on hyperbolic equations (e.g. Equation (2- 33)) are also calculated.

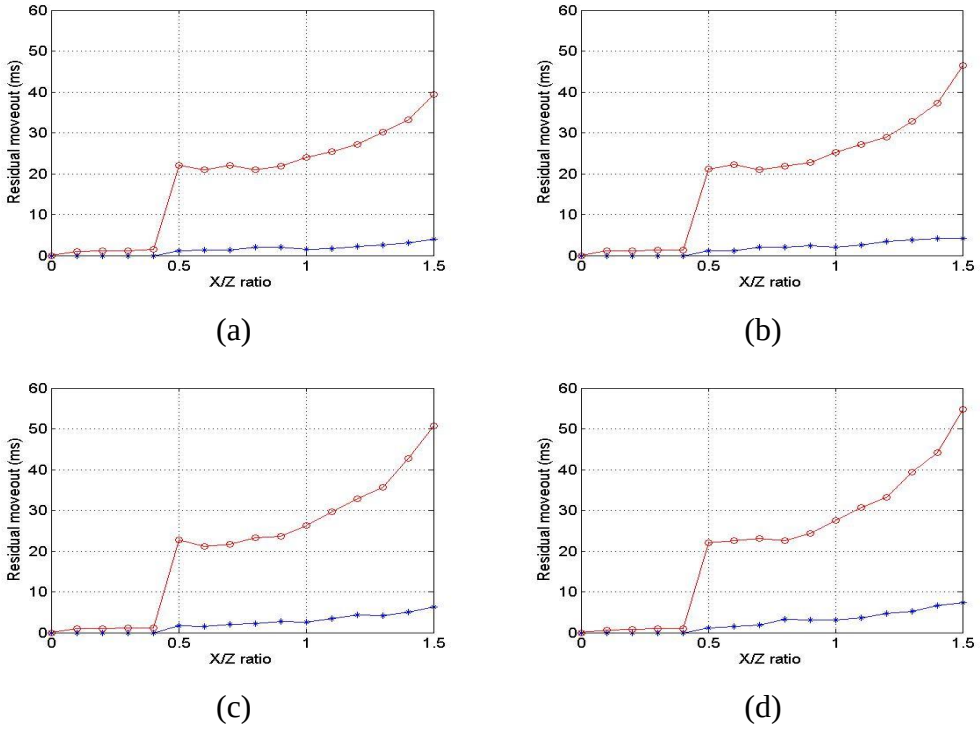

Figure 5- 5: Largest residual moveouts resulted from hyperbolic equation (red) and non-hyperbolic equation (blue). (Fracture density is: (a) 0.04 (b) 0.06 (c) 0.08 (d) 0.1)

The calculation result for P-SV1 waves is displayed in Figure 5- 5 as an example. In each figure, the vertical axis is the largest residual moveout and the units are milliseconds. The horizontal axis represents different X/Z ratios. The residual moveouts are calculated at every 2^{o} and the largest value is selected to represent the error. The red colour represents the result calculated by the hyperbolic equation (2-33) and the blue color is the result calculated by the non-hyperbolic equation (5- 64).

For fracture densities 0.04, 0.06, 0.08 and 0.1, the accuracy of the non-hyperbolic equation is overall better than the accuracy of the hyperbolic equation. The largest residual moveouts calculated by Equation (5- 64) are all less than 10ms for all fracture densities. The largest residual moveouts calculated by Equation (2- 33) are

all larger or equal than 40ms for all fracture densities. The difference between the two equations is trivial for small X/Z ratios but more significant for moderate and large X/Z ratios. This fact proves that it is necessary to apply the non-hyperbolic equation when data with large X/Z ratios is involved. Moreover, as the fracture density increases, the accuracies of both equations both decrease but in a less severe manner.

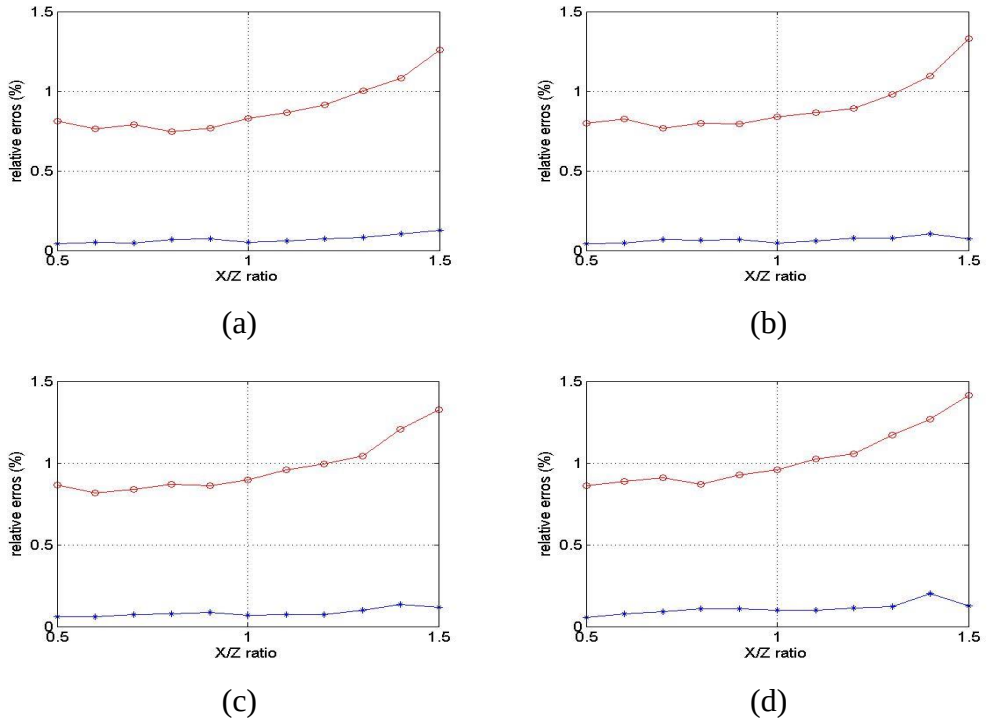

Figure 5- 6: Relative errors resulted from hyperbolic equation (red) and non-hyperbolic equation (blue). Fracture density is: (a) 0.04 (b) 0.06 (c) 0.08 (d) 0.1

The relative error is also calculated to obtain a better understanding of the accuracy of the non-hyperbolic azimuthal moveout equation, and it is shown in Figure 5- 6. For all fracture densities, the relative errors resulting from Equation (5- 64) are smaller than 0.25% while the relative errors resulted from Equation (2- 33) are larger than 0.5%. Relative errors similarly increase as the X/Z ratio increases for both equations.

This synthetic study and accuracy test proves that the non-hyperbolic moveout equation is more accurate than the hyperbolic moveout equation when the fracture density is as large as 0.1 and the offset-to-depth ratio is as large as 1.5. Therefore,

this moveout equation can be used in the analysis of PS-converted moveout azimuthal variations in HTI media.

5.8 Summary

The azimuthal variation of the NMO velocity of pure-mode waves in a HTI medium is elliptical, which can be described by a simplified cosine function if the anisotropy is weak. Based on this cosine function, an azimuthal equation for PS-converted wave NMO velocity is derived. The influence of shear-wave splitting on the azimuthal behaviour of PS converted waves in HTI media is also considered. For both P-SV1 and P-SV2 waves, their NMO velocities can be approximated into ellipses in a HTI medium. With the elliptical NMO velocity equations, moveout equations of PS-converted waves are also approximated into elliptical equations, which makes it possible to determine azimuthal variations from PS-converted wave moveouts. By defining internal and effective parameters, the moveout equations of P-SV1 and P-SV2 waves are extended to multi-layered media. By making a synthetic study, the accuracy of the elliptical moveout equation is tested. The non-hyperbolic moveout equation is more accurate than the hyperbolic moveout equation when the fracture density is as large as 0.1 and the offset-to-depth ratio is as large as 1.5.. This result implies that the azimuthal moveout equations can be used for azimuthal analysis in HTI media.

Chapter 6

Analysis of the azimuthal variations of PS-converted wave NMO velocities for improved imaging

6.1 Introduction

As technology and theory have developed, the importance of azimuthal anisotropy has become widely accepted. Therefore, wide azimuth PS-converted wave seismic data are more frequently acquired than before for different purposes. Specifically, azimuthal variations induced by HTI anisotropy are usually observed on wide azimuth data. Imaging quality will be degraded if azimuthal variations are simply neglected and conventional processing methods are applied. Moreover, azimuthal variations of PS-converted waves are affected by shear-wave splitting. How to compensate for azimuthal variations of PS-converted waves while taking the splitting effect into account is not solved yet.

In this chapter, I have developed algorithms for estimating azimuthal variations of the velocity and a work flow to apply the azimuthal velocity model to improve imaging. The work flow involves several processing steps including: pre-processing, coordinate rotation, separation of split PS-converted waves, azimuthal binning, estimation of the velocity ellipse, NMO correction and stacking.

In the pre-processing stage, static correction, amplitude compensation, noise elimination and other methods are essential for enhancing the data quality. CCP binning and velocity analysis of PS-converted wave seismic data are also important procedures, which were introduced in Chapter 2. Coordinate rotation, separation of split PS-converted waves are discussed in Chapter 3. Other processing steps involved in the workflow are discussed in this Chapter. Analysis of the azimuthal variation is also applied to a synthetic dataset to demonstrate improved imaging.

6.2 Consideration of azimuthal binning

Each direction represents different wavefield information in the presence of azimuthal anisotropy. Theoretically, all azimuth angles in the azimuthal plane should be considered and analysed to study azimuthal anisotropy. However, in the context of vertically aligned fractures, the azimuthal analysis can be simplified by the symmetric features of the Cartesian coordinate system. The symmetry is demonstrated in Figure 6-1. Black dotted lines are a set of vertical fractures. The red solid arrow represents the azimuth angle θ, and the red dashed arrow represents the azimuth which is opposite to angle θ. Therefore, an arbitrary azimuth angle is symmetric to its opposite azimuth angle ($\theta \pm 180^o$) in the Cartesian coordinate system. This feature halves the azimuth range needed to accomplish azimuthal analysis, which is very beneficial to seismic data processing. As a result, symmetrical azimuth angles can be sorted into the same azimuth bin to simplify the processing procedure.

Although the 360^o azimuth range is halved into the 180^o range by the symmetric feature, it is still difficult to treat each azimuth angle differently. Firstly, it is inefficient to study every azimuth angle. Working with 180 azimuth angles is still a massive task for either computers or data processors. Secondly, rocks are usually affected by weak anisotropy in the context of seismic exploration. This fact results in negligible differences for two immediately adjacent azimuth angles. Even azimuth angles over a small range (e.g. 10^o -20^o) can be regarded as having the same anisotropic parameters.

Moreover, in terms of data processing, dealing with large numbers of azimuth angles could bring errors, which has negative influences on imaging quality and inversion for fracture parameters. Therefore, azimuth angles in a certain range are preferably

sorted into one common azimuth bin. Azimuthal binning is described in Figure 6-(a). Azimuth angles in one common azimuth bin, which is indicated by the red sector, are considered to have the same anisotropic parameters. The accuracy of anisotropic parameters will not be significantly affected, and data processing can be simplified, if an appropriate bin size is selected.

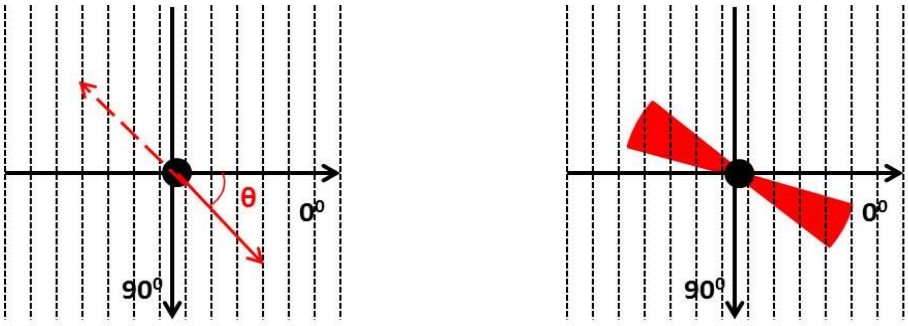

(a) (b)

Figure 6-1: Demonstration of symmetric azimuth angles (a) and common azimuth binning (b) in Cartesian coordinate system.

Another consideration of azimuthal binning concerns seismic data acquisition. In a synthetic data study with a single shot, it is easy to obtain uniform azimuth coverage. This special case is described in Figure 6- 2(a), where one single shot is uniformly circled by many closely-spaced receivers. For each offset, full azimuth coverage can be acquired. This data geometry makes the analysis of azimuthal anisotropy very accurate. But in real data acquisition, which is shown in Figure 6- 2(b), receivers are usually arranged in a number of receiver lines. It can be seen that azimuth angles for certain offsets cannot be fully covered. Some azimuth angles are missing, which makes it impossible to study all azimuth angles. Therefore, sorting data into azimuth bins significantly improves the analysis of azimuthal anisotropy. Moreover, involving a number of azimuth angles in one azimuth bin can enhance the signal-to-noise ratio, which is also beneficial for real data processing.

The selection of azimuth bin size is critical to the analysis of azimuthal variation. If the size is large, more azimuth angles can be contained in one common azimuth bin. It can provide better signal-to-noise ratio but might fail to recover reliable azimuthal variations by using only a small number of azimuth bins. If the size is small, more azimuth bins are involved, which may provide a more accurate result. However,

fewer azimuth angles are contained in each azimuth bin, which could degrade the signal-to-noise ratio. Therefore, the final choice of appropriate azimuth bin size is a compromise between accuracy consideration and a good signal-to-noise ratio.

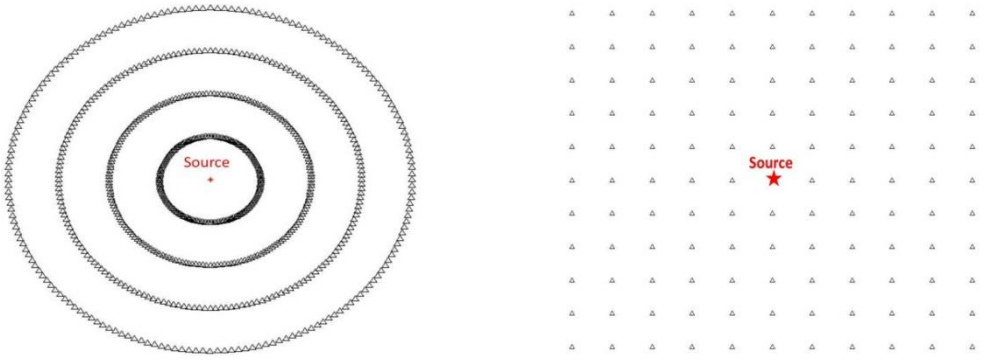

(a) (b)

Figure 6- 2: Description of data acquisition for a single-shot synthetic data (a) and real field data (b) (red star is the source, black triangles are receivers).

6.3 Azimuthal velocity analysis of PS-converted waves

After obtaining individual P-SV1 and P-SV2 components, azimuthal velocity analysis should be performed to study the velocity variations. The azimuthal velocity analysis should be separately applied to both P-SV1 and P-SV2 components to acquire their individual velocity models. These velocity models all contain important information on azimuthal anisotropy.

Firstly, conventional velocity analysis is applied to a ACP or super-ACP gather. All azimuth angles are included in this initial velocity analysis. The main purpose of this procedure is to obtain a reference velocity model. Because it represents all azimuth angles, it can be used to detect velocity variations among different azimuth angles. This procedure can be accomplished in the CxTools environment, which is displayed in Figure 6- 3. The first panel on the left is the velocity spectrum used to pick the stacking velocity. The velocity range on the top can be manually specified. The second panel is used to estimate the velocity ratio R_0 described by the red curve and the effective velocity ratio R_{eff} described by the blue curve. The third panel is used to obtain the anisotropic parameter χ, which is introduced to represent the anisotropy of

PS-converted waves. The fourth panel shows the input ACP or super-ACP gather, which is sorted by offset values. The velocity analysis involves picking the appropriate values of velocity, velocity ratio R_0, effective velocity ratio R_{eff} and anisotropic parameter χ, which could provide the best fit to the approximately hyperbolic events on the input gather.

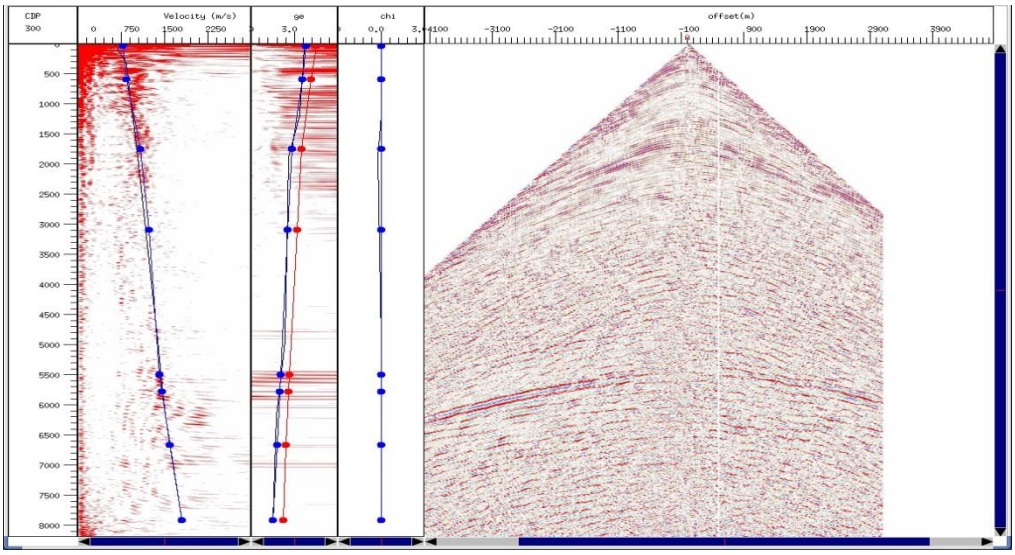

(a)

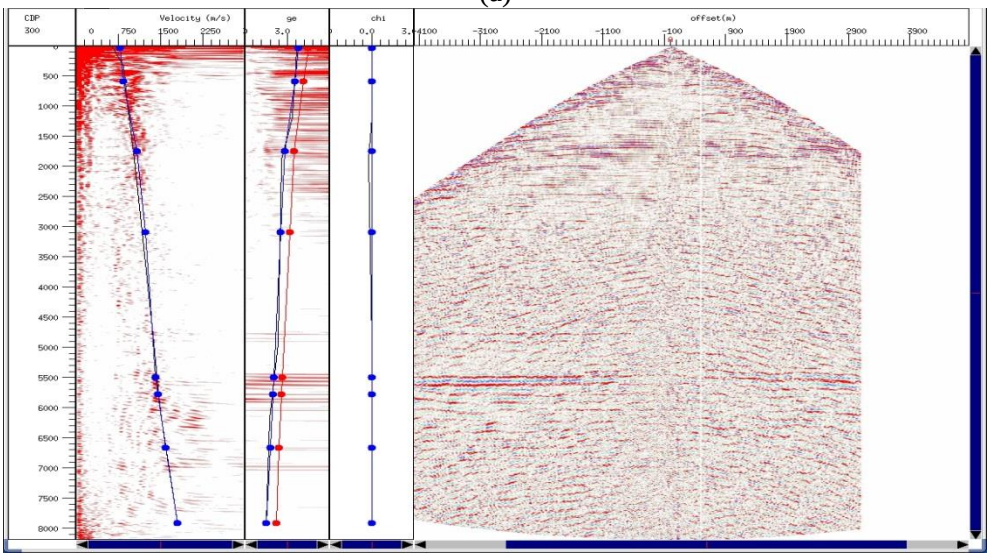

(b)

Figure 6- 3: Examples of PS-converted wave velocity analysis in CxTools. (a): Velocity picking procedure; (b): Verifying if the correct velocity value is selected.

This velocity process is demonstrated in Figure 6- 3(a). Figure 6- 3(b) is used to check if the picked parameters well-correct the normal moveout and flat events.

After picking and checking the reference velocity model, velocity analysis of the different azimuth bins can be performed.

The next work is to use the reference velocity model acquired in the initial velocity analysis to study the velocity variations. The major contribution of the azimuthal variation on moveout is provided by the velocity itself. Therefore, only the azimuthal velocity variation is estimated in the process of azimuthal analysis. Other parameters including velocity ratio R_0, effective velocity ratio R_{eff} and anisotropic parameter χ are kept constant.

Before performing azimuthal velocity analysis, azimuthal binning must be accomplished. The ACP or super-ACP gather are sorted by azimuth angles, which are calculated using the coordinates of sources and receivers. To facilitate the azimuthal binning, the azimuth range is set to be from -90^o to 90^o. If the azimuth bin size is selected as 60^o, as displayed in Figure 6- 4, velocity analysis will be applied to only three different common azimuth bins. The circles in Figure 6- 4 represent azimuthal planes and the red sectors indicate the individual common azimuth bins. The work load for a single ACP or super-ACP gather is relatively small. However, azimuth angles over a 60-degree-range are regarded as having the same velocity parameters. This assumption is too coarse to obtain the true azimuth variation. If the bin size is set to be 30^o, six azimuth bins are involved in the azimuthal velocity analysis. This case is described in Figure 6- 5. It is easy to understand that the work load is twice the work load created by the 60^o bin size. However, its efficiency is still acceptable in most cases. Meanwhile, estimation over azimuth angle is specified for a smaller 30-degree-range. This increased accuracy is surely beneficial for inverting for anisotropic parameters. The selection of 15-degree-size is displayed in Figure 6- 6. Twelve azimuth bins means more velocity models are involved in the azimuthal analysis. Theoretically, accuracy would be successfully maintained if the true velocity parameters for each azimuth bin are obtained. However, the real case is not as simple as the theory suggests. The data quality in some azimuth bins might be low, which could make it difficult to pick correct velocity values for velocity analysis. Moreover, the azimuth coverage of real data is not as uniform as the azimuth coverage of synthetic data. Large offsets, where more significant anisotropy is

contained, might be not available for some azimuth bins. As a result, the accuracy provided by a 15^{o} bin size may not be as high as expected.

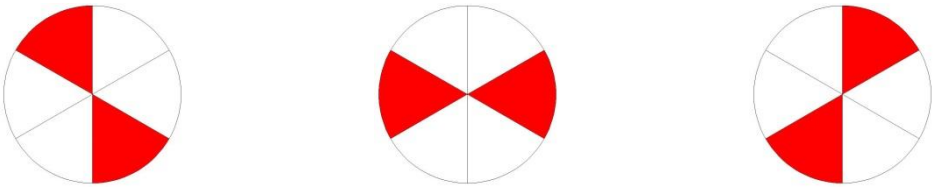

Figure 6- 4: Velocity analysis of 3 azimuth bins when the bin size is 60^{o}.

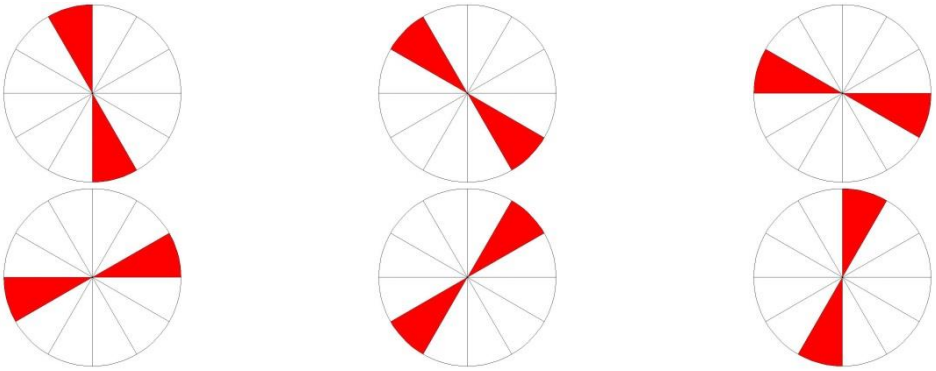

Figure 6- 5: Velocity analysis of 6 azimuth bins when the bin size is 30^{o}.

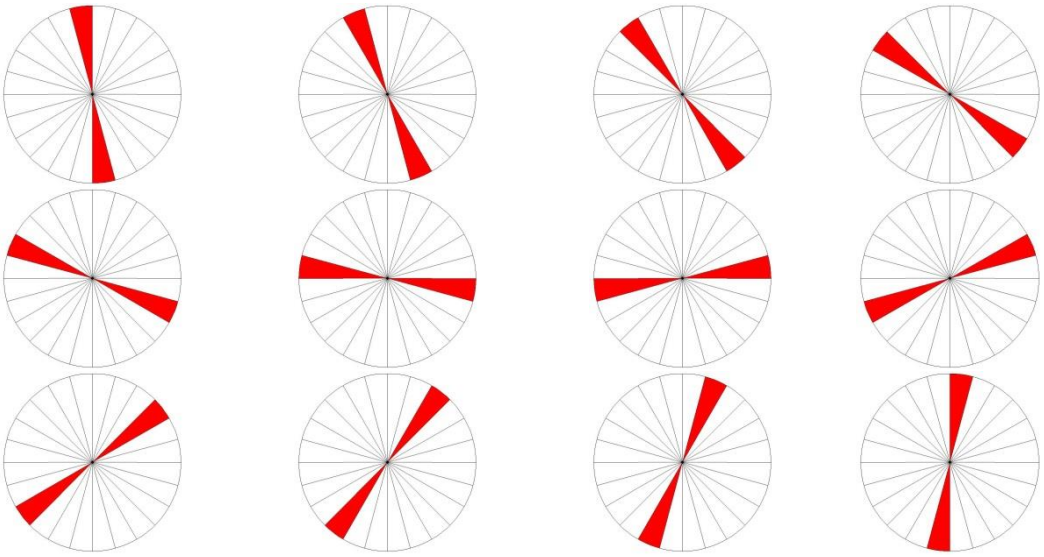

Figure 6- 6: Velocity analysis of 12 azimuth bins when the bin size is 15^{o}.

The above discussion only provides general considerations on azimuth binning. The appropriate selection of azimuth bin size for the velocity analysis is dependent on real data. A preliminary evaluation can be used to find out the bin size which delivers the best results.

6.4 Least-square fitting for velocity ellipses

To fit the velocities of several azimuth bins into elliptical models, an ellipse fitting algorithm is necessary. Ellipse fitting methods have been intensively studied and applied in many fields. A least-square method is introduced in this chapter to accomplish the fitting procedure.

The azimuthal variation of stacking velocity can be expressed by the following equation:

$$v_{ps}(\theta) = v_0 + \Delta\cos 2(\theta - \beta) \tag{6- 1}$$

where V_0 is the base velocity, Δ is the velocity perturbation, β is the direction of the maximum velocity (e.g. the fracture direction), and θ is the ray path azimuth. For each azimuth bin of the data, a velocity and azimuth pair (V_{psi}, θ_i) based on PS-converted wave velocity analysis can be obtained. The parameters are derived as:

$$\begin{aligned}\tan 2\beta == \frac{\begin{array}{l} n\sum v_{psi}\cos 2\theta_i \sum \cos 2\theta_i \sin 2\theta_i - n\sum (\cos 2\theta_i)^2 \sum v_{psi}\sin 2\theta_i \\ +\sum v_{psi}\sin 2\theta_i (\sum \cos 2\theta_i)^2 - \sum v_{psi}\cos 2\theta_i \sum \cos 2\theta_i \sum \sin 2\theta_i \\ +\sum v_{psi}\sum (\cos 2\theta_i)^2 \sum \sin 2\theta_i - \sum v_{psi}\sum \cos 2\theta_i \sin 2\theta_i \sum \cos 2\theta_i \end{array}}{\begin{array}{l} n\sum v_{psi}\sin 2\theta_i \sum \cos 2\theta_i \sin 2\theta_i - n\sum v_{psi}\cos 2\theta_i \sum (\sin 2\theta_i)^2 \\ +\sum v_{psi}\cos 2\theta_i (\sum \sin 2\theta_i)^2 - \sum v_{psi}\sin 2\theta_i \sum \cos 2\theta_i \sum \sin 2\theta_i \\ +\sum v_{psi}\sum (\sin 2\theta_i)^2 \sum \cos 2\theta_i - \sum v_{psi}\sum \cos 2\theta_i \sin 2\theta_i \sum \sin 2\theta_i \end{array}}\end{aligned} \tag{6- 2}$$

$$\Delta = \frac{n\sum v_{psi}\cos 2(\theta_i - \beta) - \sum v_{psi}\sum \cos 2(\theta_i - \beta)}{n\sum [\cos 2(\theta_i - \beta)^2] - [\sum \cos 2(\theta_i - \beta)]^2} \tag{6- 3}$$

$$v_0 = \frac{\sum v_{psi} - \Delta\sum \cos 2(\theta_i - \beta)}{n} \tag{6- 4}$$

The detailed derivation of this least-square fitting algorithm can be found in Appendix E.

Azimuth(degree)	**-75°**	**-45°**	**-15°**	**15°**	**45°**	**75°**
Velocity(m/s)	1805.1	1805.1	1850	1894.9	1894.9	1850

Table 6- 1: six correct velocity models of different azimuth angles are used to fit the velocity ellipse.

A numerical study is performed to test the least-square fitting algorithm. The main purpose of this study is to test the sensitivity of the elliptical model to velocity errors. In this study, an initial velocity ellipse is fitted by 5 azimuthal velocity values. Those six velocity values correspond to five angles in the azimuthal plane, which are listed in Table 6- 1. By using the above least-square method, a velocity ellipse can be fitted, which can be expressed as:

$$1856 + 51.97\cos 2(\theta - 30^o) \qquad (6\text{- }5)$$

The base velocity v_0 is 1856 m/s and the velocity perturbation Δ is 51.97 m/s. The fracture direction, where the maximum velocity appears, is 30° in the azimuthal plane. The elliptical velocity model is indicated by the black ellipse in Figure 6- 7. The fracture direction is indicated by the green double arrow in Figure 6- 7. The given velocity points are indicated by five black stars for reference. The black velocity ellipse fits those five stars well because the five stars represent correct velocity values.

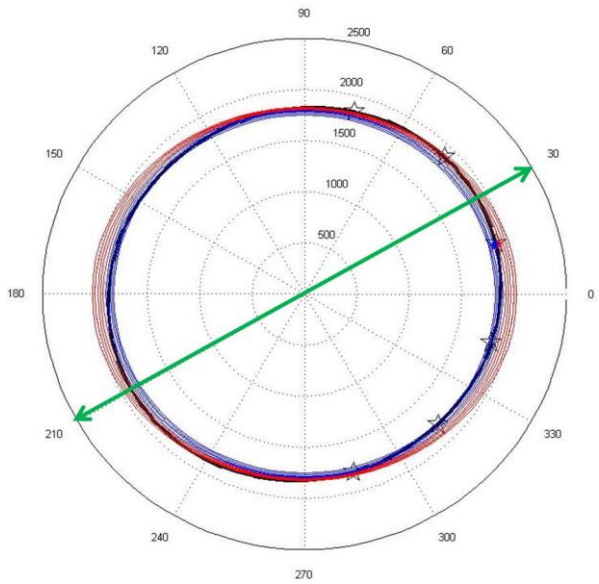

Figure 6- 7: Velocity ellipses using different velocity values at azimuth 15°. The green double arrow indicates that the fracture direction is 30°. Six black stars represent velocities of 6 azimuth angles (-75°, -45°, -15°, 15 °, 45°, 75°). The black ellipse is the elliptical velocity model fitted by those 5 velocity values. Red ellipses

and blue ellipses are results of increased and decreased velocities at azimuth 15^o.

Then the velocity at azimuth 15^o is changed while velocities at other five azimuth angles remain unchanged. This velocity is firstly increased by 0.2%, 0.6%, 1%, 1.4% and 1.8%. Using increased velocities at azimuth 15^o and unchanged velocities at other azimuth angles, velocity ellipses can also be obtained. Those velocity ellipses fitted from the incorrect velocity values at azimuth 15^o are drawn by red ellipses in Figure 6- 7. The test is also applied when the velocity at azimuth 15^o is decreased. The initial velocity at azimuth 15^o is decreased by 0.2%, 0.6%, 1%, 1.4% and 1.8%. The corresponding elliptical models are indicated by the blue ellipses in Figure 6- 7. It can be seen that the red and blue ellipses all deviate from the black ellipse by different amounts. It looks like that the deviation of the blue ellipses is less significant than the deviation of the red ellipses. It seems to indicate that the black velocity ellipse is more affected by increased velocity values at azimuth 15^o. The complete information on these deviations is presented in Table 6- and Table 6- 3. The notations of variables listed in the first columns of both Table 6- and Table 6- 3 are provided in Table 6- 6.

$E(v_{ps+15^0})$ (%)	0.2	0.6	1	1.4	1.8
v_{ps+15^o} (m/s)	1894.9	1894.9	1894.9	1894.9	1894.9
v_{ps+15^o-E} (m/s)	1898.6	1906.2	1913.8	1921.4	1929
v_0 (m/s)	1856	1856	1856	1856	1856
v_{0-E} (m/s)	1863.8	1879.5	1895.4	1911.3	1927.3
$\lvert E(v_0)\rvert$ (%)	0.4179	1.267	2.122	2.981	3.842
Δ (m/s)	51.97	51.97	51.97	51.97	51.97
Δ_E (m/s)	57.14	67.27	78.02	89.16	100.6
$\lvert E(\Delta)\rvert$ (%)	9.949	29.45	50.12	71.56	93.5
β (degree)	30	30	30	30	30
β_E (degree)	26.25	23.33	21.19	19.6	18.37
$\lvert E(\beta)\rvert$ (%)	1.041	1.854	2.447	2.89	3.229

Table 6- 2: Measurement of elliptical parameters when velocity at azimuth 15^o is increased (Variables in the first column are explained in Table 6- 6).

$E(v_{ps+15^0})$ (%)	-0.2	-0.6	-1	-1.4	-1.8
v_{ps+15^o} (m/s)	1894.9	1894.9	1894.9	1894.9	1894.9
v_{ps+15^o-E} (m/s)	1891.1	1883.5	1875.9	1868.3	1860.8
v_0 (m/s)	1856	1856	1856	1856	1856
v_{0-E} (m/s)	1848.1	1832.7	1817.4	1802.4	1787.6
$\lvert E(v_0)\rvert$ (%)	0.424	1.257	2.078	2.888	3.684
Δ (m/s)	51.97	51.97	51.97	51.97	51.97
Δ_E (m/s)	47.95	40.3	35.09	33.34	35.43
$\lvert E(\Delta)\rvert$ (%)	7.726	22.45	32.48	35.85	31.83
β (degree)	30	30	30	30	30
β_E (degree)	30.36	36.19	44.13	53.69	63.02
$\lvert E(\beta)\rvert$ (%)	0.1014	1.719	3.926	6.581	9.173

Table 6- 3: Measurement of elliptical parameters when velocity at azimuth 15^o is decreased (Variables in the first column are explained in Table 6-).

The base velocity, velocity perturbation and fast direction are changed as the velocity at azimuth 15^o is increased. The base velocity v_{0-E} gradually increases as a result of increased v_{ps+15^o}. The absolute value of $|E(v_0)|$ is only 0.4179% when v_{ps+15^o} is increased by 0.2%. This value increases to 3.842% when v_{ps+15^o} is increased by 1.8 %. The velocity perturbation Δ_E increases more rapidly as v_{ps+15^o} increases. When v_{ps+15^o} is increased by 0.2%, the $|E(\Delta)|$ is 9.949%. However, $|E(\Delta)|$ reaches up to 93.5% when v_{ps+15^o} is increased by 1.8%. The fast direction is also influenced by increased v_{ps+15^o} and also has a gradual variation. As v_{ps+15^o} increases, azimuth 15^o is approaching the major axis of velocity ellipse. Therefore the fast direction approaches to 15^o in the azimuthal plane. The largest $|E(\beta)|$ is 3.229% when v_{ps+15^o} is increased by 1.8%. It can be found that $|E(\beta)|$ and $|E(v_0)|$ are similar, and are much smaller than $|E(\Delta)|$ for different velocity errors.

The changes resulted from decreased velocities at azimuth 15^o are the same to changes resulted from increased velocities, which are listed in Table 6- 3. $|E(\Delta)|$ is still overall larger than $|E(v_0)|$ and $|E(\beta)|$. v_{0-E} is following the decreasing trend as

v_{ps+15^o} is decreased by different rates. The largest $|E(v_0)|$ is 3.684% when v_{ps+15^o} is decreased by 1.8%. It is close to $|E(v_0)|$ when v_{ps+15^o} is increased by 1.8%. The variation of Δ_E is complicated. As v_{ps+15^o} decreases by 0.2%, 0.6%, 1% and 1.4%, Δ_E is also decreasing. But Δ_E starts to increase when v_{ps+15^o} is decreased by 1.8%. Moreover, $|E(\Delta)|$ is generally smaller than its counterparts when v_{ps+15^o} is increased by different rates. The largest $|E(\Delta)|$ is not in accordance with the largest decreasing rate 1.8% but with the decreasing rate 1.4%. As v_{ps+15^o} decreases, the azimuth 15^o is becoming the slow direction. As a result, the fast direction is approaching azimuth 105^o. Meanwhile, $|E(\beta)|$ increases and reaches up to 9.173% when v_{ps+15^o} is decreased by 1.8%. It is larger than the maximum $|E(\beta)|$ in Table 6- 2.

The above discussion focuses on the velocity at azimuth 15^o, which is close to the fracture direction. Then the velocity at azimuth -75^o is also tested because azimuth -75^o is close to the fracture normal direction. The corresponding ellipses resulting from increased and decreased velocities are drawn in red and blue colours in Figure 6- 8, respectively. Those red and blue ellipses also deviate from the black ellipse by different amounts. Similar comparisons of different elliptical parameters are provided in Table 6- 4 and Table 6- 5.

As v_{ps-75^o} increases, v_{0-E} also gradually increases. The largest $|E(v_0)|$ is 3.771%, which corresponds to the increasing rate 1.8%. It is close to the largest $|E(v_0)|$ in both Table 6- 2 and Table 6- 3. Δ_E is increasing more rapidly than V_{0-E}, which results in the rapid increase of $|E(\Delta)|$. The largest $|E(\Delta)|$ is 69.66%, which is smaller than the largest $|E(\Delta)|$ when the velocity at azimuth 15^o is increased by 1.8% but is larger than the largest $|E(\Delta)|$ when the velocity at azimuth 15^o is decreased by 1.4%. The fast direction also deviates from the azimuth 30^o, resulting in the increased $|E(\beta)|$. The largest $|E(\beta)|$ is 1.717%, which also results from the largest increase rate 1.8%. It is smaller than the largest $|E(\beta)|$ in both Table 6- 2 and Table 6- 3. It can be

seen that both $|E(\beta)|$ and $|E(v_0)|$ are much smaller than $|E(\Delta)|$ while $|E(\beta)|$ is slightly smaller than $|E(v_0)|$ in this case.

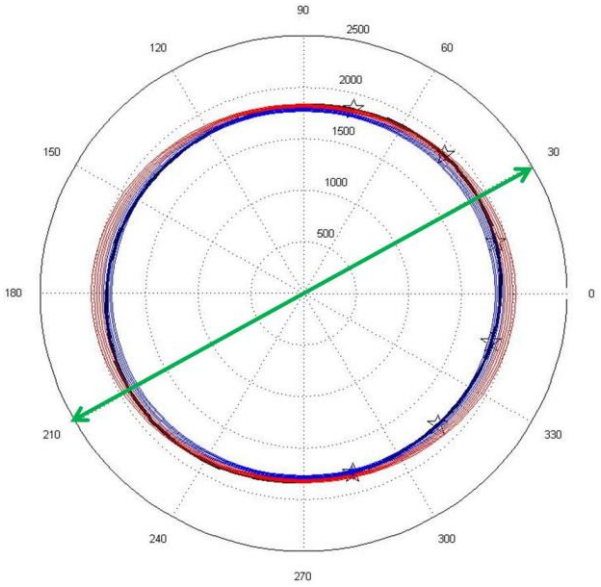

Figure 6- 8: Velocity ellipses using different velocity values at azimuth -75°. The green double arrow indicates that the fracture direction is 30°. Five black stars represent velocities of 5 azimuth angles (-75°, -45°, -15°, 15°, 45°, 75°). Black ellipse is the elliptical velocity model fitted by those 5 velocity values. Red ellipses and blue ellipses are results of increased and decreased velocities at azimuth 75°.

The case of decreased v_{ps-75^o} is displayed in Table 6- 5. v_{0-E}, Δ_E and β_E uniformly varies as v_{ps-75^o} decreases. v_{0-E} is also decreased as v_{ps-75^o} decreased. The largest $|E(v_0)|$ is 3.771%, which is similar to its counterparts in Table 6- 2, Table 6- 3 and Table 6- 4. Δ_E decreases as v_{ps-75^o} decreases, which results in increased $|E(\Delta)|$. The largest $|E(\Delta)|$ is 51.44%, which is larger than the largest $|E(\Delta)|$ in Table 6- 3 but smaller than the largest $|E(\Delta)|$ in Table 6- 3 and Table 6- 4. The fast direction β_E also deviates from the azimuth 30° as v_{ps-75^o} decreases. The largest $|E(\beta)|$ is 3.308, which is close to the largest $|E(\beta)|$ in Table 6- 2.

In conclusion, velocity errors at different azimuths cause different deviations from the correct velocity ellipse. Even at the same azimuth, the deviations resulted from increased and decreased velocities are different. However, it can be found that $|E(\Delta)|$ is always much larger than $|E(v_0)|$ and $|E(\beta)|$ in the above four tables. It implies that velocity perturbations are more sensitive to velocity errors. Therefore velocity

perturbations are not reliable representations of fracture densities if incorrect velocity values are included. But the deviation of the fast direction from the fracture direction is not very significant. The largest $|E(\beta)|$ appears in Table 6- 3, which is 9.173%. Therefore it is acceptable to regard the fast directions fitted from the least-square method as the dominant fracture directions.

$E(v_{ps-75^0})$ (%)	0.2	0.6	1	1.4	1.8
v_{ps-75^o} (m/s)	1805.1	1805.1	1805.1	1805.1	1805.1
v_{ps-75^o-E} (m/s)	1808.8	1816	1823.2	1830.4	1837.6
v_0 (m/s)	1856	1856	1856	1856	1856
v_{0-E} (m/s)	1863.2	1878.1	1893.6	1909.5	1926
$\|E(v_0)\|$ (%)	0.3886	1.193	2.024	2.883	3.771
Δ (m/s)	51.97	51.97	51.97	51.97	51.97
Δ_E (m/s)	56.03	63.55	71.42	79.63	88.17
$\|E(\Delta)\|$ (%)	7.808	22.29	37.43	53.22	69.66
β (degree)	30	30	30	30	30
β_E (degree)	27.42	26.23	25.26	24.48	23.82
$\|E(\beta)\|$ (%)	0.7164	1.048	1.316	1.535	1.717

Table 6- 4: Measurement of elliptical parameters when velocity at azimuth -75^o is increased (Variables in the first column are explained in Table 6-).

$E(v_{ps-75^0})$ (%)	-0.2	-0.6	-1	-1.4	-1.8
v_{ps-75^o} (m/s)	1805.1	1805.1	1805.1	1805.1	1805.1
v_{ps-75^o-E} (m/s)	1801.5	1794.3	1787.1	1779.9	1772.6
v_0 (m/s)	1856	1856	1856	1856	1856
v_{0-E} (m/s)	1848.8	1834.7	1821.2	1808	1795.2
$\|E(v_0)\|$ (%)	0.3906	1.146	1.877	2.586	3.274
Δ (m/s)	51.97	51.97	51.97	51.97	51.97
Δ_E (m/s)	48.86	42.1	35.82	30.12	25.23
$\|E(\Delta)\|$ (%)	5.973	18.98	31.08	42.04	51.44
β (degree)	30	30	30	30	30
β_E (degree)	28.93	30.89	33.49	37.02	41.91
$\|E(\beta)\|$ (%)	0.2963	0.2474	0.9691	1.951	3.308

Table 6- 5: Measurement of elliptical parameters when velocity at azimuth -75^o is decreased (Variables in the first column are explained in Table 6-).

$E(v_{ps+15^0})$ (%) $E(v_{ps-75^0})$	Increased or decreased rates of velocity at azimuth 15° (V_{ps-15^o}) or -75° (V_{ps-75^0})
v_{ps+15^o} (m/s) v_{ps-75^0}	Initial velocity at azimuth 15° or -75°
v_{ps+15^o-E} (m/s) v_{ps-75^0-E}	Increased or decreased velocities at azimuth 15° or -75°
v_0 (m/s)	Base velocity of initial velocity ellipse
v_{0-E} (m/s)	Base velocity of velocity ellipses from increased or decreased V_{ps-15^o} (V_{ps-75^0})
$\lvert E(v_0)\rvert$ (%)	Absolute value of relative change between V_0 and V_{0-E}
Δ (m/s)	Perturbation of initial velocity ellipse
Δ_E (m/s)	Perturbation of velocity ellipses from increased or decreased V_{ps-15^o} (V_{ps-75^0})
$\lvert E(\Delta)\rvert$ (%)	Absolute value of relative change between Δ and Δ_E
β (degree)	Fast direction of initial velocity ellipse
β_E (degree)	Fast direction of velocity ellipses from increased or decreased V_{ps-15^o} (V_{ps-75^0})
$\lvert E(\beta)\rvert$ (%)	Absolute value of relative Change between β and β_E

Table 6- 6: Notations of variables in Table 6- 2, Table 6- 3, Table 6- 4 and Table 6- 5.

6.5 Analysis of the azimuthal anisotropy induced by water-saturated fractures

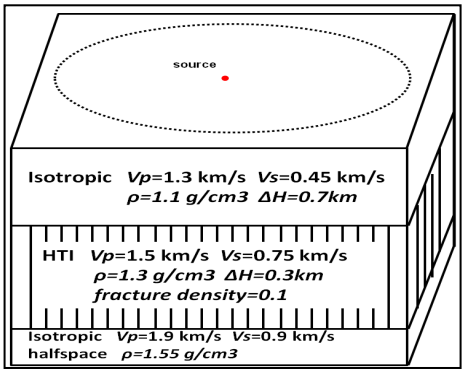

Figure 6- 9: Description of the three-layer synthetic model

A synthetic data study is performed to demonstrate the compensation for the azimuthal variation of converted-waves. This synthetic model is created by ANISEIS

and its parameters are displayed in Figure 6- 9. This model contains three layers. The first layer is an isotropic layer. The second layer is a HTI layer and the third layer is an isotropic halfspace. The HTI layer is induced by vertical fractures using Hudson theory. In this study, the crack radius a is 0.001m, aspect ratio α is 0.01 and fracture density e is 0.01. Both dry and water-saturated fractures are considered. The fracture orientation in this example is 120^o in the horizontal plane. The azimuth coverage is from 0^o to 360^o with a 2^o interval. The offset range is selected to be between 500 and 1500 meters with a 50m receiver space.

I first simulate data for water-saturated fractures. Using horizontal rotation, the original X and Y components are rotated into radial and transverse components. The azimuth gathers for the radial, transverse and vertical components are displayed in Figure 6- 10. The horizontal axis represents the azimuth angle. The target event affected by vertical fractures is emphasised by red ellipses and enlarged to facilitate observation. It can be seen that both the fast P-SV1 wave and the slow P-SV2 waves are projected into the radial and transverse components. A clear time delay can be discovered between the fast P-SV1 and slow P-SV2 components. Near the directions perpendicular to the fracture direction, the energy of the P-SV1 component is nearly zero. But near the fracture direction, the P-SV2 energy is nearly zero. This can be explained by the different polarisations of the P-SV1 and P-SV2 components. The fast P-SV1 component is polarised in the fracture direction while the P-SV2 component is polarised in the direction perpendicular to the fracture direction. Unlike the azimuthal behaviour of the PS-converted waves, the P-wave azimuthal variation contained in the vertical component is clear. The fast and slow directions for P-waves are the direction parallel and perpendicular to the fracture orientation, respectively.

Analysis of the azimuthal variation of PS-converted waves is complicated by converted-wave splitting. It is difficult to directly use either the radial or transverse component to compensate for the azimuthal variation. Therefore, it is important to separate the P-SV1 wave from the P-SV2 wave for PS-converted data processing in HTI media. By horizontal rotation, the radial and transverse component data can be rotated into the fast P-SV1 and slow P-SV2 components. In this study, the fracture

direction is 120^o in the azimuthal plane, which is treated as a known parameter. After horizontal rotation, the individual P-SV1 component can be separated from the P-SV2 component. Azimuth gathers of individual P-SV1 and P-SV2 components are displayed in Figure 6- 11. The P-wave azimuth gather is also displayed in Figure 6-11 for comparison.

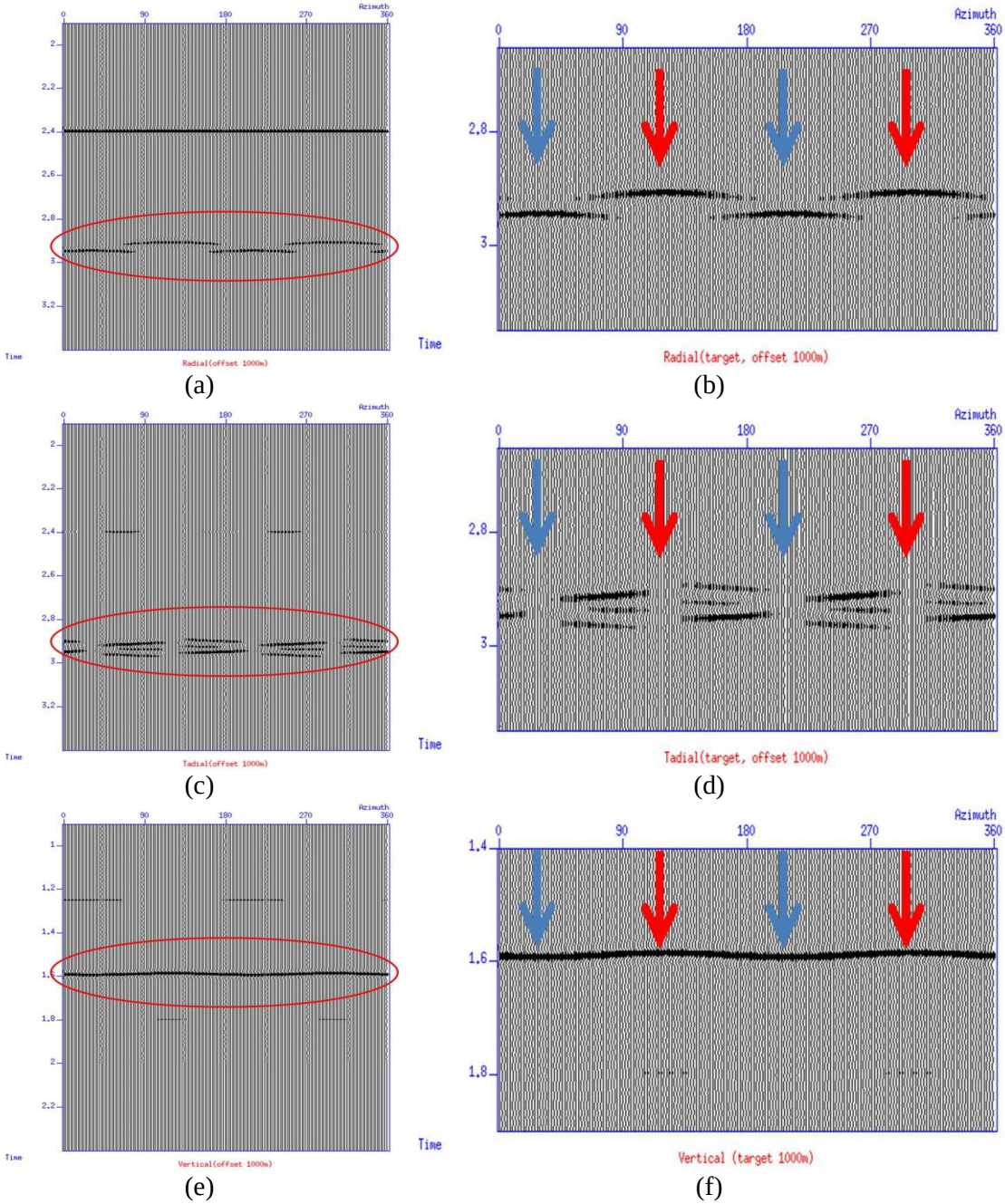

Figure 6- 10: Azimuth gathers (offset 1000m) of radial (a), transverse (c), and vertical (e) components in the water-saturated model. (b), (d) and (f) are enlargements of the target event emphasized by red ellipses in (a), (c) and (e), respectively. (The directions parallel and perpendicular to the fracture direction are indicated by red and blue arrows, respectively).

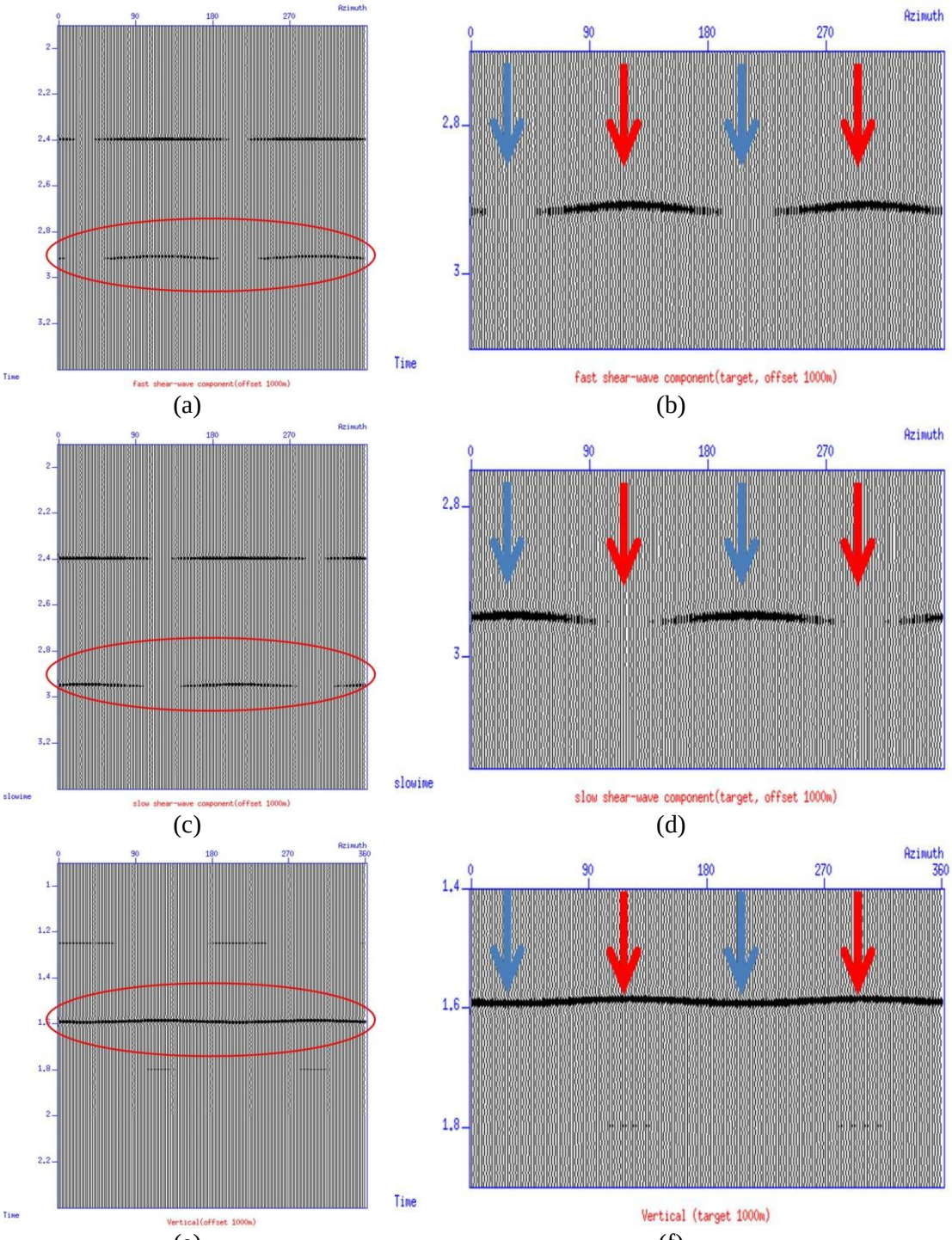

Figure 6- 11: Azimuth gathers (offset 1000m) of P-SV1 (a), P-SV2 (c), and vertical (e) components in the water-saturated model. (b), (d) and (f) are enlargements of the target event emphasized by red ellipses in (a), (c) and (e), respectively. (The directions parallel and perpendicular to the fracture direction are indicated by red and blue arrows, respectively).

After horizontal rotation, azimuthal variations of the P-SV1 and P-SV2 components are both clearly shown. It can be seen that the azimuthal variations of P-SV1 and P-SV2 components are different. The fast directions for P-SV1 and P-SV2 are along the directions parallel (120^o and 300^o) and perpendicular (30^o and 210^o) to the fracture direction, respectively. If rotation to P-SV1 and P-SV2 components is not applied, two different patterns of azimuthal variations could disturb the compensation for the azimuthal variation of radial and transverse components. Moreover two orthogonal fast directions may be obtained if the separation is not applied, which has negative influences on the fracture characterisation. Therefore the different azimuthal variations caused by water-saturated fractures prove again the necessity of separating the fast P-SV1 and slow P-SV2 components. The azimuthal variation of the P-SV1 component is similar to that of the P-wave. However, it can be carefully observed that azimuth variation magnitudes of both P-SV1 and P-SV2 components are similar. Moreover the P-wave azimuth variation has a smaller magnitude, compared with the P-SV1 and P-SV2 components. This indicates that the P-wave data is less significantly affected by the water-saturated fractures than both the P-SV1 and P-SV2 waves. It also provides encouragement for using PS-converted wave seismic data to perform fractured reservoir characterization.

With individual P-SV1 and P-SV2 components, it is possible to use the estimation method introduced above to compensate for the azimuthal variations. Then the P-SV1 and P-SV2 components are all binned into several azimuth bins. The azimuth bin size in this study is set to be 30 °. To facilitate the analysis, the azimuth range is set to be between -90 ° and 90 °. The dataset for any particular azimuth gather is assumed to have the same velocity and anisotropy parameters. Conventional velocity analysis is applied to six azimuth gathers in sequence to obtain individual velocity models. Figure 6- 12 shows the azimuthal velocity analysis of the P-SV1 component for the water-saturated model.

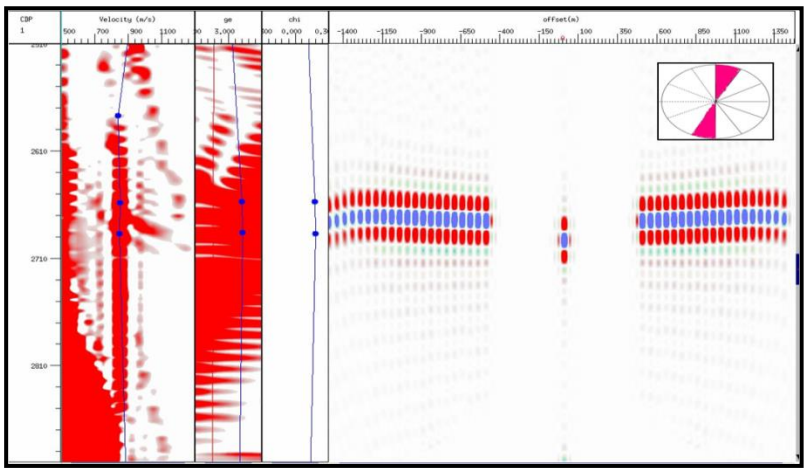

(a)

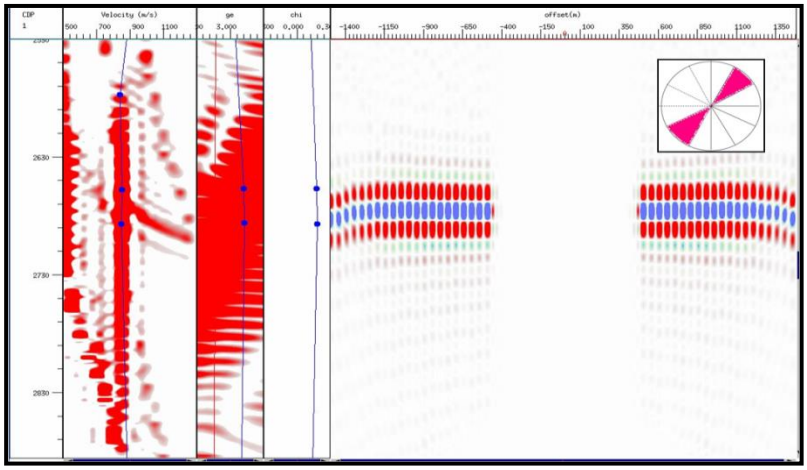

(b)

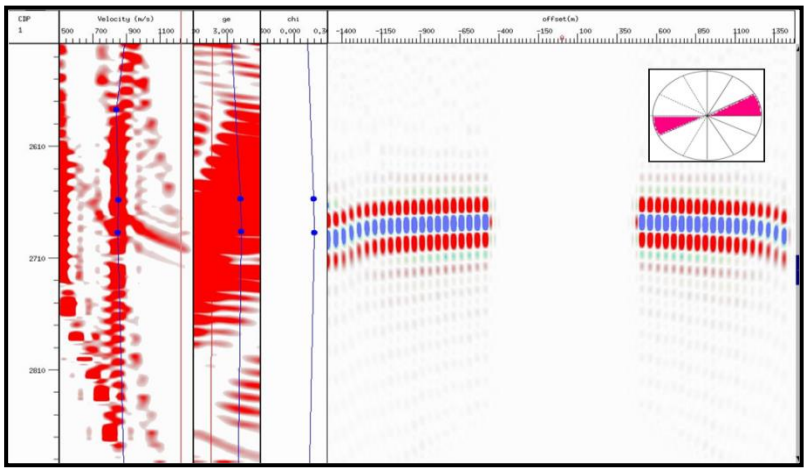

(c)

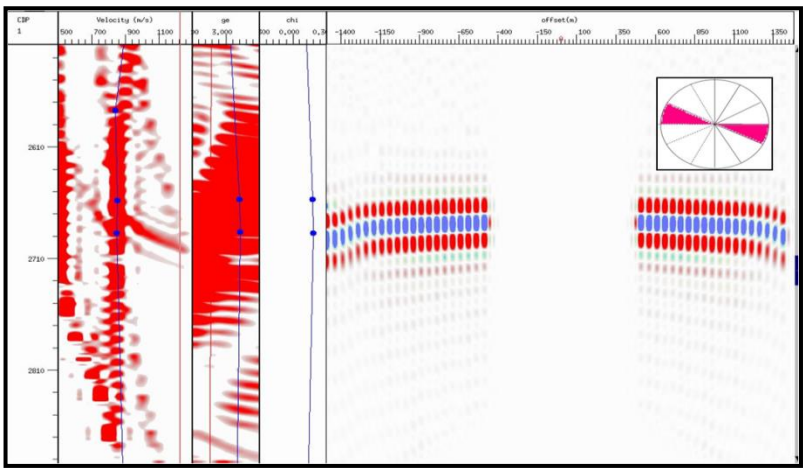

(d)

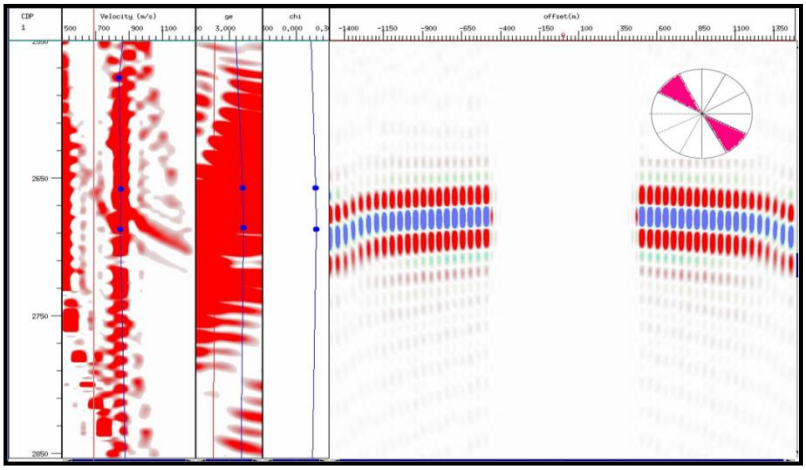

(e)

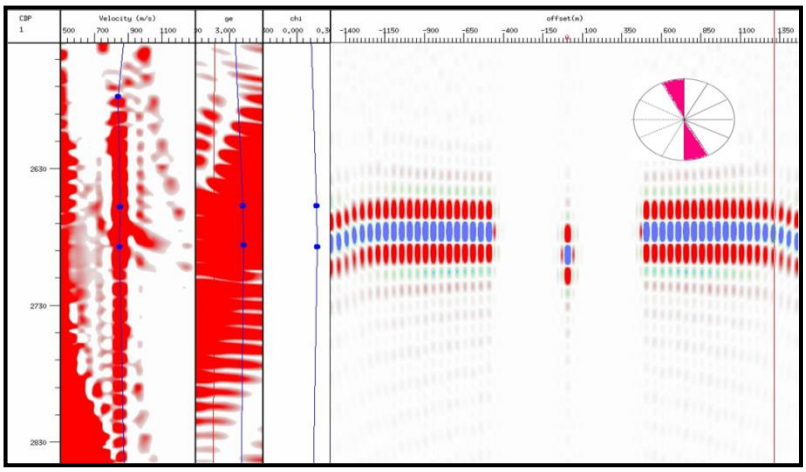

(f)

Figure 6- 12: Velocity analysis of the azimuthal bins of the water-saturated model (P-SV1 component). (a): (-90 °to -60 °); (b): (-60 °to -30 °); (c): (-30 °to 0 °); (d): (0 ° to 30 °); (e): (30 °to 60 °); (f): (60 °to 90 °).

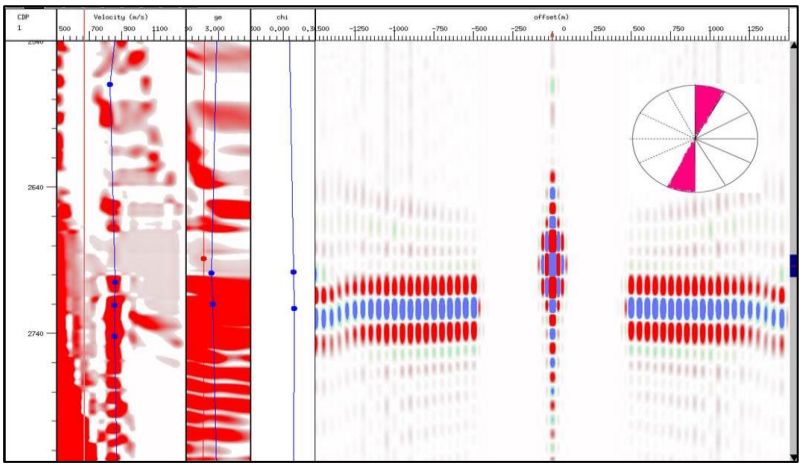
CDP
1
Velocity (m/s)
500
700
900
1100
ge
chi
offset(m)
2640
2740

(a)

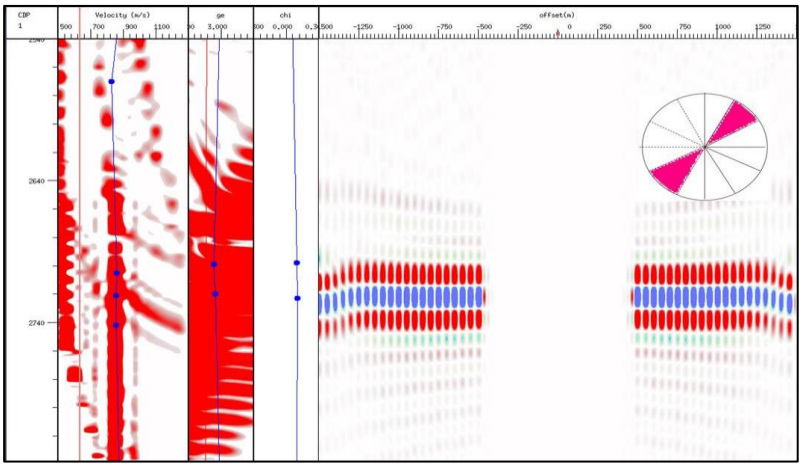
CDP
1
Velocity (m/s)
500
700
900
1100
ge
chi
offset(m)
2640
2740

(b)

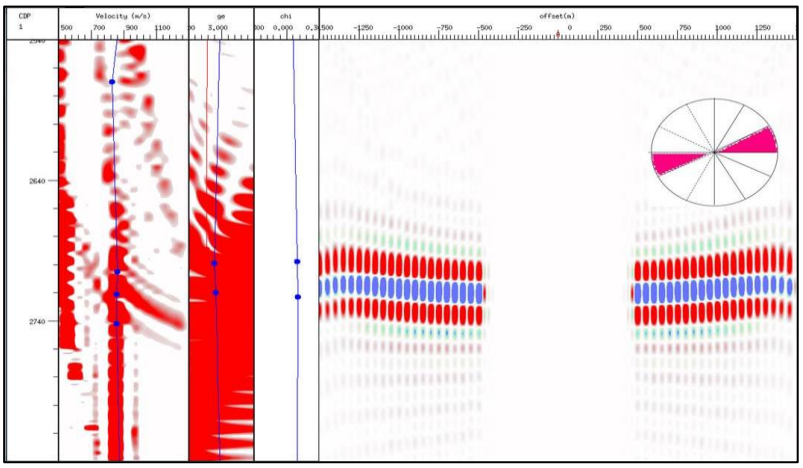
CDP
1
Velocity (m/s)
500
700
900
1100
ge
chi
offset(m)
2640
2740

(c)

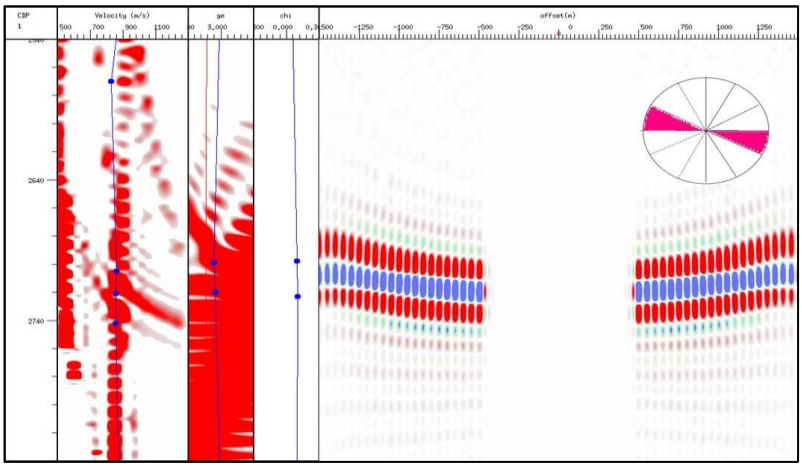

(d)

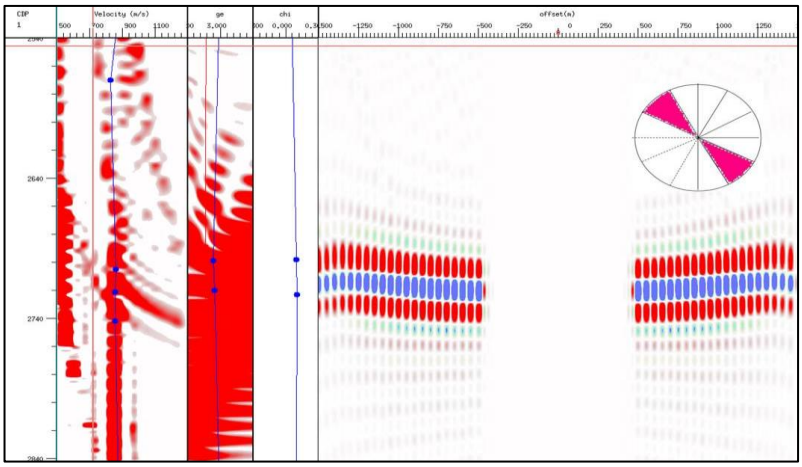

(e)

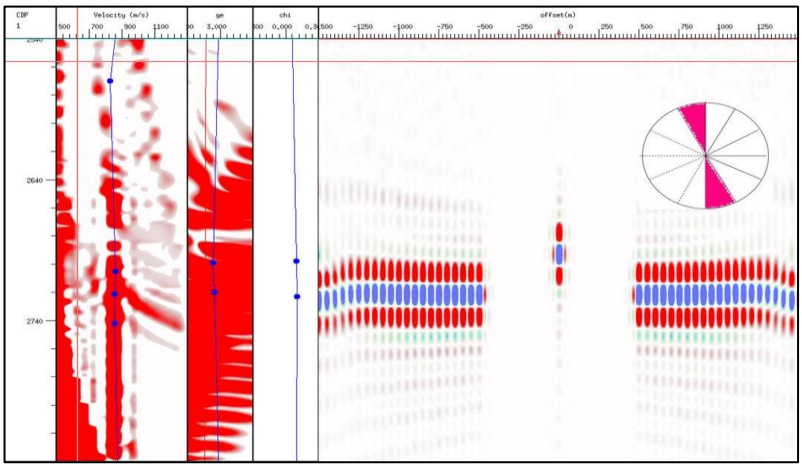

(f)

Figure 6- 13: Velocity analysis of the azimuthal bins of the water-saturated model (P-SV2 component). (a): (-90 °to -60 °); (b): (-60 °to -30 °); (c): (-30 °to 0 °); (d): (0 ° to 30 °); (e): (30 °to 60 °); (f): (60 °to 90 °).

When a single velocity model is applied to the P-SV1 component, the target event is over-corrected in Figure 6- 12(a) and Figure 6- 12(b), but under-corrected in Figure 6- (d) and Figure 6- 12(e). The velocity analysis of the P-SV2 component is different, which is displayed in Figure 6- 13. The target is under-corrected in Figure 6- (a) and Figure 6- 13(b), but over-corrected in Figure 6- 13(d) and Figure 6- (e). This indicates that both P-SV1 and P-SV2 velocities are affected by the azimuthal variation. It implies that a single velocity is not accurate enough for all azimuth bins and an azimuthal velocity model is necessary to improve the NMO correction. Moreover, the target event for both P-SV1 and P-SV2 components has different behaviour in the same azimuth bin. This proves that the azimuthal variation of the P-SV1 component is different from the azimuthal variation of the P-SV2 component. It is in accordance with the observation of azimuth gathers of fast P-SV1 and slow P-SV2 components in Figure 6- 11.

Then six different velocity models are fitted to elliptical velocity models by the least-square method. The NMO velocity ellipses of the P-wave, fast P-SV1 and slow P-SV2 wave are all acquired by this analysis, and are displayed in Figure 6- 14. Individual elliptical velocity equations are also listed in Figure 6- 14. The fitted fast direction for the P-SV1 component is 122^o, which is slightly different from the 120^o fracture direction. Considering the 30^o azimuth bin size, this is an acceptable result. The velocity perturbation is only 10.29m/s, which suggests weak azimuthal variation. For the P-SV2 component, the fast direction is 34^o, which is close to the fracture normal direction, because the velocity perturbation has a negative sign. The absolute value of the velocity perturbation of P-SV2 component is 13.5m/s, which is larger than the absolute value of the P-SV1 component velocity perturbation. The P-wave velocity ellipse is also calculated in this study. The fast direction of P-waves is 112^o, which is also slightly different from the 120^o fracture direction. However, its velocity perturbation is only 1.5m/s, suggesting an even weaker azimuthal variation.

From the above velocity analysis and fitting, the azimuthal variation of the P-SV1 component is similar to the azimuthal variation of P-waves. The fast directions of both P-SV1 and P-waves are close to the fracture direction. The P-SV2 wave is different from both P-SV1 and P-waves. Its fast direction is close to the fracture

normal direction. Moreover, the P-wave is less affected by the water-saturated fractures than the P-SV1 and P-SV2 waves. Therefore, it is more important to compensate for the azimuthal variation of PS-converted waves than the azimuthal variation of P-waves in water-saturated fractures.

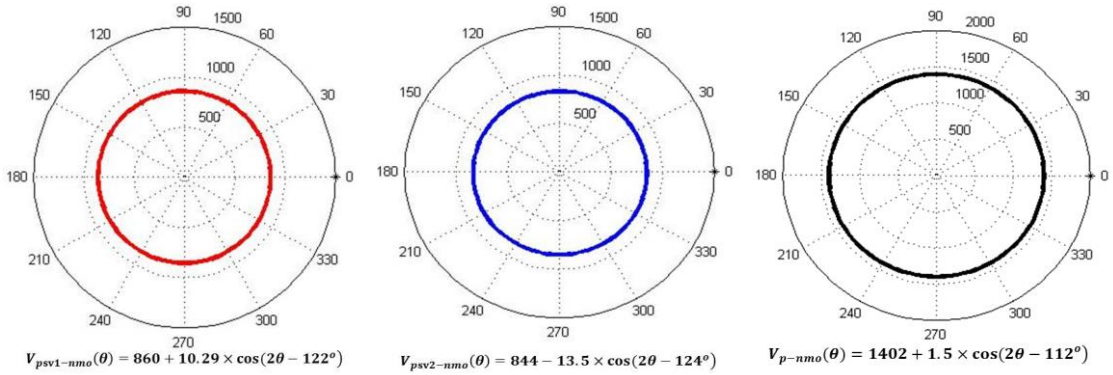

(a) (b) (c)

Figure 6- 14: Velocity ellipses of P-SV1 waves (a), P-SV2 waves (b) and P-waves (c).

By individually applying the velocity ellipses to the P-SV1 and P-SV2 components, the NMO correction can be improved. Results for the NMO correction at the offset 1000m with and without azimuthal compensation for water-saturated fractures are shown in Figure 6- 15, Figure 6- 16 and Figure 6- 17. NMO corrections of P-SV1, P-SV2 and P-waves are all improved. The target event is better aligned and well-focused.

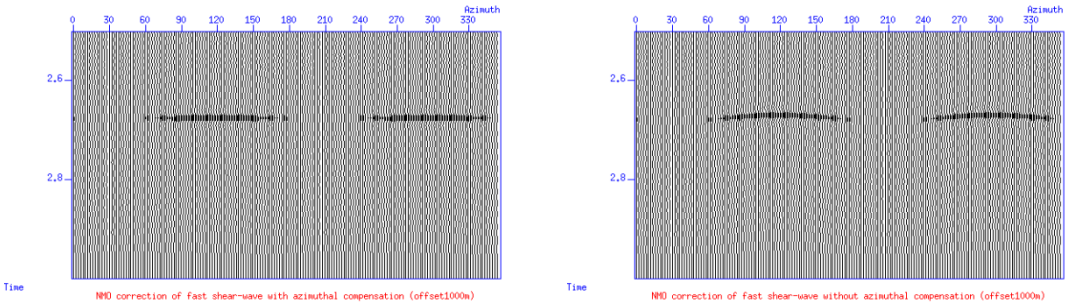

(a) (b)

Figure 6- 15: NMO correction results for the water-saturated model at the offset 1000m for the P-SV1 wave. (a): with the velocity ellipse; (b): without the velocity ellipse.

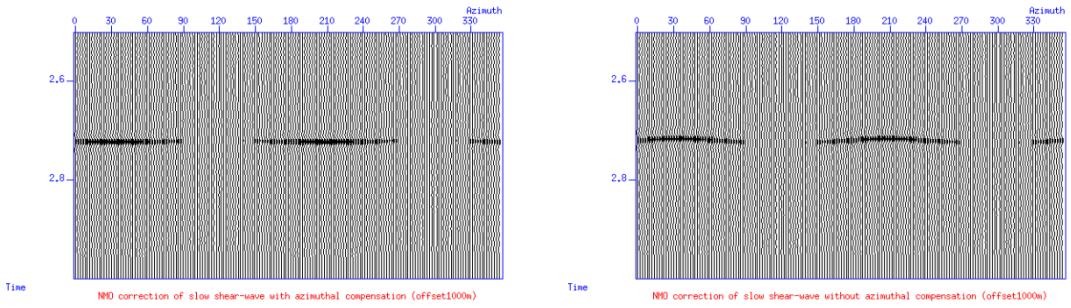

(a) (b)

Figure 6- 16: NMO correction results for the water-saturated model at the offset 1000m for the P-SV2 wave. (a): with the velocity ellipse; (b): without the velocity ellipse.

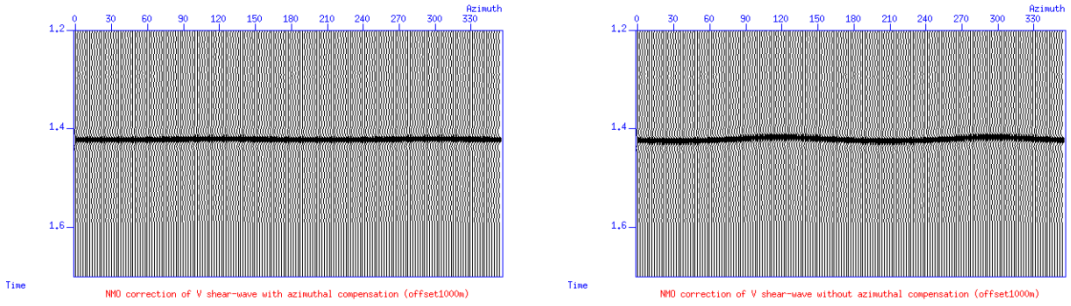

(a) (b)

Figure 6- 17: NMO correction results for the water-saturated model at the offset 1000m for the P-wave. (a): with the velocity ellipse; (b): without the velocity ellipse.

Then the NMO results are stacked into a single trace to analyse the improvement of amplitude spectrum. The stacked traces and their amplitude spectrums are displayed in Figure 6- 18, Figure 6- 19 and Figure 6- 20. Dashed lines represent amplitude spectra of traces without compensation for azimuthal variation. Solid lines represent amplitude spectra of traces with compensation for the azimuthal variation.

It is not easy to see that the stacked wavelet becomes sharper when the velocity ellipse is applied. However, this improvement can be found by comparison of amplitude spectra. By applying the elliptical velocity model, the dominant frequency has been enhanced. This is beneficial to the improvement of seismic resolution. Specifically, the peak amplitudes for the P-SV1 wave and P-SV2 wave are increased by 58% and 28% respectively. P-wave peak amplitude is increased by 31.2%. The improvement for P-wave data is less significant than for P-SV1 wave data and is similar to P-SV2 wave data. It also proves the importance of compensating for the

azimuthal variation of PS-converted waves. With the improved NMO-corrected dataset, subsequent processing and inversion will benefit.

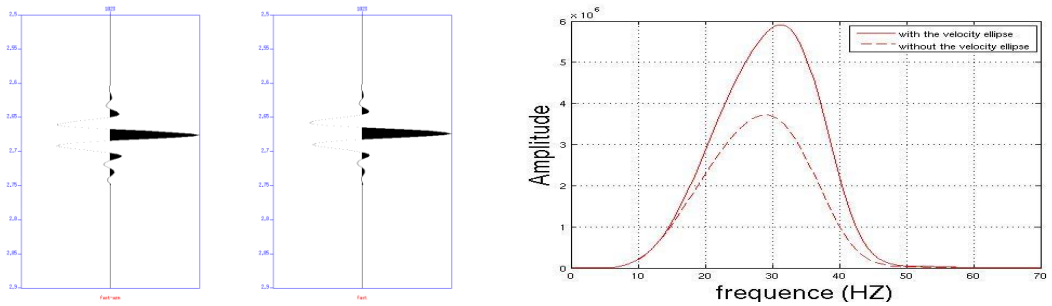

(a) (b) (c)

Figure 6- 18: Stack results for the water-saturated model at offset 1000m for the P-SV1 wave. (a): with the velocity ellipse; (b): without the velocity ellipse; (c): the amplitude spectrum comparison between (a) indicated by the red solid curve, and (b) indicated by the red dashed curve .

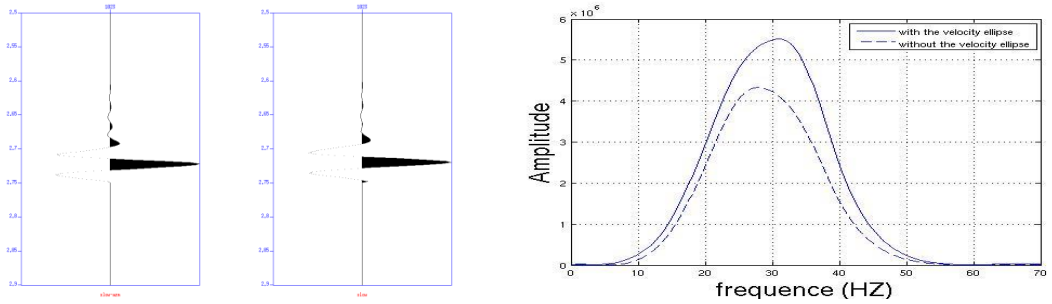

(a) (b) (c)

Figure 6- 19: Stack results for the water-saturated model at offset 1000m for the P-SV1 wave. (a): with the velocity ellipse; (b): without the velocity ellipse; (c): the amplitude spectrum comparison between (a) indicated by the red solid curve, and (b) indicated by the red dashed curve.

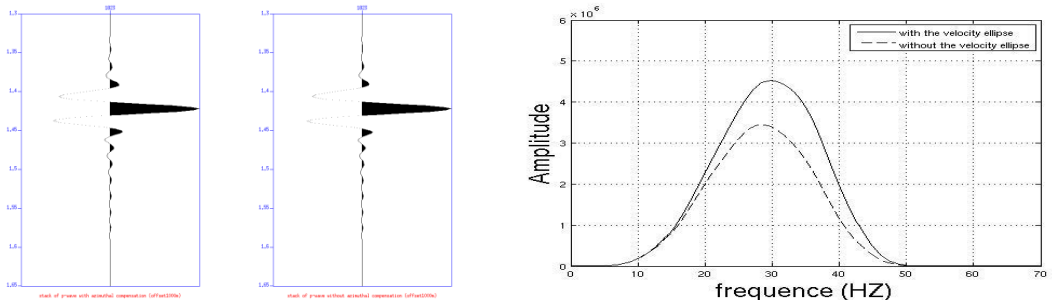

(a) (b) (c)

Figure 6- 20: Stack results for the water-saturated model at offset 1000m for the P-wave. (a): with the velocity ellipse; (b): without the velocity ellipse; (c): the amplitude spectrum comparison between (a) indicated by the red solid curve, and (b) indicated by the red dashed curve .

6.6 Noise testing of the azimuthal analysis

Gaussian noise is added to the dataset to test the analysis of the azimuthal variation. The noise is added by setting different signal-to-noise ratios. The tested signal-to-noise ratios in this study are 1, 3, 5 and 7. Azimuth gathers are displayed in Figure 6-21, Figure 6- 22 and Figure 6- 23 to show how the target event is affected by added noise. When the signal-to-noise ratio is as low as 1, the data quality is very poor. The target event is seriously disturbed by strong noise. It is hard to observe reliable azimuthal variations. Therefore, it will be difficult to apply azimuthal analysis to data with a low signal-to-noise ratio. When the signal-to-noise is 7, the data quality is acceptable. The contrast between effective signal and noise is strong enough to analyse the target event. Azimuthal variations can also be observed, which are similar to the azimuthal variations of the dataset without added noise (Figure 6- 11). Therefore, reliable results can be obtained by applying the same analysis method to this dataset.

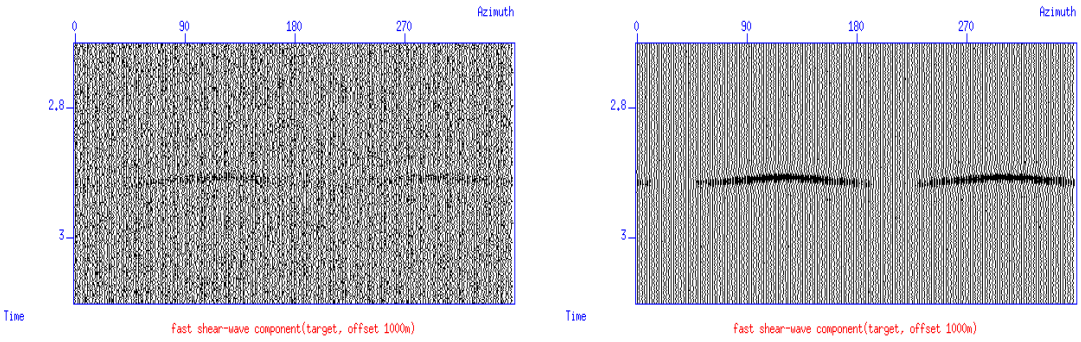

(a) (b)

Figure 6- 21: Azimuth gathers of P-SV1 components when signal-to-noise ratio is 1 (a) and 7 (b), respectively.

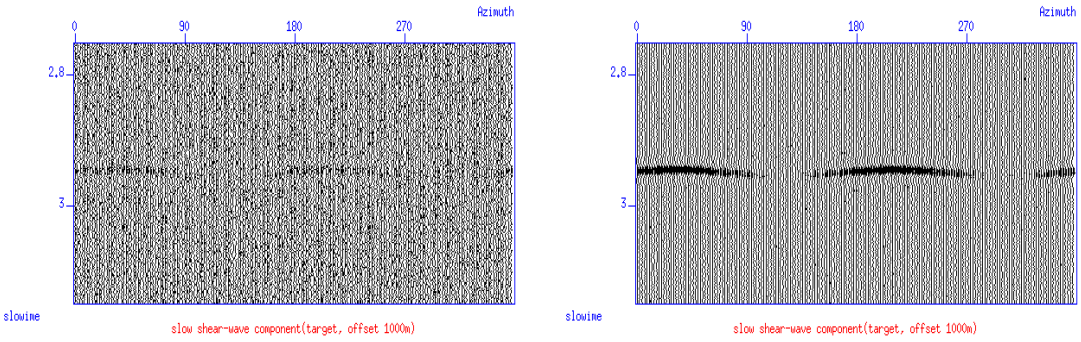

(a) (b)

Figure 6- 22: Azimuth gathers of P-SV2 components when signal-to-noise ratio is 1 (a) and 7 (b), respectively.

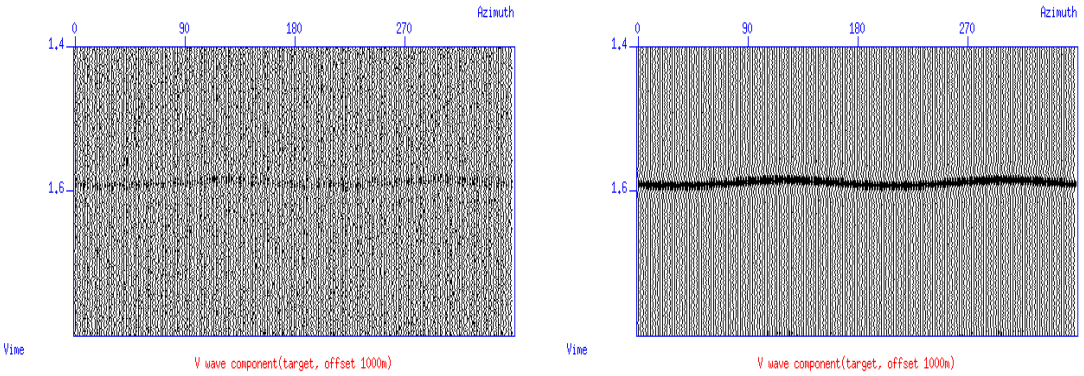

(a) (b)

Figure 6- 23: Azimuth gathers of P-waves when signal-to-noise ratio is 1 (a) and 7 (b), respectively.

Velocity analysis is applied to the dataset with different signal-to-noise ratios. An example of velocity analysis for noisy data is shown in Figure 6- 24. It is the velocity analysis for the azimuth bin (-90 ° to -60 °) of P-SV1 waves. It can be compared with Figure 6- 12(a), in which velocity analysis is applied to the same azimuth bin (-90 ° to -60 °) when no noise is added. When the signal-to-noise ratio is only 1, it is nearly impossible to find the effective reflection event in Figure 6- 24(a). Therefore, it is too difficult to apply reliable analysis to this dataset if the signal-to-noise ratio is only 1. When the signal-to-noise ratio is 7, the data quality is not as bad as the data quality shown in Figure 6- 24(a). The target event can be still successfully observed with the noise interference. But the event is also affected by noise, especially at large offsets. Due to the added noise, the event is not in the exactly same form as that in Figure 6- 12(a). When the noise is not added, the target event is over-corrected in the azimuth bin (-90 ° to -60 °). But it is not easy to find a similar over-correction in Figure 6- 24(b). Therefore, the velocity acquired in this azimuth bin can be different to the velocity when noise is not added. The final elliptical velocity model can also be different, which may cause errors in the determination of fracture properties. The P-SV2 wave and P-wave are similarly influenced by added noise, which could cause inaccurate velocity models.

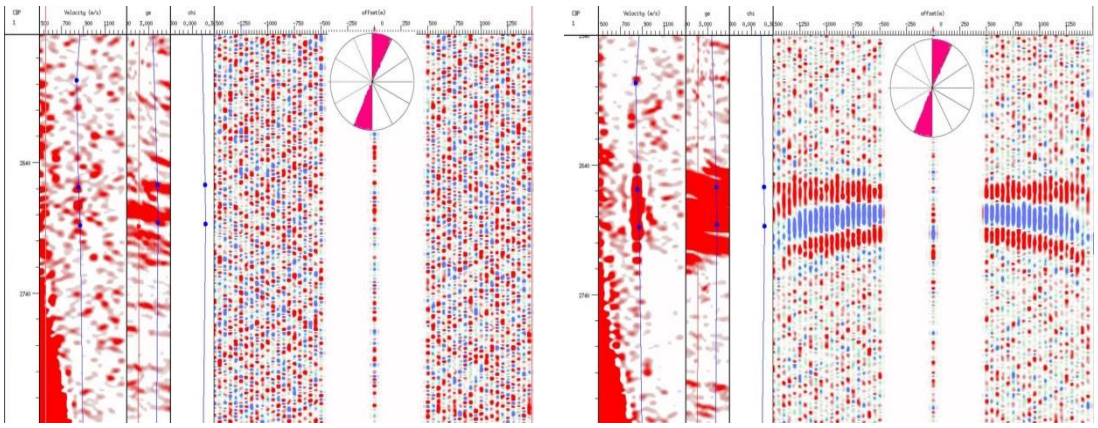

Figure 6- 24: Velocity analysis for the azimuth bin (-90 ° to -60 °) of the P-SV1 component when signal-to-noise ratio is 1 (a) and 7 (b), respectively.

The noise testing is continued for other signal-to-noise ratios. Similar azimuthal velocity analysis is applied to obtain elliptical velocity models. Velocity ellipses for different signal-to-noise ratios are also acquired. They are listed in Table 6- 7, Table 6- 8 and Table 6- 9 to facilitate comparison for different signal-to-noise ratios. The notations of variables used in Table 6- 7, Table 6- 8 and Table 6- 9 can also be found in Table 6- 6. The relative differences are calculated between the dataset without added noise and the datasets with specified signal-to-noise ratios.

For all three types of waves, the accuracy of elliptical velocity models is affected by noise. Moreover, different signal-to-noise ratios cause different amounts of error. When the SN=7, the data is not significantly interfered by the noise. Therefore the relative changes are all smaller than the relative changes when SN is 5 or 3. However, when SN is 5, it does not always provide more accurate parameters. It indicates that more uncertainties are brought when the signal-to-noise ratio is lowered to a certain value. The base velocity and fast direction all have small relative changes for different signal-to-noise ratios. It still suggests that the velocity perturbation is more sensitive to inaccurate parameters.

Velocity analysis is more affected by noise for the P-wave than for both P-SV1 and P-SV2 waves. The relative changes of the three parameters are overall larger than their counterparts for both P-SV1 and P-SV2 waves. The P-wave is found to be less influenced by the azimuthal variation. Therefore, significant errors might be caused if small anisotropic parameters are dealt with. Generally for the P-SV1 wave, small

signal-to-noise ratios cause more inaccurately fitted parameters. For the P-SV2 wave, when the SN=3, the relative changes of three parameters are not always larger than their counterparts when the SN=5. This is similar to the P-wave. It can also be seen that the influences of noise on both P-SV1 and P-SV2 components are similar, providing similar relative changes for different signal-to-noise ratios.

	No noise	**SN=7**	**SN=5**	**SN=3**
v_{0-p}	1402	1407	1415	1412
$\lvert E(v_{0-p})\rvert$	0	0.36	0.93	0.71
Δ_p	1.5	1.8	2.5	2.3
$\lvert E(\Delta_p)\rvert$	0	20	66.67	46.67
β_p	112	122	102	129
$\lvert E(\beta_p)\rvert$	0	2.7	2.7	4.72

Table 6- 7: Comparisons of P-wave elliptical parameters affected by different SN (signal-to-noise ratio).

	No noise	SN=7	SN=5	SN=3
v_{0-psv1}	860	863	851	868
$\lvert E(V_{0-psv1})\rvert$	0	0.35	1.05	0.93
Δ_{psv1}	10.29	8.92	5.79	8.01
$\lvert E(\Delta_{psv1})\rvert$	0	13.7	15.6	16.7
β_{psv1}	122	117	129	130
$\lvert E(\beta_{psv1})\rvert$	0	1.39	1.94	2.22

Table 6- 8: Comparisons of P-SV1 wave elliptical parameters affected by different SN (signal-to-noise ratio).

	No noise	SN=7	SN=5	SN=3
v_{0-psv2}	844	839	836	854
$\lvert E(v_{0-psv2})\rvert$	0	0.59	0.95	1.18
Δ_{psv2}	-13.5	-9.79	-5.5	-6.5
$\lvert E(\Delta_{psv2})\rvert$	0	19.17	34.5	22.6
β_{psv2}	126	120	134	134
$\lvert E(\beta_{psv2})\rvert$	0	1.67	2.22	2.22

Table 6- 9: Comparisons of P-SV2 wave elliptical parameters affected by different SN (signal-to-noise ratio).

In conclusion, analysis of the azimuthal variation is affected by different magnitudes of noise, especially for weak azimuthal anisotropy. In water-saturated fractures, the azimuthal variation of P-waves is weak, compared with the azimuth variations of P-SV1 and P-SV2 waves. Therefore, P-wave data is more sensitive to noise for water-saturated fractures. The fast direction and base velocity are less affected by noise than the velocity perturbation. When the signal-to-noise ratio is poor, the fitted velocity perturbation, which is supposed to indicate the magnitude of azimuthal anisotropy, might not be a reliable parameter.

6.7 Analysis of the azimuthal anisotropy induced by dry fractures and multi-layer fractures

Dry fractures are also simulated in this synthetic study. The azimuth gathers for radial, transverse and vertical components at offset 1000m are displayed in Figure 6-25. Fast P-SV1 and slow P-SV2 components are both projected into the radial and transverse components. Polarisation reversals at every $90°$ can also be found on the transverse component. From both radial and transverse components, the projected P-SV1 and P-SV2 components are found to have a similar azimuthal variation. The fast direction of the P-wave is still the fracture direction, which is similar to the result for water-saturated fractures. Moreover, the azimuthal variation induced by dry fractures is more significant than the azimuthal variation induced by water-saturated fractures. This contrast is found to be more profound in the P-wave data.

Then the same horizontal rotation algorithm is applied to the data. The radial and transverse components are rotated into fast P-SV1 and slow P-SV2 components. Azimuth gathers of P-SV1, P-SV2 and vertical components are shown in Figure 6-26. In Figure 6- 26, it is easy to see that the magnitude of the azimuthal variation is larger than the magnitude of the azimuthal variation induced by water-saturated fractures. It implies that dry fractures cause more significant azimuthal variation, compared with water-saturated fractures. Moreover, P-SV1 and P-SV2 components are found to have a similar pattern of azimuth variation. The fast directions for both

P-SV1 and P-SV2 components are the fracture direction, which is indicated by red arrows. This result is different from the result of water-saturated fractures.

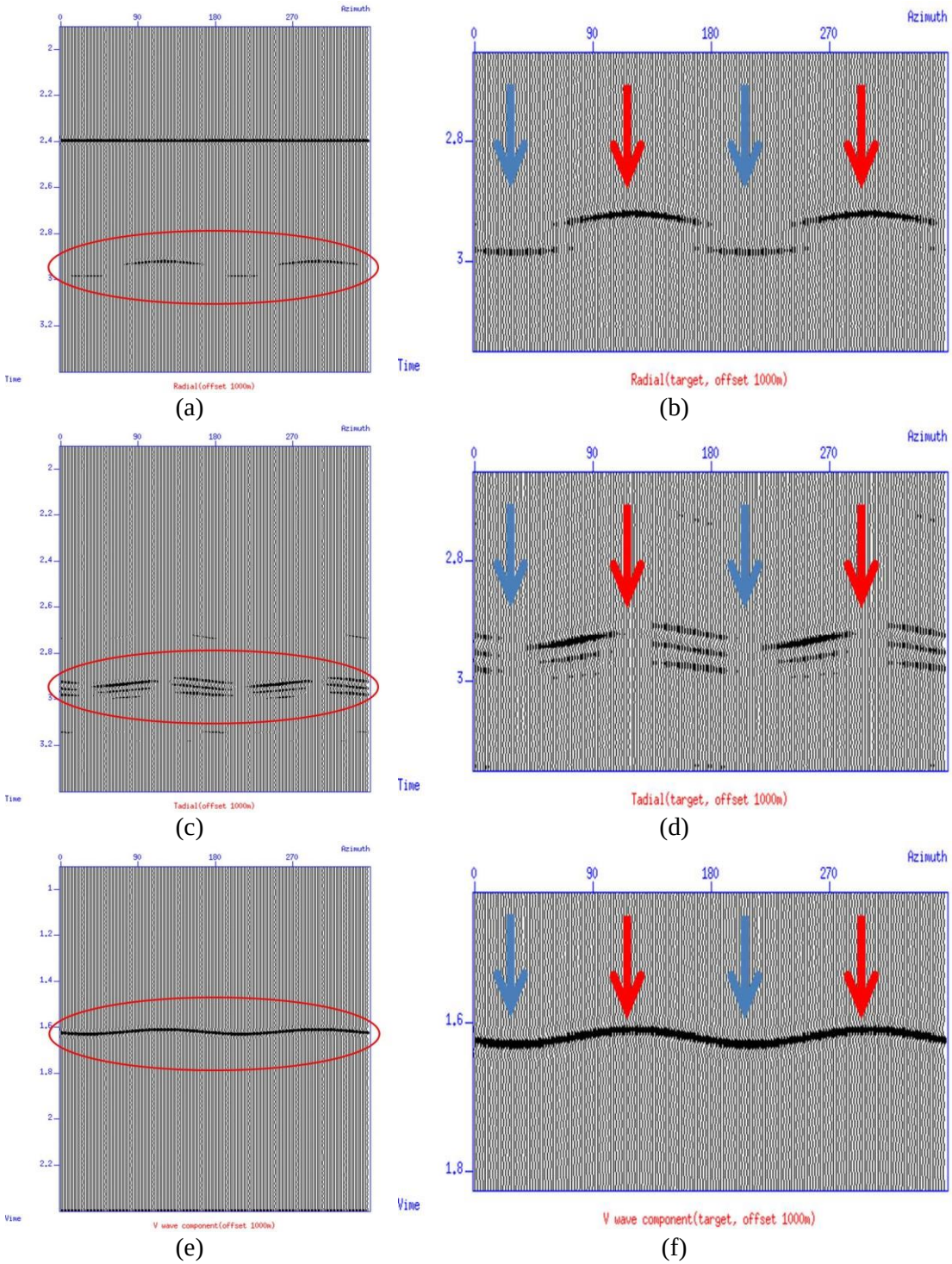

Figure 6- 25: Azimuth gathers (offset 1000m) of radial (a), transverse (c), and vertical (e) components in dry fractures. (b), (d) and (f) are enlargements of the target event emphasized by red ellipses in (a), (c) and (e), respectively. (The directions parallel and perpendicular to the fracture direction are indicated by red and blue arrows, respectively).

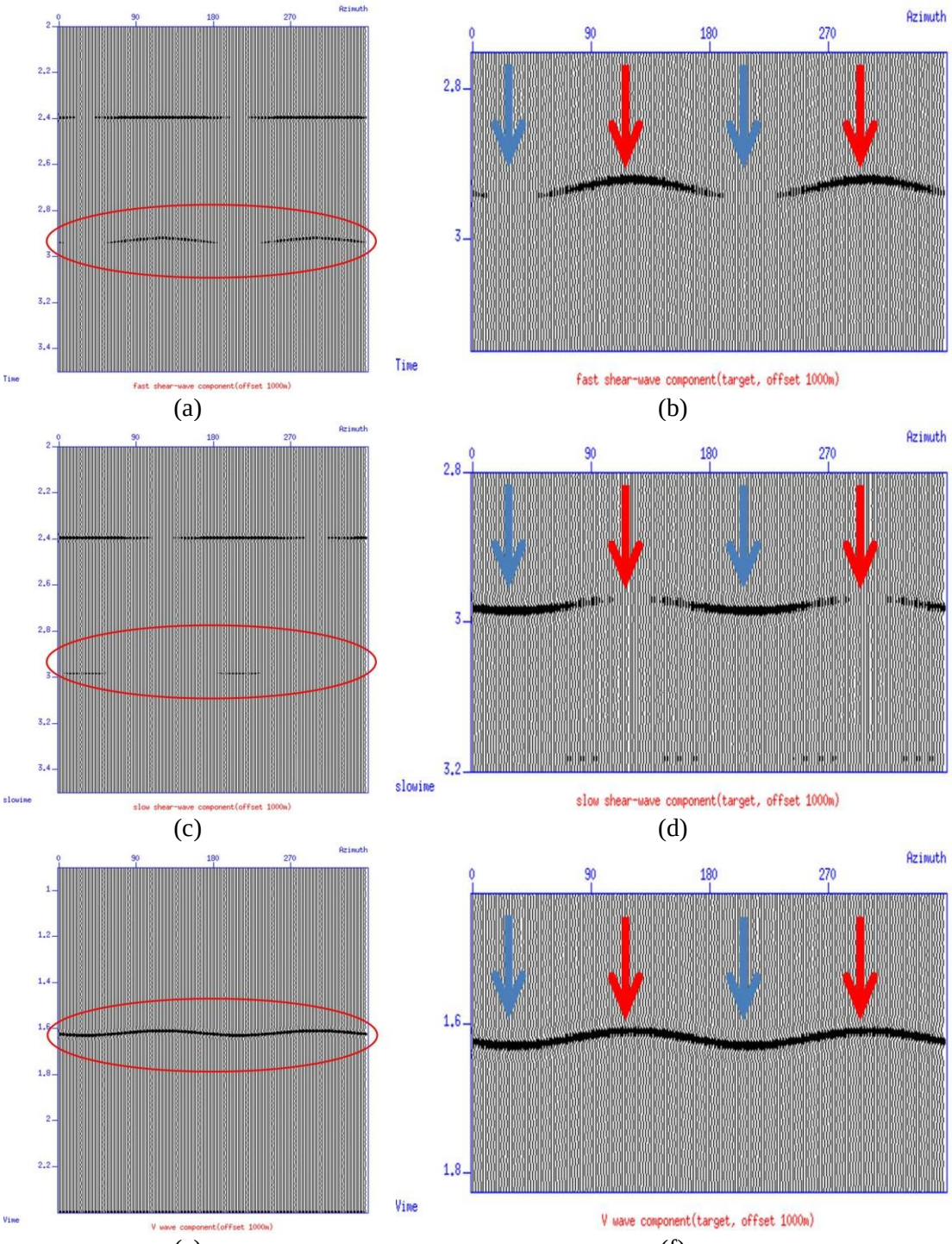

Figure 6- 26: Azimuth gathers (offset 1000m) of P-SV1 (a), P-SV2 (c), and vertical (e) components in the water-saturated model. (b), (d) and (f) are enlargements of the target event emphasized by red ellipses in (a), (c) and (e), respectively. (The directions parallel and perpendicular to the fracture direction are indicated by red and blue arrows, respectively).

Then azimuthal velocity analysis is also applied to the data to obtain an elliptical velocity model. The velocity analysis for the P-SV1 component is displayed in Figure 6- 27 and the velocity analysis for the P-SV2 component is displayed in Figure 6- 28. It is seen that no single velocity model is accurate enough over all the different azimuth bins. For the P-SV1 component, the target event is over-corrected in Figure 6- 27(a) but is under-corrected in Figure 6- 27(c), Figure 6- 27(d) and Figure 6- 27(e). A similar phenomenon can also be observed for the P-SV2 component. The target event is over-corrected in Figure 6- 28(a) but is under-corrected in Figure 6- 28(d) and Figure 6- 28(e). It implies that higher velocities are necessary for the azimuth bin (-90 ° to -60 °) and lower velocities are needed for azimuth bins (+00 °to +30 °) and (+30 °to +60 °). But this special feature shown in the P-SV1 components is more significant than the similar feature shown in the P-SV2 component. It suggests that the azimuthal variation magnitude of P-SV1 components may be larger than the azimuthal anisotropy magnitude of P-SV2 components.

Applying the same least-square fitting method, the elliptical velocity model can be obtained. The NNO velocity ellipses of P-wave, fast P-SV1 and slow P-SV2 wave are displayed in Figure 6- 29. The elliptical velocity equations are still listed in Figure 6- 29. The fitted fast direction for P-SV1 component is 118^o, which is slightly different from the 120^o fracture direction. The velocity perturbation is 21.8m/s. For the P-SV2 component, the fast direction is 124^o, which is also close to the fracture direction. The velocity perturbation of P-SV2 component is 13.99m/s, which is smaller than the P-SV1 component velocity perturbation. The fast direction of P-waves is 116^o, which is also slightly different from the 120^o fracture direction. Its velocity perturbation is 42.47m/s, which is much larger than its counterparts in water-saturated fractures.

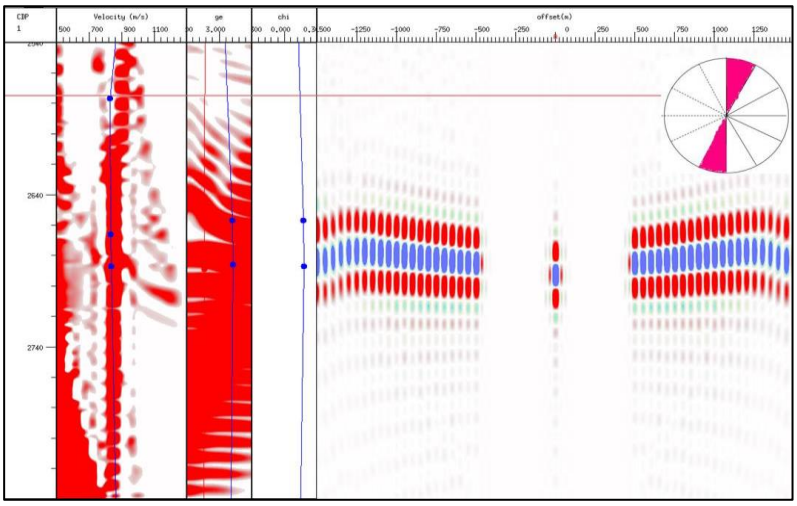
CDP
1
Velocity (m/s)
500
700
900
1100
ge
0
3.000
chi
0.000
0.3500
offset(m)
-1250
-1000
-750
-500
-250
0
250
500
750
1000
1250
2640
2740

(a)

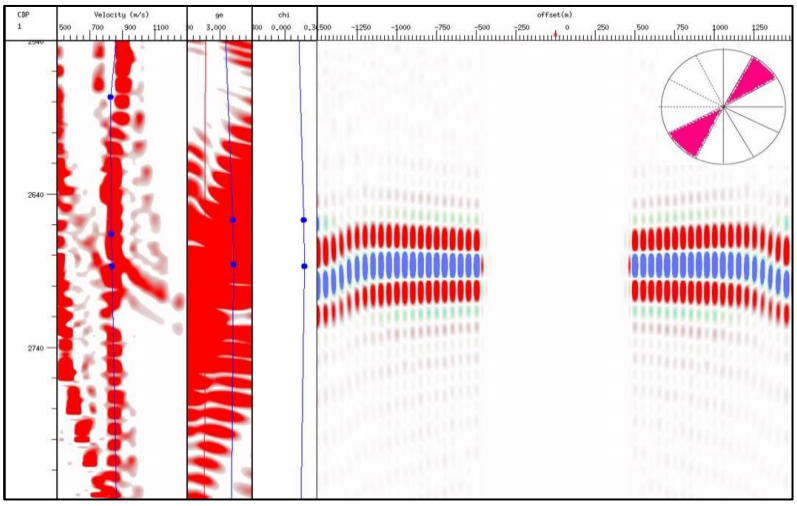
CDP
1
Velocity (m/s)
500
700
900
1100
ge
0
3.000
chi
0.000
0.3500
offset(m)
-1250
-1000
-750
-500
-250
0
250
500
750
1000
1250
2640
2740

(b)

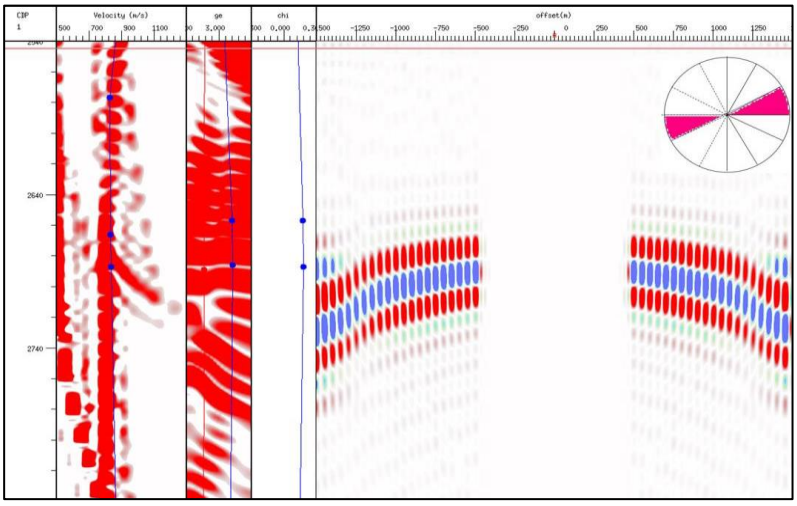
CDP
1
Velocity (m/s)
500
700
900
1100
ge
0
3.000
chi
0.000
0.3500
offset(m)
-1250
-1000
-750
-500
-250
0
250
500
750
1000
1250
2640
2740

(c)

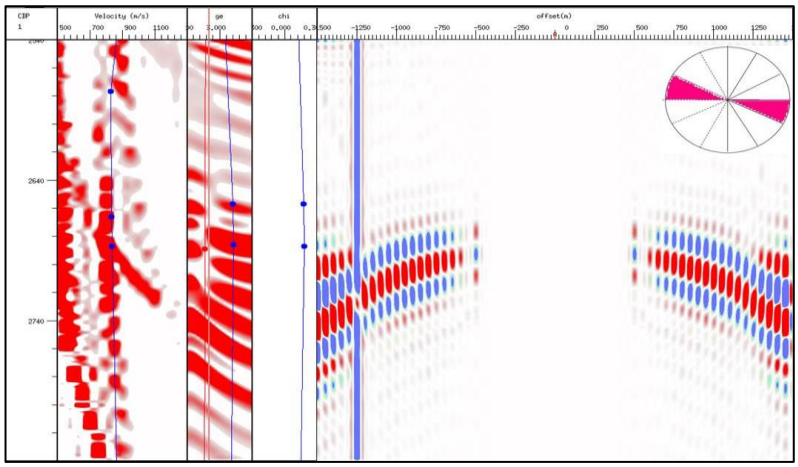

(d)

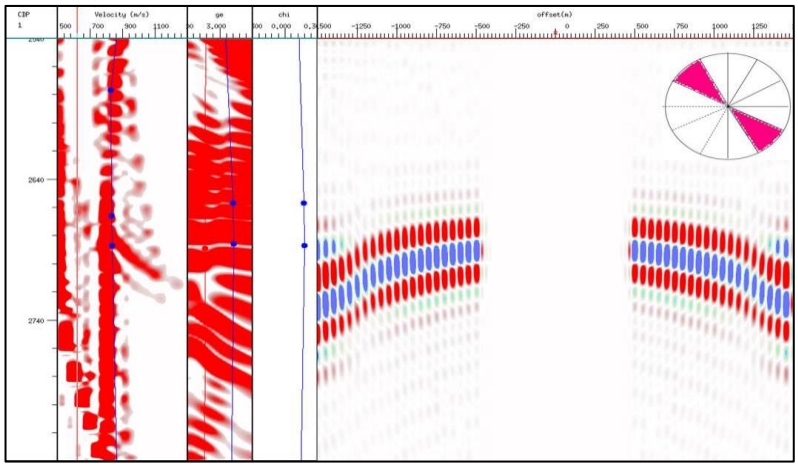

(e)

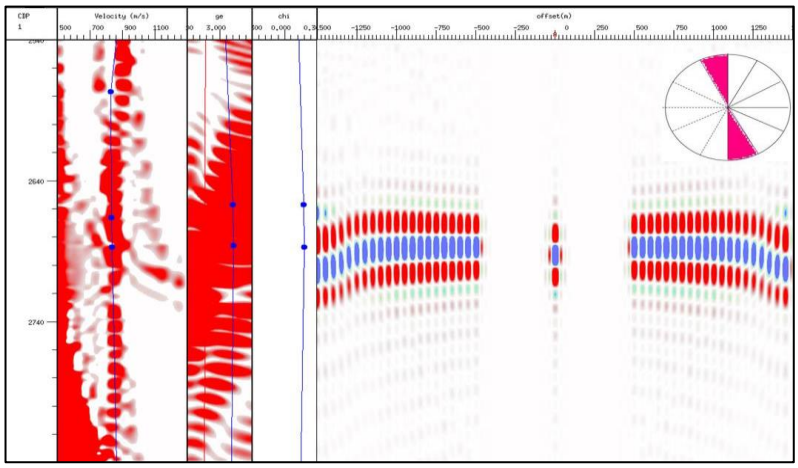

(f)

Figure 6- 27: Velocity analysis of the azimuthal gathers of the dry fracture model (P-SV1 component). (a): (-90 °to -60 °); (b): (-60 °to -30 °); (c): (-30 °to 0 °); (d): (0 ° to 30 °); (e): (30 °to 60 °); (f): (60 °to 90 °).

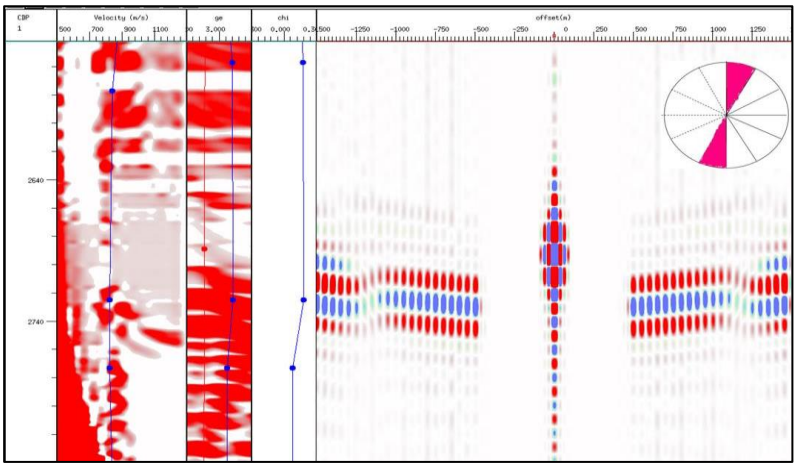
CDP
1
Velocity (m/s)
500 700 900 1100
ge
0 3,000
chi
0.000 0.3500
offset(m)
-1250 -1000 -750 -500 -250 0 250 500 750 1000 1250
2640
2740

(a)

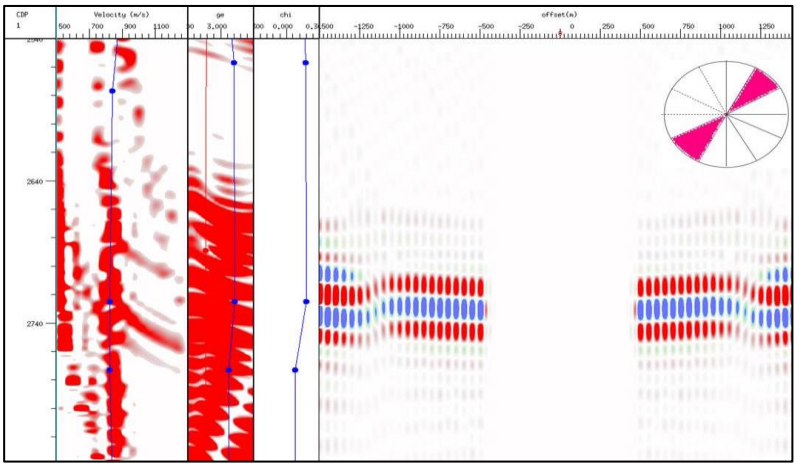
CDP
1
Velocity (m/s)
500 700 900 1100
ge
0 3,000
chi
0.000 0.3500
offset(m)
-1250 -1000 -750 -500 -250 0 250 500 750 1000 1250
2640
2740

(b)

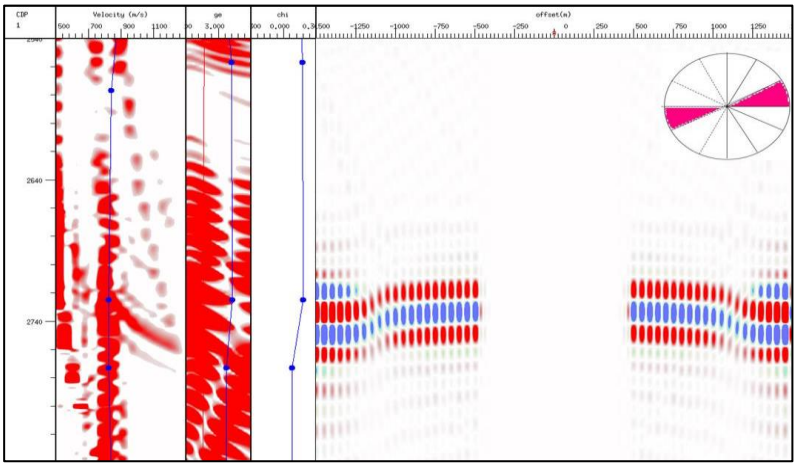
CDP
1
Velocity (m/s)
500 700 900 1100
ge
0 3,000
chi
0.000 0.3500
offset(m)
-1250 -1000 -750 -500 -250 0 250 500 750 1000 1250
2640
2740

(c)

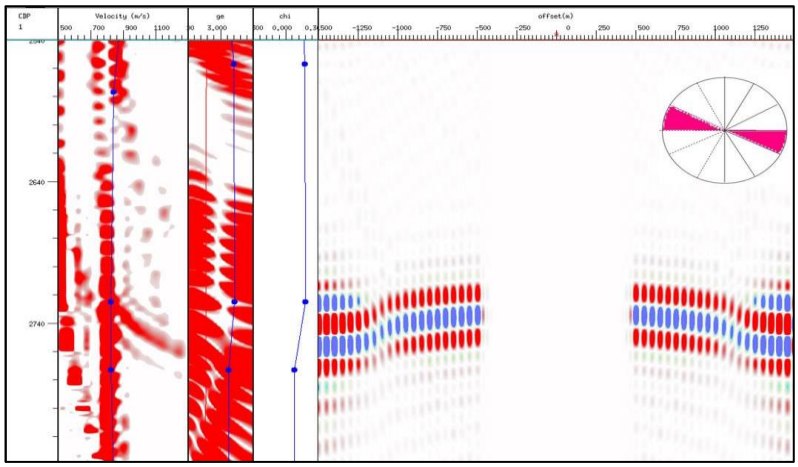

(d)

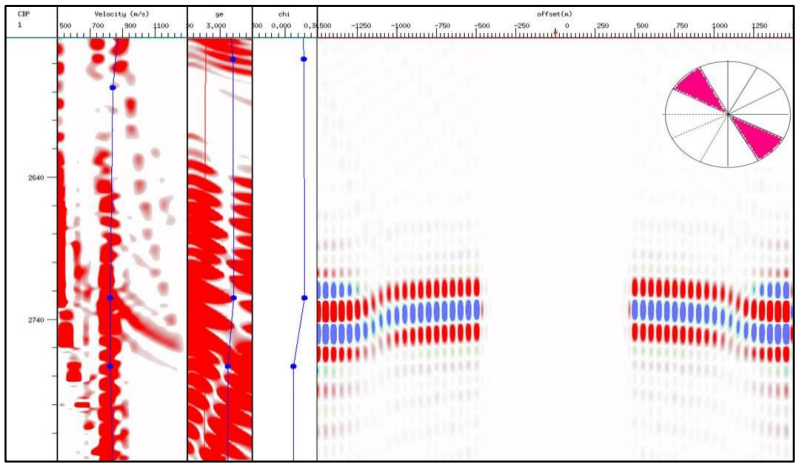

(e)

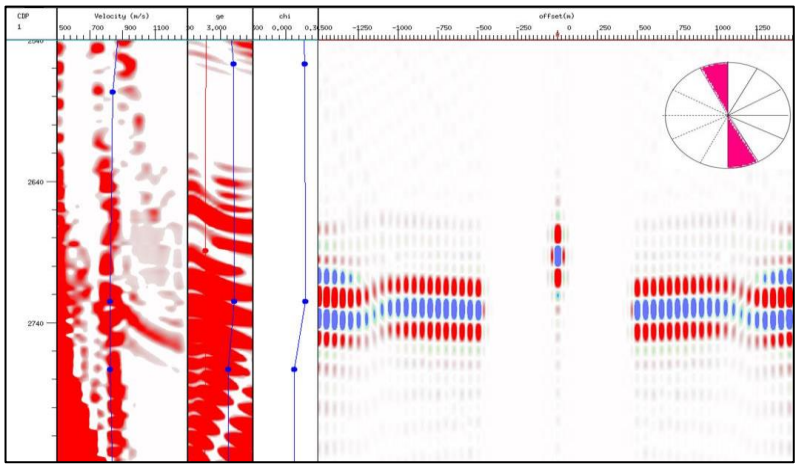

(f)

Figure 6- 28: Velocity analysis of the azimuthal gathers of the dry fracture model (P-SV2 component). (a): (-90 °to -60 °); (b): (-60 °to -30 °); (c): (-30 °to 0 °); (d): (0 ° to 30 °); (e): (30 °to 60 °); (f): (60 °to 90 °).

From analysis of the velocity ellipses of the dry-fracture model, the azimuthal variation of P-wave is similar to the azimuthal variations of P-SV1 and P-SV2 waves. The fast directions of both P-SV1 and P-SV2 waves are the fracture direction. The velocity perturbations for the dry-fracture model are larger than the velocity perturbations for the water-saturated-fracture model. This implies that more significant azimuthal variation is induced by dry fractures.

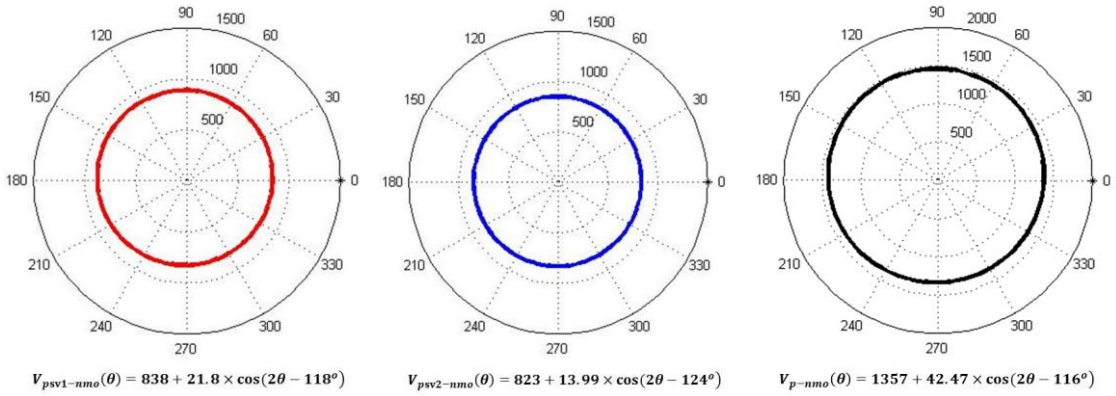

(a) (b) (c)

Figure 6- 29: Velocity ellipses of P-SV1 waves (a), P-SV2 waves (b) and P-waves (c).

Then those velocity ellipses are individually applied in the NMO correction. The NMO correction results at offset 1000m with and without azimuthal compensation for dry fractures are shown in Figure 6- 30, Figure 6- 31 and Figure 6- 32. It is not difficult to notice that the NMO corrections of P-SV1, P-SV2 and P-waves are all improved. The target is better aligned and well-focused. This improvement is similar to the NMO correction improvement for water-saturated fractures.

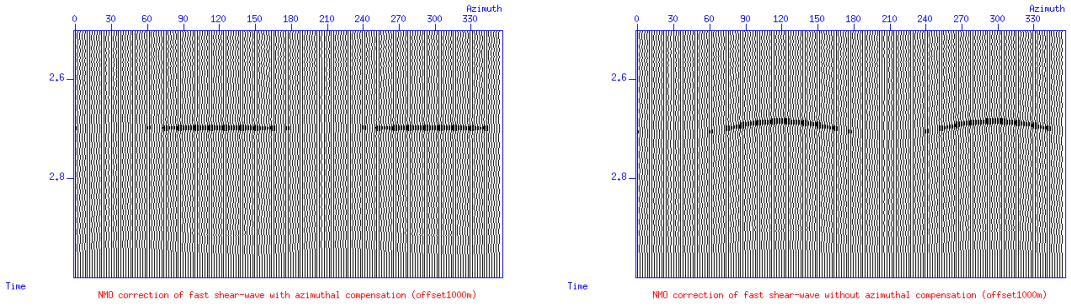

(a) (b)

Figure 6- 30: NMO correction results for the dry-fracture model at the offset 1000m for the P-SV1 wave. (a): with the velocity ellipse; (b): without the velocity ellipse.

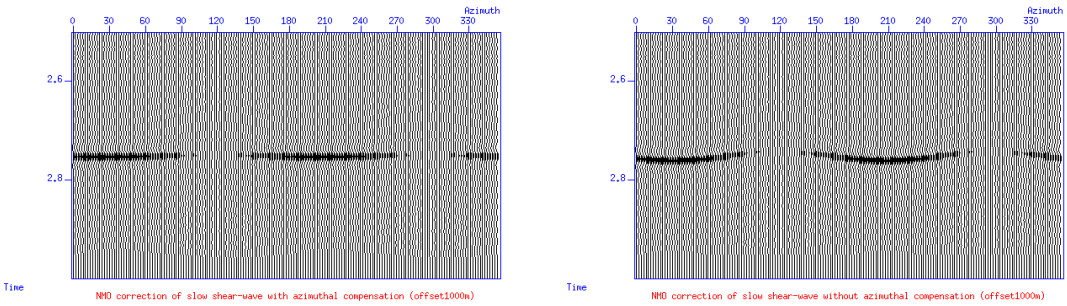

(a) (b)

Figure 6- 31: NMO correction results for the dry-fracture model at the offset 1000m for the P-SV2 wave. (a): with the velocity ellipse; (b): without the velocity ellipse.

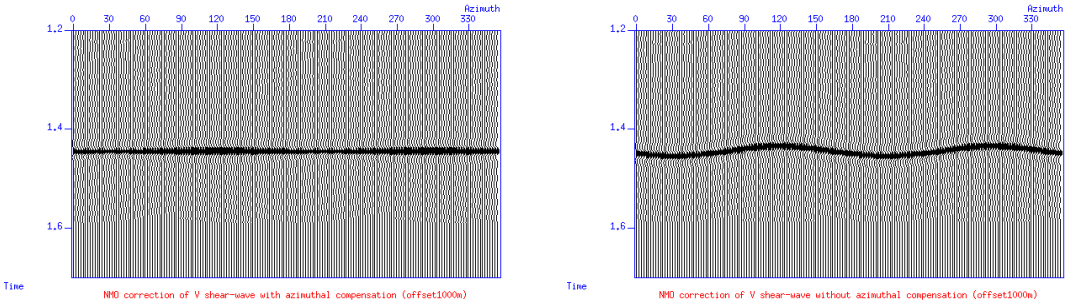

(a) (b)

Figure 6- 32: NMO correction results for the dry-fracture model at the offset 1000m for the P-wave. (a): with the velocity ellipse; (b): without the velocity ellipse.

Then similar stacking and spectrum analysis was applied to the NMO-corrected dataset. The stacked traces and their amplitude spectrums are displayed Figure 6- 33, Figure 6- 34 and Figure 6- 35.

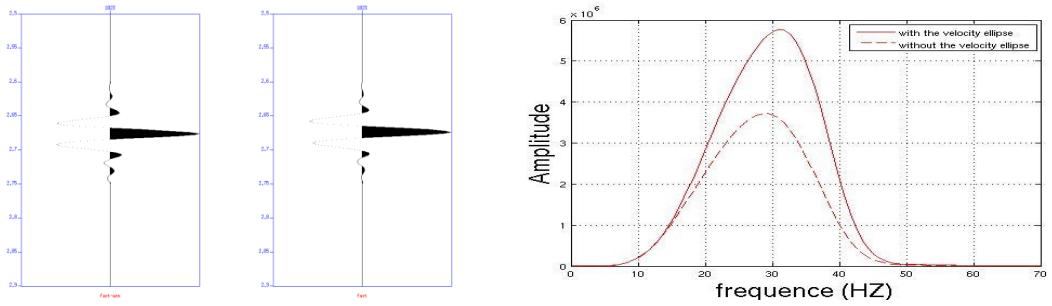

(a) (b) (c)

Figure 6- 33: Stack results for the dry-fracture model at the offset 1000m for the P-SV1 wave. (a): with the velocity ellipse; (b): without the velocity ellipse; (c): the amplitude spectrum comparison between (a) indicated by the red solid curve, and (b) indicated by the red dashed curve .

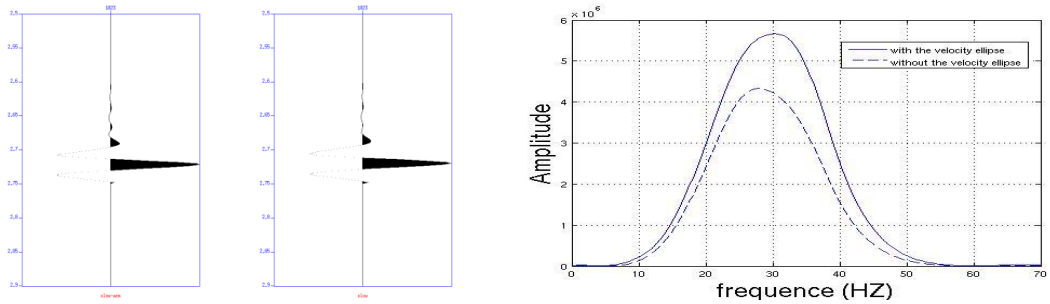

(a) (b) (c)

Figure 6- 34: Stack results for the dry-fracture model at the offset 1000m for the P-SV1 wave. (a): with the velocity ellipse; (b): without the velocity ellipse; (c): the amplitude spectrum comparison between (a) indicated by the red solid curve, and (b) indicated by the red dashed curve .

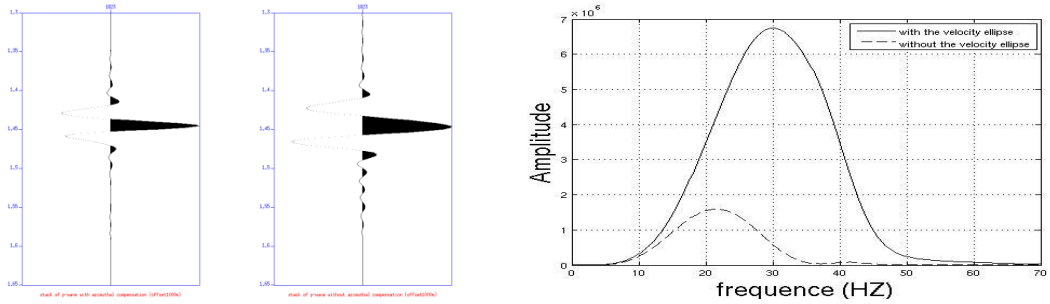

(a) (b) (c)

Figure 6- 35: Stack results for the dry-fracture model at the offset 1000m for the P-wave. (a): with the velocity ellipse; (b): without the velocity ellipse; (c): the amplitude spectrum comparison between (a) indicated by the red solid curve, and (b) indicated by the red dashed curve .

It is possible to notice the improvement on the single stack trace, especially for P-waves. Similarly, this improvement is more significant in comparison of the amplitude spectra. The amplitude spectra are improved by applying velocity ellipses. This improvement is important to the enhancement of seismic resolution. Specifically, the peak amplitudes for the P-SV1 wave and P-SV2 wave are increased by 55% and 30.9% respectively. P-wave peak amplitude is increased by 322%. The improvement of the P-wave is much more significant than improvements to the P-SV1 and P-SV2 waves. This is different from the water-saturated fractures.

The synthetic study is further extended to the model containing two HTI layers with different fracture orientations. The azimuthal anisotropy of the lower HTI layer is expected be influenced by the upper HTI layer. The azimuthal gathers may be more complex to analyse than the azimuthal gathers of the model with a single set of

vertical fractures. A synthetic model containing four layers is simulated, in which the second and third layers are HTI layers with different fracture orientations.

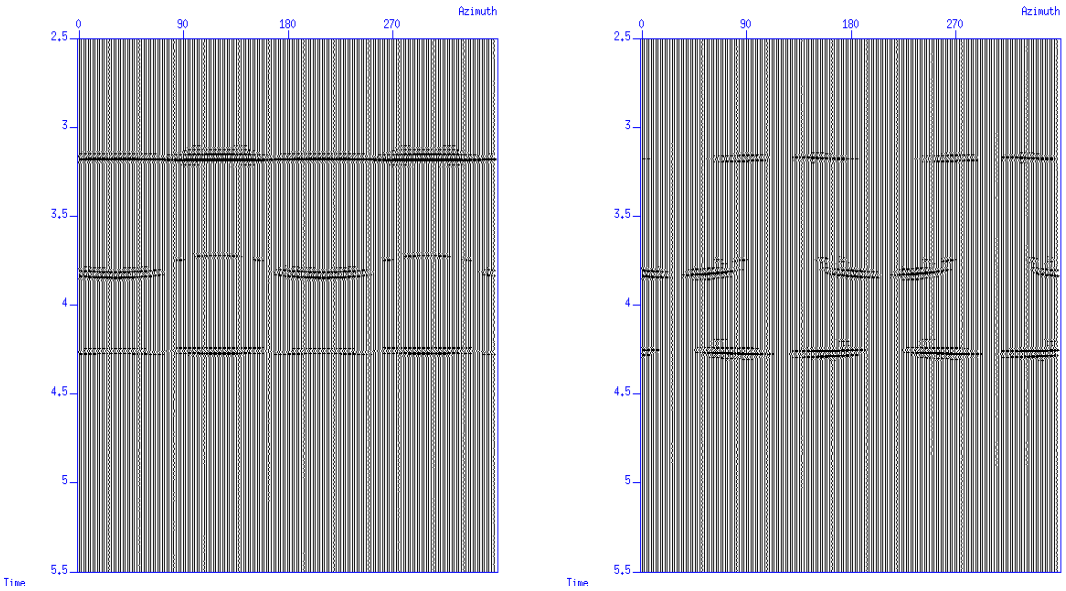

(a) (b)

Figure 6- 36: Azimuth gathers of radial (a), transverse components (b) in the model containing two HTI layers with different fracture directions.

Azimuth gathers for the radial and transverse components are shown in Figure 6- 36. It can be seen that the third event is affected by its upper HTI layer. The azimuthal variation is complicated by the anisotropy induced by fractures in the second HTI layer. Therefore, a layer stripping method may be needed to compensate for the azimuthal anisotropy, and this is discussed in Chapter 7.

6.8 Summary

Compensation for azimuthal anisotropy was studied in this Chapter. I developed a specific work flow to compensate for azimuthal variations of PS-converted waves, which includes several important steps. Transformations between different coordinate systems have an influence on the analysis of azimuthal variation of PS-converted waves. It is necessary to separate the fast P-SV1 wave from the P-SV2 wave before compensating for the azimuthal variation. Azimuthal binning is also important in the study of azimuthal anisotropy. Small azimuth bin size is beneficial to the accuracy of azimuthal analysis. But a large azimuth bin size can provide a good signal-to-noise ratio, especially for field data. Therefore the actual bin size

should be a compromise between these two considerations. A least-square algorithm is used to fit azimuthal velocity models into velocity ellipses. The accuracy of this algorithm is affected by velocity errors. Velocity perturbations are more sensitive to velocity errors than base velocities and fast directions. Therefore, velocity perturbations may not be a robust representation of azimuthal variation.

Then the procedure of compensating for the azimuthal variation was applied to a synthetic dataset. Both dry and water-saturated fractures were considered in this synthetic study. It is found that more significant azimuthal variation is induced by dry fractures. Therefore, it is essential for dry fractures that compensation is made for the induced azimuthal variation. For water-saturated fractures, the magnitude of the azimuthal variation is smaller. Compensation for the azimuthal variation induced by water-saturated fractures may not be needed if the fracture density is small. It is seen that P-wave azimuthal variations are more significant in dry fractures, and therefore compensation for azimuthal variation is needed.

Chapter 7

Analysis of azimuthal variations of PS-converted waves in HTI media for fracture detection

7.1 Introduction

In this chapter, I analysed PS-converted splitting and azimuthal variations of both P-waves and PS-converted waves, and assess their merits for characterising fracture orientations and densities, in particular, for distinguishing dry and water-saturated fractured reservoirs. Several synthetic models are used to simulate and analyse PS-converted wave azimuthal variations. Those models are all based on the synthetic model used in Chapter 6. The model parameters are displayed again in Figure 7- 1. The fracture orientation in this example is still 120^o in the horizontal plane. The same acquisition is used in this synthetic study. The azimuth coverage is from 0^o to 360^o with a 2^o interval. The source-receiver separation range is selected to be between 500 and 1500 meters with a 50m receiver space. Both dry and water-saturated fractures are considered. Moreover, responses of PS-converted wave seismic data to fractures with different fracture densities are also studied. Fracture densities 0.1, 0.08, 0.06 and 0.04 are all tested. In the presence of multi-sets fractures, a specific layer-stripping method is developed to obtain the true fracture properties.

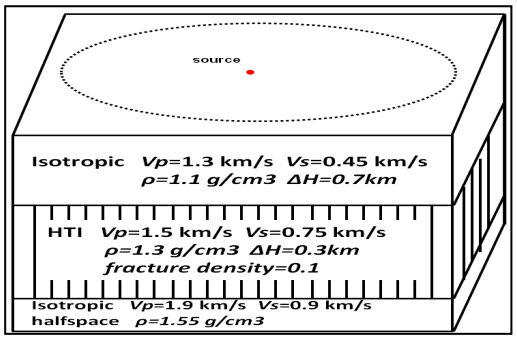

Figure 7- 1: Description of the three-layer synthetic model

7.2 P-wave azimuthal variation

Azimuth gathers of P-wave data at different offsets are displayed in Figure 7- 2 and Figure 7- 3. The P-wave azimuthal variation can be clearly found in the azimuth gathers. The fast and slow directions of the P-wave azimuthal variation are the directions parallel and perpendicular to the fracture direction, respectively. At the same offset, the azimuthal variation induced by dry fractures is more significant than that of water-saturated fractures. This comparison was made in Chapter 6 and is further studied in this chapter. It can be seen that the P-wave azimuthal variation is related to the offset-to-depth ratio (X/Z ratio). In this synthetic study, offset 500m corresponds to the X/Z ratio 0.5. Offsets 1000m and 15000m correspond to X/Z ratios 1 and 1.5, respectively. For both dry and water-saturated fractures, the azimuthal variation shown on the azimuth gathers becomes more obvious as the offset-to-depth ratio increases.

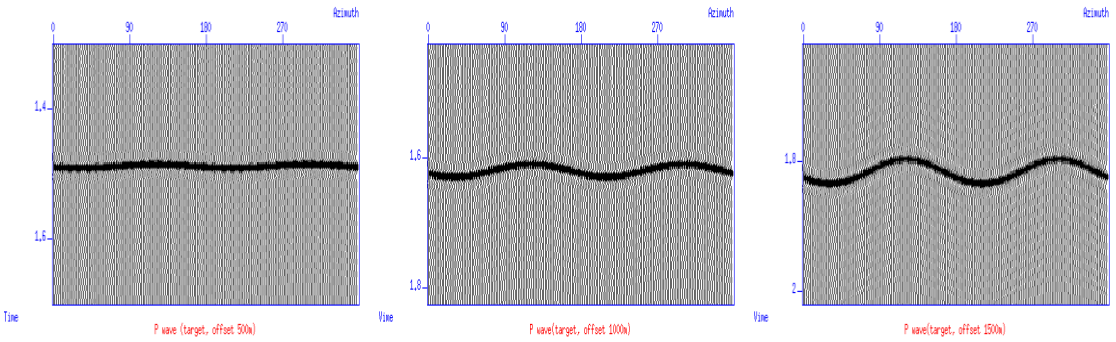

(a) (b) (c)

Figure 7- 2: P-wave azimuth gathers of dry model when the X/Z ratio is equal to 0.5 (a), 1.0 (b) and 1.5 (c), respectively.

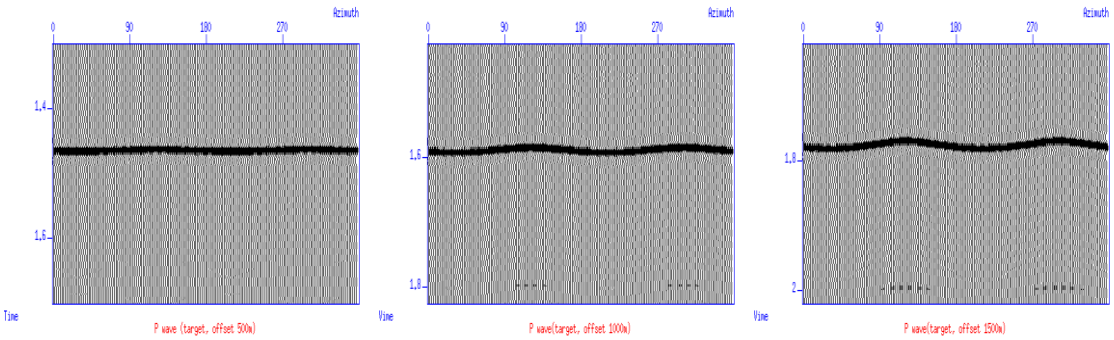

(a) (b) (c)

Figure 7- 3: P-wave azimuth gathers of water-saturated model when the X/Z ratio is equal to 0.5 (a), 1.0 (b) and 1.5 (c), respectively.

Parameter Δt_p is introduced here to represent the azimuthal moveout difference between the directions parallel and perpendicular to the fracture direction. Values of Δt_p for different X/Z ratios are calculated and listed in Table 7- 1. A quantitative understanding of the relationship between azimuthal variation and the X/Z ratio can be obtained from Table 7- 1. The azimuthal moveout difference in dry fractures increases from 6ms to 38ms when the X/Z ratio increases from 0.5 to 1.5. This parameter goes through a similar increasing trend in water-saturated fractures when the X/Z ratio increases. This observation and analysis suggests that data with large X/Z ratios are better for studying azimuthal variations of P-wave data. If the X/Z ratio is 0.5, the influence of azimuthal variations on P-wave data is very small.

X/Z	**0.5 (Dry)**	**1.0 (Dry)**	**1.5 (Dry)**	**0.5 (Water)**	**1.0 (Water)**	**1.5 (Water)**
Δt_p (ms)	6	20	38	2	8	12

Table 7- 1: P-wave moveout differences with different X/Z ratios

The similar parameter Δt_p is also calculated for different fracture densities and listed in Table 7- 2. The data shown in Table 7- 2 corresponds to the observations in the azimuth gathers. For both dry and water-saturated fractures, the size of the P-wave azimuthal variation decreases as the fracture density decreases. When the fracture density is small, the induced azimuthal variation has limited influence on the P-wave data. Moreover, the different responses for different fracture densities provide a potential way to deduce fracture density. However, when the fracture density is not

large, the P-wave azimuthal variation is not significant. It might be difficult to apply azimuthal analysis on P-wave data and inaccurate results might be obtained.

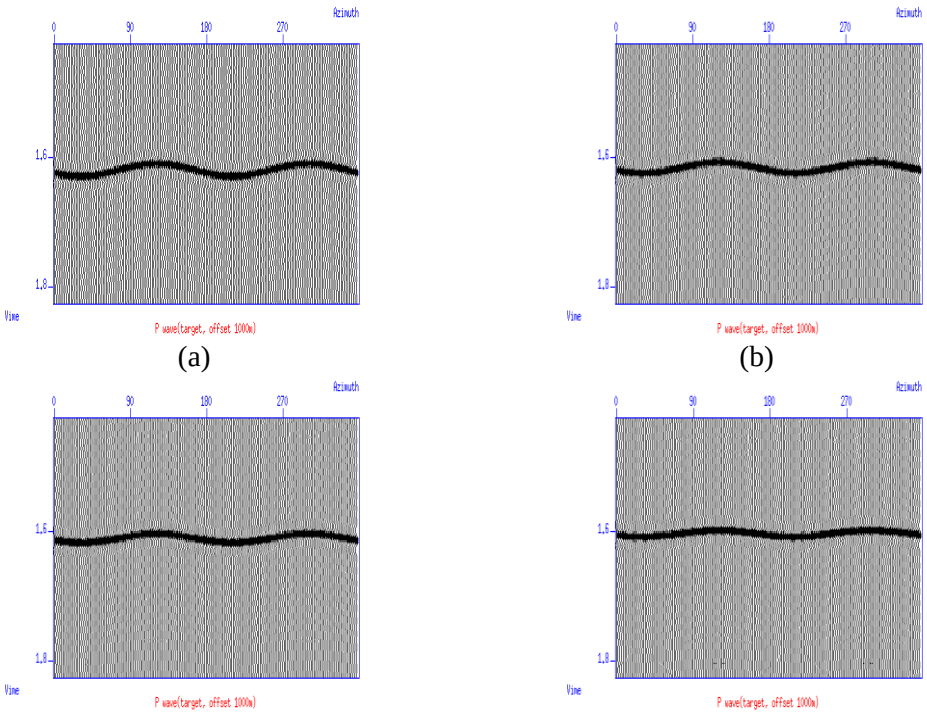

(a) (b)

(c) (d)

Figure 7- 4: P-wave azimuth gathers at offset 1000m of dry model with fracture density 0.1 (a), 0.08 (b), 0.06 (c) and 0.04 (d).

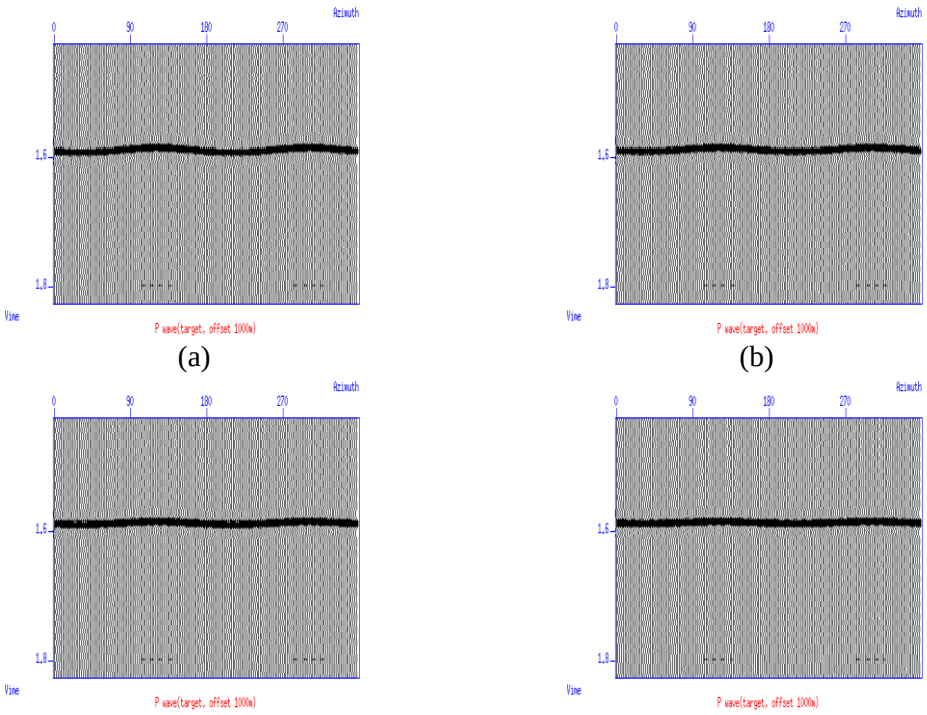

(a) (b)

(c) (d)

Figure 7- 5: P-wave azimuth gathers at offset 1000m of water-saturated model with fracture density 0.1 (a), 0.08 (b), 0.06 (c) and 0.04 (d).

The azimuthal velocity analysis is applied to the P-wave data, with decreasing fracture densities. The azimuth bin is still 30^o for this synthetic study and six corresponding velocity models are fitted to a velocity ellipse. The parameter β_p in the elliptical velocity equation is the fast direction of P-wave velocity, which represents the fracture direction. The parameter Δ_p is the measured P-wave velocity difference along directions parallel and perpendicular to the fracture direction, which can be related to fracture density. These two parameters are acquired for different fracture densities, and listed in Table 7- 3.

Fracture density	**0.10**	**0.08**	**0.06**	**0.04**
Δt_p (ms) (Dry)	20	18	14	10
Δt_p (ms) (Water)	8	6	4	2

Table 7- 2: P-wave azimuthal moveout differences with different fracture densities.

Fracture density	**0.10**	**0.08**	**0.06**	**0.04**
β_p (Dry)	116	116	124	126
Δ_p (m/s) (Dry)	47.49	34.32	27.56	20.7
β_p (Water)	112	114	106	106
Δ_p (m/s) (Water)	1.5	1.2	1.1	1.1

Table 7- 3: P-wave elliptical parameters with different fracture densities.

7.3 PS-converted wave splitting

PS-converted wave data is also influenced by shear-wave splitting in the presence of vertically aligned fractures. It is useful to project both fast P-SV1 and slow P-SV2 components into the radial and transverse components. Here the radial component is used to show the PS-converted wave splitting effect. Azimuth gathers of radial components at different offsets are displayed in Figure 7- 6 and Figure 7- 7. It can be seen that the converted-wave splitting is not as sensitive as azimuthal variations to the offset-to-depth ratio (X/Z ratio). As this ratio increases, time delays between the fast P-SV1 and slow P-SV2 component do not change significantly. This feature is true for both dry and water-saturated fractures. However, the time delay for water-saturated fractures is found to be slightly smaller than that for dry fractures.

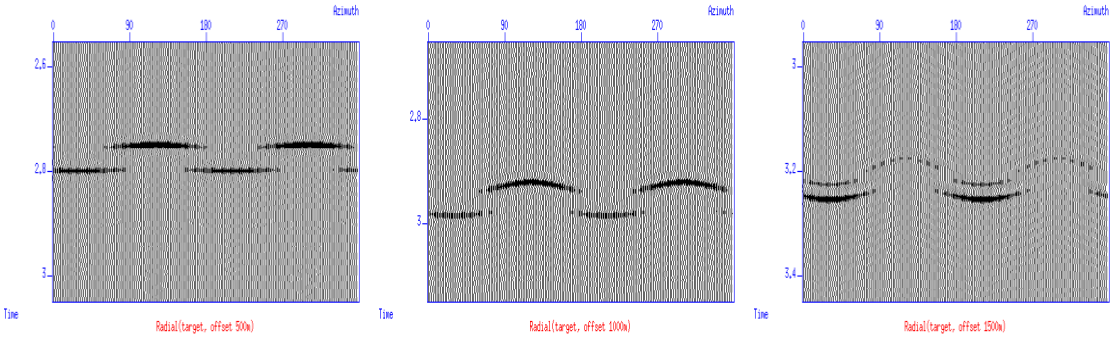

(a) (b) (c)

Figure 7- 6: Azimuth gathers of radial component of the dry model when the X/Z ratio is equal to 0.5 (a), 1.0 (b) and 1.5 (c), respectively.

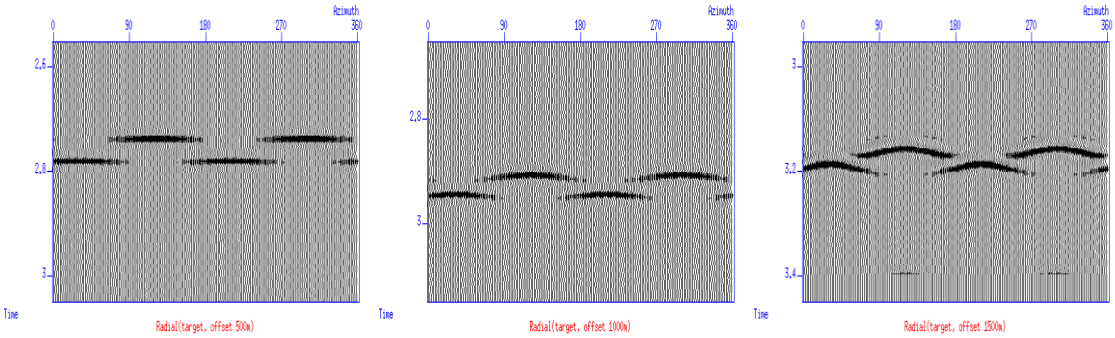

(a) (b) (c)

Figure 7- 7: Azimuth gathers of radial component of the water-saturated model when the X/Z ratio is equal to 0.5 (a), 1.0 (b) and 1.5 (c), respectively.

Assuming the fast P-SV1 and slow P-SV2 waves have similar waveforms with only a time delay, an objective function (equation (4-1)), which measures the similarity of the two waveforms, can be used to obtain the fracture direction and time delay value.

The scanning results of azimuth gathers at offset 1000m are displayed in Figure 7- 8. The horizontal axis is a range of time delay values. The vertical axis is a range of azimuth angles. For dry fractures, the scanned fracture direction is 120^{o} and the time delay is 50ms. For water-saturated fractures, the fracture direction is also 120^{o} but the time delay is 36ms.

This scanning process is also applied to data at offsets 500m and 1500m, which correspond to X/Z ratios 0.5 and 1.5, respectively. Splitting parameters are obtained and listed in Table 7- 4. β represents the fracture direction and ΔT represents the time delay between the fast P-SV1 and slow P-SV2 components. It can be seen that the splitting analysis is not sensitive to different X/Z ratios. For both dry and water-

saturated fractures, the same splitting parameters are obtained from data with different X/Z ratios.

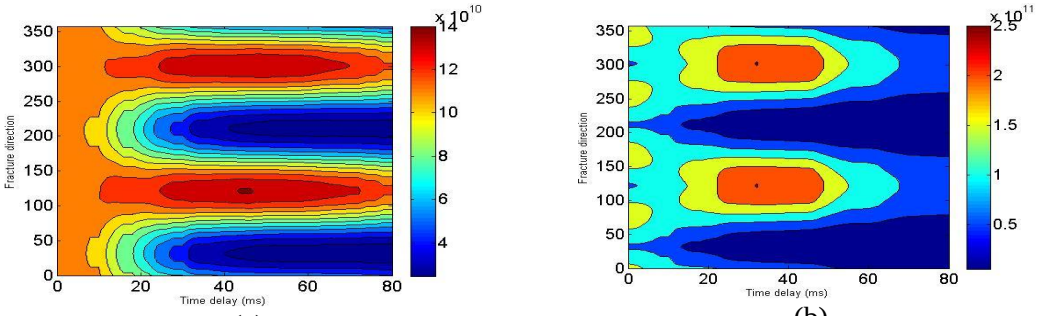

(a) (b)

Figure 7- 8: Scanning for fracture directions and time delays for dry (a) and water-saturated (b) fractures.

X/Z ratio	β (Dry)	ΔT(Dry) (ms)	β (Water)	ΔT (Water) (ms)
0.5	120	48	120	34
1	120	48	120	34
1.5	120	48	120	34

Table 7- 4: Splitting parameters with different X/Z ratios.

The influence of fracture density on PS-converted wave splitting is also studied. The fracture density sequentially decreases to 0.08, 0.06 and 0.04. Radial components with these different fracture densities are displayed in Figure 7- 9 and Figure 7- 10 to show the splitting effect. For both dry and water-saturated fractures, the fast P-SV1 and slow P-SV2 component become closer to each other as the fracture density decreases. When the fracture density is 0.04, P-SV1 and P-SV2 components on the radial component exhibit a sinusoidal feature. This special feature drives some data processors to directly analyse the azimuthal variation of the radial components, which is actually not accurate.

The individual splitting parameters are listed in Table 7- 5. It is true that the time delay decreases as the fracture density decreases, which is in accordance with observations of the radial components. It can be found that the splitting analysis is still a robust algorithm when the fracture density is small. The obtained fracture directions are all the same as the true fracture direction 120^{o}. Moreover, the time delays for dry fractures are larger than the time delays for water-saturated fractures. However, this difference is also not sufficient to discriminate dry fractures from water-saturated fractures.

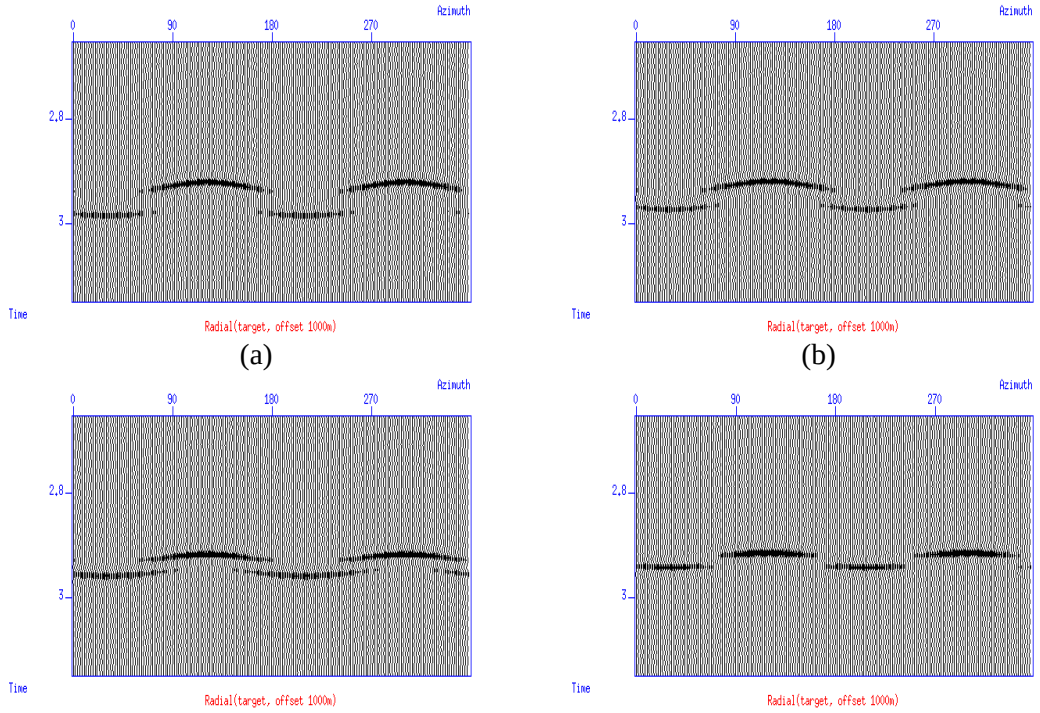

Figure 7- 9: Azimuth gathers of radial component of the dry model at offset 1000m with fracture density 0.1 (a), 0.08 (b), 0.06 (c) and 0.04 (d).

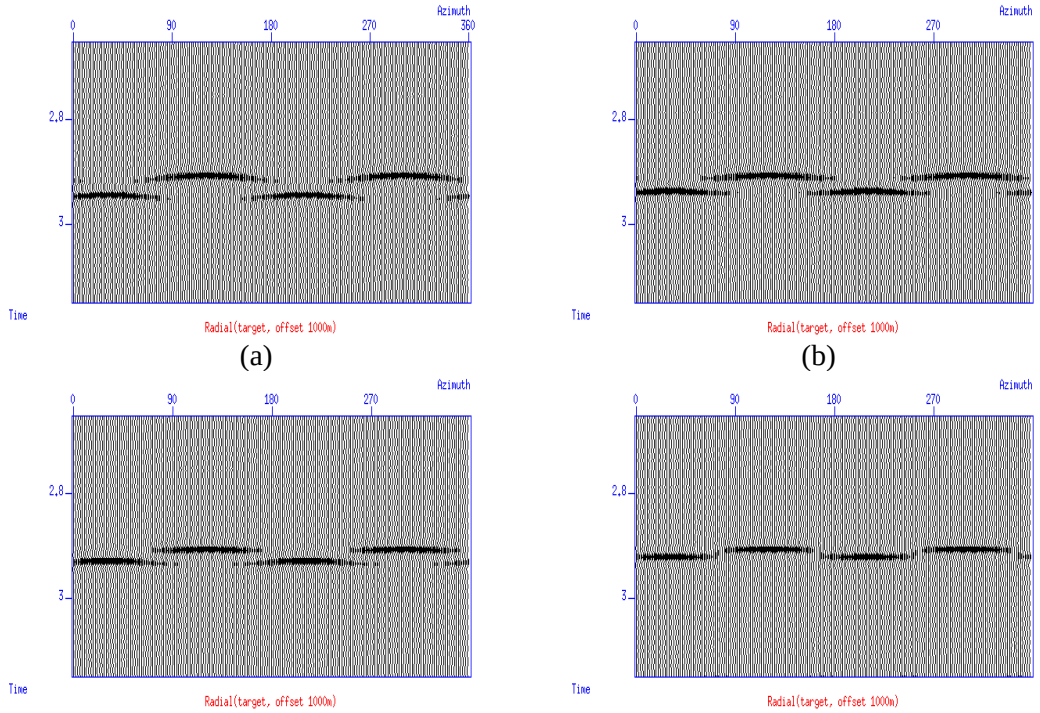

Figure 7- 10: Azimuth gathers of radial component of the water-saturated model at offset 1000m with fracture density 0.1 (a), 0.08 (b), 0.06 (c) and 0.04 (d).

Fracture density	β (Dry)	ΔT(Dry)(ms)	β (Water)	ΔT (Water) (ms)
0.1	120	48	120	34
0.08	120	38	120	26
0.06	120	28	120	22
0.04	120	20	120	16

Table 7- 5: Splitting parameters with different fracture densities.

7.4 PS-converted wave azimuthal variation

The azimuthal variation of PS-converted waves is complicated by the splitting effect. By horizontal rotation, the individual P-SV1 and P-SV2 components are obtained. Azimuth gathers of the P-SV1 component at different offsets are displayed in Figure 7- 11 and Figure 7- 12.

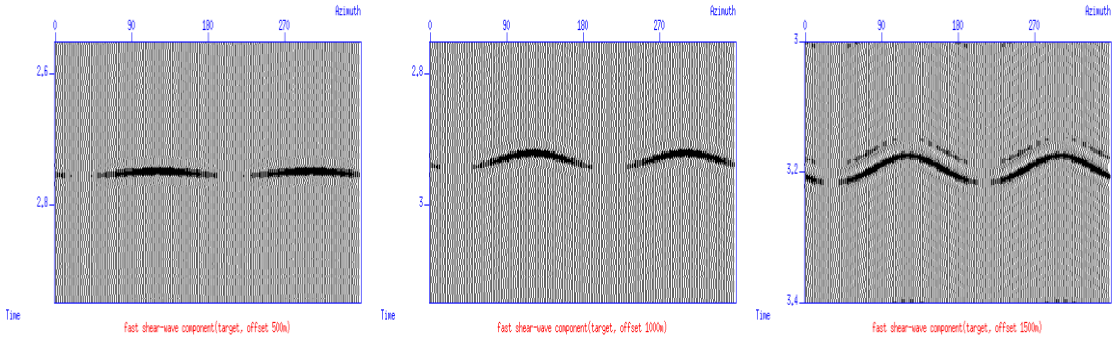

(a) (b) (c)

Figure 7- 11: Azimuth gathers of P-SV1 component of the dry model when the X/Z ratio is equal to 0.5 (a), 1.0 (b) and 1.5 (c), respectively.

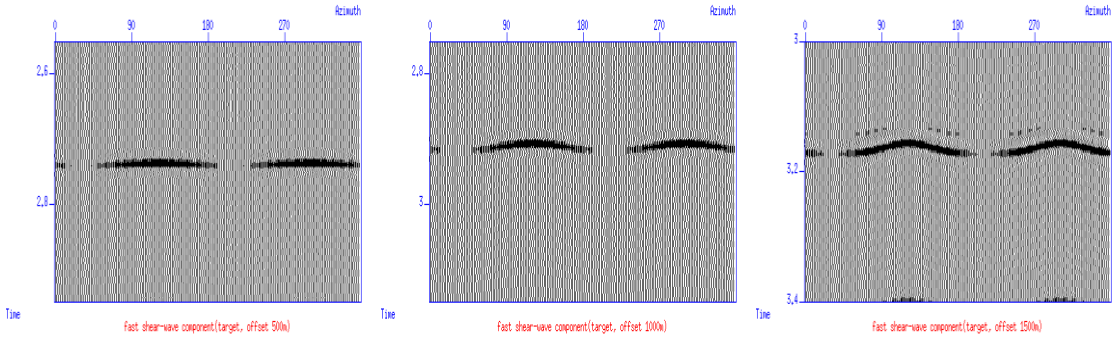

(a) (b) (c)

Figure 7- 12: Azimuth gathers of P-SV1 component of the water-saturated model when the X/Z ratio is equal to 0.5 (a), 1.0 (b) and 1.5 (c), respectively.

It can be seen that the P-SV1 component is affected by different X/Z ratios for both dry and water-saturated fractures. As the X/Z ratio increases, the azimuthal variations

of the P-SV1 components become more significant. Therefore, data with medium or large X/Z ratios is essential for applying azimuthal analysis to the P-SV1 component. It is more important for water-saturated fractures, because the azimuthal variation induced by water-saturated fractures is only significant for large X/Z ratios. Inaccurate azimuthal parameters can be obtained if data with large X/Z ratios is not available for water-saturated fractures.

Azimuth gathers of the P-SV2 component for different X/Z ratios are displayed in Figure 7- 13 and Figure 7- 14. For the P-SV2 component, a similar relationship between azimuthal variations and X/Z ratios can be found. In both dry and water-saturated fractures, the azimuthal variation of P-SV2 components becomes stronger as the X/Z ratio increases. Therefore data with large X/Z ratios are equally important for the azimuthal analysis of P-SV2 components, especially for water-saturated fractures.

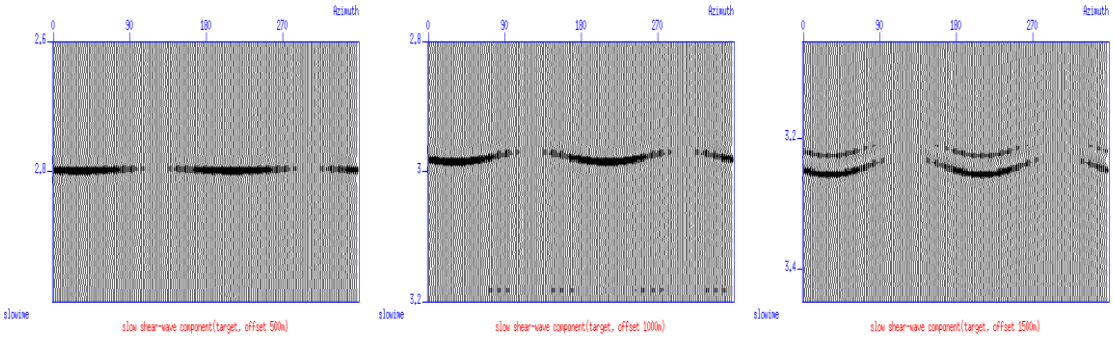

(a) (b) (c)

Figure 7- 13: Azimuth gathers of P-SV2 component of the dry model when the X/Z ratio is equal to 0.5 (a), 1.0 (b) and 1.5 (c), respectively.

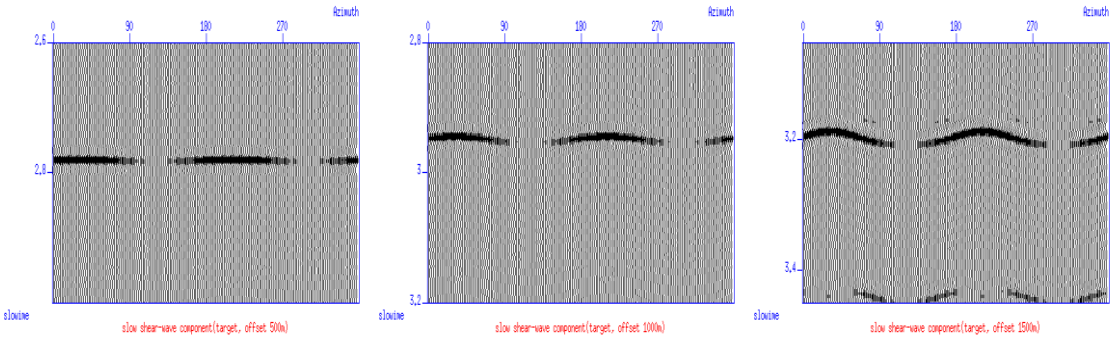

(a) (b) (c)

Figure 7- 14: Azimuth gathers of P-SV2 component of the water-saturated model when the X/Z ratio is equal to 0.5 (a), 1.0 (b) and 1.5 (c), respectively.

The above discussion is based on observations of azimuth gathers of P-SV1 and P-SV2 components. The azimuthal moveout differences of P-SV1 and P-SV2 components are also calculated and listed in Table 7- 6 to quantitatively show the azimuthal variation against different X/Z ratios. The moveout difference is calculated between directions parallel and perpendicular to the fracture direction. For both dry and water-saturated fractures, the moveout difference increases as the X/Z ratio increases. This increasing trend can be found on both P-SV1 and P-SV2 components. For dry fractures, the moveout differences of the P-SV1 component are larger than those of the P-SV2 component. This indicates the P-SV1 component suffers more significant azimuthal variations. In water-saturated fractures, moveout differences are positive for the P-SV1 component but negative for the P-SV2 component. This contrast provides a potential way to distinguish dry fractures from water-saturated fractures, which will be discussed later in this chapter. Moreover, in water-saturated fractures, the absolute value of Δt_{psv1} is generally smaller than the absolute values Δt_{psv2}. This implies that the P-SV2 component shows more significant azimuthal variations than the P-SV1 component for water-saturated fractures.

X/Z	0.5 (Dry)	1.0 (Dry)	1.5 (Dry)	0.5 (Water)	1.0 (Water)	1.5 (Water)
Δt_{psv1} (ms)	6	24	42	4	10	16
Δt_{psv2} (ms)	4	16	28	-4	-14	-20

Table 7- 6: PS-converted wave azimuthal moveout differences with different X/Z ratios

Then similar observation and analysis was carried out on fracture models with different fracture densities. Azimuth gathers of the P-SV1 component with different fracture densities are displayed in Figure 7- 15 and Figure 7- 16. The fast direction for the P-SV1 component with different fracture densities is the fracture direction 120^o. As the fracture density decreases, the size of the P-SV1 wave azimuthal variation also decreases. This decreasing trend is true for both dry and water-saturated fractures. Specifically, when the fracture density is 0.04, the azimuthal variation induced by water-saturated fractures is very small. The target event is nearly flat and azimuthal analysis might not be possible.

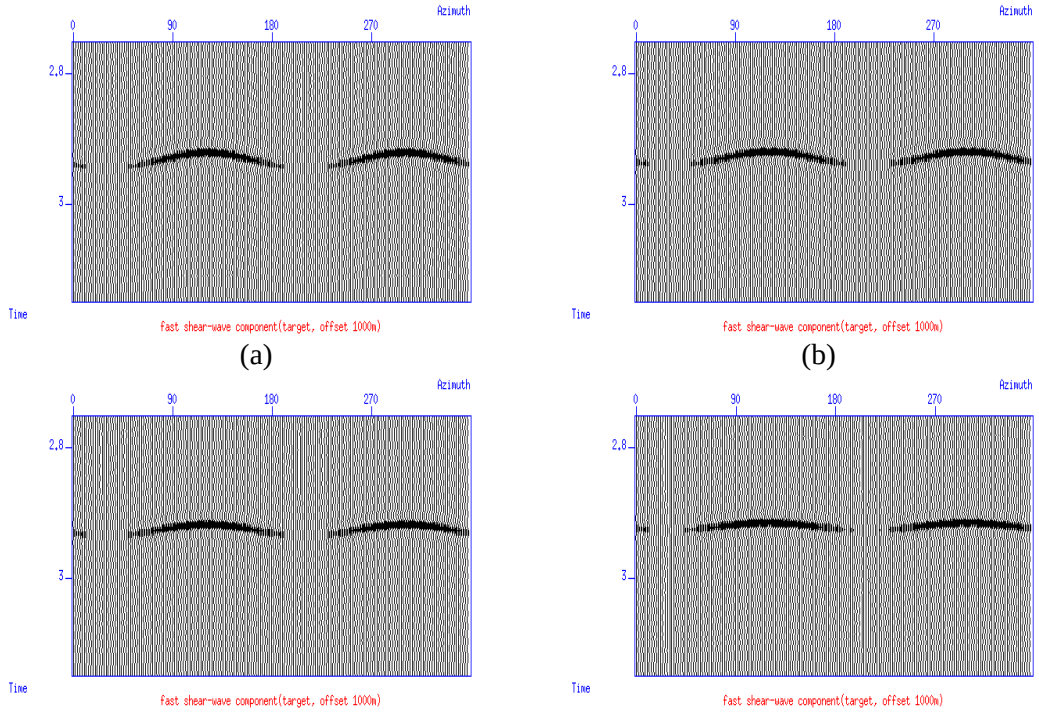

Figure 7- 15: Azimuth gathers of P-SV1 component of the dry model at offset 1000m with fracture density 0.1 (a), 0.08 (b), 0.06 (c) and 0.04 (d).

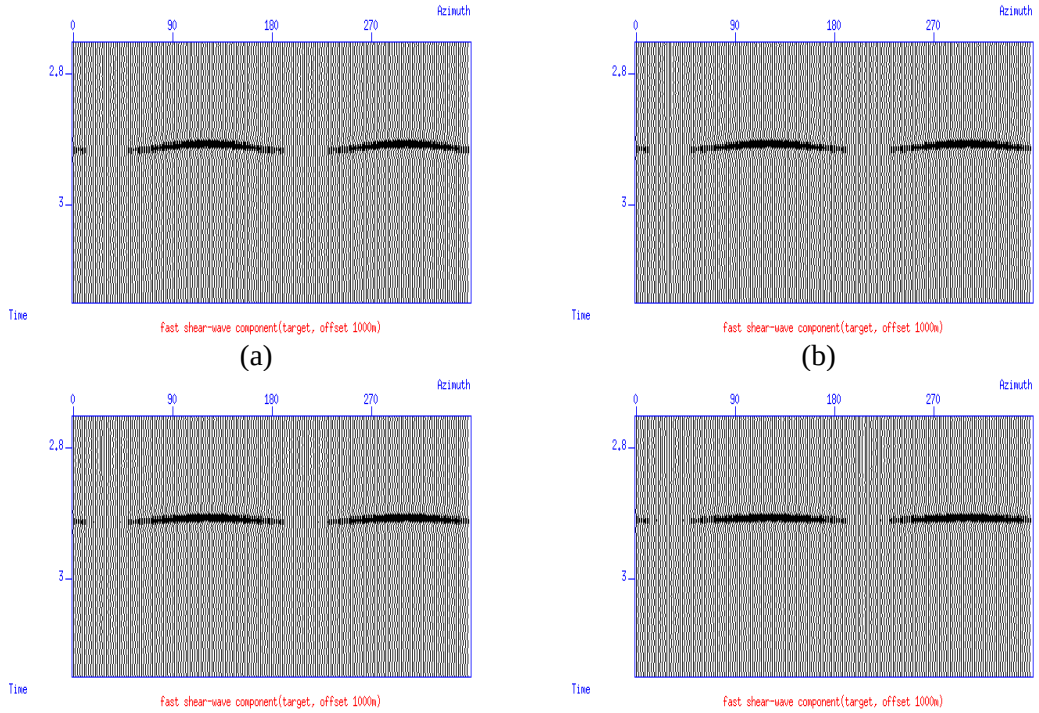

Figure 7- 16: Azimuth gathers of P-SV1 component of the water-saturated model at offset 1000m with fracture density 0.1 (a), 0.08 (b), 0.06 (c) and 0.04 (d).

Azimuth gathers of P-SV2 component with different fracture densities are shown in Figure 7- 17 and Figure 7- 18. The P-SV2 component shows a similar relationship between azimuthal variation and fracture density. As the fracture density decreases, the azimuthal variation of the P-SV2 components becomes small. Similarly, when the fracture density is 0.04 in water-saturated fractures, the influence of azimuthal anisotropy on the P-SV2 components is so small that it can be neglected for simplification.

Azimuthal moveout differences for PS-converted waves between the directions parallel and perpendicular to the fracture directions are similarly calculated and listed in Table 7- 7. For both P-SV1 and P-SV2 components, the azimuthal moveout differences between the two orthogonal directions decrease as the fracture density decreases. For dry fractures, the Δt_{psv1} is always larger than Δt_{psv2}. For water-saturated fractures, Δt_{psv1} and Δt_{psv2} have different signs for all fracture densities. When the fracture density is lower than 0.01, the absolute value of Δt_{psv1} is equal to the absolute value of Δt_{psv2}, implying both P-SV1 and P-SV2 components are influenced by azimuthal variations of the same magnitude.

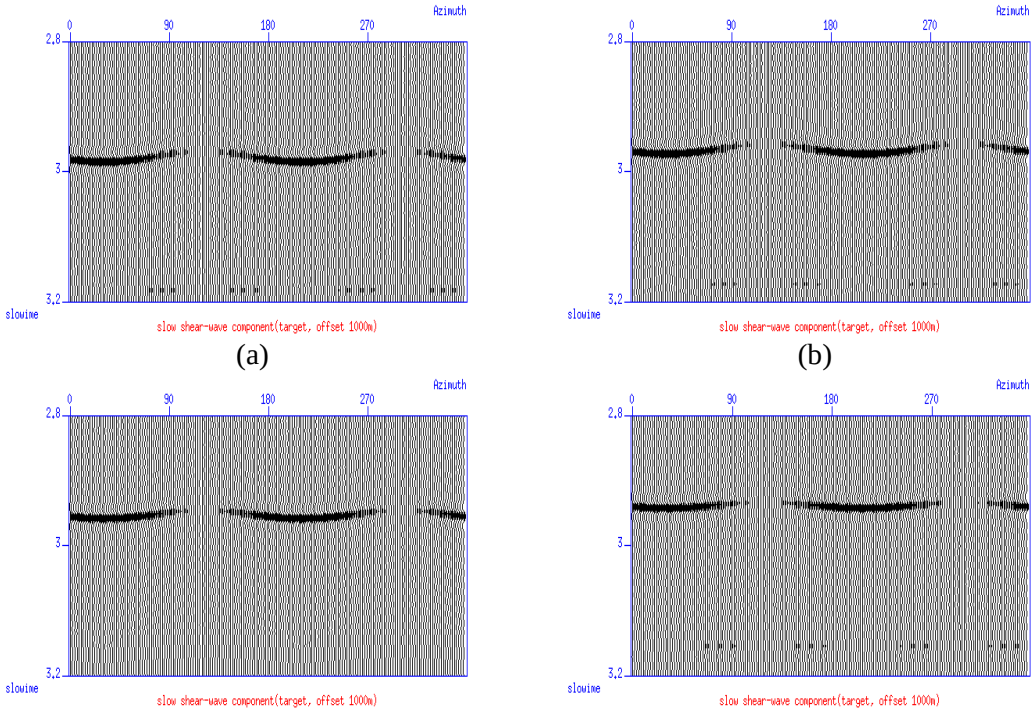

Figure 7- 17: Azimuth gathers of P-SV2 component of the dry model at offset 1000m with fracture density 0.1 (a), 0.08 (b), 0.06 (c) and 0.04 (d).

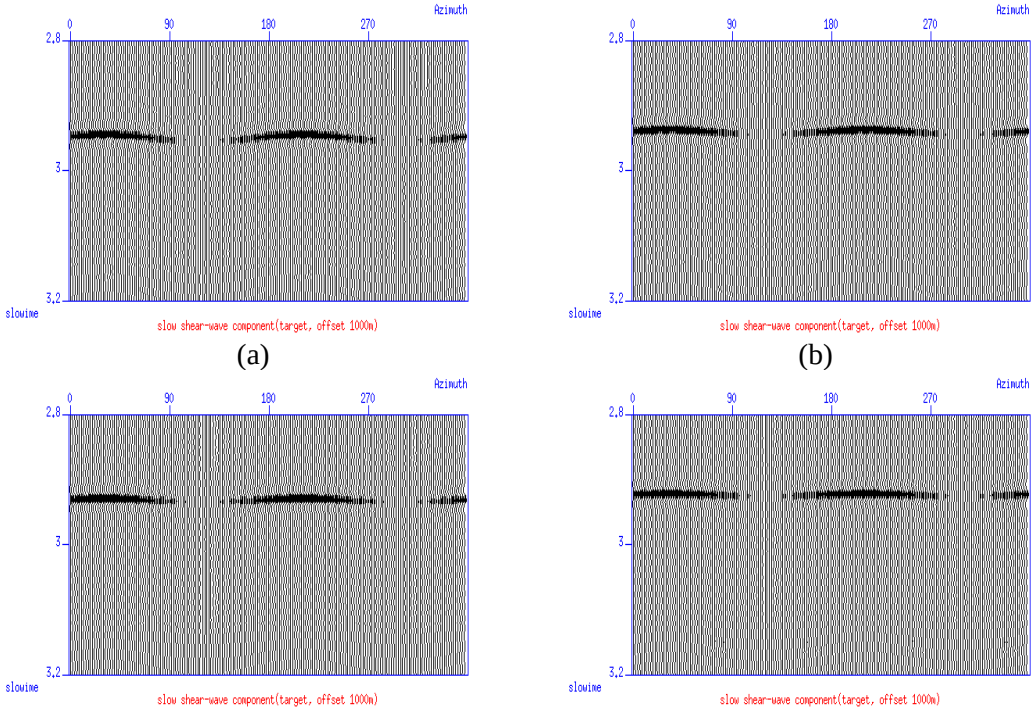

Figure 7- 18: Azimuth gathers of P-SV2 component of the water-saturated model at offset 1000m with fracture density 0.1 (a), 0.08 (b), 0.06 (c) and 0.04 (d).

Then azimuthal velocity analysis was applied to the individual P-SV1 and P-SV2 components to obtain the elliptical velocity parameters. Those parameters result from the same least-square fitting method and are listed in Table 7- 8. As the fracture density decreases, the magnitudes of the azimuthal variations induced by both dry and water-saturated fractures also decrease. Therefore, smaller velocity perturbations are obtained for fractures with smaller fracture densities. Those small azimuthal variations bring more errors, which cause fast directions to deviate from the fracture direction. The azimuthal analysis of P-SV1 and P-SV2 components is also influenced by small values of azimuthal variations. Inaccurate azimuthal parameters might be obtained if small fracture densities are dealt with. However, in water-saturated fractures with different fracture densities, the velocity perturbations of P-SV2 components are always negative, which differs from the velocity perturbations of P-SV1 components. This feature is good for discrimination between dry and water-saturated fractures.

Fracture density	0.01	0.08	0.06	0.04
Δt_{psv1} (ms) (Dry)	24	22	18	12
Δt_{psv2} (ms) (Dry)	16	15	14	10
Δt_{psv1} (ms) (Water)	10	8	6	4
Δt_{psv2} (ms) (Water)	-14	-8	-6	-4

Table 7- 7: PS-converted wave moveout differences with different fracture densities.

Fracture density	0.1	0.08	0.06	0.04
β_{psv1} (Dry)	118	122	114	112
Δ_{psv1} (m/s) (Dry)	21.8	18.1	16.9	13.53
β_{psv2} (Dry)	124	124	128	130
Δ_{psv2} (m/s) (Dry)	13.99	11.52	9.88	7.4
β_{psv1} (Water)	122	114	130	110
Δ_{psv1} (m/s) (Water)	10.29	8.51	6.45	4.73
β_{psv2} (Water)	124	126	112	110
Δ_{psv2} (m/s) (Water)	-13.1	-11.39	-9.2	-8.04

Table 7- 8: PS-converted wave elliptical parameters with different fracture densities.

7.5 Discussions of estimating fracture directions and densities

P-wave azimuthal variation, PS-converted wave splitting and PS-converted wave azimuthal variation are all discussed in this chapter. They can be used to detect fractures and obtain fracture properties, including fracture orientations and densities. Velocity perturbations of either the P-wave or PS-converted waves (Δ_p, Δ_{psv1} and Δ_{psv2}) can be used to invert for fracture densities. Different magnitudes of azimuthal variations result in different azimuthal moveout differences (Δt_p, Δt_{psv1} and Δt_{psv2}). Time delays (ΔT) are also directly related to fracture densities. These parameters are listed in Table 7- 9 to Table 7- 12 to make comparisons.

In Table 7- 9, which refers to dry fractures, Δt_{psv1} is larger than Δt_p and Δt_{psv2} for different fracture densities. Moreover, Δt_{psv1} is close to ΔT for different fracture densities. It can also be seen that Δt_p is larger than Δt_{psv2} and both Δt_p and Δt_{psv2} are smaller than ΔT. This implies that the time delays are more significant than the azimuthal variations of P-waves and P-SV2 waves. Moreover, ΔT is found to be more sensitive to different fracture densities, which is better for estimating fracture densities than azimuthal analysis. When the fracture density is 0.04, Δt_p is equal to

ΔT . The magnitude of the splitting effect is similar to the magnitude of P-SV1 azimuthal variation. It suggests that azimuthal analysis of the P-SV1 component can also be useful for detecting fractures. Compared to splitting analysis, analysis of the P-wave and P-SV2 wave is affected by slightly smaller magnitudes of azimuthal variations. Therefore, the use of P-waves and P-SV2 waves is not as efficient as for P-SV1 waves.

For water-saturated fractures, the contrast between azimuthal moveout differences and time delays is much clearer. Regardless of the negative signs of Δt_{psv2}, ΔT is always much larger than Δt_p, Δt_{psv1} and Δt_{psv2}. Azimuthal moveout differences are all subject to small values for water-saturated fractures. This makes the time delay obtained from splitting parameters a better representation of fracture properties.

From Table 7- 11 and Table 7- 12, all the fitted fast directions for dry and water-saturated fractures deviate from the fracture direction. This deviation is more significant when smaller fracture densities are considered. Moreover, the deviation is also more significant for water-saturated fractures. However, the polarisation direction of the fast P-SV1 components, obtained from the splitting analysis, turns out to be a robust parameter. It is equal to the fracture direction and is not influenced by different fracture densities. Different fracture saturations also have no impact on this parameter.

In conclusion, P-wave azimuthal variations are sensitive to different offset-to-depth ratios. They are also influenced by different fluid saturations and different fracture densities. PS-converted wave splitting is not sensitive to offset-to-depth ratio and fluid saturation. However, it is directly linked to fracture density. Azimuthal variations of P-SV1 and P-SV2 components are redundant information. They can be used to improve the robustness of results from the variation of P-waves. Fracture orientations obtained from the splitting analysis are more stable than the orientations from elliptical fitting. However, P-wave data is more widely available and P-wave data processing is easier than PS-converted wave data processing.

Fracture density	**0.1**	**0.08**	**0.06**	**0.04**
Δt_p (ms) (Dry)	38	34	26	20
Δt_{psv1} (ms) (Dry)	42	38	28	22
Δt_{psv2} (ms) (Dry)	28	26	22	14
ΔT (ms) (Dry)	48	38	30	20

Table 7- 9: Comparisons between moveout differences and time delays in dry fractures

Fracture density	**0.1**	**0.08**	**0.06**	**0.04**
Δt_p (ms) (Water)	12	10	8	4
Δt_{psv1} (ms) (Water)	16	12	10	8
Δt_{psv2} (ms) (Water)	-20	-18	-14	-10
ΔT (ms) (Water)	34	26	22	16

Table 7- 10: Comparisons between moveout differences and time delays in water-saturated fractures

Fracture density	**0.1**	**0.08**	**0.06**	**0.04**
β_p (Dry)	116	116	124	126
β_{psv1} (Dry)	118	122	114	112
β_{psv2} (Dry)	124	124	128	130
β_{split} (Dry)	120	120	120	120

Table 7- 11: Comparisons of fracture directions obtained between azimuthal analysis and splitting analysis in dry fracture

Fracture density	**0.1**	**0.08**	**0.06**	**0.04**
β_p (Water)	112	114	106	106
β_{psv1} (Water)	122	114	130	110
β_{psv2} (Water)	124	126	110	110
β_{split} (Water)	120	120	120	120

Table 7- 12: Comparisons of fracture directions obtained between azimuthal analysis and splitting analysis in water-saturated fractures

7.6 Effects of dry and water-saturated fractures

Distinguishing between dry and fluid-saturated fractures using seismic data is difficult but has attracted a lot of interest from many research communities. It is very important to distinguish between oil- and gas-filled fractures in practical applications. As we know, dry (gas-filled) fractures will enhance the anisotropic response, compared with fluid-filled fractures. This information alone is not sufficient for

discriminating fluid saturations. Given a set of seismic measurements, can we distinguish between oil and gas saturation, and how? The following discussion focuses on this specific problem.

From Chapter 2, the Thomsen's parameters for HTI media can be defined as:

$$\varepsilon = \frac{C_{33} - C_{11}}{2C_{11}} \tag{7- 1}$$

$$\delta = \frac{(c_{13} + c_{55})^2 - (c_{11} - c_{55})^2}{2c_{11}(c_{11} - c_{55})} \tag{7- 2}$$

$$\gamma = \frac{C_{44} - C_{55}}{2C_{55}} \tag{7- 3}$$

Those Thomsen's parameters for HTI media can be used to study velocities and polarisations as a function of azimuth angle.

Assuming Hudson theory for penny-shaped cracks, effective stiffness tensors can be defined accordingly. These definitions have been introduced in Chapter 2:

$$C_{ij}^{eff} = C_{ij}^{0} + C_{ij}^{1} \tag{7- 4}$$

where C_{ij}^{0} are isotropic background stiffness tensors. C_{ij}^{1} are first-order corrections, which can be defined as:

$$C_{11}^{1} = -\frac{\lambda^2}{\mu} e U_3 \tag{7- 5}$$

$$C_{13}^{1} = -\frac{\lambda(\lambda + 2\mu)}{\mu} e U_3 \tag{7- 6}$$

$$C_{33}^{1} = -\frac{(\lambda + 2\mu)^2}{\mu} e U_3 \tag{7- 7}$$

$$C_{44}^{1} = -\mu e U_1 \tag{7- 8}$$

$$C_{66}^{1} = 0 \tag{7- 9}$$

where e is the crack density U_1 and U_3 are terms which depend on crack conditions. Their definitions and formulas for different fracture inclusions can be found in Appendix B.

Those equations provide a theoretical basis for studying azimuthal variations induced by different types of fracture. Thomsen parameters can also be calculated for different saturations.

Here a numerical test is performed to show the possible range of those parameters. A HTI layer is created by incorporating a set of vertical fractures into an isotropic background. The P-wave velocity in the isotropic background is in the range between 1 km/s and 4 km/s. The velocity ratio R_0 is between 1.5 and 3. The density of the HTI layer varies from 1.5 g/cm^3 to 4.5 g/cm^3. The fracture density is between 0.01 and 0.1. Both dry fractures and water-saturated fractures are considered in this study. Using Equations above, the effective stiffness tensors can be calculated. Then the Thomsen's parameters can be obtained by using Equation (7- 1) to (7- 3).

The distribution of parameter δ is shown in Figure 7- 19. Results for dry and water-saturated fractures are indicated by black and red colours, respectively. It can be seen that δ is negative for both dry and water-saturated fractures. However, the absolute values of δ in dry fractures are larger than those in water-saturated fractures. The parameter γ is also studied in Figure 7- 20. Parameter γ is also in the negative range and is not sensitive to the type of fluid saturation. This result proves that shear-wave splitting is not sensitive to fluid saturation. The results for parameter ε in dry and water-saturated fractures are shown in Figure 7- 21. The parameter ε is also negative for HTI media. Moreover, the absolute value of ε in dry fractures is larger than that in water-saturated fractures.

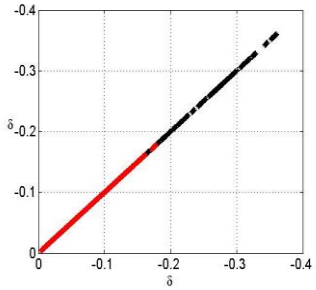

Figure 7- 19: Possible ranges of parameter δ in HTI media. (Black: dry fractures; Red: water-saturated fractures)

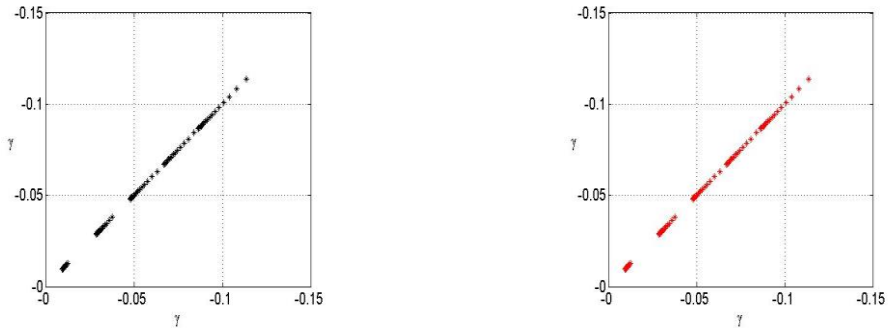

(a) (b)

Figure 7- 20: Possible ranges of parameter γ in HTI media. (a): dry fractures; (b): water-saturated fractures.

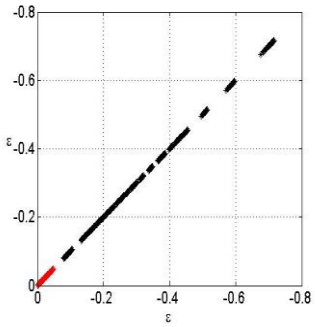

Figure 7- 21: Possible ranges of parameter ε in HTI media. (Black: dry fractures; Red: water-saturated fractures)

Parameters δ and γ both have a direct impact on the azimuthal variations of P-waves and shear-waves. From Chapter 5, the velocity differences between the directions parallel and perpendicular to the fracture direction are introduced to describe the azimuthal variations. We have:

$$\Delta_p^2 = -\delta v_{p0}^2 \tag{7- 10}$$

$$\Delta_{s1}^2 = -\gamma v_{s10}^2 \tag{7- 11}$$

$$\Delta_{s2}^2 = -v_{p0}^2(\varepsilon - \delta) \tag{7- 12}$$

Parameters δ and γ are both negative in dry and water-saturated fractures. Therefore both Δ_p^2 and Δ_{s1}^2 are positive, which implies that the P-wave and fast S1-wave are affected by a similar azimuthal variation in dry and water-saturated fractures. The azimuthal variation of the slow S2-wave is controlled by the term $(\varepsilon - \delta)$. A cross-

plot of δ and ε is illustrated in Figure 7- 22. The horizontal axis represents parameter ε and the vertical axis represents the parameter δ. For water-saturated fractures, the term $(\varepsilon-\delta)$ is generally positive. In this case, the azimuthal variation of the slow S2-waves is different from the azimuthal variations of the P-waves and fast S1-waves. For dry fractures, the term $(\varepsilon-\delta)$ is generally negative, which indicates a similar azimuthal variation for the P-waves and fast S1-waves.

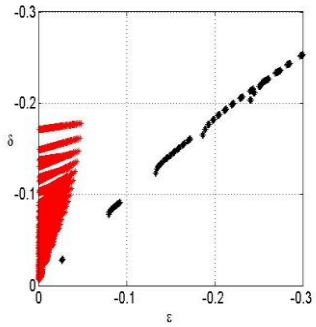

Figure 7- 22: Cross-plot of δ and ε in HTI media. (Black: dry fractures; Red: water-saturated fractures)

The velocity differences for fast P-SV1 and slow P-SV2 components are also defined in Chapter 5:

$$\Delta^2_{psv_1} = \left(\frac{1}{1+R_0}\Delta^2_p + \frac{R_0}{1+R_0}\Delta^2_{s_1}\right) \tag{7- 13}$$

$$\Delta^2_{psv_2} = \left(\frac{1}{1+R_0}\Delta^2_p + \frac{R_0}{1+R_0}\Delta^2_{s_2}\right) \tag{7- 14}$$

Substituting equations (7- 10), (7- 11) and (7- 12) into (7- 13) and (7- 14):

$$\Delta^2_{psv_1} = -\frac{1}{1+R_0}(\delta v^2_{p0} + R_0\gamma v^2_{S_1 0}) \tag{7- 15}$$

$$\Delta^2_{psv_2} = -\frac{v^2_{p0}}{1+R_0}[\delta - R_0(\delta-\varepsilon)] \tag{7- 16}$$

Considering that both δ and γ are negative, $\Delta^2_{psv_1}$ is positive in both dry and water-saturated fractures. But as | δ | becomes larger in dry fractures, $\Delta^2_{psv_1}$ is also larger in dry fractures than in water-saturated fractures. $\Delta^2_{psv_2}$ is more complicated and its sign

is determined by the term $[\delta - R_0(\delta - \varepsilon)]$. The cross-plot of δ and $R_0(\delta - \varepsilon)$ is shown in Figure 7- 23. The horizontal axis represents parameter $R_0(\delta - \varepsilon)$ and the vertical axis represents the parameter δ. For dry fractures, $R_0(\delta - \varepsilon)$ is generally positive and δ is negative. Therefore $[\delta - R_0(\delta - \varepsilon)]$ is negative and $\Delta^2_{psv_2}$ is positive. In this case, the azimuthal variation of the P-SV2 component is similar to that of the P-SV2 component. However for water-saturated fractures, both δ and $R_0(\delta - \varepsilon)$ are negative. The absolute value $|R_0(\delta - \varepsilon)|$ is generally larger than the absolute value | δ |, which results in the positive $[\delta - R_0(\delta - \varepsilon)]$. In this case, $\Delta^2_{psv_2}$ is negative, which is different from $\Delta^2_{psv_1}$.

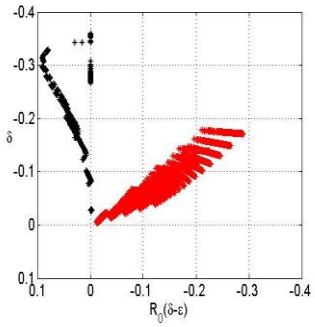

Figure 7- 23: Cross-plot of δ and $R_0(\delta - \varepsilon)$ in HTI media. (Black: dry fractures; Red: water-saturated fractures)

7.7 Synthetic study

Synthetic data including both dry and water-saturated fractures are introduced above. Some typical azimuth gathers will be displayed again to facilitate comparisons between dry and water-saturated fractures.

P-wave azimuth gathers at 1000m offset in both dry and water-saturated fractures are displayed in Figure 7- 24. It can be seen that the P-wave azimuthal variation is stronger in dry fractures than water-saturated fractures. This phenomenon is in accordance with the distribution of parameter δ, which is shown in Figure 7- 19. | δ | is smaller in water-saturated fractures than in dry fractures, which results in different magnitudes of azimuthal variations. Azimuthal moveout differences for both dry and water-saturated fractures are provided in Table 7- 1. The moveout differences for

water-saturated fractures are always smaller than their counterparts for dry fractures. Specifically, the largest moveout difference for water-saturated fractures is only 12ms, which is much smaller than the largest moveout difference for dry fractures.

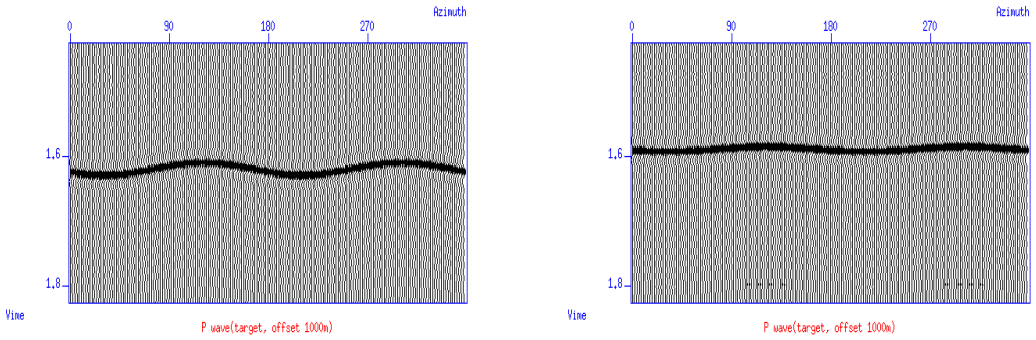

(a) (b)

Figure 7- 24: P-wave azimuth gathers at 1000m offset in (a) dry and (b) water-saturated fractures.

Radial components are selected again to show the PS-converted wave splitting. Azimuth gathers of radial components at offset 1000m of both dry and water-saturated fractures are shown in Figure 7- 25. Time delays between P-SV1 and P-SV2 components can be clearly observed. The detailed comparison of time delays between dry and water-saturated fractures is provided in Table 7- 4. The time delay is 48ms and 34ms in dry and water-saturated fractures, respectively. The time delay in dry fracture is larger than that in water-saturated fractures. Considering that shear-waves are not sensitive to fluid saturations, this difference is attributed to different P-wave velocities in dry and water-saturated fractures. The time delay obtained from splitting analysis is not sufficient to distinguish dry fractures from water-saturated fractures.

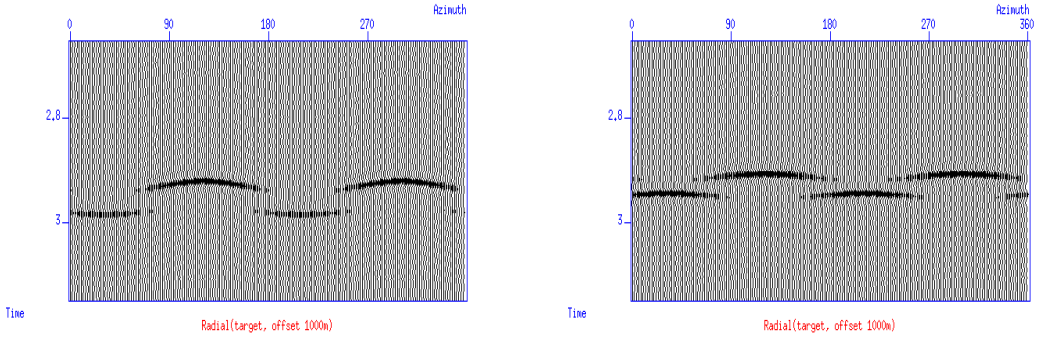

(a) (b)

Figure 7- 25: Azimuth gathers of radial components at 1000m offset in (a) dry and (b) water-saturated fractures.

PS-converted wave azimuthal responses for dry and water-saturated fractures are also different. This comparison should be individually applied to the P-SV1 and P-SV2 components. Azimuth gathers of P-SV1 and P-SV2 components are shown in Figure 7- 26 and Figure 7- 27, respectively. The P-SV1 azimuthal variations in dry and water-saturated fractures are similar. However, the azimuthal variation is stronger for dry fractures than for the water-saturated fractures. This is also attributed to the fact that $|\delta|$ is larger for dry fractures than for water-saturated fractures, which is discussed above. Similarly, the azimuthal variation of the P-SV1 components is not sufficient to allow discrimination between dry and water-saturated fractures. The P-SV2 responses for dry and water-saturated fractures are completely different. In dry fractures, the azimuthal variation of the P-SV2 component is similar to that of the P-SV1 component but with a lower magnitude. Their fast directions are both parallel to the fracture direction.

However for water-saturated fractures, the fast direction of the P-SV2 component is the direction perpendicular to the fracture direction, which is different from the fast direction of the P-SV1 component. This phenomenon is quantitatively illustrated in Table 7- 6. In water-saturated fractures, azimuthal moveout differences between directions parallel and perpendicular to the fracture direction are positive for P-SV1 components but negative for P-SV2 components. This contrast is in accordance with previous theoretical analysis. The azimuthal variation of P-SV2 components is determined by $\Delta^2_{psv_2}$. It has been found that $\Delta^2_{psv_2}$ is generally positive in dry fractures but negative in water-saturated fractures. Therefore, the azimuth variations of P-SV2 components for dry and water-saturated fractures are different.

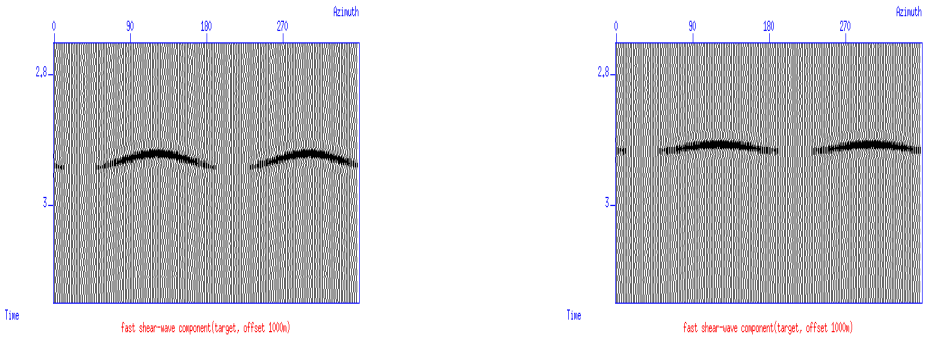

(a) (b)

Figure 7- 26: Azimuth gathers of P-SV1 components at offset 1000m in (a) dry and (b) water-saturated fractures.

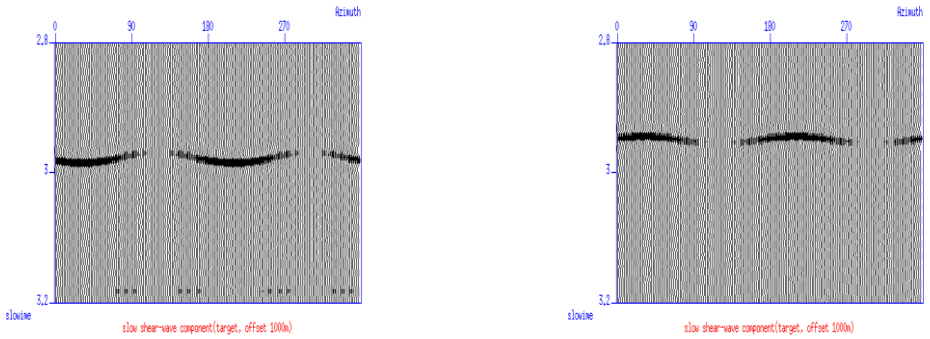

(a) (b)

Figure 7- 27: Azimuth gathers of P-SV2 components at offset 1000m in (a) dry and (b) water-saturated fractures.

It can be deduced that the azimuthal variations of P-SV1 and P-SV2 components show a similar trend for dry fractures. In this case, the P-SV1 and P-SV2 components are in phase. But in water-saturated fractures, the azimuthal variations of P-SV1 and P-SV2 components show an opposite trend, indicating that the P-SV1 and P-SV2 components are out of phase. This feature can be used to distinguish oil-filled and gas-filled fractures, which is important for exploration and production in hydrocarbon reservoirs. Moreover, the comparison of azimuthal trends between P-SV1 and P-SV2 components opens new applications for wide azimuth PS-converted wave data.

7.8 Effects of multiple fractures

Models with two or more sets of fractures are also of great interest in seismic exploration. Differently orientated fracture networks are often found in the characterisation of fractured reservoirs. If multiple sets of fractures are contained in one layer, the final effect is a combination of all effects from each individual set of fractures. The individual effect is calculated in the coordinate system with the 3-axis normal to the fracture plane and then transformed back into the stiffness tensor coordinate system.

For three sets of fractures with fracture densities *e1*, *e2* and *e3*, and fracture normals aligned along the 1-, 2- and 3-axes, respectively, the overall correction is based on Hudson theory and can be described as (Hudson, 1980, 1981):

$$C_{11}^{1(all)} = C_{33}^{1}(e1) + C_{11}^{1}(e2) + C_{11}^{1}(e3) \qquad (7\text{- }17)$$

$$C_{12}^{1(all)} = C_{13}^{1}(e1) + C_{13}^{1}(e2) + C_{12}^{1}(e3) \quad (7\text{- }18)$$

$$C_{13}^{1(all)} = C_{13}^{1}(e1) + C_{12}^{1}(e2) + C_{13}^{1}(e3) \quad (7\text{- }19)$$

$$C_{22}^{1(all)} = C_{11}^{1}(e1) + C_{33}^{1}(e2) + C_{11}^{1}(e3) \quad (7\text{- }20)$$

$$C_{23}^{1(all)} = C_{12}^{1}(e1) + C_{13}^{1}(e2) + C_{13}^{1}(e3) \quad (7\text{- }21)$$

$$C_{33}^{1(all)} = C_{11}^{1}(e1) + C_{11}^{1}(e2) + C_{33}^{1}(e3) \quad (7\text{- }22)$$

$$C_{44}^{1(all)} = C_{44}^{1}(e2) + C_{44}^{1}(e3) \quad (7\text{- }23)$$

$$C_{55}^{1(all)} = C_{44}^{1}(e1) + C_{44}^{1}(e3) \quad (7\text{- }24)$$

$$C_{66}^{1(all)} = C_{44}^{1}(e1) + C_{44}^{1}(e2) \quad (7\text{- }25)$$

$C_{ij}^{1}(e)$ is separately calculated from the individual fracture densities (*e1*, *e2* or *e3*). The final correction $C_{ij}^{1(all)}$ is a linear combination of different $C_{ij}^{1}(e)$.

Two or more sets of fractures in a medium generally give rise to orthorhombic anisotropy or anisotropy with lower symmetries. Specific parameterisations and more complicated processing techniques may be required to describe the anisotropic effect, which is beyond the scope of this thesis.

It is important to examine the case of a model with multiple fractured layers. Assuming each fractured layer only contains a single set of vertical fractures, the final anisotropic effects are combinations of the effects of the different HTI layers. The azimuthal variations induced by the lower HTI layers are then influenced by the upper HTI layers. If the HTI layers have different orientations, the azimuth variation of the lower HTI layers may suffer severe interference. Direct analysis can fail to estimate the true azimuthal parameters, causing errors in fracture characterisation.

A model with two HTI layers was examined to show the overall effect. The second and third layers are both HTI layers but have orthogonal fracture orientations. The azimuthal gathers for radial and transverse components are shown in Figure 7- 28. It can be seen that the azimuthal variation induced by the second layer is shown on both radial and transverse components, and is similar to the azimuthal variation shown in previous synthetic studies. Therefore a similar separation and azimuthal analysis can also be applied to estimate the azimuthal parameters of the second layer.

However, the third layer is more complicated. The fracture direction in the second layer is orthogonal to the fracture direction in the third layer. Due to the interference caused by the second layer, it is difficult to find clear azimuthal variations in the third event in both radial and transverse components. In this case, a layer-stripping method is necessary to recover the azimuthal variations induced by lower HTI layers.

However, the third layer is more complicated. The fracture direction in the second layer is orthogonal to the fracture direction in the third layer. Due to the interference of the second layer, it is difficult to find clear azimuthal variations on the third event on both radial and transverse components. In this case, a layer-stripping method is necessary to recover azimuthal variations induced by lower HTI layers.

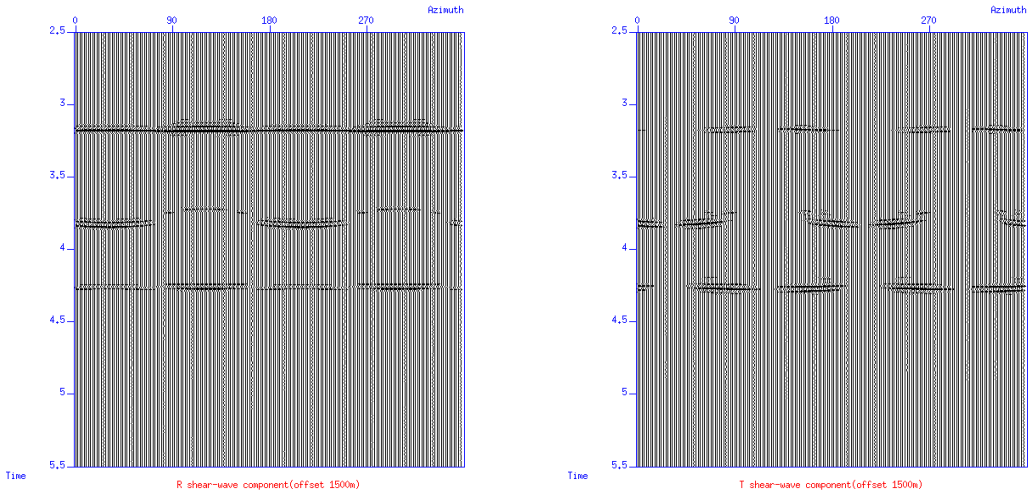

(a) (b)

Figure 7- 28: Azimuth gathers of radial (a) and transverse (b) components of the model containing two HTI layers.

7.9 Layer-stripping procedures

The layer-stripping method normally follows a top-down procedure so that a given layer is modelled after all upper layers have been inverted. The layer-stripping algorithm has been widely used in P-wave data processing to either improve imaging or obtain internal seismic attributes. It has also been applied to study the PS-converted wave splitting effect. However, how the layer-stripping method is performed to compensate for PS-converted azimuthal variations has not been well studied. In this chapter, I show how a specific work flow was built to apply the layer-stripping method to the azimuthal analysis of PS-converted wave seismic data.

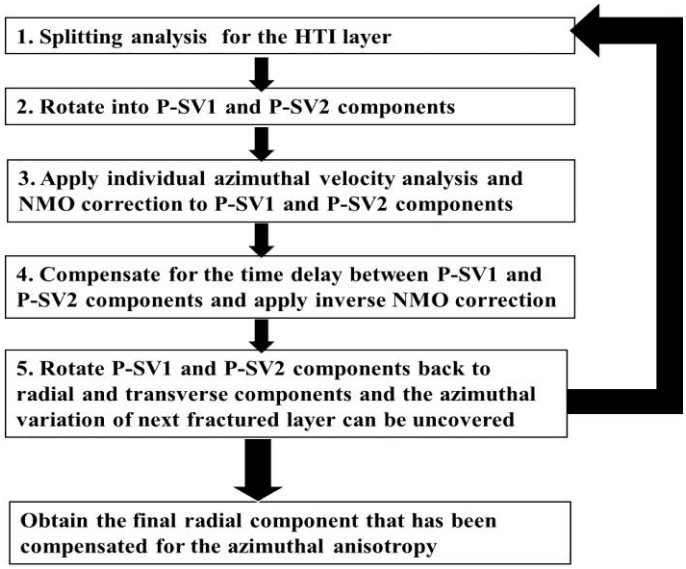

Figure 7- 29: Layer-stripping workflow for compensation for azimuthal variations induced by multiple HTI layers.

The workflow is illustrated in Figure 7- 29. The layer-stripping procedure starts from the reflector associated with the first HTI layer. Splitting analysis is applied to the time window in which only the target event is considered. The fracture direction and time delay between P-SV1 and P-SV2 components can be obtained. Using the acquired fracture direction, the original radial and transverse components can be rotated into fast P-SV1 and slow P-SV2 components. With separated P-SV1 and P-SV2 components available, azimuthal analysis can be applied to both the P-SV1 and P-SV2 components. Then elliptical velocity models of the P-SV1 and P-SV2 components can be fitted, which can then be applied in a NMO correction to compensate for the azimuthal variation induced by the upper HTI layer. Then the time delay is compensated for by applying a time shift to the slow P-SV2 component. The azimuthal variation and splitting effect induced by the first HTI layer have been compensated for. Then a conventional inverse NMO correction is applied to the updated P-SV1 and P-SV2 components. Then they can be rotated back into radial and transverse components. Since the effect of the first HTI layer has been removed, the pure azimuthal variation and splitting effect of the next HTI layer can be uncovered. Similar analysis and compensation are applied to the next HTI layer and the true azimuthal variations and splitting effect of this HTI layer can be studied. Finally, after azimuthal variations and splitting effects of all HTI layers have been successfully compensated for, the final radial component can be obtained. This radial

component has a better imaging quality, which is beneficial for subsequent data processing and interpretation.

I performed a synthetic study to illustrate the layer-stripping procedure introduced above. The model containing multiple HTI layers and its parameters are shown in Figure 7- 30. Four layers are incorporated in this model. The first layer is an isotropic layer. The second and third layers are both HTI layers. They are both generated by inserting dry fractures into an isotropic medium, based on Hudson theory. The fracture orientation in the upper HTI layer is 120 ° in the azimuthal plane and the fracture density is 0.1. The fracture orientation of the lower HTI layer is 30 ° and its fracture density is also 0.1. The fracture directions in the two HTI layers are orthogonal to each other. The acquisition geometry is similar to the geometry used in the previous synthetic study. The offset range is from 100m to 2000m. The azimuthal coverage for the synthetic dataset is from 0 °to 360 °with a 2 °interval.

Azimuth gathers of the radial and transverse components at 1500m offset are displayed in Figure 7- 28. To allow a comparison, the vertical component is also shown in Figure 7- 31. The azimuthal variation for the upper HTI layer is similar to the azimuthal behaviour shown in the previous synthetic study involving a single set of vertical fractures. Both P-SV1 and P-SV2 waves are projected into the radial and transverse components, which are more complicated than the vertical component. Because the HTI layer contains dry fractures, the azimuthal variations of the P-SV1 and P-SV2 components are in phase, and similar to the azimuthal variation of the P-wave data. However, the third reflector, which is associated with the lower HTI layer, is more complicated. The third reflector should exhibit similar azimuthal variations but with different fast directions. However, in both radial and transverse components, it is difficult to find azimuthal variations. It seems that the azimuthal variation produced by the lower HTI layer is cancelled by the azimuthal variation produced by the upper HTI layer. The splitting effect is also influenced by the upper HTI layer. The azimuthal variation and splitting effect both suffer interference due to propagation through the upper HTI layer. P-wave data suffers similar interference. The third reflector is nearly flat, which indicates no azimuthal variations. Therefore, the assumption of a single set of vertical fractures can cause the wrong azimuthal

parameters to be deduced for lower fractured layers. This proves the necessity of applying a layer-stripping algorithm in the context of multiple HTI layers.

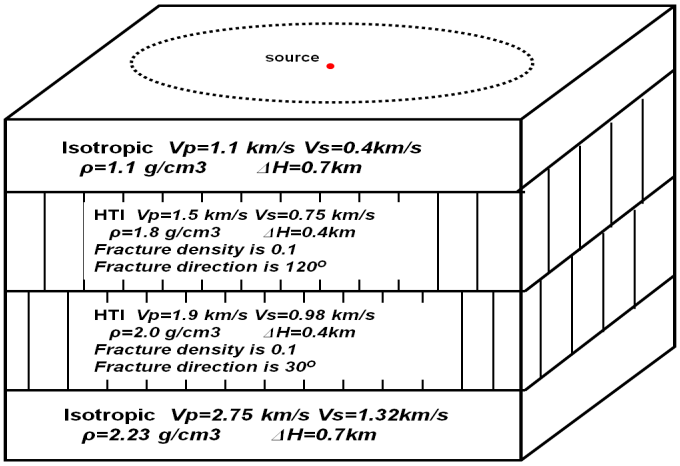

Figure 7- 30: Parameters of the model containing two HTI layers. The fracture direction is 120 °in the upper HTI layer and is 30 °in the lower HTI layer.

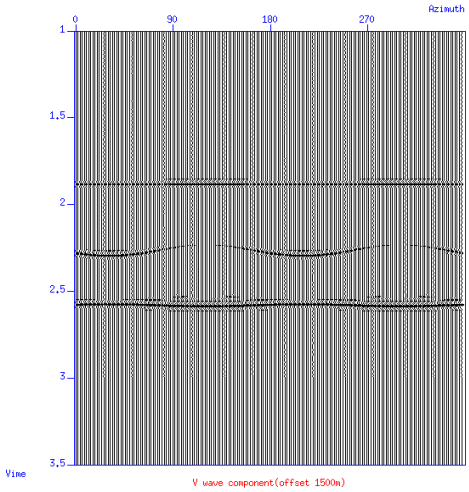

Figure 7- 31: Azimuth gathers at offset 1500m of vertical component

The layer-stripping procedure now focuses on the second reflector, which is associated with the upper HTI layer. By applying similar splitting analysis, the fracture direction is obtained as 120 ° and the time delay is 68ms. According to this fracture direction, the radial and transverse components were rotated into P-SV1 and P-SV2 components. Azimuth gathers of the P-SV1 and P-SV2 components are shown in Figure 7- 32. As discussed before, the azimuthal variations shown for this reflector are only caused by the upper HTI layer. Both P-SV1 and P-SV2 components show in-phase azimuthal variations. Azimuthal velocity analysis is

similarly applied to both the P-SV1 and P-SV2 components. The azimuth bin size in this study is also 30°. By picking velocity models for different azimuth bins and fitting them into velocity ellipses, the NMO correction can be improved. The P-SV1 and P-SV2 components after azimuthal NMO correction are shown in Figure 7- 33 and Figure 7- 34, respectively. Similar improvements can be found for both the P-SV1 and P-SV2 components. By applying velocity ellipses, the azimuthal variations can be compensated for. Events are well-aligned and better focused, which is beneficial for imaging quality. Then a time shift is applied to the slow P-SV2 component to compensate for the time delay between the P-SV1 and P-SV2 components. Both the azimuthal variation and time delay caused by the upper HTI layer have been compensated for.

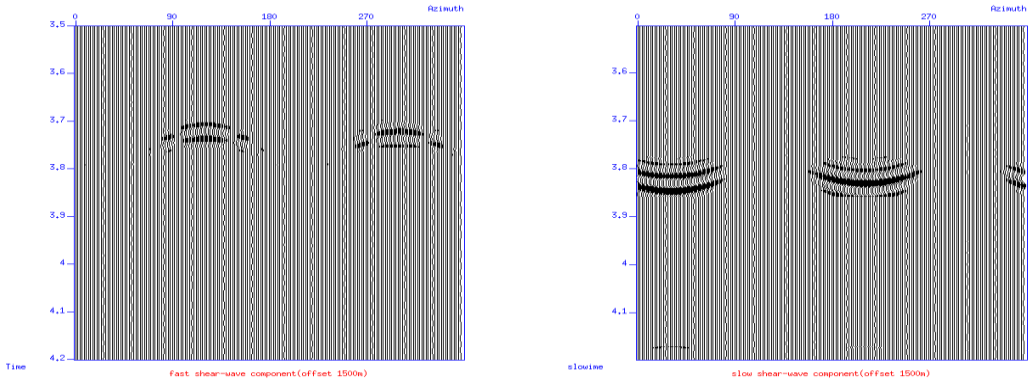

(a) (b)

Figure 7- 32: Azimuth gathers of (a) P-SV1 and (b) P-SV2 components for the second reflector at offset 1500m.

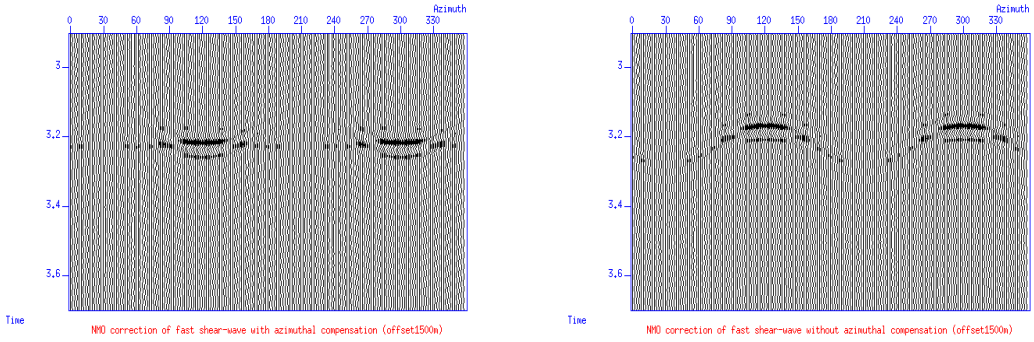

(a) (b)

Figure 7- 33: NMO correction results for the upper HTI layer at offset 1500m for the P-SV1 component. (a): with the velocity ellipse; (b): without the velocity ellipse

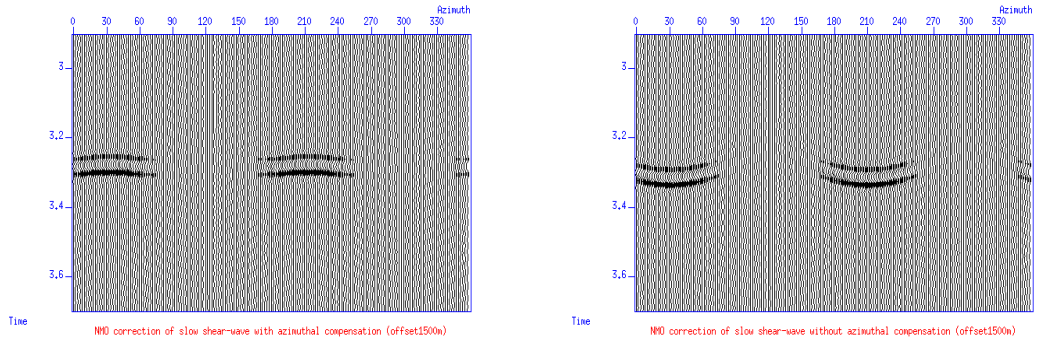

(a) (b)

Figure 7- 34: NMO correction results for the upper HTI layer at offset 1500m for the P-SV2 component. (a): with the velocity ellipse; (b): without the velocity ellipse

In order to study the lower HTI layer, a conventional inverse NMO correction is applied to both P-SV1 and P-SV2 components. Because the azimuthal variation induced by the upper HTI layer has been compensated for, a constant velocity model using the base velocity is applied in the inverse NMO correction. In other words, the data is regarded as having no azimuth variations, therefore a single velocity is enough for all azimuth angles in the inverse NMO correction.

After the inverse NMO correction, the P-SV1 and P-SV2 components are rotated back into radial and transverse components. The following analysis will focus on the third reflector, which is associated with the lower HTI layer. Azimuth gathers of updated radial and transverse components at offset 1500m are shown in Figure 7- 35.

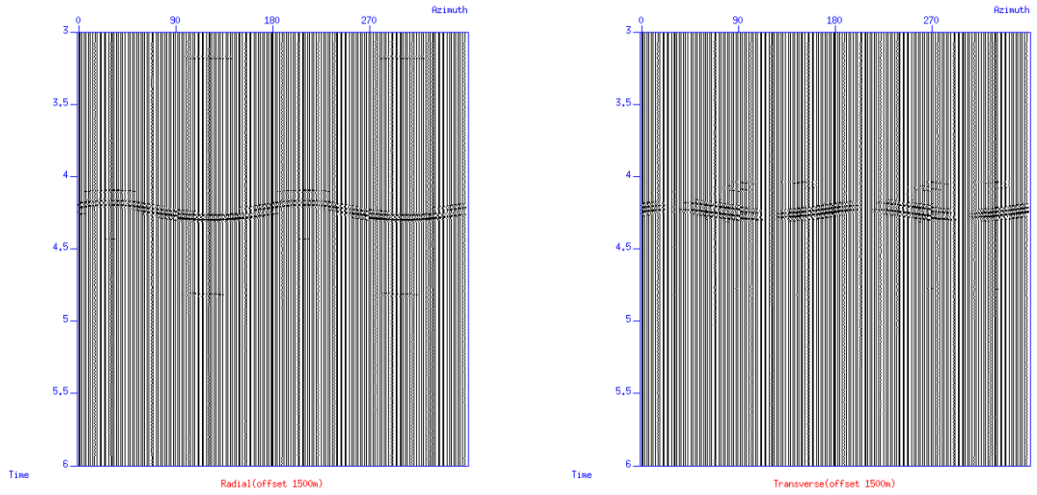

(a) (b)

Figure 7- 35: Azimuth gathers of (a) radial and (b) transverse components for the third event at offset 1500m.

Updated radial and transverse components are much clearer than the original radial and transverse components because the influence of the upper HTI layer has been removed. Similar azimuthal behaviour can be found on both radial and transverse components. The fast P-SV1 and slow P-SV2 components are both projected into radial and transverse components. The fast direction of the lower HTI observed from either the radial or transverse component is different from the fast direction of the upper HTI layer. This is in accordance with the fact that the fracture directions in the upper and lower HTI layers are orthogonal to each other.

Then the same splitting analysis is applied to the third reflector. The fracture direction is 30 ° and the time delay is 56ms. Radial and transverse components are rotated into fast P-SV1 and slow P-SV2 components based on the same horizontal rotation. The azimuth gathers of the P-SV1 and P-SV2 components at offset 1500m are shown in Figure 7- 36. Azimuth variations of P-SV1 and P-SV2 components induced by the lower HTI layer are successfully exhibited. The fast directions of both P-SV1 and P-SV2 components correspond to the fracture direction. This in-phase feature is in accordance with the fact that HTI in the lower layer is also caused by dry fractures.

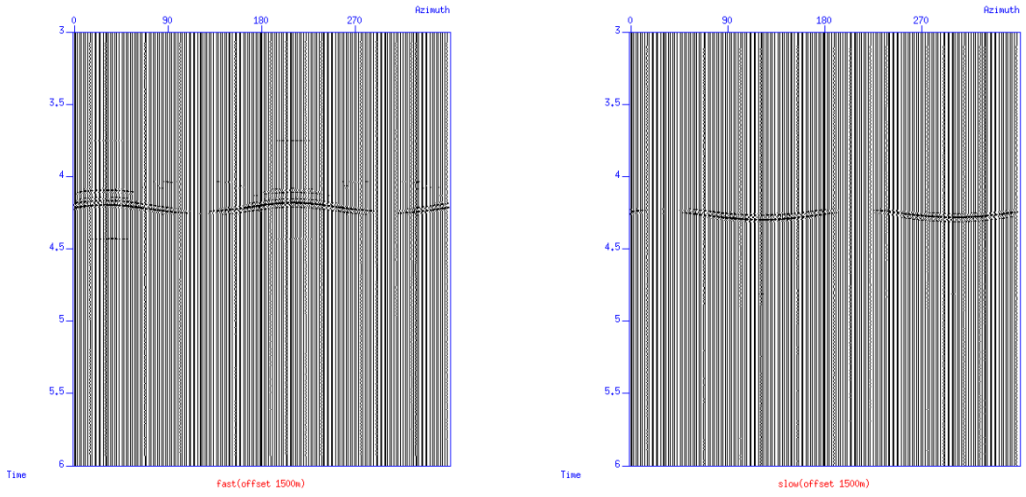

(a) (b)

Figure 7- 36: Azimuth gathers of (a) P-SV1 and (b) P-SV2 components for the third reflector at offset 1500m.

Azimuthal velocity analysis and NMO corrections are applied to the P-SV1 and P-SV2 components associated with the lower HTI layer. The azimuth bin size is still

30 °. Using velocity analysis of six different azimuth bins and the least-square fitting method, elliptical velocity models for the third reflector are obtained. Those velocity ellipses of P-SV1 and P-SV2 components are similarly applied to the NMO correction. NMO corrected results for the P-SV1 and P-SV2 components are shown in Figure 7- 37 and Figure 7- 38, respectively.

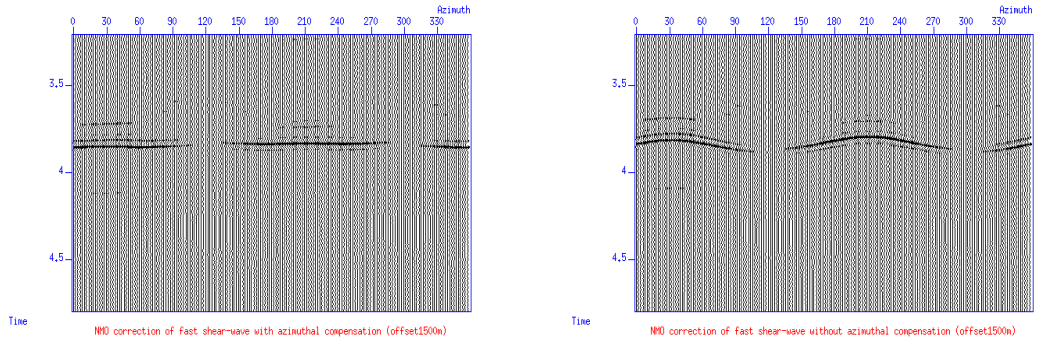

(a) (b)

Figure 7- 37: NMO correction results for the lower HTI layer at offset 1500m for the P-SV1 component. (a): with the velocity ellipse; (b): without the velocity ellipse

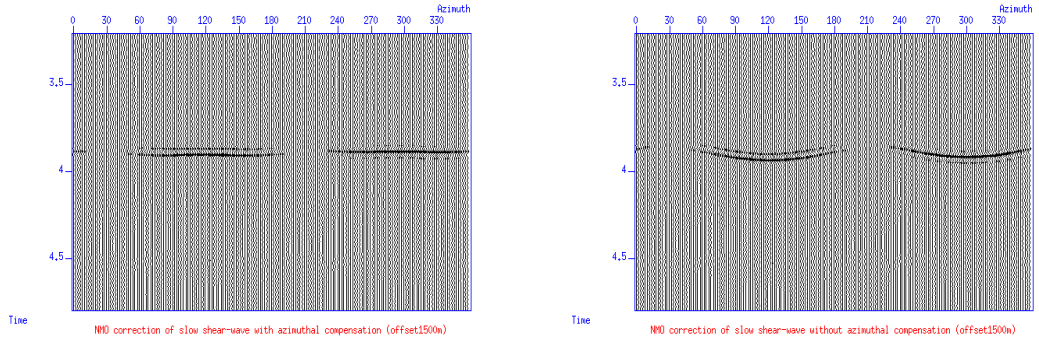

(a) (b)

Figure 7- 38: NMO correction results for the lower HTI layer at offset 1500m for the P-SV2 component. (a): with the velocity ellipse; (b): without the velocity ellipse

Following the same procedure as before, a time shift is applied to the slow P-SV2 component to compensate for the time delay between the P-SV1 and P-SV2 components. The azimuth variations and splitting effect induced by the lower HTI layer have now been successfully compensated for. An inverse NMO correction involving a constant velocity model for all azimuth angles is also applied to both P-SV1 and P-SV2 components. They are rotated back to the radial and transverse components by horizontal rotation. Then the final radial and transverse components can be obtained, which are shown in Figure 7- 39. In contrast to the original radial

component shown in Figure 7- 28(a), the complicated effects of azimuthal anisotropy cannot be found on the updated radial component. The azimuthal variations of the upper and lower HTI layers have been successfully compensated for, and the time delays between the fast P-SV1 and slow P-SV2 components have been removed. Due to the compensation for azimuthal variations and splitting effects, the effective reflection energy on the transverse component has been reduced. With the updated radial component, subsequent data processing and interpretation will be improved.

However, special care should be taken to select appropriate time windows. This issue is particularly important in field data study. The final data quality might be significantly degraded if different time windows are combined.

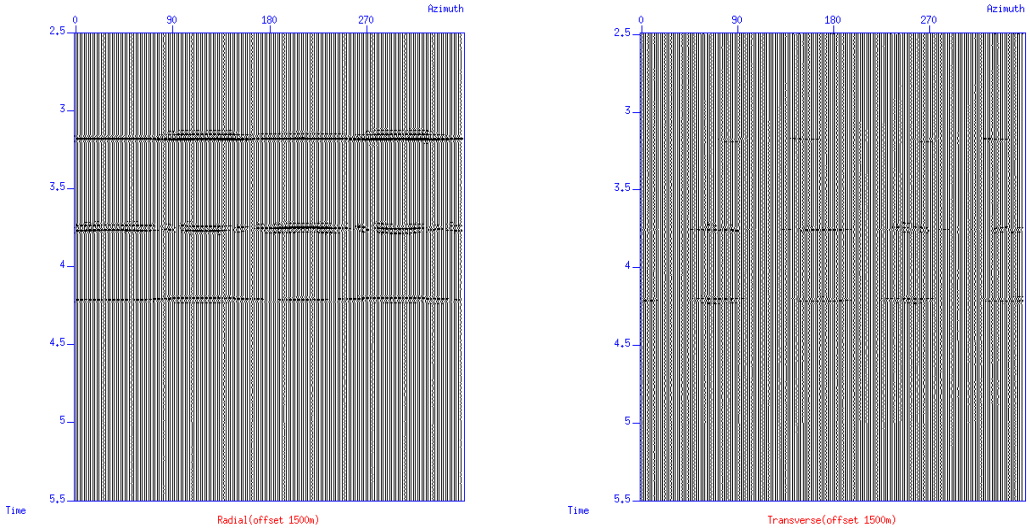

(a) (b)

Figure 7- 39: Azimuth gathers of update (a) radial and (b) transverse components at offset 1500m

7.10 Summary

Fractures produce azimuthal variations and splitting effects, which are both discussed in this chapter. PS-converted wave splitting provides a robust way to estimate fracture directions, and the associated time delays can be directly used to interpret for fracture density. However, PS-converted wave splitting is not sensitive to the type of fluid saturation. So splitting analysis fails to distinguish between different fracture saturations. For both P-waves and PS-converted waves, azimuthal variations also

provide a way to estimate fracture properties, and they are sensitive to the offset-to-depth ratio. Azimuthal variations are stronger for large offset-to-depth ratios, which makes it essential to use data with large offset-to-depth ratios to apply appropriate azimuthal analysis. Moreover, different fracture densities result in different magnitudes of azimuthal variations. Azimuthal variations become weaker as the fracture density decreases. With small fracture densities, weak azimuthal variations cause errors in the estimation of azimuthal parameters.

P-wave azimuthal variations are sensitive to fluid saturations. Although P-wave azimuthal variation is stronger for dry fractures than for water-saturated fractures, it is not sufficient for distinguishing dry fractures from water-saturated fractures. Due to the effects of the P-wave leg, the PS-converted wave azimuthal variations are also sensitive to fluid saturations. The azimuthal variations of both P-SV1 and P-SV2 waves are stronger for dry fractures than for water-saturated fractures. Moreover, P-SV1 and P-SV2 components exhibit in-phase azimuthal variations for dry fractures. However their azimuthal variations are out-of-phase for water-saturated fractures. This feature creates a new way to distinguish oil-filled fractures from gas-filled fractures, which is extremely important in hydrocarbon exploration and production.

When multiple HTI layers are involved, the lower HTI layers are influenced by the upper HTI layers. A specific layer-stripping method is necessary to compensate for the azimuthal variations and splitting effects produced by the different HTI layers. By applying my layer-stripping procedure, each HTI layer can be individually studied and the anisotropic effects can be compensated for. The quality of data after the layer-stripping algorithm is applied is clearly improved, which is beneficial for subsequent data processing and interpretation.

Chapter 8

Analysis of the azimuthal anisotropy of Daqing 3D3C data

8.1 Introduction

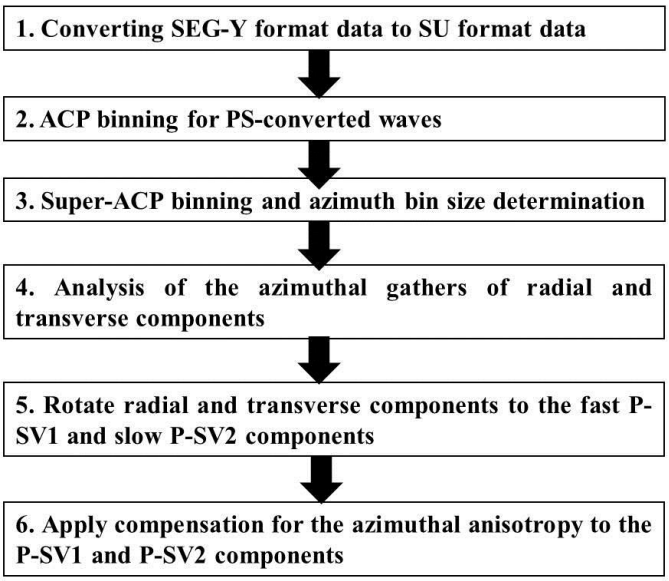

Figure 8- 1: Summary of processing workflow

In this chapter, Daqing 3D3C seismic data is analysed to study the azimuthal anisotropy. The processing workflow is displayed in Figure 8- 1. In order to process the Daqing 3D3C dataset in the environment of Seismic Unix and CxTools, the SEG-Y format dataset must first be converted into SU format. Then ACP binning rather than CDP binning is applied to the PS-converted wave data. Super-ACP gathers, which are formed by combining several ACP numbers and ACP lines, can be used to enhance the signal-to-noise ratio. As discussed in previous chapters, the inline and

crossline components have to be rotated into radial and transverse components to improve the effective PS-converted wave energy. Then the radial and transverse components of a single super-ACP gather can be analysed to separate the P-SV1 component from the P-SV2 component, which is essential to compensate for the azimuthal anisotropy of PS-converted waves. With separate P-SV1 and P-SV2 components available, azimuthal analysis and compensation for the azimuthal variation can be individually applied to improve the NMO correction and stacking results. Finally, a similar procedure can be applied to other super-ACP gathers and final images can be obtained. The acquired and fitted parameters of the azimuthal anisotropy are analysed and are related to the fracture properties.

8.2 3D3C seismic survey in Daqing oilfield

Daqing oilfield, within Songliao Basin, is located in Heilongjiang province, NE China. 3D3C seismic acquisition was performed in 2005 directly in the region where there has been hydrocarbon production for 30 years. The 3D3C survey area (Figure 8- 2) is 18.85 km ESE-WNW and 6.4 km in a NNE-SSW trending direction

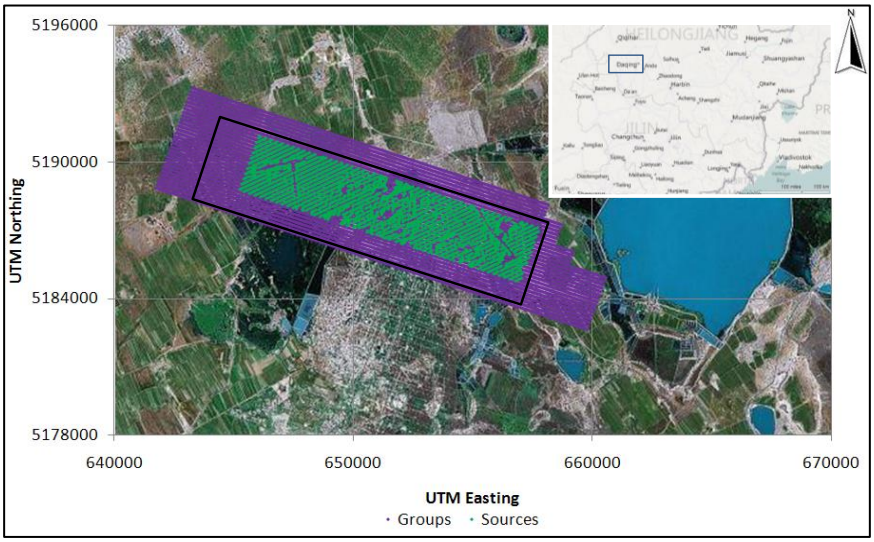

Figure 8- 2: The geometry of 3D acquisition in the Daqing oilfield. Green markers show locations of dynamite sources and purple points indicate receiver locations. Coordinates are UTM zone 51. The highlighted region (denoted by the black border) represents the survey area used in the calculation of fold-of-coverage in Figure 8- .

3-Component (3C) geophones were used, with the sole purpose of extending previous methods of characterising the reservoir by processing PS-converted waves. The acquisition is characterised by a high fold-of-coverage towards the centre of the survey (Figure 8- 3(a)), although it is variable due to effects such as noisy geophones and non-uniform distribution of sources (Figure 8- 3(b)) in the field. Further details of the acquisition can be found in Table 8- 1. For the most part, the dataset has been processed internally by PetroChina and the results remain confidential, while external work has been performed by the Edinburgh Anisotropy Project (EAP). External studies have largely focused on the use of the multi-component aspect for image enhancement, and investigating the azimuthal variation of PS-converted waves(Dai et al., 2010).

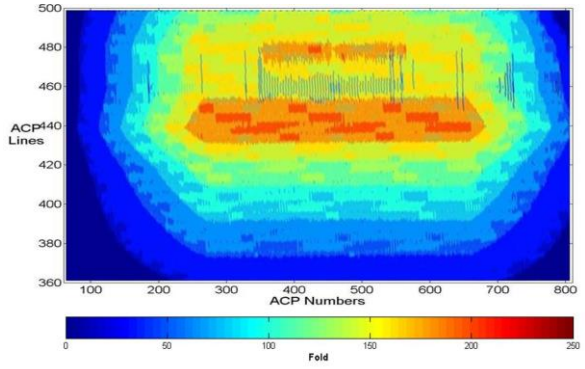

(a)

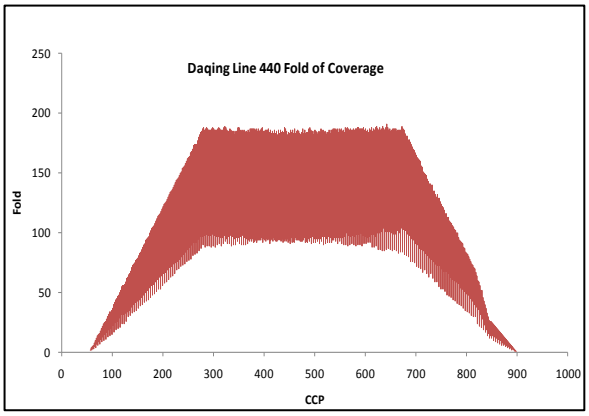

(b)

Figure 8- 3: Maps showing the fold-of-coverage for the Daqing seismic survey. (a) A plan-view map of the fold-of-coverage, where view is constrained by the sectioned region in Figure 8- . (b) Fold-of-coverage along line 440 running WNW-ESE through the centre of the survey.

Daqing seismic survey acquisition parameters	
Source type	Dynamite
Source line azimuth	NE-SW
Source line interval	200 m
Shot interval	50 m
Receiver line interval	160 m
Receiver line azimuth	ESE-WNW
Receiver interval	40 m
Number of channels per shot	2688
Number of swaths	2
Minimum offset	50 m
Maximum offset	3750 m
Sampling rate	4 ms
Recording length	5 s

Table 8- 1: Acquisition parameters for the Daqing seismic survey.

8.3 Geological background of the Daqing oilfield

The Songliao Basin is defined as a Cretaceous rift depression basin located in a complicated tectonic region between the North China and Siberian plates (Desheng, 1995). The large-scale tectonic regime was N-S in direction in the Early Mesozoic, driven by the interaction of these two plates. The tectonic setting changed with the assembly of the European-Asian continent in the Late Mesozoic and has since become part of the aforementioned active China belt. A series of NE-NNE trending faults now characterise the orientation of the tectonic belt, which encompasses the Songliao, West Liaoning, and North Liaoning Basins (Ren and Xiao, 2002). Figure 8- 4 shows this NE-NNE trending fault zone in the region of the Songliao Basin with an uplift zone to the east and a plunge zone to the west.

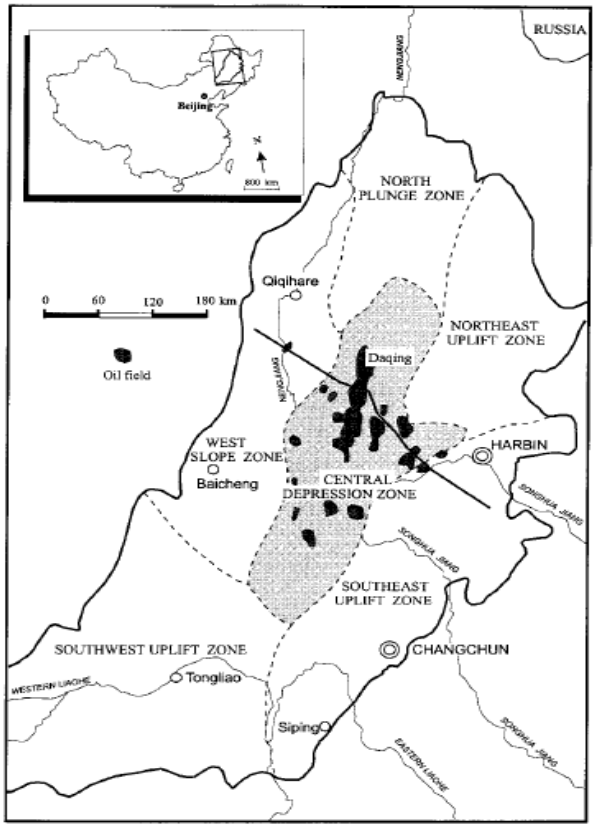

Figure 8- 4: Local tectonic map of the major fault zones of the Songliao Basin and Daqing oilfield, NE China. The E-W line corresponds to the cross-section shown in Figure 8- .

Cenozoic tectonics in NE China have been complicated by tectonic activity from the east (interaction of the Pacific and Philippine plates) and south (collision of India with the SE Asian craton). The present major stress direction is determined by using fault plane solutions from earthquakes (Chi-Tung et al., 1979; Li et al., 1985). The regional principal stress-direction in the Songliao Basin region shows variability between an orientation of NE-SW and E-W. The development of the Songliao Basin is categorised into four evolutionary stages, spanning the Triassic to Late Cretaceous periods. The four stages were defined by Desheng (1995) and are depicted in Figure 8- 5; a description of each stage follows:

II. Thermal Arch and Tension rift stage – Large-scale tectonic uplift created by the Hercynian orogenic event in the Late Devonian to Carboniferous. This stage was characterised by extensive magmatic activity;

III. Taphrogenic stage – In the interval of the Late Jurassic until the Early Cretaceous an extensional regime was the predominant tectonic setting. Extensional stresses were induced at the junctions of different tectonic units by block faulting subsequently creating many of the rift valleys of varying size currently observable in the region;

IV. Depression stage – In the time of the Early to Late Cretaceous rapid subsidence occurred leading to deposition of interbedded sandstones and shales. The deposited shales are deltaic and shallow lacustrine in origin; they provide the source rocks for the Daqing oilfield;

V. Shrink-folding stage – At the end of the Late Cretaceous, the Sea of Japan became tectonically active and began to spread. This created a strong west-trending stress regime on the Songliao Basin region inducing a system of alternating anticlines and synclines, the former representing the trap system for the majority of reservoirs in the basin. In this stage, there were a number of inversion styles creating a number of hydrocarbon traps including rollover anticlines (Song, 1997).

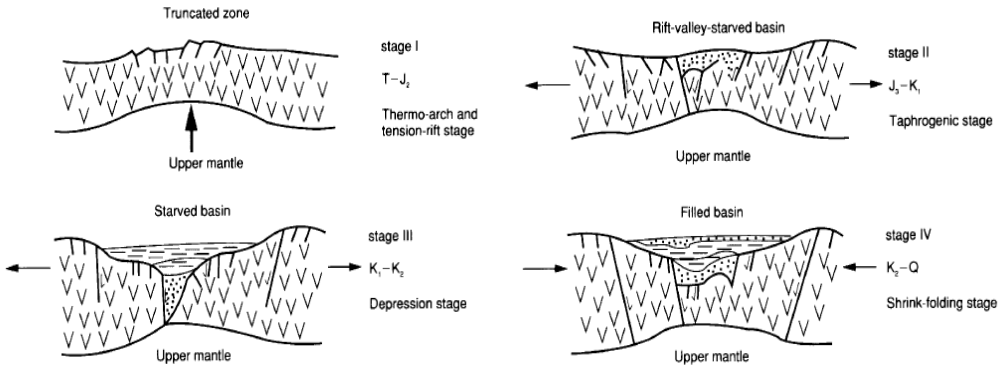

Figure 8- 5: An E-W oriented depiction of the four evolutionary basin-forming stages. Stage I – Triassic; Stage II – Late Jurassic – Early Cretaceous; Stage III – Early Cretaceous – Late Cretaceous; Stage IV – Late Cretaceous – Quaternary.

8.4 Data format conversion

The original dataset is in SEG-Y format, which is one of several seismic data formats conforming to the standard of the Society of Exploration Geophysicists (SEG). This

is an open standard format, and is mainly based on the format and sizes of traces and file headers describing the data (Norris and Faichney, 2002). Direct processing of seismic data with SEG-Y format is supported by some open-source and commercial software but not Seismic Unix. However Seismic Unix provides a conversion between SEG-Y and SU format. The program "SEGYREAD" provides the conversion from SEG-Y data to SU data. The conversion from SU data back to SEG-Y data is supported by the program "SEGYWRITE". Many optional parameters can be specified during the conversion to cope with different cases.

The whole dataset contains three components: one vertical component and two orthogonal components. The header word "trid" is used to identify the three components and extract each component's data from the whole dataset. In this study the SEG-Y data has already had a static correction applied, which is critically important to subsequent processing results.

8.5 Consideration of coordinate systems

Before any subsequent processing is applied, the coordinates of sources and receivers must be carefully considered. Otherwise, incorrect ACP gathers could be binned. Moreover, incorrect azimuth angles could distort the compensation for the azimuthal anisotropy and bring out unreliable fracture properties. Therefore, the coordinate systems of the original data and the CxTools should first be compared. The original data is in the Universal Transverse Mercator (UTM) coordinate system, which gives locations on the surface of the earth. This notation involves larger numbers and characters, which could cause inconveniences in subsequent processing. The internal coordinate system in CxTools is a user-specified Cartesian coordinate system. This system uses the CDP line number on the Y-axis and common depth points on the X-axis (Figure 8- 6). It is more efficient to convert the UTM coordinate system into the CxTools coordinate system. This is achieved by specifying points A and B, which determine the first line of the survey. The coordinates of point A and B are used and calculated to convert the UTM to the CxTools internal coordinate system. Then the ACP binning, super-ACP binning and the calculation of the azimuth angle can be

accomplished in this internal coordinate system. After processing, the CxTools coordinate system can be converted back to the UTM coordinate system.

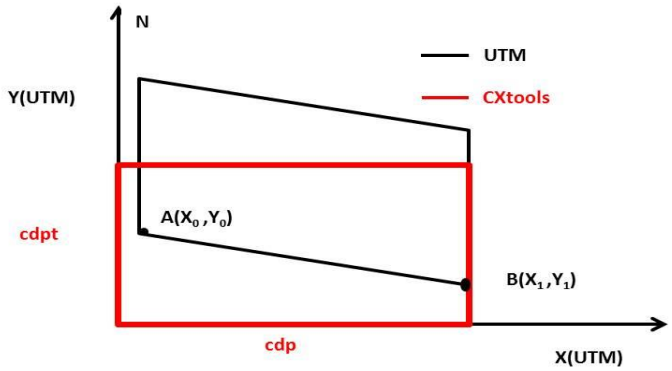

Figure 8- 6: Coordinate systems of UTM (black) and CxTools (red)

8.6 ACP binning and super-ACP binning

As discussed in Chapter 2, the asymmetric path caused by different velocities of P- and shear-waves makes CMP binning inaccurate for PS-converted waves. Horizontal resolution could be reduced by using CMP binning. Direct CCP binning by calculating exact conversion points is theoretically accurate (Tessmer and Behle, 1988), and it is expressed as equation:

$$x_c = \frac{x}{1+V_s^2 t_s / V_p^2 t_p} \tag{8- 1}$$

where t_p and t_s are the one-way traveltime of the P-wave and S-wave legs. V_p and V_s are the internal velocities of P- and S-waves. x is the offset between the source and the receiver. t_p and t_s are functions of x, which are always complicated. Therefore it is not easy to implement CCP binning in PS-converted wave data processing. Based on the theory provided by (Thomsen, 1999) and the program "CXACP", the horizontal X and Y component data are binned into ACP gathers. In this study, the ratio of v_p to v_s is set to be 2.0, which is suggested from previous experiments (Dai and Li, 2010).

Subsequent to ACP binning, ACP gathers are combined to form super-ACP gathers, which is important for obtaining enough energy and a wide azimuthal coverage. The

program “CXSUPERCDP” is used to perform the super-ACP combination. The range of ACP line is from 300 to 500 and the range of ACP numbers is from 100 to 820. The selection of super-bin size is dependent on the consideration of resolution and energy. Including a small number of ACP numbers and lines would increase the resolution of the super-ACP gather and the accuracy of the velocity model. Including a large number of ACP numbers and lines would improve the signal in order to to perform velocity analysis for the super-ACP gather. In this study, the super-bin size is chosen as involving 20 ACP lines and 20 ACP numbers (Figure 8- 7). This selection provides a good compromise of these factors, as suggested from the study by (Dai and Li, 2010).

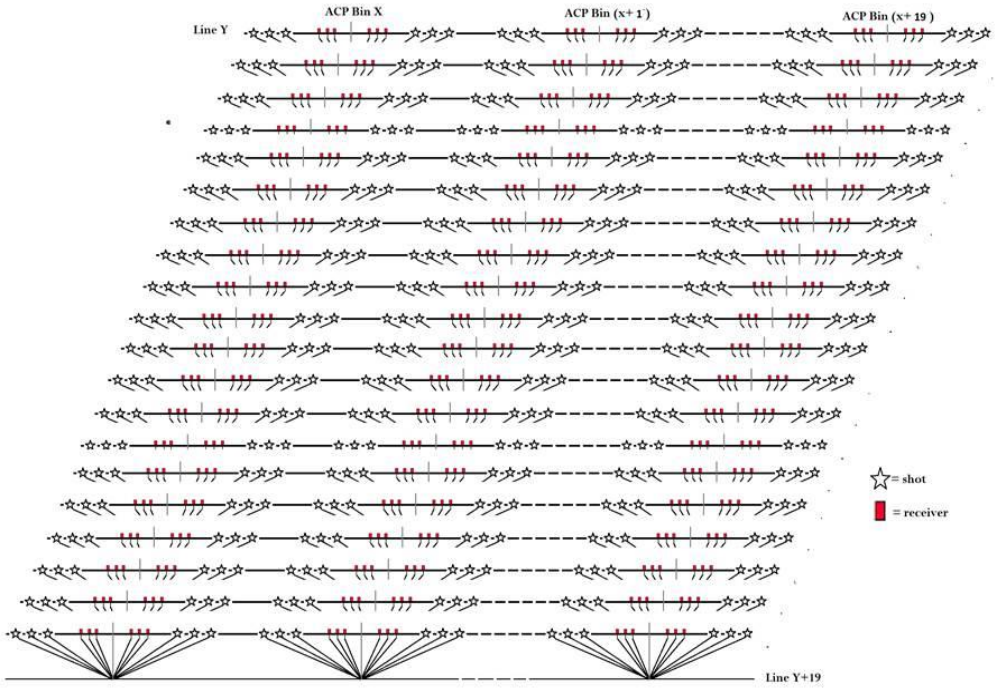

Figure 8- 7: Super-ACP binning for PS-converted waves.

8.7 Azimuth coverage consideration

Azimuth coverage is important to the validity of performing the analysis of azimuthal anisotropy. A reliable analysis of the azimuthal variation cannot be performed by a narrow azimuthal coverage. Wide azimuthal coverage is beneficial to

the azimuthal processing of both P-wave and PS-converted wave seismic data, but it is more expensive.

Super-ACP gather 420-420 is selected as an example for discussing the azimuth coverage. The first number 420 indicates that the super-ACP gather involves ACP lines from number 420 to 439. The last number 420 indicates that the super-ACP gather involves ACP numbers 420 to 439. The azimuth-versus-offset map of super-ACP gather 420-420 is shown in Figure 8- 8. In super-ACP gather 420-420, which has the greatest folds, nearly all azimuth angles are covered when the offset is smaller than 1200m. As the offset increases, the azimuth coverage becomes poor. Specifically, the azimuth ranges 0^o-90^o and 170^o-260^o are not covered when offsets are over 2000m.

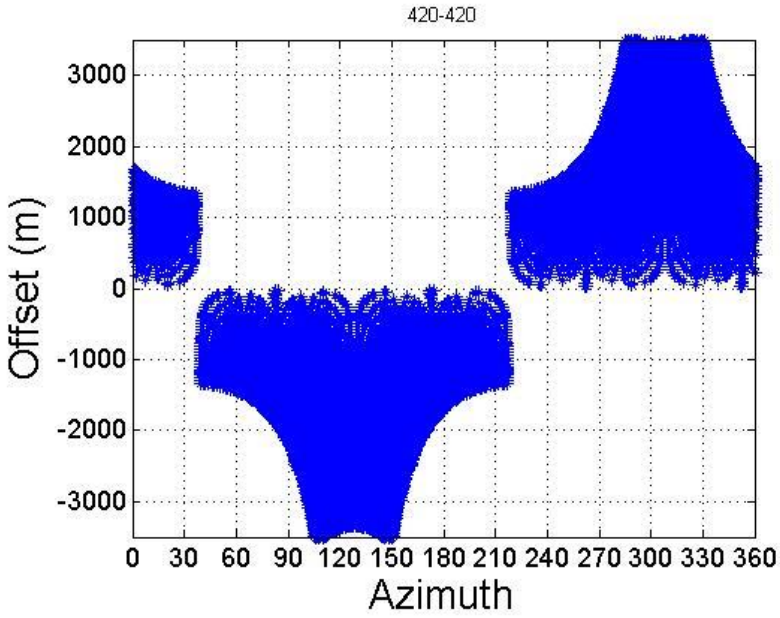

Figure 8- 8: Azimuth-versus-offset map of super-ACP gather 420-420

The azimuth bin size should be carefully chosen before applying azimuthal analysis of different azimuth bins. It is easily understood that small azimuth bins are theoretically beneficial to the accurate analysis of azimuth variations. However, small azimuth bin sizes may cause the data in some azimuth bins to have limited offset and lower energy, which reduces the effectiveness of conventional velocity analysis. Moreover a small bin size means a large number of azimuth bin gathers, which could bring some errors. A large azimuth bin size can greatly enhance the

energy in each azimuth bin and decrease the total processing time. However, results coming from a few azimuth bins may not be accurate enough.

Three azimuth bin sizes, including 15°, 30° and 60°, are studied for the super-ACP gather 420-420. The azimuth coverage of azimuth bins when the size is 15° is displayed in Figure 8- 9. Only a limited number of traces with small offsets are included in some azimuth bins, which are shown in Figure 8- 9 (a), (b), (c), (d) and (e). Therefore the processing and analysis in those azimuth bins are expected to be difficult. Moreover, applying conventional velocity analysis 12 times for a single super-ACP gather is not very efficient.

The results for an azimuth bin size of 30° are shown in Figure 8- 10. For the azimuth ranges from 0° to 90° and 180° to 270°, large offsets are still not available. Compared with the results in Figure 8- 9, more traces are included in each azimuth bin. It is important to retain enough energy to apply conventional velocity analysis for each azimuth bin. Furthermore, the repetition of velocity analysis is halved, compared with results for 15° bin-size, which significantly improves the efficiency.

60° bin-size is also considered and displayed in Figure 8- 11. It is easy to find that more traces are contained in each azimuth bin, which could provide a good signal-to-noise ratio to apply velocity analysis. There are only three azimuth bins which contain more azimuth angles. It certainly simplifies the analysis, because only three bins need to be studied for one super-ACP gather. However, obtaining the desired azimuth angle of azimuthal anisotropy from only three bins might introduce significant errors.

For comparison, the azimuth coverage of super-ACP gather 420-220 is shown in Figure 8- 12, which has lower folds than super-ACP gather 420-420. The azimuth distribution in super-ACP gather 420-220 is similar to the azimuth distribution in super-ACP gather 420-420. But unlike super-ACP gather 420-420, super-ACP gather 420-220 fails to provide large offsets in the azimuth range from 90° to 170°. It can be concluded that the 15^{o} bin-size will not bring extra benefits for the super-ACP gather 420-220. The errors resulting from 60° bin-size still have influence on the accuracy of the azimuthal analysis in super-ACP gather 420-220.

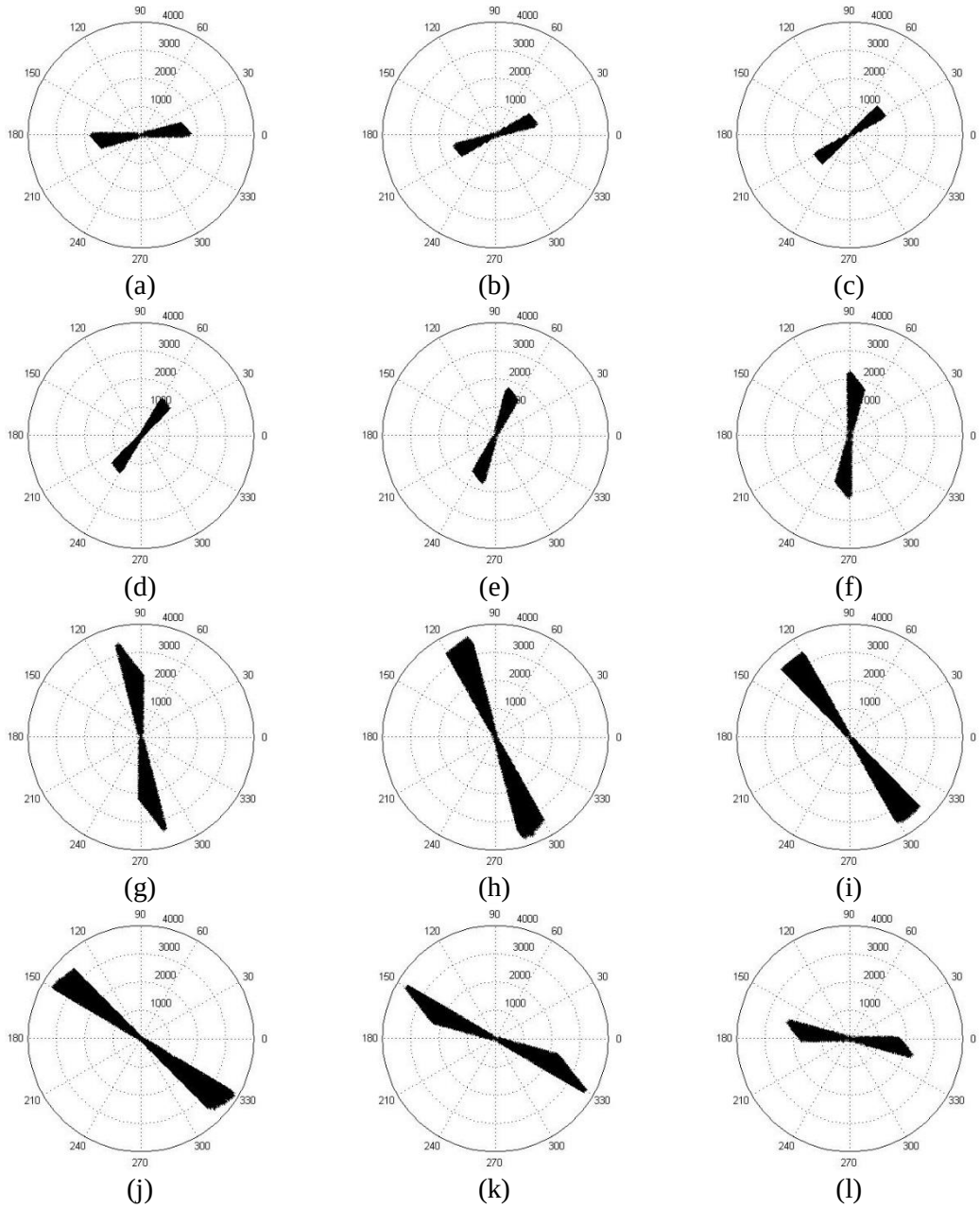

Figure 8- 9: Azimuth bins for the super-ACP gather 420-420 when the bin size is 15^o. (a): 0^o to 14^o and 180^o to 194^o; (b): 15^o to 29^o and 195^o to 209^o; (c): 30^o to 44^o and 210^o to 224^o; (d): 45^o to 59^o and 225^o to 239^o; (e): 60^o to 74^o and 240^o to 254^o; (f): 75^o to 89^o and 255^o to 269^o; (g): 90^o to 104^o and 270^o to 284^o; (h): 105^o to 119^o and 285^o to 299^o; (i): 120^o to 134^o and 300^o to 314^o; (j): 135^o to 149^o and 315^o to 329^o; (k): 150^o to 164^o and 330^o to 344^o; (l): 165^o to 179^o and 345^o to 359^o.

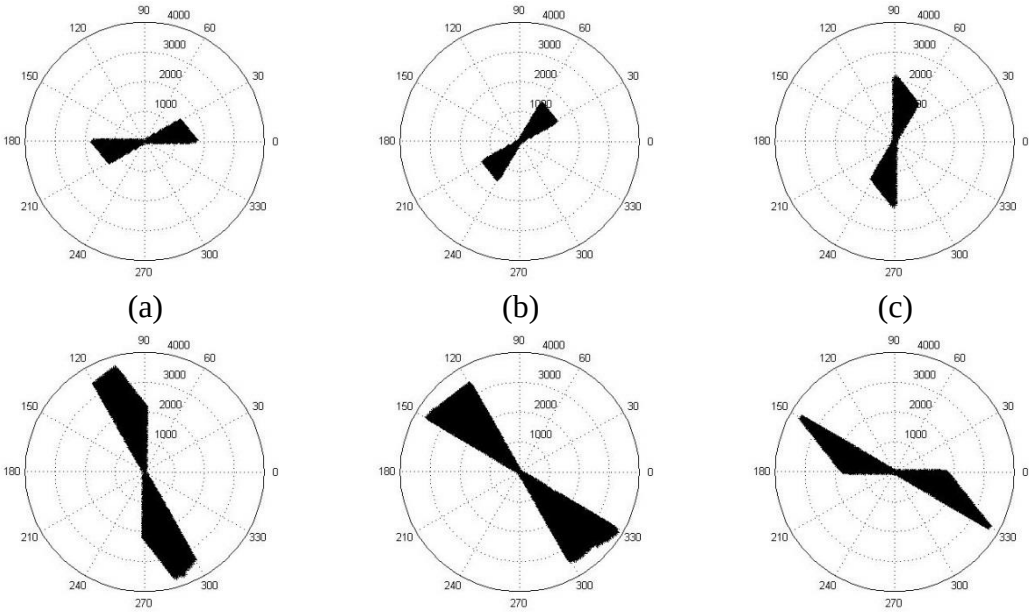

(a) (b) (c)

(d) (e) (f)

Figure 8- 10: Azimuth bins for the super-ACP gather 420-420 when the bin size is 30^o. (a): 0^o to 29^o and 180^o to 209^o; (b): 30^o to 59^o and 210^o to 239^o; (c): 60^o to 89^o and 240^o to 269^o; (d): 90^o to 119^o and 270^o to 299^o; (e): 120^o to 149^o and 300^o to 329^o; (f): 150^o to 179^o and 330^o to 359^o

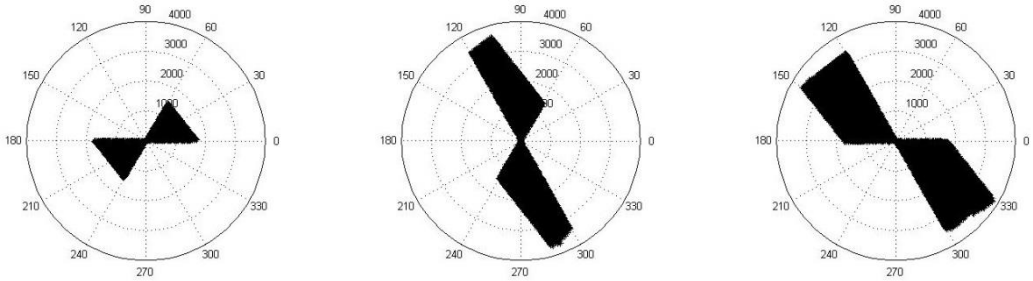

(a) (b) (c)

Figure 8- 11: Azimuth bins for the super-ACP gather 420-420 when the bin size is 60^o. (a): 0^o to 59^o and 180^o to 239^o; (b): 60^o to 119^o and 240^o to 299^o (c): 120^o to 179^o and 300^o to 359^o.

From the above analysis and discussion, I conclude that the 30° bin-size is the best option for this dataset. It provides enough energy for each azimuth bin and reduces the workload. Compared with the 60° bin-size, its accuracy is more acceptable.

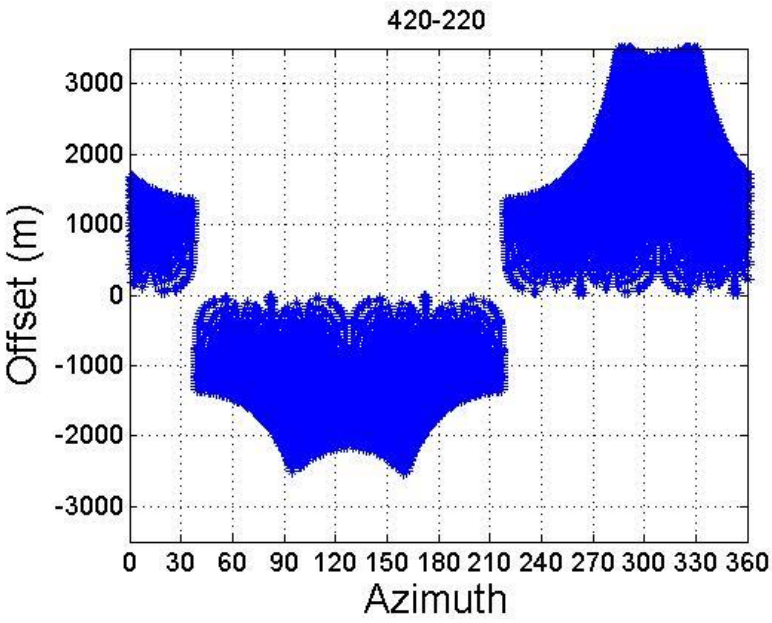

Figure 8- 12: Azimuth-versus-offset map of super-ACP gather 420-220

8.8 Initial evaluation of Daqing data

Prior to applying horizontal rotation and azimuthal analysis, super-ACP gathers are evaluated. It can be found that the effective reflections suffer interference from ground roll and other noise (Figure 8- 13). These negative effects can cause a problem when velocity analysis is applied in CxTools environment using a semblance cross-correlation function. This problem will become more serious in gathers with lower folds because lower energy is contained in those gathers. Suppressing ground roll in either prestack or post-stack datasets can be achieved by many methods, which is beyond the scope of this thesis. Normally, a high-pass filter can be used to remove the ground roll to some extent, because the frequency of ground roll is usually much smaller than the effective signals. A high-pass filter might remove some low-frequency reflections, however this negative effect is less significant compared to the signal-to-noise improvement.

A 5-8-15-100 band-pass filter is then applied to both inline and crossline components (Figure 8- 13). After applying this high-pass filter, the strong ground roll is suppressed in both in-line and cross-line components. This is very important to maintain a good signal-to-noise ratio for performing subsequent processing. It is seen

that the major events between 1.5s to 3s are not seriously affected by the filtering procedure. Note that the shallow events are not significantly improved, which might be caused by near-surface effects or static problems.

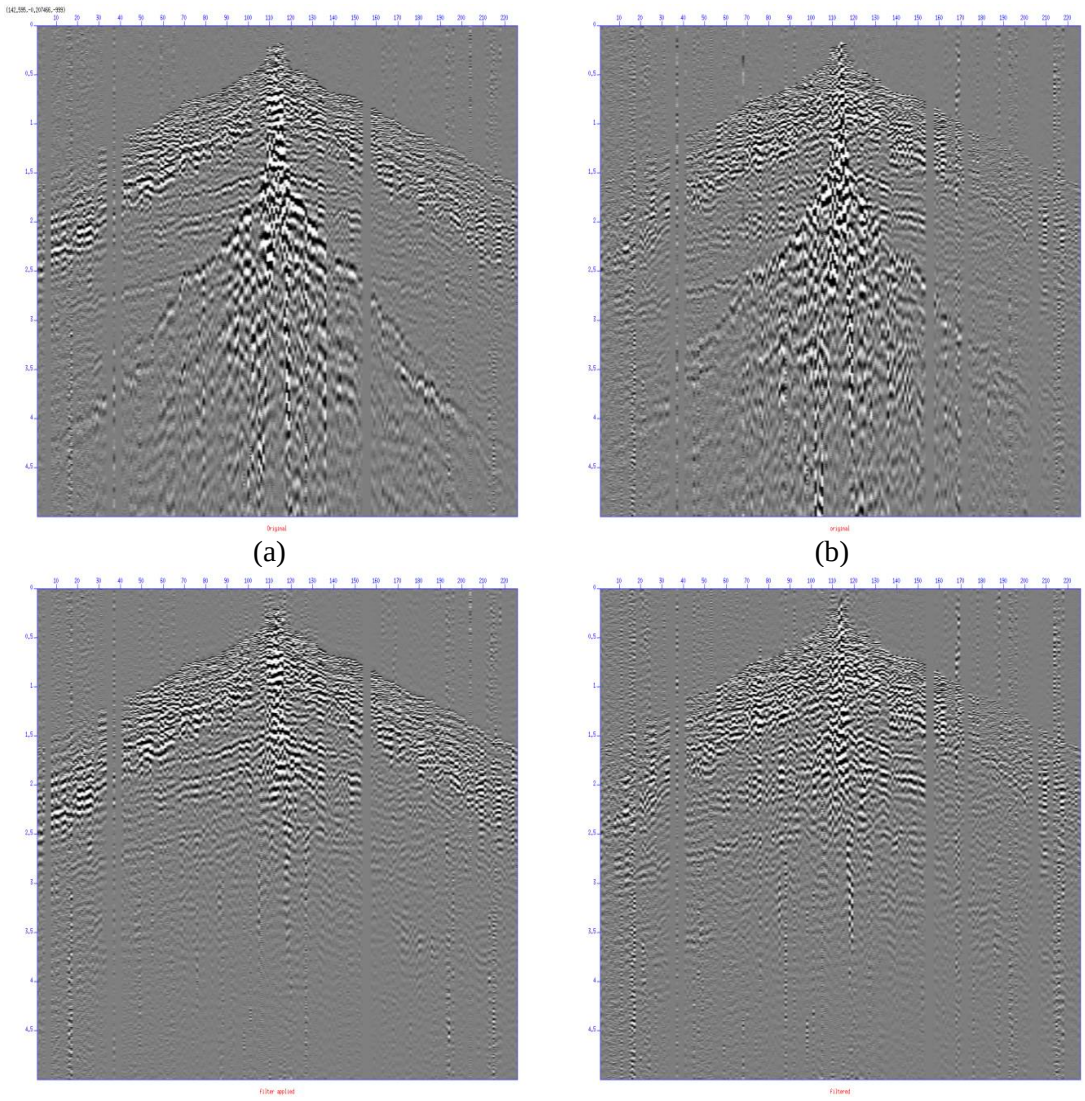

(a) (b)

(c) (d)

Figure 8- 13: Data comparison before and after applying the 5-8-15-100 high-pass filter. (a) and (b) are inline and crossline components before applying the filter. (c) and (d) are inline and crossline components after applying the filter.

8.9 Rotation to radial and transverse components

As discussed in Chapter 2, the P-SV converted wave which is confined to the incident plane is regarded as the main PS-converted wave. Therefore it is essential to

rotate the original inline and crossline components into radial and transverse components. Then proper processing and azimuthal analysis can be applied.

The rotation angle is determined by the coordinates of a source-receiver pair (Figure 8- 14). The rotation algorithm can be described by the following equation:

$$\begin{bmatrix} R(\mathrm{t}) \\ \mathrm{T}(\mathrm{t}) \end{bmatrix} = \begin{bmatrix} \cos(\theta) & \sin(\theta) \\ -\sin(\theta) & \cos(\theta) \end{bmatrix} \begin{bmatrix} X(\mathrm{t}) \\ \mathrm{Y}(\mathrm{t}) \end{bmatrix} \tag{8- 2}$$

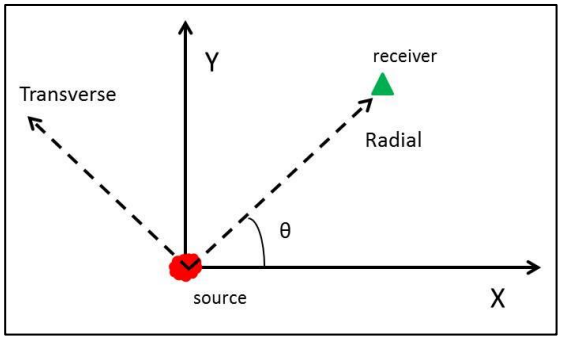

Figure 8- 14: Demonstration of horizontal rotation to radial and transverse components

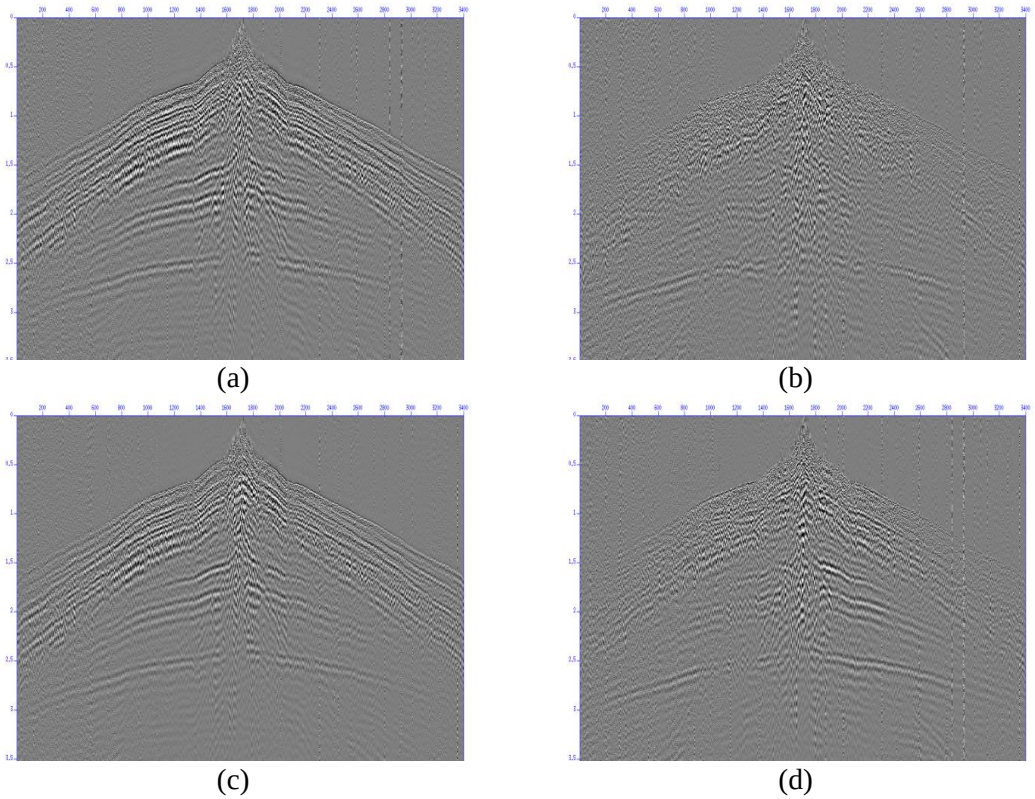

(a) (b)

(c) (d)

Figure 8- 15: Comparison between X-Y coordinates and radial-transverse coordinates. (a): Radial component; (b): Transverse component; (c): X component; (d): Y component.

The horizontal rotation provided in Seismic Unix is specifically designed for data in which three adjacent traces are considered to be the Z, North and East components. Using this program is not efficient in this study. So I developed a new horizontal rotation program by using the Seismic Unix Libraries. This program firstly calculates the rotation angle by using the source-receiver coordinates stored in header words. Then horizontal rotation based on Equation (8- 2) is applied to the X (inline) and Y (crossline) components at the same time. The comparison between the X-Y coordinates and Radial-Transverse coordinates is shown inFigure 8- 15. After rotation, the energy in the radial component is enhanced, for instance in the time window between 1.5s and 2.5s. The energy on the transverse component decreases after horizontal rotation. This proves that the rotation to radial and transverse components is essential for performing proper PS-converted wave data processing.

8.10 Azimuthal analysis of radial and transverse components

Considering the limited azimuthal coverage of super-ACP gathers 420-420 and 420-220, efficient analysis could not be performed at large offsets. Therefore the azimuth-stack gathers must be used to study the azimuthal variation. To obtain the azimuth-stack gathers, conventional velocity analysis should be applied to both radial and transverse component data (Figure 8- 16). At this stage, an initial velocity model is obtained for the radial and transverse components for all azimuths. Then the NMO correction is applied to remove the effects of non-zero offsets. Finally both radial and transverse components can be stacked into azimuth-stack gathers by stacking the traces of the same azimuth angles.

The azimuth-stack gathers of both radial and transverse components are shown in Figure 8- 17. The horizontal axis represents different azimuth angles in the CxTools coordinate systems. The vertical axis is the time axis, which only covers the specific window 1.2s to 3s, in which major reflection events of interest are included. To view the azimuthal behavior in more detail, the time windows are enlarged to provide a clearer observation. The first time window is between 1.2s to 2.2s, which is shown in **Figure 8-** 18. It can be seen that the azimuth variation displayed in the radial

component is not clear. This proves that the azimuthal variation of PS-converted waves usually suffers from the effect of converted-wave splitting. The energy on the transverse component is weaker than the energy on the radial component. Moreover, the phenomenon of 90^{o} polarity reversal can be observed in the azimuth-stack gathers of the transverse component. The approximate azimuth angles for the polarity reversal are 84^{o}, 174^{o}, 264^{o} and 354^{o}. However, which azimuth angles represent the true dominant fracture direction, and which represent the fracture normal direction, is not clear. The time window between 2.2s and 2.8s is enlarged in **Figure 8-** 19. The azimuthal variation in the radial component is not clear and similar polarity reversals can be found in the transverse component. Therefore, direct analysis of either the radial or transverse component is not efficient to compensate for azimuthal anisotropy. Moreover, it is also not useful for fracture property inversions.

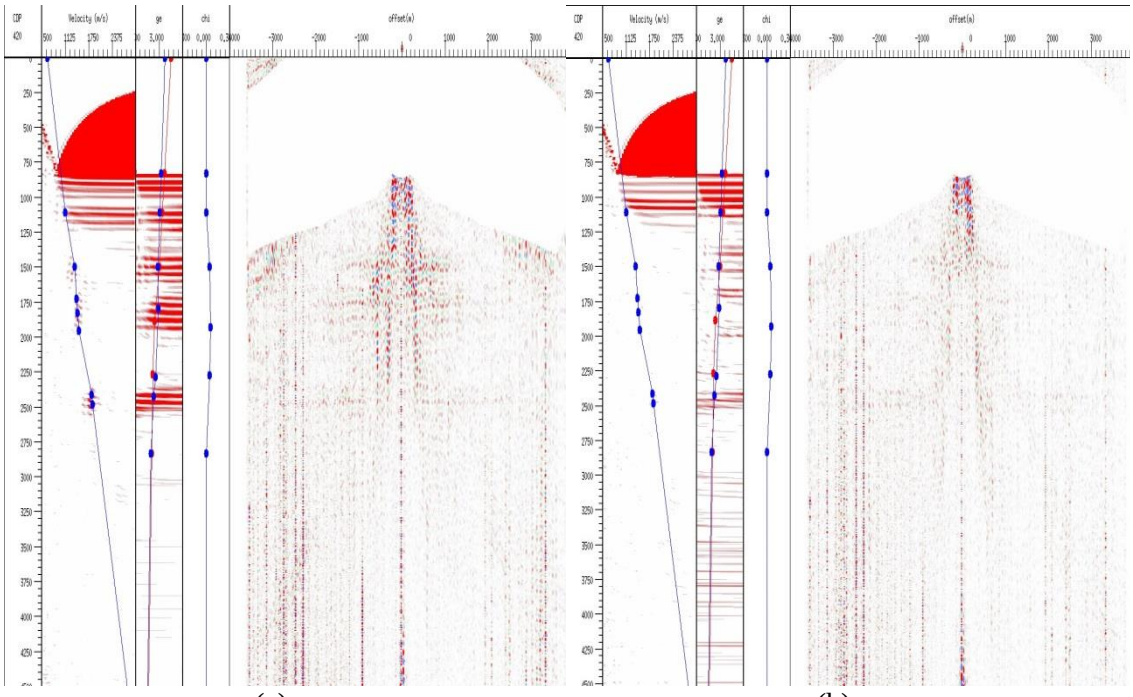

(a) (b)

Figure 8- 16: Initial velocity analysis for the radial (a) and transverse (b) components of super-ACP gather 420-420.

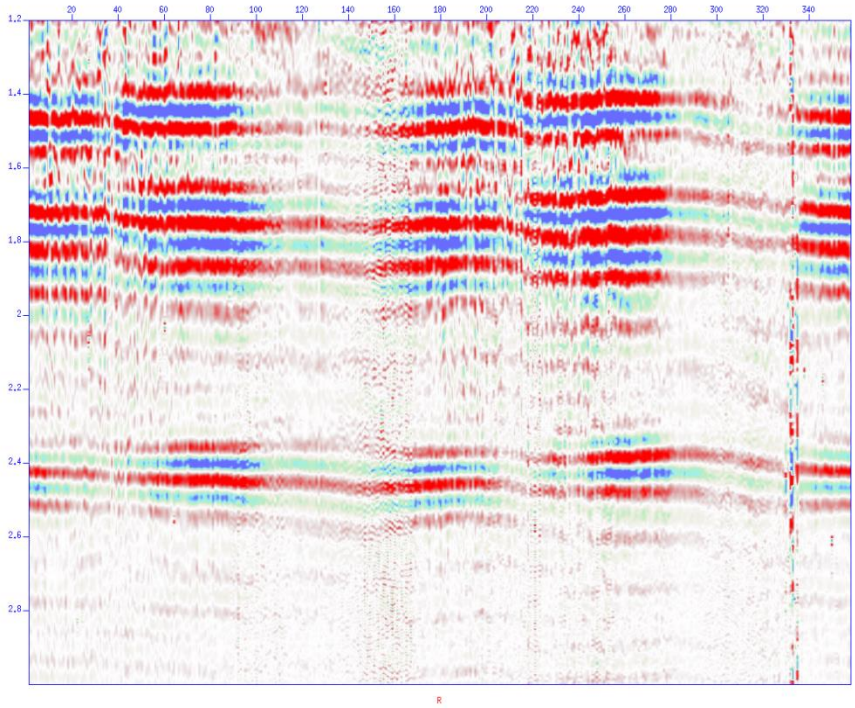

(a)

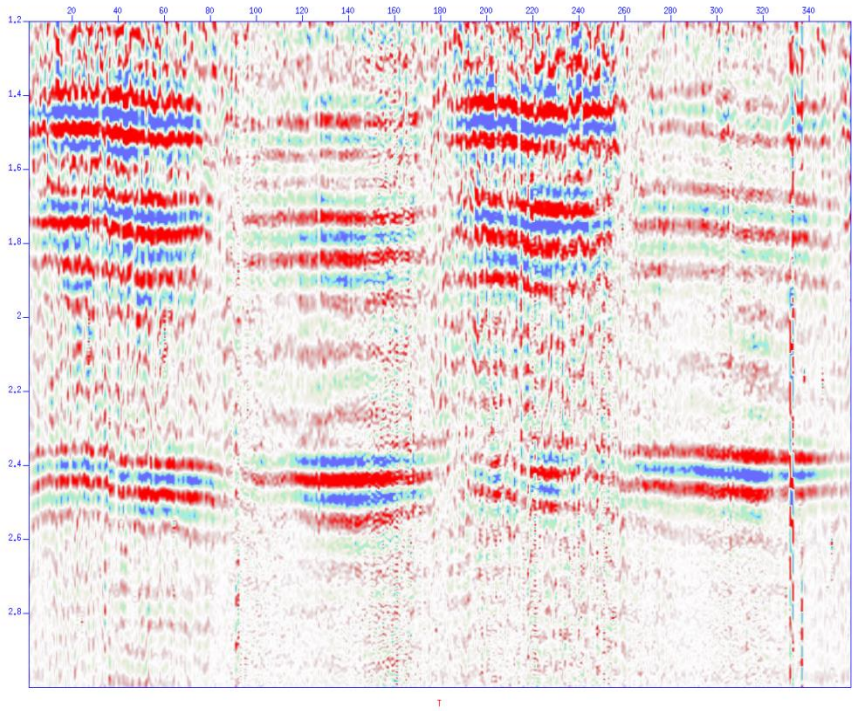

(b)

Figure 8- 17: Azimuth-stack gathers of radial (a) and transverse (b) components of super-ACP gather 420-420

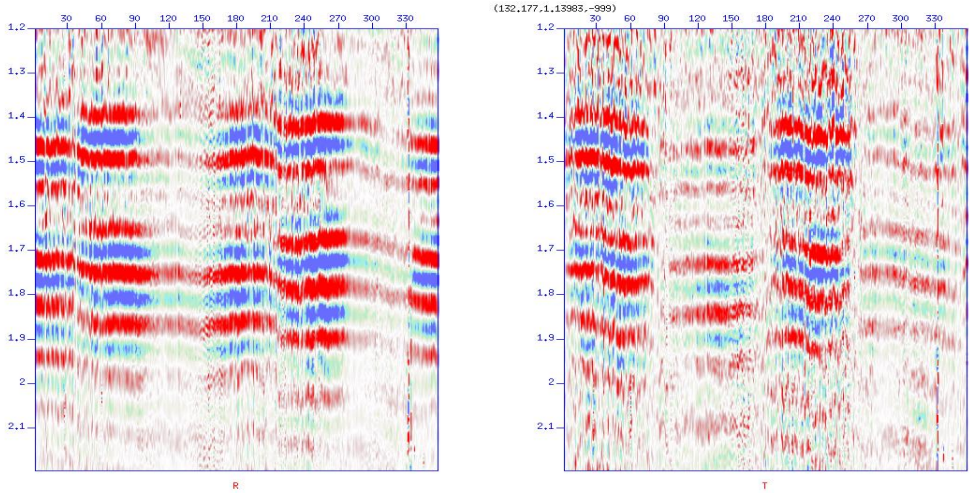

(a) (b)

Figure 8- 18: Enlarged time window between 1.2 and 2.2s of radial (a) and transverse (b) components

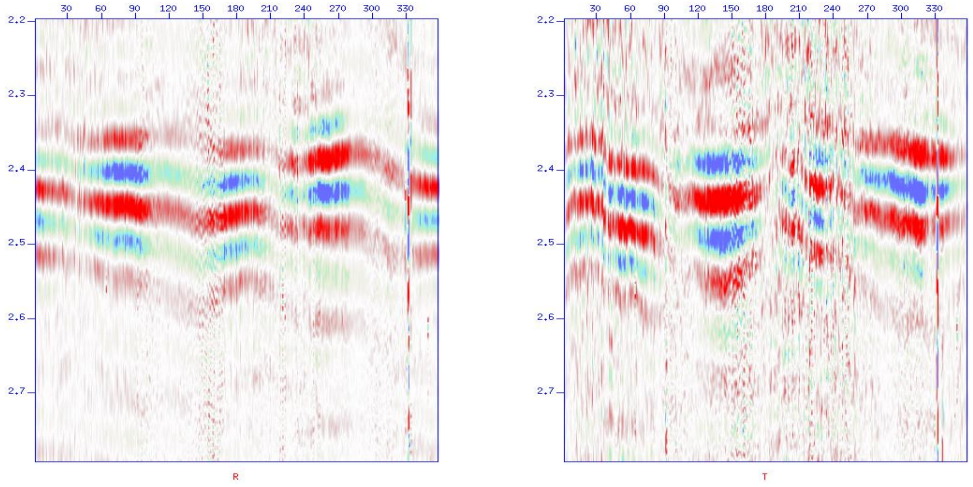

(a) (b)

Figure 8- 19: Enlarged time window between 2.2 and 2.8s of radial (a) and transverse (b) components

8.11 Rotation to fast P-SV1 and slow P-SV2 components

Due to the influence of converted-wave splitting on azimuthal anisotropy, it is essential to separate the fast P-SV1 wave from the slow P-SV2 wave. The separation can be achieved by horizontal rotation to the dominant fracture direction and the fracture normal direction, which is based on Alford rotation. If the P-SV1 wave and P-SV2 wave are assumed to have similar waveforms with only a time-delay, an

object function can be built to obtain the fracture direction and time-delay. This function is explained in Chapter 4 (4-1) and is shown here again:

$$F(\theta,\Delta T)=\sum_{t=win1}^{win2} PSV1(\theta,t)PSV2(\theta,t-\Delta T) \qquad (8\text{- }3)$$

The same super-ACP gather 420-420 is rotated into the relevant fast P-SV1 and slow P-SV2 components. After calculation, the desired angel θ is 86^{o}, which represents the fracture direction. The time-delay between the fast P-SV1 and slow P-SV2 wave is 40ms. Then the original data set can be rotated into the P-SV1 and P-SV2 component (Figure 8- 20). An initial velocity analysis and NMO correction are also applied to both P-SV1 and P-SV2 components. Thus, the corresponding azimuth-stack of the P-SV1 and P-SV2 component can be obtained. Compared with the reflection events displayed in the radial component (Figure 8- 17), the reflections displayed in the fast P-SV1 and slow P-SV2 component are much clearer. Besides, the time-delay between the fast P-SV1 and slow P-SV2 wave can be observed. The enlarged time windows are displayed in Figure 8- 21 and Figure 8- 22. The azimuthal variations shown in the P-SV1 and P-SV2 azimuth-stack gathers are similar in both time windows. This implies that the azimuthal variation could be induced by gas-saturated fractures. Moreover, the azimuth velocity variation of the P-SV2 component is less significant than the azimuth velocity variation of the P-SV1 component. This is another important feature of gas-saturated fractures.

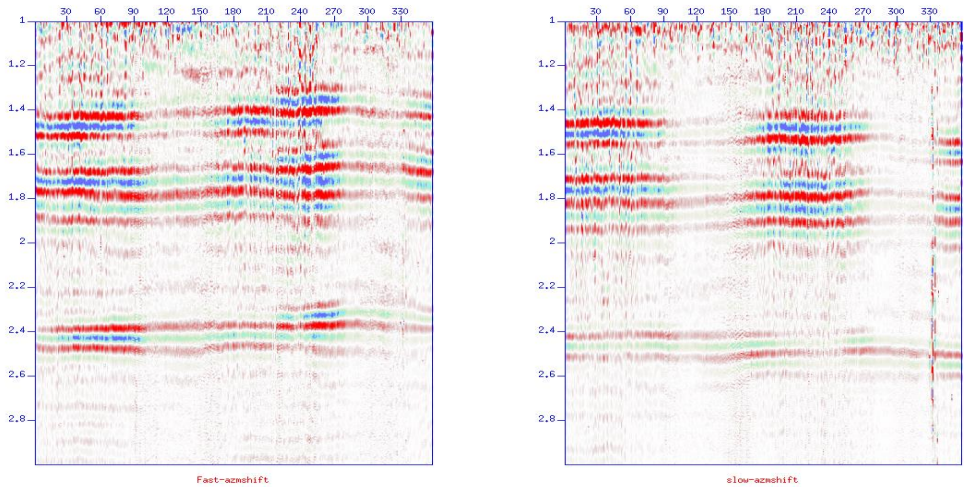

(a) (b)

Figure 8- 20: Azimuth-stack gathers of the P-SV1 (a) and P-SV2 (b) component.

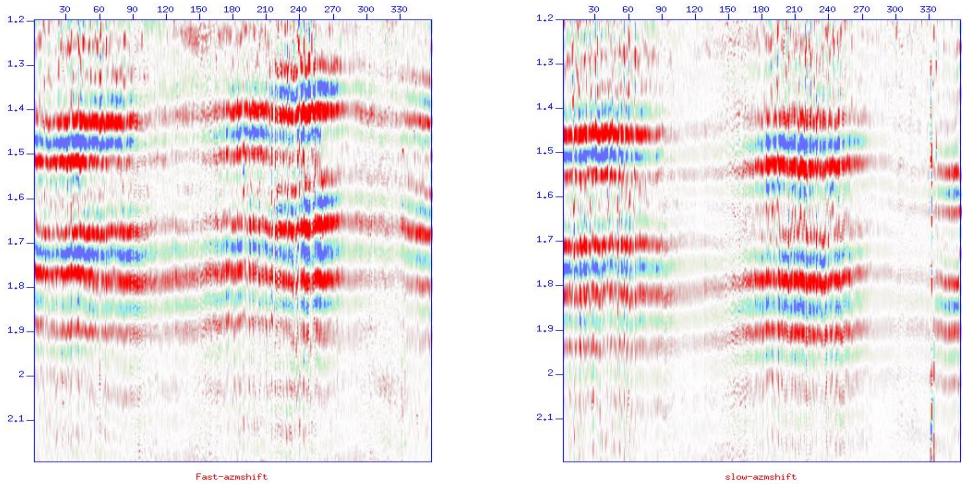

(a) (b)

Figure 8- 21: Enlarged time window between 1.2 and 2.2s of the P-SV1 (a) and P-SV2 (b) components

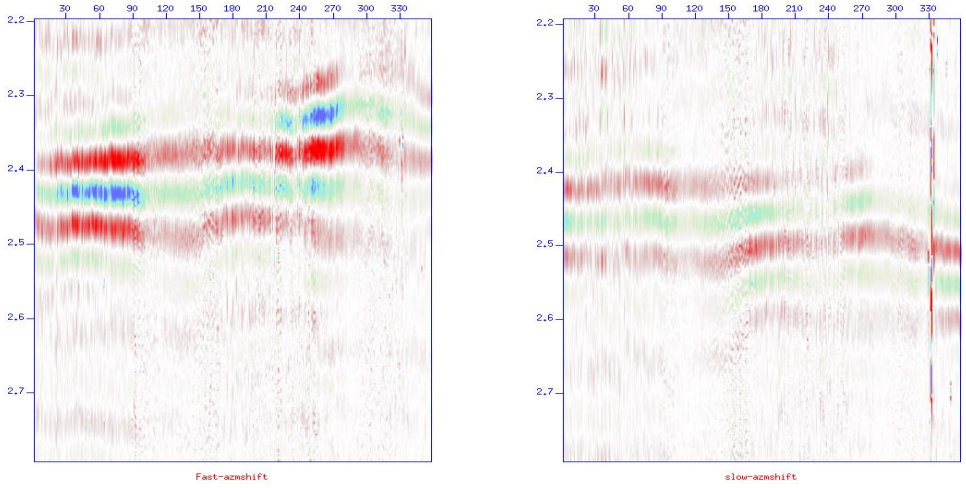

(a) (b)

Figure 8- 22: Enlarged time window between 2.2 and 2.8s of the P-SV1 (a) and P-SV2 (b) components

8.12 Application of azimuthal velocity analysis

After the separation of the P-SV1 wave from the P-SV2 wave, an individual velocity analysis can be applied to both P-SV1 and P-SV2 components. Firstly, conventional velocity analysis is applied to the whole super-ACP gather to acquire an initial velocity model. The azimuth range is reset to -90^o to 90^o to facilitate the processing and estimation procedure. By applying a bin size of 30^o, the super-ACP gather is binned into six azimuth gathers. For example, the azimuth bin -90^o covers the

azimuth range between -90^o to -61^o. Only the velocity is assumed to be subject of azimuthal variation, so other parameters are kept constant in the different azimuth gathers. Based on the initial velocity file, the velocity analysis is individually applied to the six azimuth gathers. Figure 8- 23 and Figure 8- 24 show the process of velocity analysis for six different azimuth bins. Figure 8- 23 is for the fast P-SV1 component and Figure 8- 24 is for the slow P-SV2 component. It can be seen that the energy of ground roll is still strong in some azimuth bins, which introduces some difficulties in picking an accurate velocity. Moreover, large offset data is not available for the azimuth bins 0^o and 30^o. Therefore an azimuth variation for large offset could not be detected, which degrades the accuracy of azimuthal velocity models. In this study, the main focus will be around 1.95s and 2.47s. Different velocities at about 1.95s and 2.47s are picked, and the target events can be individually corrected for each azimuth bin. In other words, different velocities are certainly required for different azimuth bins. However, the differences among the six azimuth bins for the fast P-SV1 component are not very large, which indicates relatively weak anisotropy. The P-SV2 component is suffering from an even weaker azimuth variation, compared with the P-SV1 component. Therefore, compensation for the azimuthal variation of the P-SV2 component might not result in a significant improvement of imaging quality. Moreover, the fracture properties inverted from the P-SV2 components may be more influenced by noise and other interference.

Examples of different velocities of both P-SV1 and P-SV2 components are displayed in Table 8- 2 and Table 8- 3. The velocities of the P-SV1 and P-SV2 components at 1.95s acquired from corresponding six azimuth bins are shown in Table 8- 2. The different velocities at around 2.47s are displayed in Table 8- 3. The velocities of the P-SV1 component are larger overall than the velocities of the P-SV2 component at both 1.95s and 2.47s. This is consistent with the P-SV1 component travelling faster than the P-SV2 component.

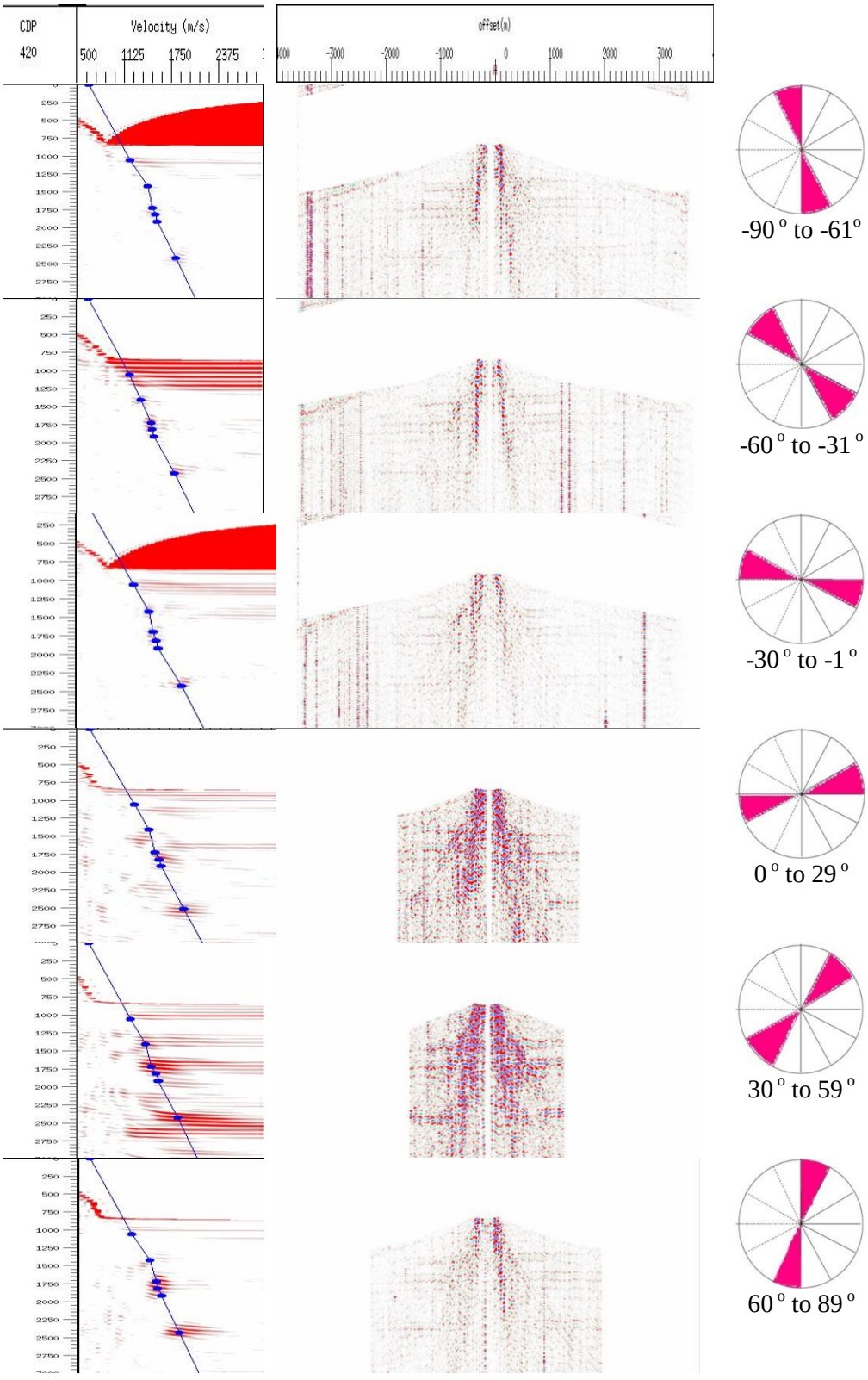

Figure 8- 23: Velocity analysis for the six different azimuth bins of the fast P-SV1 component (The bin size is 30^{o}).

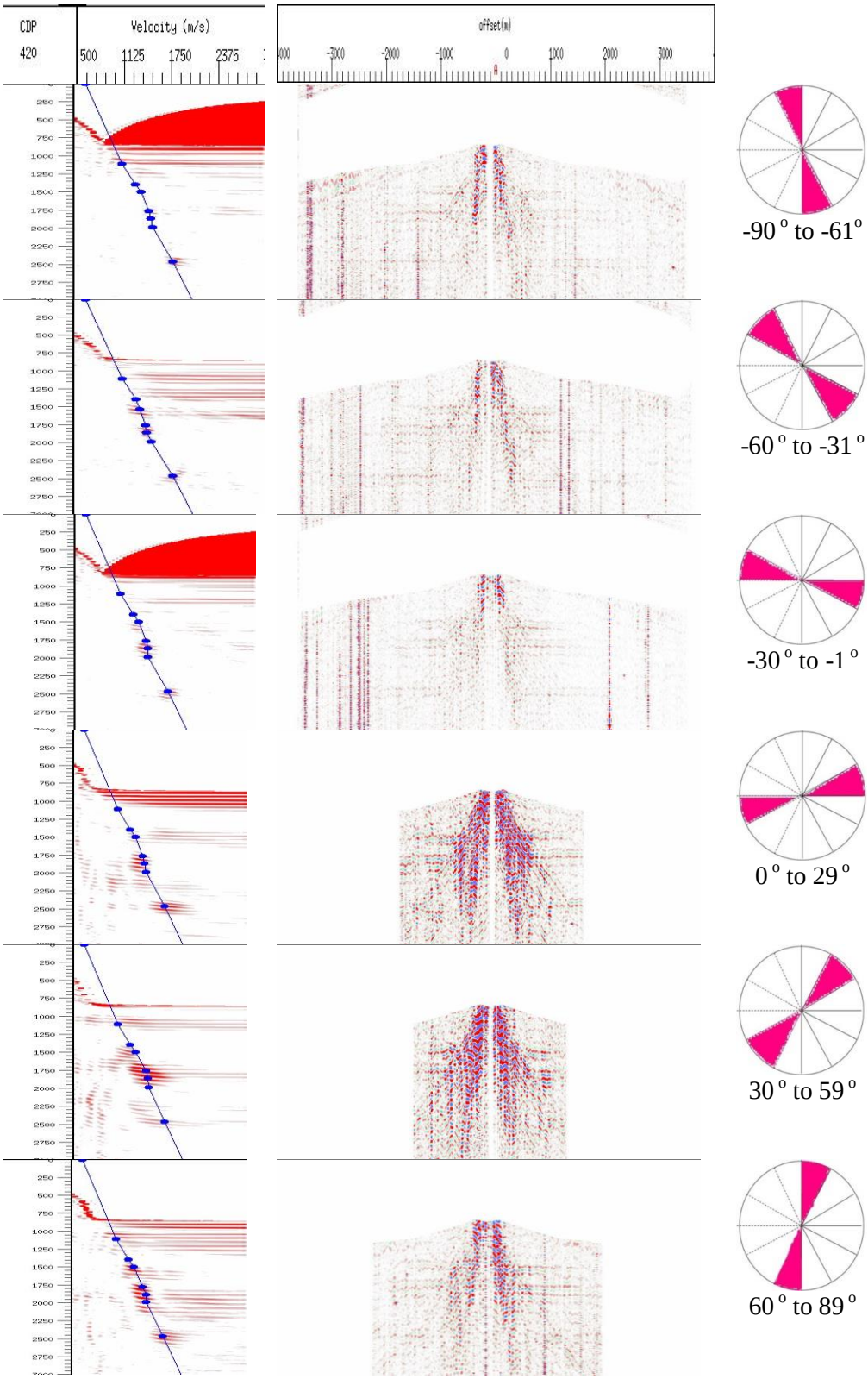

Figure 8- 24: Velocity analysis for the six different azimuth bins of the slow P-SV2 component (The bin size is 30^o).

Azimuth bins of the P-SV1	Velocity at 1.95s (m/s)
-90 ^{o}	1563
-60 ^{o}	1538
-30 ^{o}	1514
0 ^{o}	1516
30 ^{o}	1542
60 ^{o}	1565

(a)

Azimuth bins of the P-SV2	Velocity at 1.95s (m/s)
-90 ^{o}	1492
-60 ^{o}	1482
-30 ^{o}	1480
0 ^{o}	1488
30 ^{o}	1499
60 ^{o}	1500

(b)

Table 8- 2: NMO velocities for the P-SV1 (a) and P-SV2 (b) components at 1.95s

Azimuth bins of the P-SV1	Velocity at 2.47s (m/s)
-90 ^{o}	1830
-60 ^{o}	1807
-30 ^{o}	1799
0 ^{o}	1814
30 ^{o}	1837
60 ^{o}	1845

(a)

Azimuth bins of the P-SV2	Velocity at 2.47s (m/s)
-90 ^{o}	1781
-60 ^{o}	1770
-30 ^{o}	1776
0 ^{o}	1780
30 ^{o}	1784
60 ^{o}	1785

(b)

Table 8- 3: NMO velocities for the P-SV1 (a) and P-SV2 (b) components at 2.47s

8.13 Velocity ellipse fitting and improvements in imaging

After the velocities of the different azimuth bins are picked, ellipse fitting can be applied to both the fast P-SV1 and slow P-SV2 components. Here, the velocities at 1.95s and 2.47s listed in Table 8- 2 and Table 8- 3 are used again to show examples of fitted velocity ellipses. By using the least-square method introduced in Chapter 5, the velocities of different azimuth bins can be fitted into velocity ellipses. The velocity ellipses describing the azimuthal variation of the NMO velocity are incorporated in the NMO correction to improve event flattening.

The velocity ellipses are displayed in Figure 8- 25 and Figure 8- 26. Figure 8- 25 shows the velocity ellipses at 1.95s and Figure 8- 26 shows the velocity ellipses at 2.47s. At t=1.95s, the fracture direction inverted from the P-SV1 component is 88^{o} in the azimuthal plane. It is close to the fracture direction 86^{o}, which is acquired by analysing the converted-wave splitting effect. However, the fracture direction inverted from the P-SV2 component is 66^{o}, which is quite deviated from 86^{o}. This could be caused by noise contamination and inaccuracy resulting from the hand-

picking process. Because the azimuth bin size is 30 °, the azimuth angles within a certain azimuth bin can be equivalent to each other. In other words, the fracture direction for the P-SV2 component is 66°, which is in the azimuth range between 60° and 89°. Then 66° is regarded to be equivalent to 86 ° and other azimuth angles within the azimuth bin (60° to 89°). Therefore the fracture direction inverted from the P-SV2 component is still a valid result. The velocity perturbation parameters for the P-SV1 and P-SV2 component are 0.0159 and 0.0074, respectively. This indicates that the azimuthal variation of the P-SV2 component is less significant than that of the P-SV1 component. The difference between the base velocities of the P-SV1 and P-SV2 components is 56m/s (1546-1490=56). The ratio of the difference to the base velocity of the P-SV1 component is about 0.0362 (56/1546=0.0362), which is larger than the velocity perturbations of both the P-SV1 and P-SV2 components. Therefore the velocity variation at different azimuths is weaker than the velocity differences between the P-SV1 and P-SV2 components.

Similar features can be observed from the NMO velocity ellipses at t=2.47s. The fracture direction inverted from the P-SV1 component is 70°. It deviates from the 86° which is obtained from analysis of the shear-wave splitting effect. It is also not the same as the fracture direction inverted at t=1.95s. However, it is still within the azimuth range between 60° and 90°. Therefore, it is still equivalent to the fracture direction inverted at t=1.95s. The fracture direction inverted from the P-SV2 component is 65°, which is close to the fracture direction obtained from the P-SV2 component at t=1.95s. This fracture direction also agrees with the fracture directions acquired from the P-SV1 component and splitting analysis. Therefore, the fracture directions at t=1.95s and t=2.47s are similar. The velocity perturbations of the P-SV1 and P-SV2 components are 0.0126 and 0.0025, respectively. They are smaller than their counterparts at t=1.95s, which indicates the azimuthal variation at t=2.47s is generally less significant than the azimuthal variation at t=1.95s. The ratio of the difference between the base velocities of the P-SV1 and P-SV2 components to the base velocity of the P-SV1 component is about 0.0231. It is still larger than the velocity perturbations of both the P-SV1 and P-SV2 components. It indicates again that the azimuthal variation is less significant than the shear-wave splitting effect.

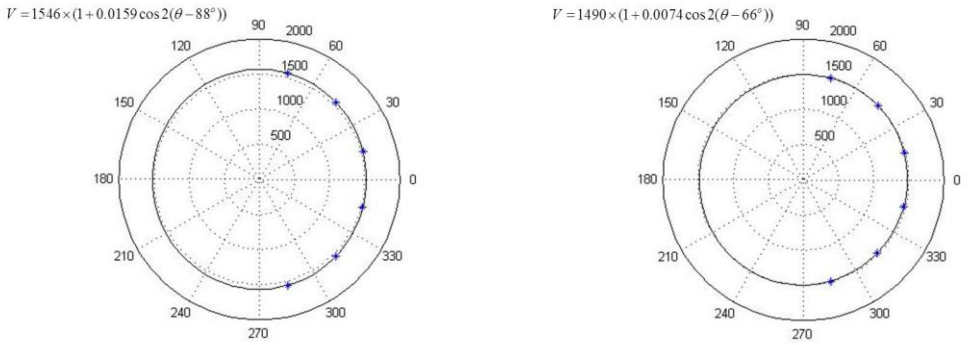

(a) (b)

Figure 8- 25: NMO velocity ellipses for both P-SV1 (a) and P-SV2 (b) components at 1.95s**.**

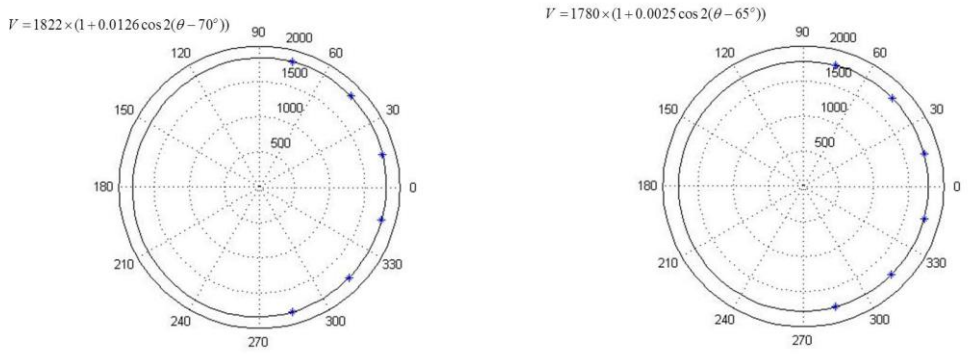

(a) (b)

Figure 8- 26: NMO velocity ellipses for both P-SV1 (a) and P-SV2 (b) components at 2.47s**.**

The fitted velocity ellipses are applied to the NMO correction. Different velocities are used for the NMO correction of traces with different azimuth angles. The NMO corrections of the P-SV1 and P-SV2 components are displayed in Figure 8- 27 and Figure 8- 28, respectively. For the P-SV1 component, the events between 1.5s and 2s are better aligned when the azimuthal variation is compensated for. A similar improvement can be found on the events at about 2.47s but it is not as significant as the improvement shown between 1.5s and 2s. This is due to the weaker azimuth variation, which is discussed above in terms of the velocity ellipse. The overall azimuthal variation of the P-SV2 component is weaker than the azimuthal anisotropy of the P-SV1 component. Therefore the improvement is not significant when the azimuthal variation of the P-SV2 component is compensated for.

Then the NMO corrected P-SV1 and P-SV2 components are both stacked. Fourier transformation is applied to obtain the frequency spectrum of both the P-SV1 and P-SV2 components (Figure 8- 29 and Figure 8- 30). The improvement of the frequency spectrum is in accordance with the NMO correction results. For the P-SV1 component, the low-frequency component is suppressed and the frequencies between 15 and 30HZ are boosted. It indicates an improvement of the signal-to-noise ratio, which is beneficial to the imaging quality. This type of improvement is very hard to find on the P-SV2 component. By applying the azimuthal velocity model, the frequency spectrum is not significantly improved for the P-SV2 component. It indicates a limited improvement of the P-SV2 component.

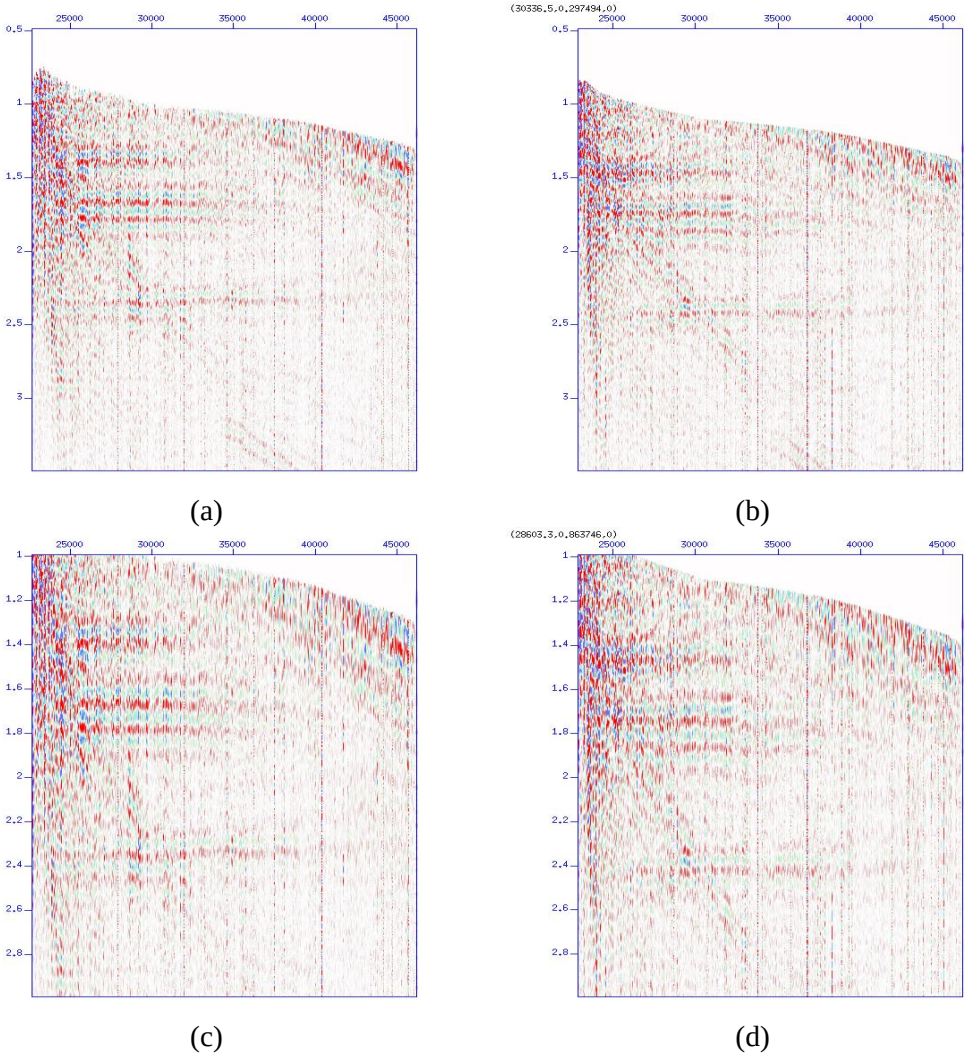

Figure 8- 27: NMO corrections for the P-SV1 components of the super-ACP gather 420-420 with (a) and without (b) the azimuthal compensation. The focused areas are enlarged in (c) and (d), respectively.

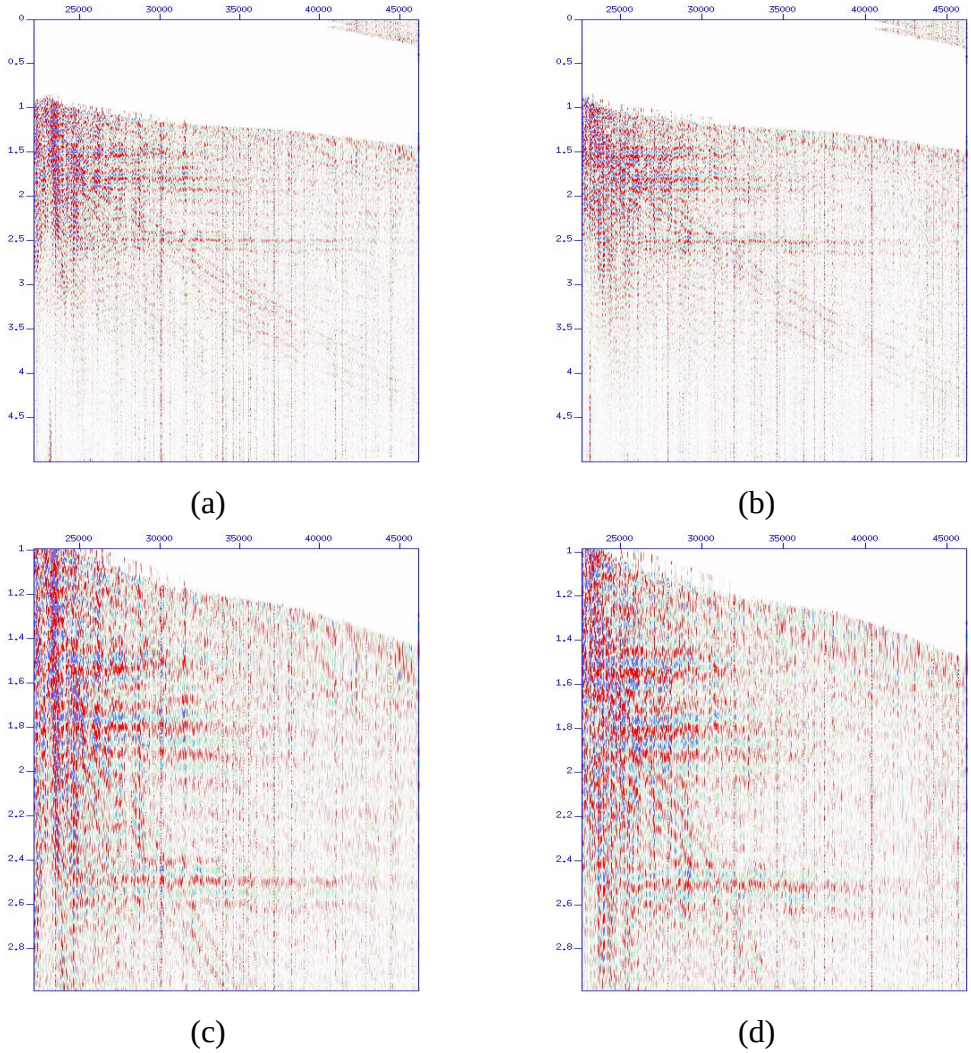

Figure 8- 28: NMO corrections for the P-SV2 components of the super-ACP gather 420-420 with and without the azimuthal compensation. The focused areas are enlarged in (c) and (d), respectively.

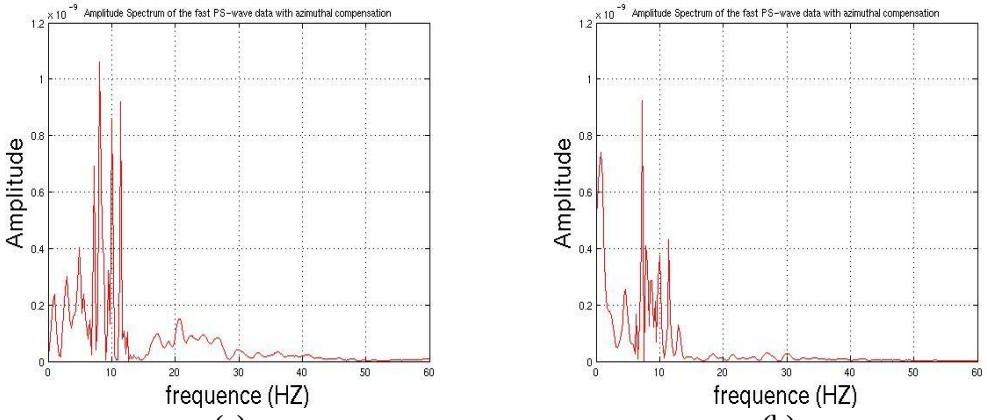

Figure 8- 29: Stack results of the P-SV1 component with (a) and without (b) azimuthal compensation.

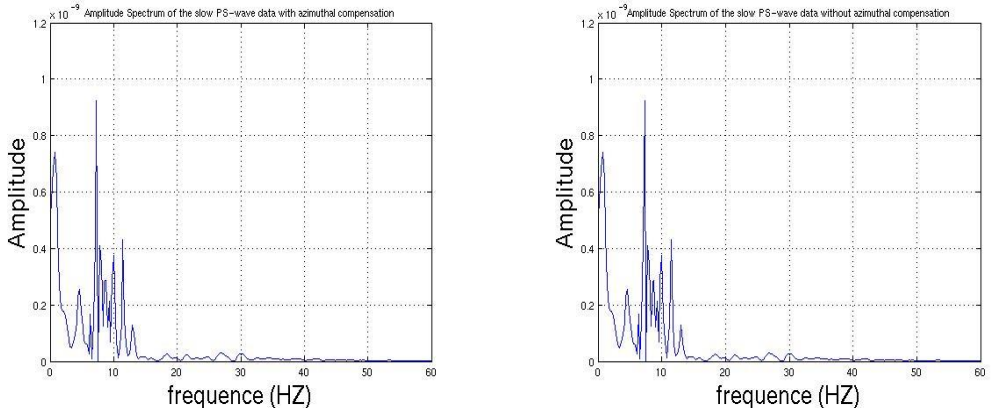

(a) (b)

Figure 8- 30: Stack results of the P-SV2 component with (a) and without (b) azimuthal compensation.

The same analysis and compensation were applied accordingly to other super-ACP gathers and elliptical velocity models for all ACP locations could be acquired. Then the velocity ellipses were applied to the NMO correction and stack of the dataset along a whole ACP line. The stack results of ACP line 420 are shown in Figure 8- 31, Figure 8- 32 and Figure 8- 33. Figure 8- 31 shows the P-SV1 component stack section. Figure 8- 32 shows results of the P-SV2 component. The stack sections of the radial and transverse components are also displayed in Figure 8- 33 for comparison. The stack section of the P-SV1 component is improved by applying the compensation for azimuthal variation. The resolution is enhanced, especially in the arched area of the anticline. The resolution enhancement for the deep events between 2.5s and 3s is not as significant as the resolution enhancement for the events between 1.5s and 2.5s. This implies that the deep events are suffering weaker anisotropy induced by fractures of relatively low intensity. The events around the ACP numbers ranging from 140 to 250 and 700 to 800 are not significantly improved. In particular, in the range of ACP numbers from 200 to 250, the resolution of the stack section is degraded by applying velocity ellipses. This might be caused by unreliable elliptical velocity models obtained from low-fold and narrow-azimuth super-ACP gathers. Therefore those velocity ellipses are not appropriate for improving imaging and inverting for fracture properties. It also indicates that wide-azimuth coverage is essential to the study of azimuthal anisotropy caused by vertical fractures. As discussed above, the P-SV2 component is less influenced by azimuthal variations. Therefore the imaging improvement of the P-SV2 stack section is not as distinct as

that of the P-SV1 component. However, similar enhancements of the resolution at arched areas of the anticline can be observed. Therefore, this implies that fractures in arched areas of the anticline are more developed.

The resolution of the transverse component data shown in Figure 8- (b) is lower than that of the radial, P-SV1 and P-SV2 components. Thus the transverse component is not appropriate for further processing and interpretation on the stack section. Comparing the radial component with the P-SV1 component, the latter would deliver similar improvements on the anticline area if azimuthal variations are compensated for. However, the improvement is hard to observe if conventional velocity analysis and NMO correction are applied to the P-SV1 component. Similarly, compared with the radial component data, the events around ACP numbers between 170 and 250 on the P-SV1 component are not well-focused. For the P-SV2 component, the anticline area is better delineated than the radial component when the azimuthal velocity model is applied. If azimuthal variations are not compensated for, the resolution on the radial component is higher than the resolution on the P-SV2 component. Therefore, the P-SV1 component is more appropriate to be used in subsequent processing and inversion in this field data study.

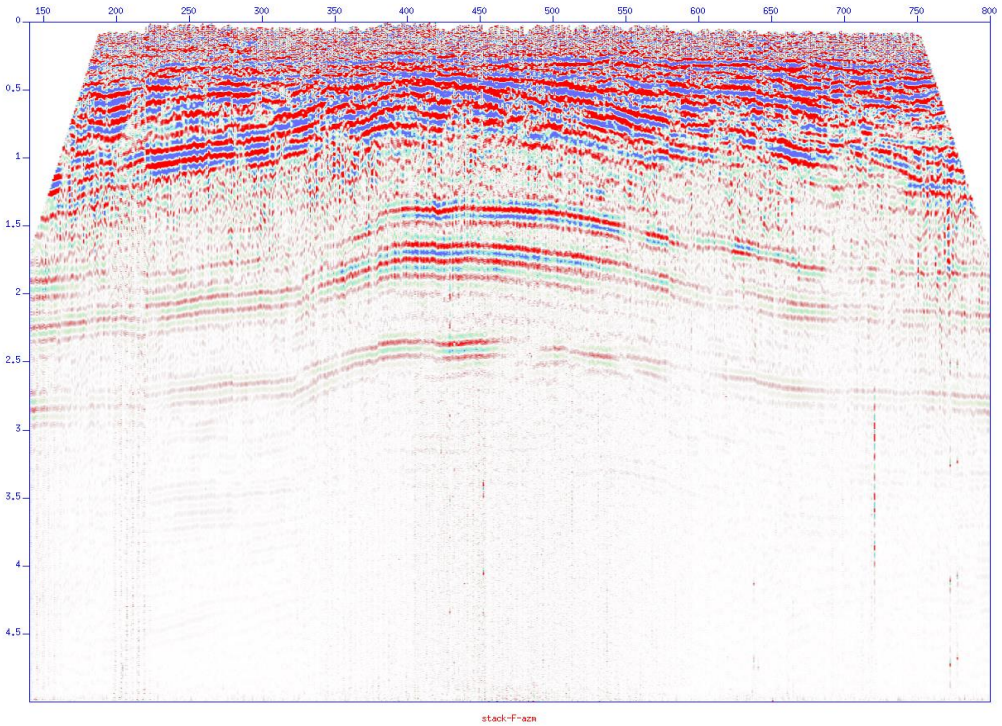

(a)

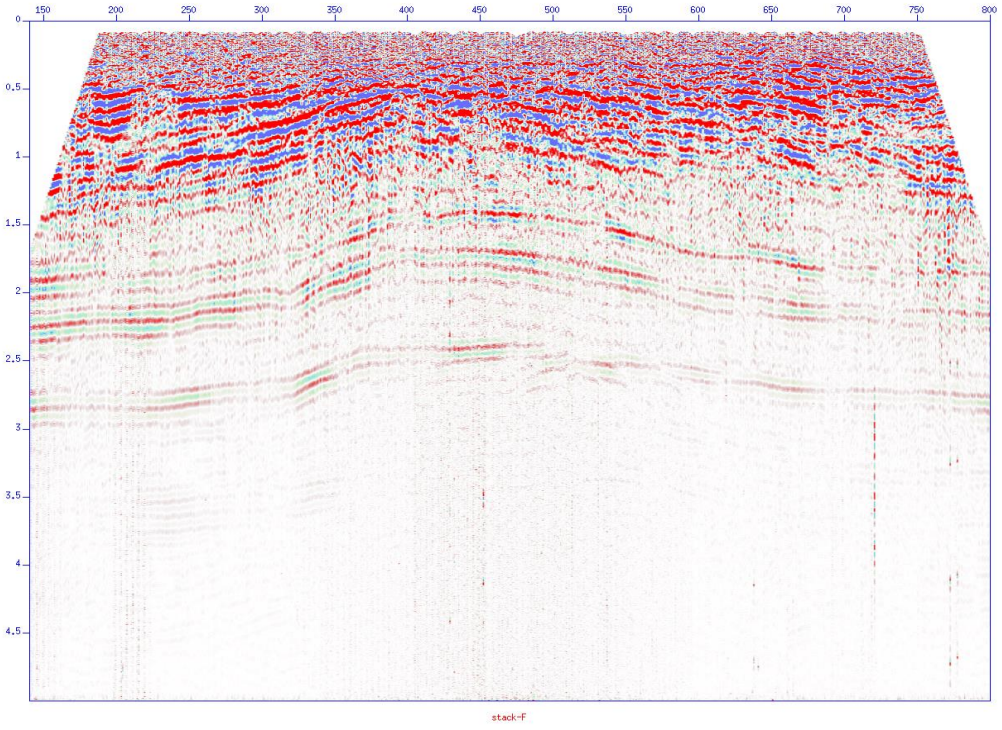

(b)

Figure 8- 31: Stack section of the P-SV1 component at ACP line 420 with (a) and without (b) azimuthal compensation

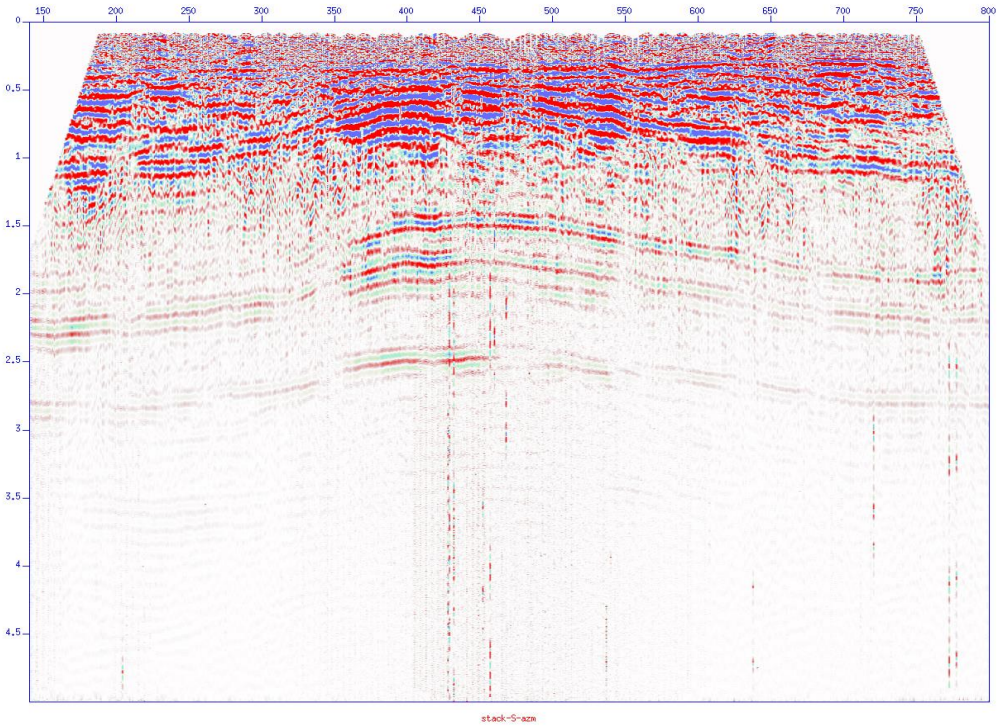

(a)

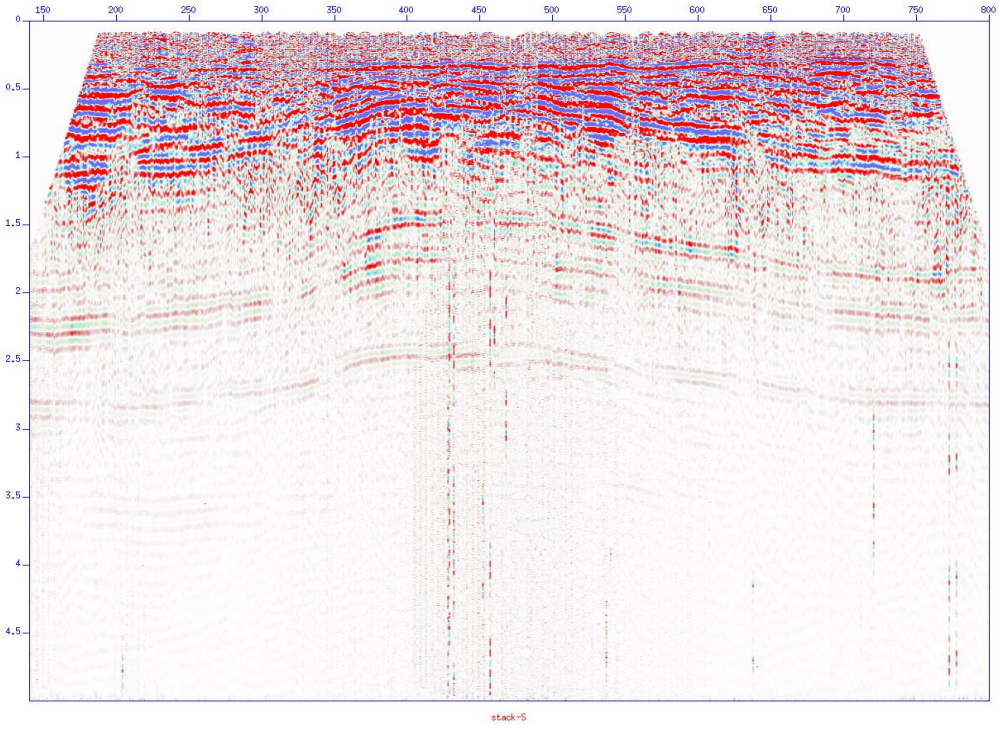

(b)

Figure 8- 32: Stack section of the P-SV2 component at ACP line 420 with (a) and without (b) azimuthal compensation

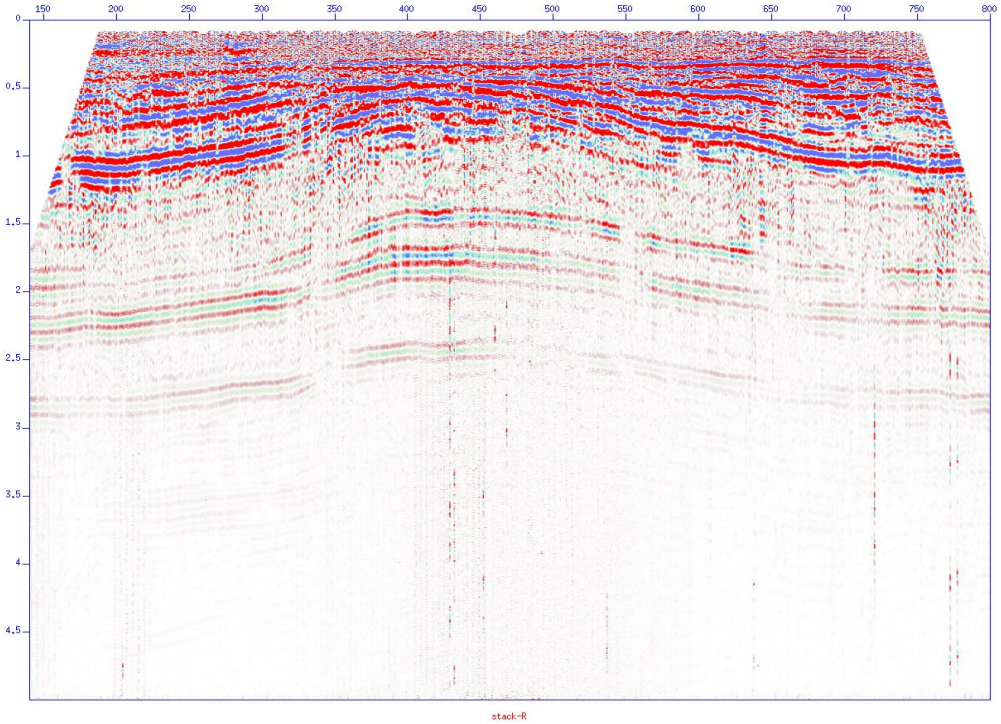

(a)

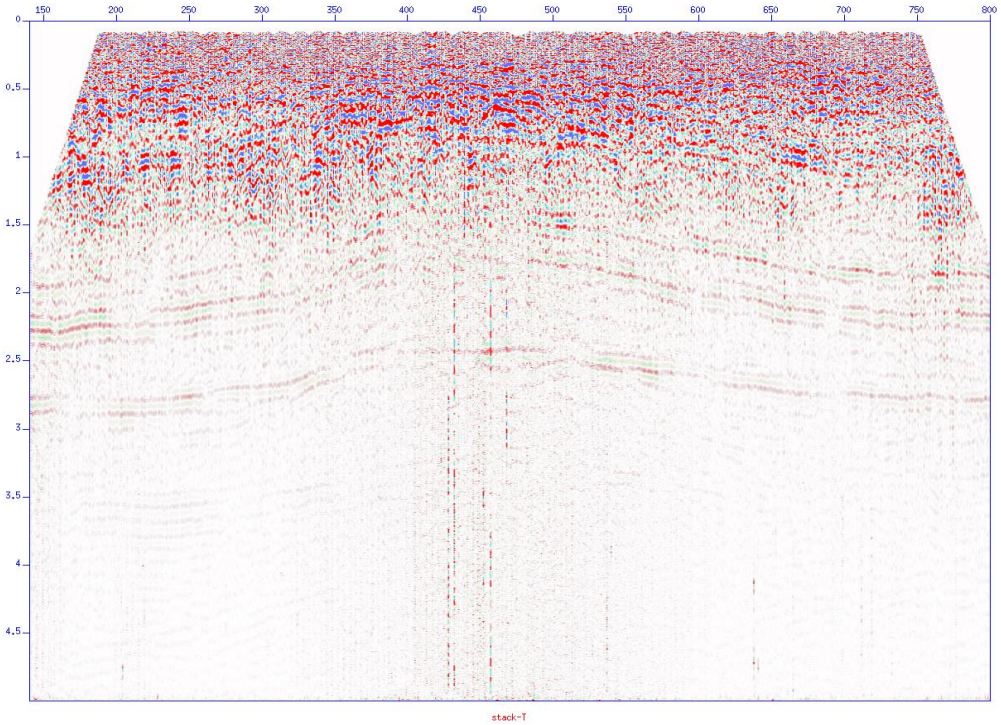

(b)

Figure 8- 33: Stack section of the radial (a) and transverse (b) components at ACP line 420 with conventional NMO correction and stack.

8.14 Fracture characterisation of one ACP line data

After applying azimuthal analysis to all super-ACP gathers along the ACP line 420, the parameters Δ and β can be obtained. The parameter Δ is called velocity perturbation, and is an estimation of the fracture density, and β represents the dominant fracture orientation. The results for the two parameters along ACP line 420 after interpolation are shown in Figure 8- 37and Figure 8- 35.

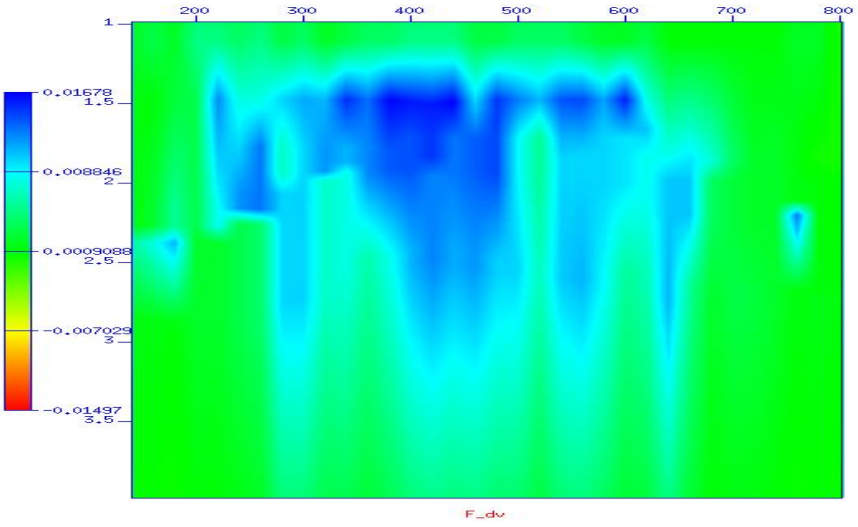

（a）

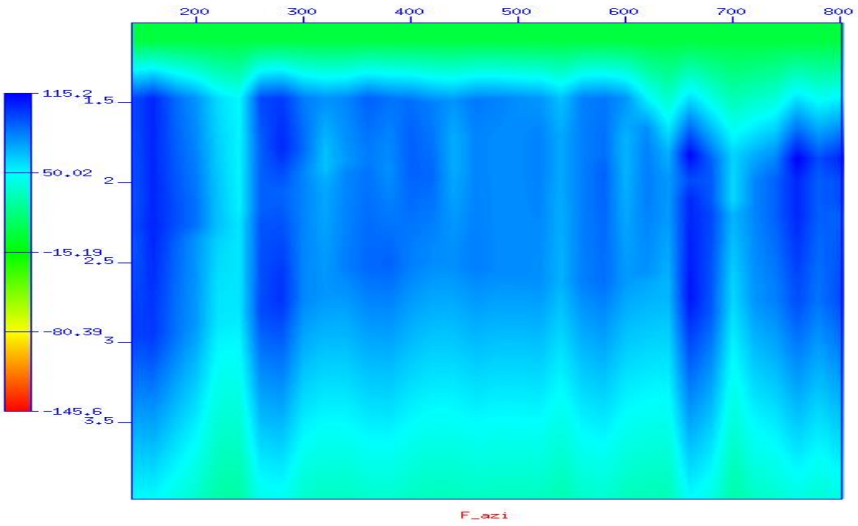

(b)

Figure 8- 34： Velocity perturbation (a) and fast direction (b) maps of the P-SV1 component along the ACP line 420

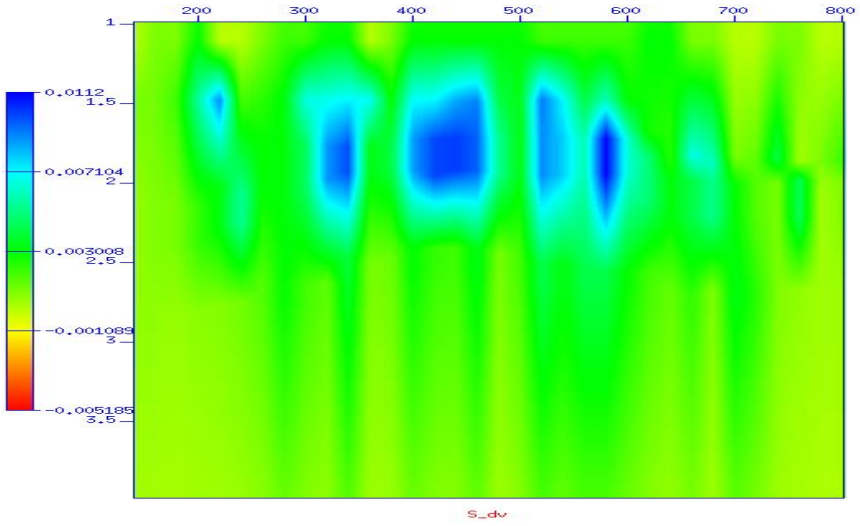

(a)

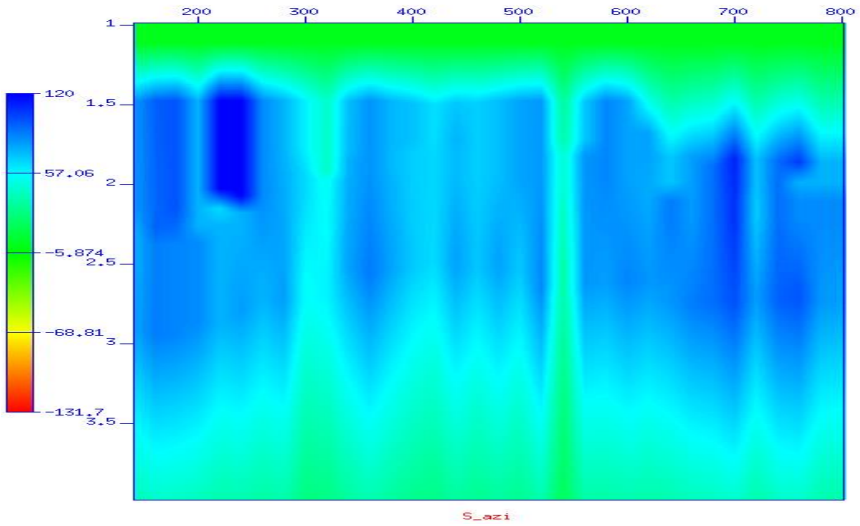

(b)

Figure 8- 35： Velocity perturbation (a) and fast direction (b) maps of the P-SV2 component along the ACP line 420

The P-SV1 component is displayed in Figure 8- 34 and the P-SV2 component is displayed in Figure 8- 35. For the P-SV1 component, velocity perturbations in the time window between 1.5s and 3.5s are approximately larger than zero and smaller than 0.017. Large-value perturbations are mainly located in the ACP range between 380 and 580 (Figure 8-), which corresponds to the arched anticline area shown in the previous stack results (e.g. Figure 8- 31). Specifically, the magnitude of the velocity perturbation decreases from the top of the anticline (about 1.55s) to the base of the anticline (about 2.5s). It implies that the top of the anticline suffers from more

significant azimuthal anisotropy, which is related to intensive fracturing and jointing induced by horizontal compressive stresses. In other words, imaging improvement in the area of the top of the anticline is more significant if compensation for the azimuthal anisotropy is applied. This conclusion has been proved by the improvement of stack results shown in Figure 8- . The fast direction, fitted by the least square method, is displayed in Figure 8- 34(b). It implies that the dominant fracture direction is generally in the range between 40° and 115°. The majority of fracture directions in the anticline area are larger than 50° and smaller than 95°, indicating a general NNE-NE fracture direction.

The velocity perturbation and fast direction parameters of the P-SV2 component along ACP line 420 are displayed in Figure 8- 35. It can be seen that the velocity perturbation parameters are all smaller than 0.012. This implies that the P-SV2 component is less affected by the azimuthal variation than the P-SV1 component. However, large perturbations can still be found in the anticline area. Similarly, velocity perturbation in the top of the anticline is smaller than the velocity perturbation in the base of the anticline. This is consistent with the P-SV1 component. It proves that this area is more influenced by fracturing effects. This area is also the drilling target-area for hydrocarbon exploration. Moreover, such small velocity perturbations may suffer from a low signal-to-noise ratio and low azimuthal coverage, resulting in unreliable fracture information. The fast direction fitted from the P-SV2 component is generally in the range between 30° and 120 °, indicating a NNE-NE-ENE fracture direction. This fracture direction range is larger than the fracture direction range fitted from the P-SV1 component. Moreover, its distribution in the anticline area is not as uniform as the distribution of the P-SV1 component, suggesting the fracture information acquired from the P-SV2 component might not be a robust parameter for hydrocarbon exploration.

8.15 Fracture characterisation of the whole survey area

Previous analysis of the velocity perturbation and the fast direction suggest that the anticline area displays significant azimuthal anisotropy. In other words, large

fracture densities are expected in this area. This is a result only concluded from ACP line 420. Similar processing procedures are applied to other super-ACP gathers to obtain the result for the whole survey area. The ACP line numbers range from 360 to 500. The distributions of velocity perturbations and fast directions can be obtained for individual lines, which are similar to the results shown in Figure 8- 34 and Figure 8- 35.

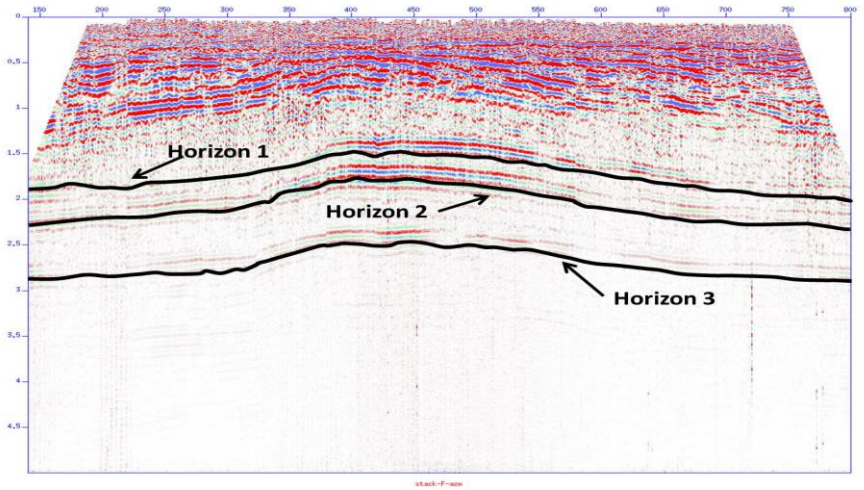

(a)

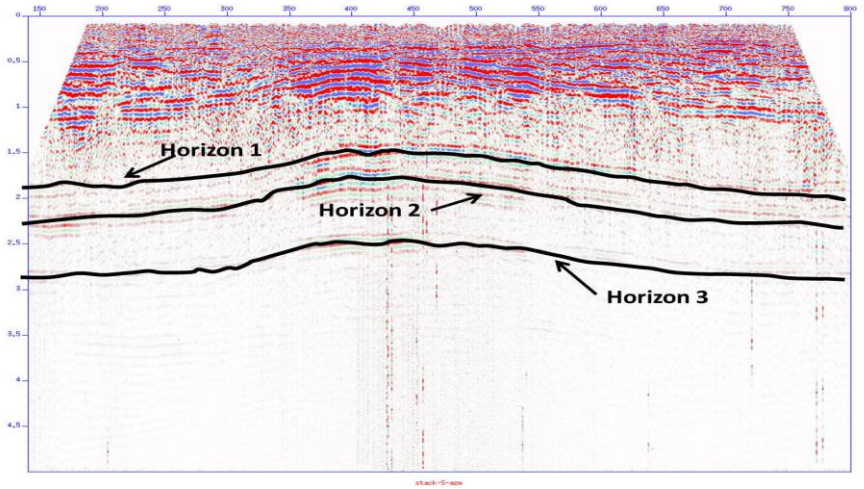

(b)

Figure 8- 36: Three different horizons in the P-SV1 (a) and P-SV2 (b) components used in fracture characterisation of the whole survey area.

Alternatively, focusing on anisotropic parameters within certain horizons can provide an important way to understand fracturing trends in the whole survey area. In this study, three different horizons are selected to reflect fracture information in the survey area. Black solid lines are drawn to delineate those three horizons for the P-

SV1 component in Figure 8- 36(a) and for the P-SV2 component in Figure 8- 36(b). Horizons 1, 2 and 3 cover the top, middle and base of the anticline area, accordingly. P-SV1 and P-SV2 components are both studied to deliver the most complete information on fracture characterisation.

Small and large ACP-number gathers, which occupy the boundary area of the survey, have limited folds and azimuthal coverage. Therefore the fracture parameters acquired from these gathers are not expected to provide reliable and consistent information. By considering this fact, the ACP number is confined to be between 200 and 700 for all the ACP lines in the whole survey area.

The distributions of velocity perturbations and fast directions of the area of interest have been studied and mapped. Selected horizons 1, 2 and 3 are individually shown for both P-SV1 (Figure 8- 37 and Figure 8- 38) and P-SV2 (Figure 8- 39 and Figure 8- 40) components. As previous discussion suggests, analysis of the azimuthal anisotropy is performed in the CxTools internal coordinate system, which is actually the inline-crossline coordinate system. The coordinates of two source-receiver pairs provided by geophysicists in Daqing Oilfield are used to calculate the angle between the UTM and CxTools coordinate systems. The angle is calculated as 19°, which is used to rotate the distribution maps from the inline-crossline coordinate system to the UTM coordinate system. Notice that the angle values shown in the colour bars of Figure 8- 38 and Figure 8- 40 are still based on the inline-crossline coordinate system.

For the P-SV1 component, the three horizons all provide high values of the velocity perturbation in the central area of the survey (Figure 8- 37). The maximum velocity perturbation of horizon 1 is about 0.0146. This value increases to 0.0165 for horizon 2. The maximum velocity perturbation of horizon 3 is 0.0126, which is lower than both horizon 1 and horizon 2. The velocity perturbations on horizon 1 which are larger than 0.012, are mainly located in the central zone. This region is roughly confined between ACP 360-440 and ACP lines 400-460, which is also considered as the target anticline area. Fractures of large fracture density are more developed in this area, which is very important to hydrocarbon exploration and extraction. Careful observation finds that this zone follows a general NNE direction. Besides, a small isolated zone, where velocity perturbations are larger than 0.012, can be found in the

northeast of the central zone. Compared with horizon 1, horizon 2 generally provides increased velocity perturbations. The zone where velocity values are approximately between 0.012 and 0.018 has a wider coverage on the distribution map. It covers the range between ACP 340-540 and ACP lines 380-480. This suggests that the zone with high fracture densities in horizon 2 has a larger lateral extent. The spread of this zone is oriented in an approximately NE direction. A remote zone of relatively high velocity perturbations is located in the northeast of the central zone. Similarly, high velocity perturbations in horizon 3 are mainly in the central zone, but their values are generally smaller. The spread of this zone follows a similar orientation, which is generally aligned with the NE-SW direction. From horizon 1 to horizon 3, the orientation of the zone, where high velocity perturbations and high fracture densities are present, migrated from the NNE direction to the NE direction. Moreover, it is clear that the asymmetry caused by fractures and their locations is depth-dependent.

The fast directions fitted from the analysis of P-SV1 components are displayed in Figure 8- 38. The relationship between the distribution of fast directions and the anticline area is not as clear as the relationship between the distribution of velocity perturbations and the anticline area. Three horizons provide similar trends for the fast direction, which suggests that the depth-dependence of the dominant fracture orientation is not very significant. This also proves that the accuracy of the azimuthal analysis based on the HTI assumption is acceptable. Small values of velocity perturbations result in poor values of fitted fast directions. Therefore, the distribution of fast directions is found to be less uniform in the boundary area of the survey for all three horizons. Moreover, the central zone, affected by stronger azimuthal anisotropy, shows a relatively uniform distribution of fast directions. The dominant fracture orientation of the central zone is approximately NE-SW. Outside the central zone, a general trend of NEE-SWW orientation can be observed.

The results of the P-SV2 component (Figure 8- 39 and Figure 8- 40) are not the same as for the P-SV1 component. The overall velocity perturbations of the P-SV1 component are smaller than the overall velocity perturbations of the P-SV2 component. The calculated maximum velocity perturbations of the three horizons 1-3 are 0.0101, 0.0113 and 0.0041, respectively. Thus the velocity perturbations of

horizon 2 are larger than the velocity perturbations of both horizon 1 and 3. For all three horizons, large velocity perturbations are mainly found in the central zone, which is consistent with the analysis of the P-SV1 component. However, some small zones containing large values are also found outside the central anticline area. For horizons 1 and 3, the orientations are generally aligned in the NE-SW direction. They change into the N-S direction in horizon 2.

The fast directions fitted from the P-SV2 component are unclear for a conclusion on its relationship with fractured zones. But in the central area, the dominant fracture orientations are NE-SW, which is consistent with the P-SV1 component. This implies that the P-SV1 and P-SV2 components follow a similar pattern of azimuthal variation in this study.

For comparison, converted-wave splitting analysis is also applied to all super-ACP gathers throughout the same survey area. The time delays between the P-SV1 and P-SV2 components, and the dominant fracture directions of all super-ACP gathers are acquired and mapped into Figure 8- 41. The largest value of time delay is about 55ms. It is not difficult to find that the distribution of large-value time delays is relatively uniform in the central zone between ACP 340-560 and ACP lines 320-480. The spread in this central zone is approximately oriented in the NNE-SSW direction. This result is in general agreement with the results obtained from azimuthal analysis of the P-SV1 and P-SV2 components. A remote zone with large time delays is also found in the east of the central zone.

The converted-wave splitting analysis provides more uniform distributions of dominant fracture directions. The central zone follows an approximate NE-SW direction, which is in agreement with the azimuthal analysis of both the P-SV1 and P-SV2 components. Moreover, there are fewer places where dominant fracture directions rapidly change.

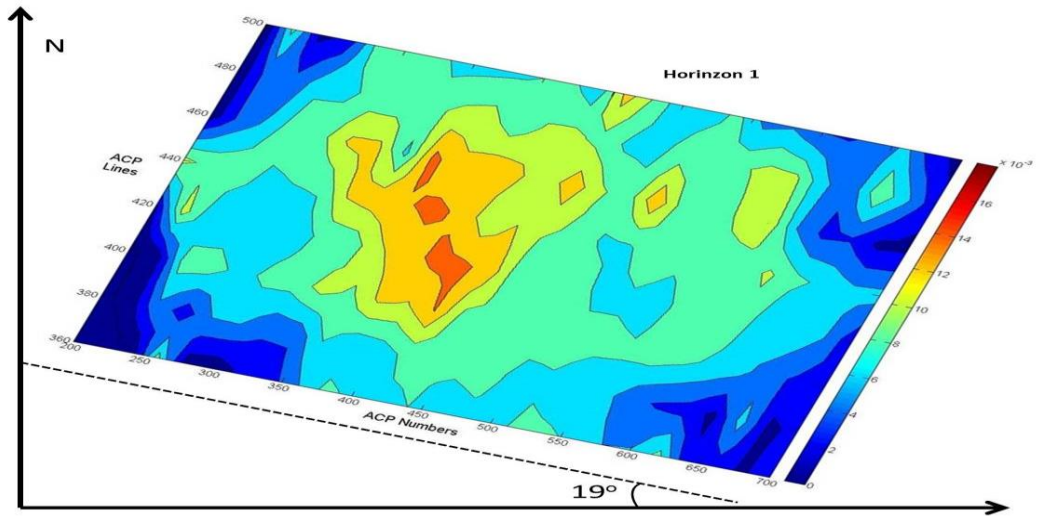

(a)

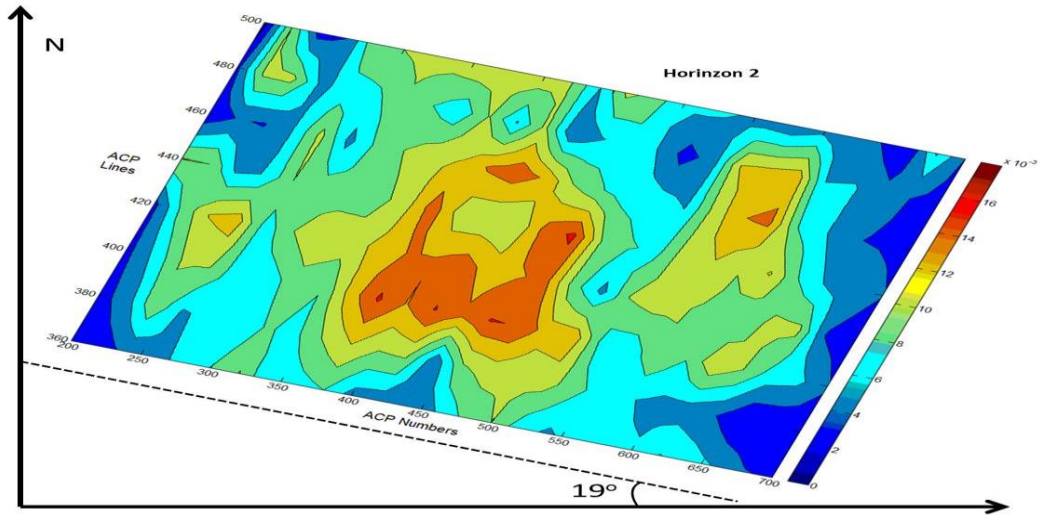

(b)

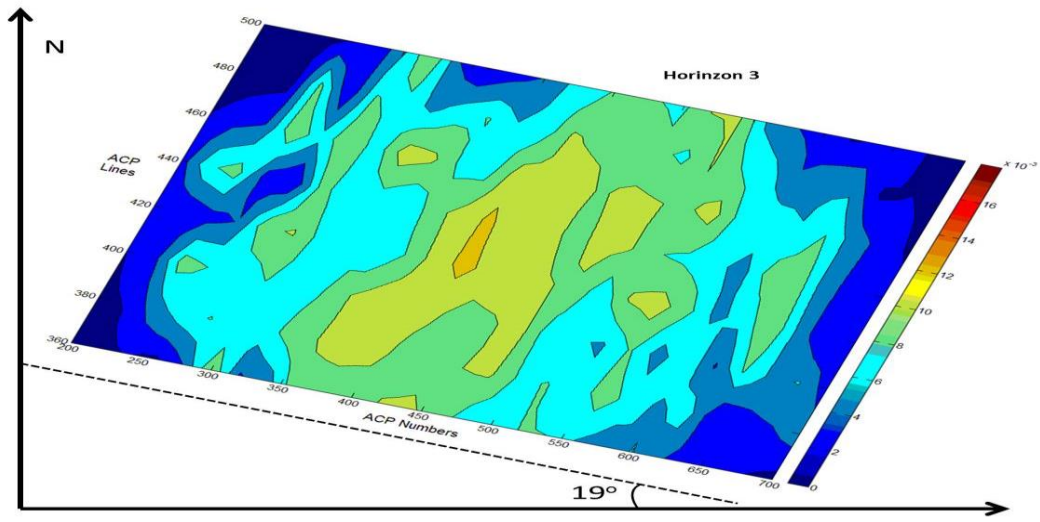

(c)

Figure 8- 37: Distribution maps of velocity perturbations of three horizons for the P-SV1 component.

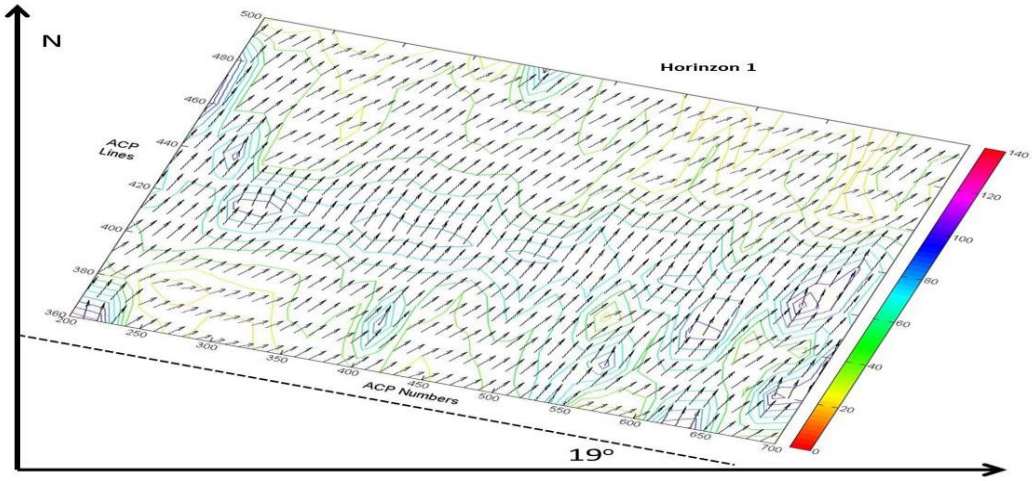

(a)

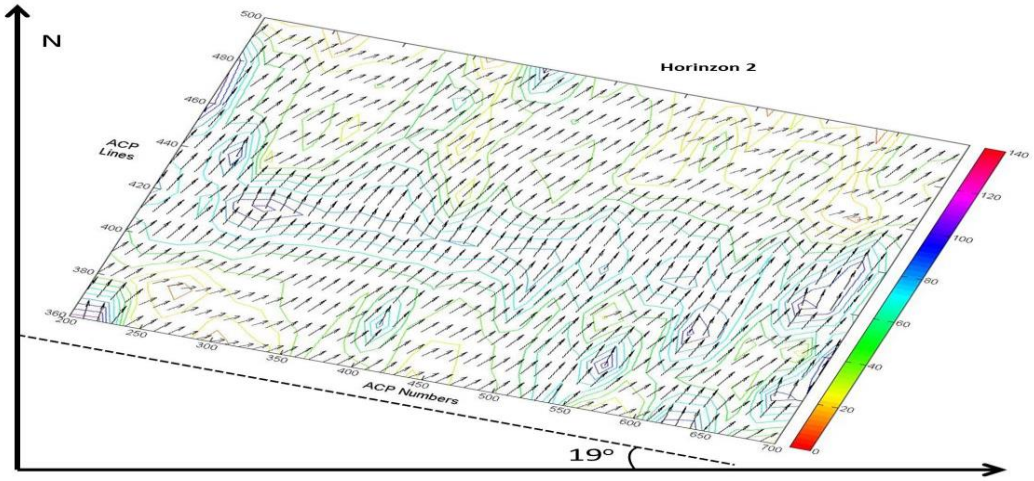

(b)

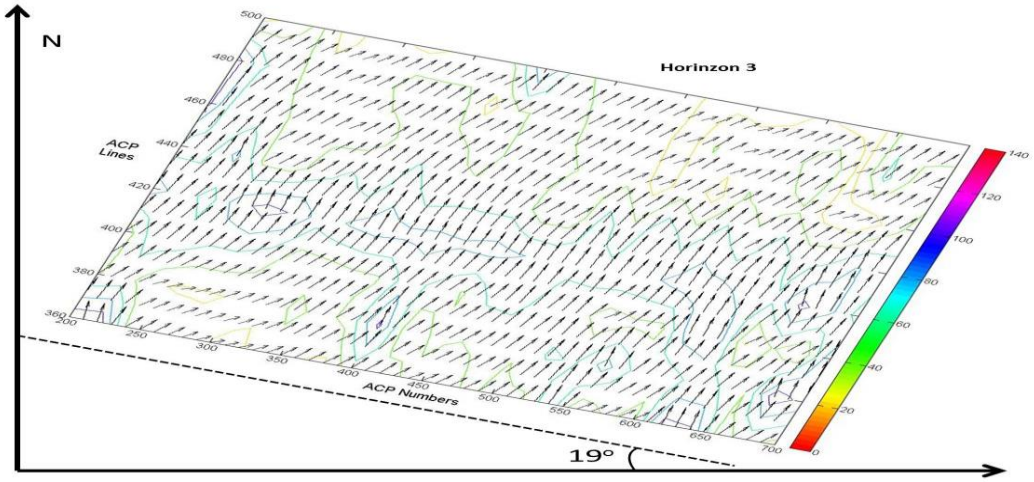

(c)

Figure 8- 38: Distribution maps of fast directions of three horizons for the P-SV1 component (Numbers on the colour bar represent the angle values based on the inline-crossline coordinate systems).

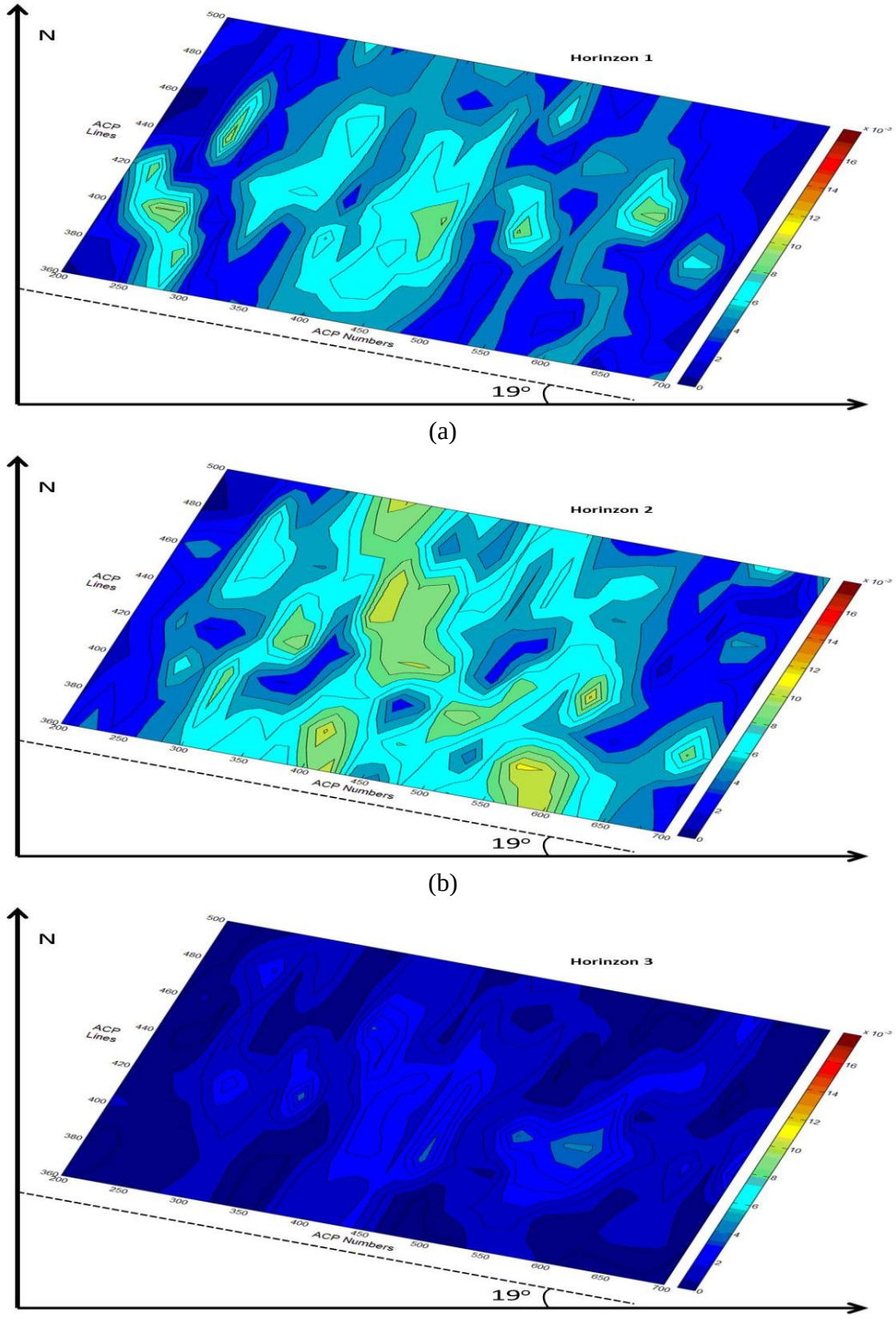

Figure 8- 39: Distribution maps of velocity perturbations of three horizons for the P-SV2 component

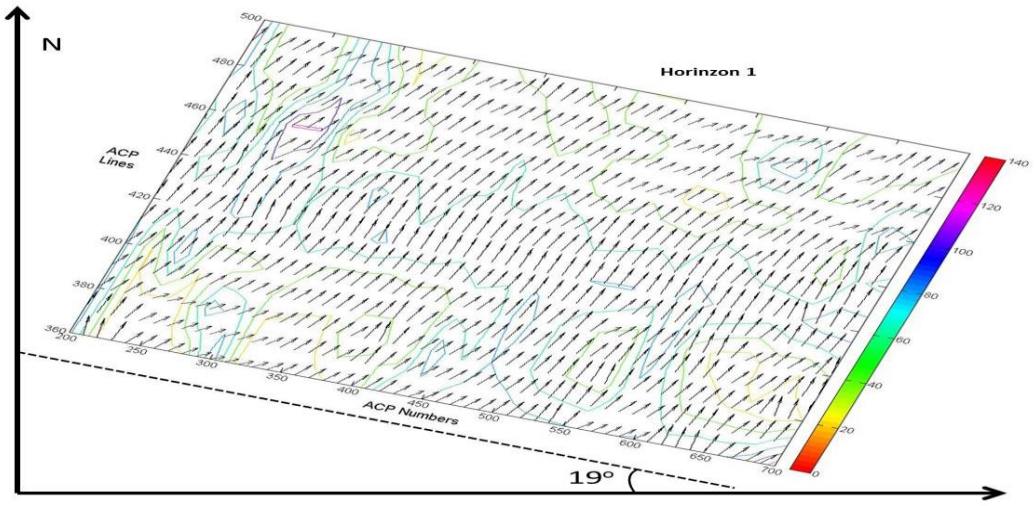

(a)

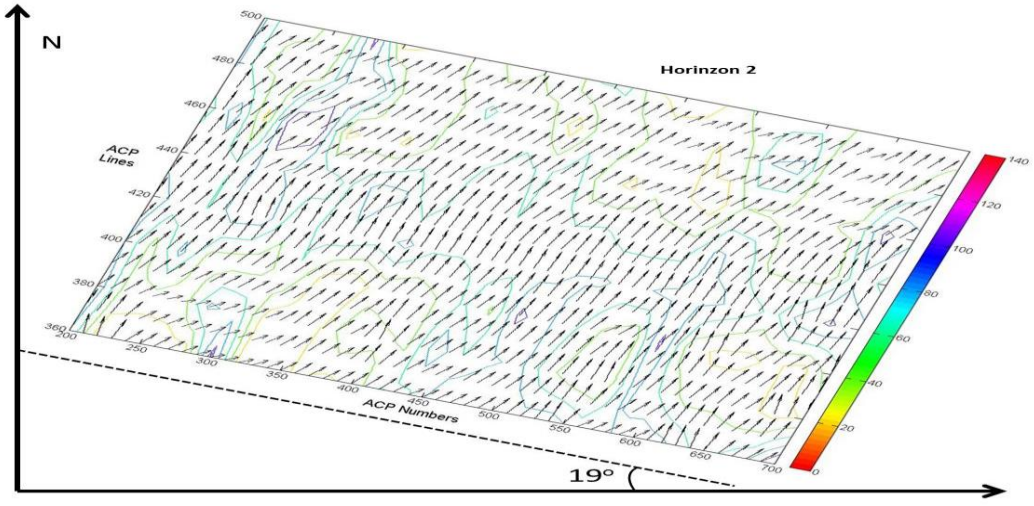

(b)

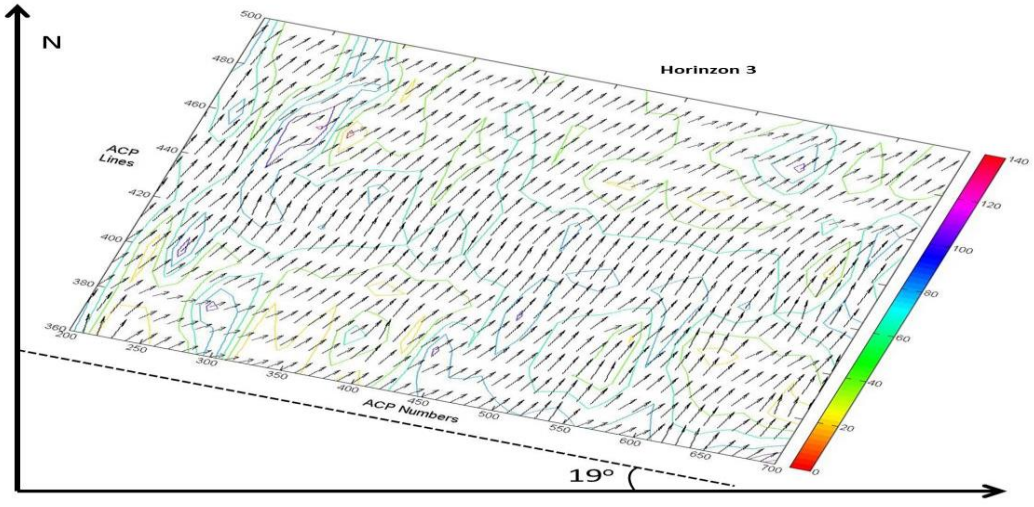

(c)

Figure 8- 40: Distribution maps of fast directions of three horizons for the P-SV2 component (Numbers on the colour bar represent the angle values based on the inline-crossline coordinate systems).

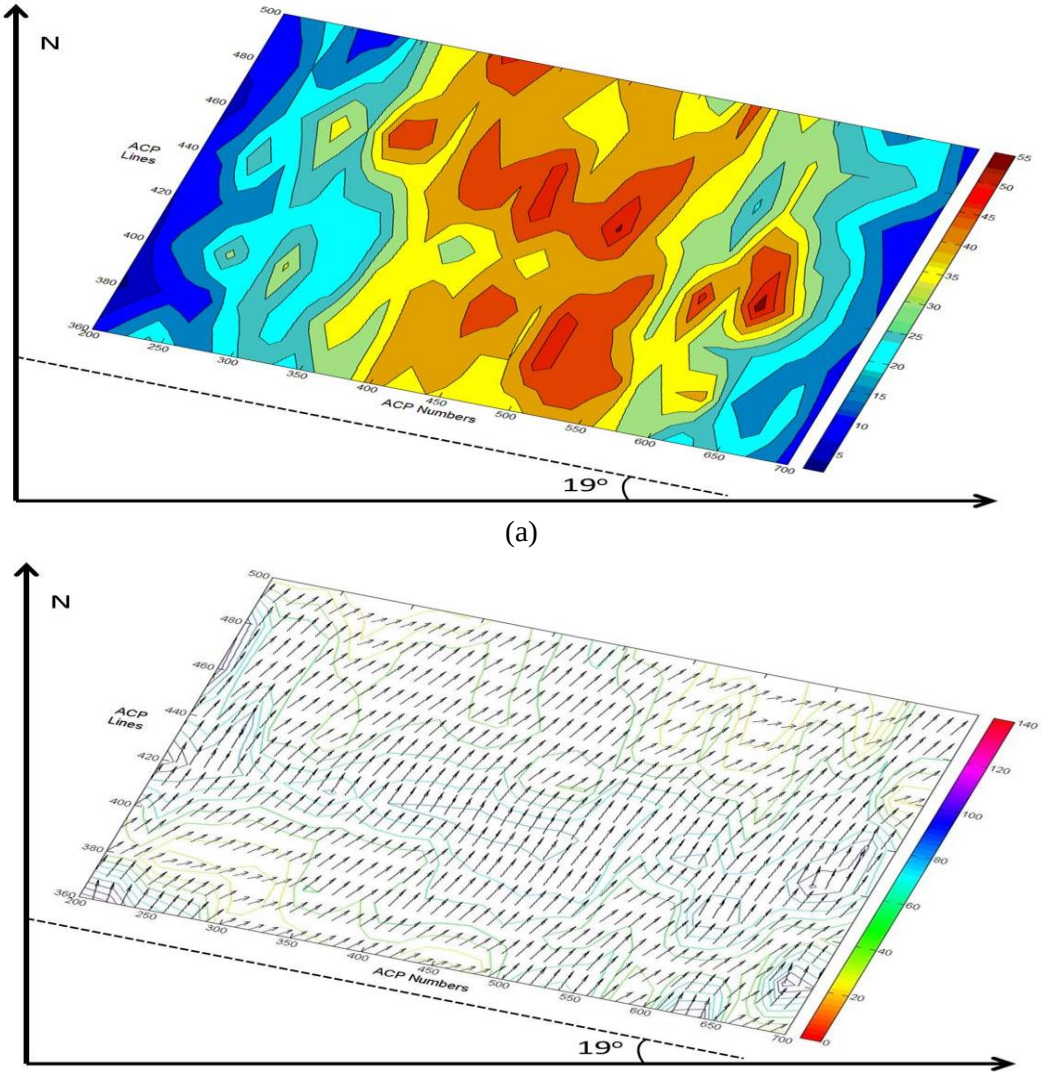

Figure 8- 41: Distribution maps of time delays between the P-SV1 and P-SV2 components (a), and the fast directions from splitting analysis (b). (Numbers on the colour bar in (a) and (b) represent time delays (ms) and angle values based on the inline-crossline coordinate systems, respectively.

8.16 Geological constraints on the fracture characterization results

In the assumption of transverse isotropy with a horizontal symmetry axis (HTI), the present-day maximum horizontal stress is parallel to the plane of isotropy and perpendicular to the symmetry axis. This understanding is essential to the exploration of fractured reservoirs. The reason is the minimum normal stress can be found perpendicular to the fracture planes, through which fluid flows have least resistance to pass. Therefore regional or tectonic stress-field maps can be used to provide

geological constraints on the fracture characterisation obtained from seismic data processing and interpretation. Although complex geological structures could significantly complicate the stress-field and negatively influence the relationship between the stress-field and fracture directions inverted from seismic data, some case studies have provided some good correlation between the two types of fracture information (Ouenes et al., 2004; Rogers et al., 2003). Therefore the stress-field information can also be used in this study for comparison with the fracture characterisation results obtained from the analysis of the azimuthal variation and converted-wave splitting.

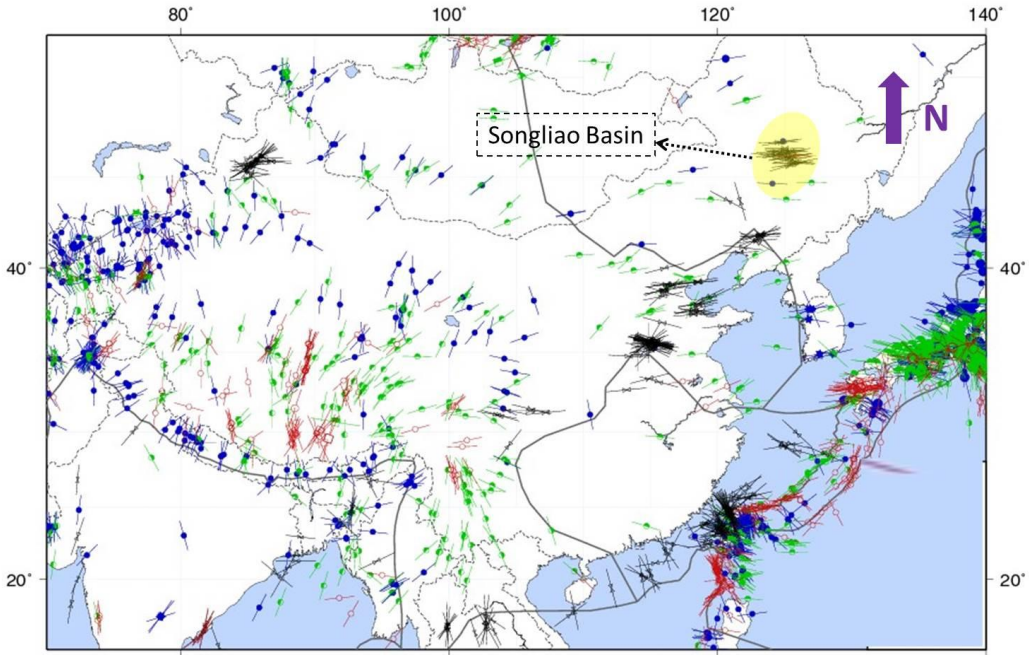

Figure 8- 42: Map of maximum stress directions in China. The image is modified from the work by Heidbach et al (2008)and the Songliao basin is highlighted in the yellow area. Blue, red, green and black indicators represent NF(normal faulting), SS(strike-slip), TF(thrust faulting) and U(unknown) tectonic stress regime, accordingly

Continuous hydrocarbon exploration has surely caused new extensive fractures in Daqing Oilfield. Thus the seismic data includes the overall effect of both natural fractures and new fractures induced by exploration activities. Earthquake focal mechanisms have been well studied, which provides a stress-field map for China (Heidbach et al., 2008). The map showing the maximum stress directions in China is displayed in Figure 8- 42. Songliao basin, where the Daqing Oilfield is developed, is

emphasized in the yellow area. The maximum stress directions generally follow an E-ENE direction in this area, which is close to the dominant NE-SW fracture direction acquired from the above analysis. This comparison supports a positive correlation between the maximum stress directions and dominant fracture directions. However, other types of data including well log data and core data might also be needed to confirm the validity of fracture properties.

8.17 Summary

Compensation for azimuthal anisotropy was applied to the PS-converted seismic data from Daqing Oilfield. The geological background of Songliao basin, where Daqing oilfield is located, was discussed in order to provide additional information on the natural fractures created by tectonic activities. The survey parameters and data quality were all evaluated to build a reasonable processing flow and analysis procedure.

The dataset was sorted into super-ACP gathers by combining certain ACPs and ACP lines. Clear polarity reversals are observed on transverse components, which indicate the PS-converted wave splitting. Horizontal rotation was performed to obtain the fast P-SV1 component and slow P-SV2 component. Azimuthal velocity analysis was applied to both P-SV1 and P-SV2 components of each super-ACP gather. An elliptical velocity model was fitted by a least-square method and used to compensate for the azimuthal variation. The NMO correction and stack were improved by using velocity ellipses in the area with high folds and wide azimuth coverage. Thus the events are better corrected and the seismic resolution of the stacked section is increased. In the area with low fold and narrow azimuth coverage, the least-square method was not capable of providing reliable anisotropic parameters and failed to improve the imaging. This was caused by significant uncertainties due to poor hand-picked velocity models. Thus the fracture information established from those low-quality super-ACP gathers might not be accurate.

Observations of P-SV1 and P-SV2 components suggest that both have a similar pattern of azimuthal variation. Compared with the P-SV2 component, the P-SV1 component exhibits stronger azimuthal anisotropy and thus provides more significant imaging improvement. The relatively weak azimuthal anisotropy of the P-SV2

component is very difficult to be studied and compensated for. Therefore using the P-SV2 component is not as efficient as using the P-SV1 component in inverting anisotropic parameters for fracture information. The processing procedure was then applied to all super-ACP gathers along an ACP line. The major imaging improvements are mainly in the anticline area where more significant azimuthal anisotropy is expected. Continuing the azimuthal analysis to the rest of the ACP lines, anisotropic parameters throughout the survey area were acquired to provide fracture information. Three different horizons of both P-SV1 and P-SV2 components were studied and compared. The azimuthal anisotropy for horizon 2 is generally larger than the azimuthal anisotropy for horizons 1 and 2, which is true for both P-SV1 and P-SV2 components. This suggests that the fracture density in the fracture system is depth-dependent. Besides, the azimuthal anisotropy distribution of P-SV2 components is less uniform, which is caused by poor fitting of small values of anisotropic parameters. Great attention was paid to the anticline area, where strong azimuthal anisotropy was found. From horizons 1 to 3, the directional spread in this target area slightly migrates from the NNE direction to the NE direction, which implies that the lateral extents of large fracture densities may be also affected by a small variation with depth. The dominant fracture directions in this area for both P-SV1 and P-SV2 components are approximately aligned with the NE-SW direction. However, the distribution of the fracture directions outside the target area are poorly characterized, which might result in failure to provide valuable information.

The converted-wave splitting effect was also considered and studied to provide relevant fracture information. The distribution of the time delays suggests a similar trend of high fracture densities with a NNE direction. The fracture directions are generally aligned with the NE-SW direction, which coincides with the azimuthal analysis of both P-SV1 and P-SV2 components. The dominant NE-SW fracture direction is close to the E-ENE direction, which is the maximum stress direction in Songliao basin. Therefore the maximum stress direction strongly supports the effectiveness of the fracture information acquired from azimuthal analysis. Moreover, the splitting analysis is a more robust method for fractured reservoir characterisation.

However, additional efforts could still be applied to the Daqing data to improve the fracture characterisation. The ground roll contained in the dataset could be suppressed to increase the signal-to-noise ratio. This could benefit the observation and analysis of weak azimuthal anisotropy. Velocity picking for different azimuth bins is time-consuming. It also brings a certain amount of error to the elliptical model. This estimation method could be improved by incorporating the velocity analysis of all azimuth bins together. This could save a great deal of time and energy. Moreover, other types of data could be studied to provide necessary calibration, which would be very beneficial for the exploration of fractured reservoirs.

Chapter 9

Conclusions and suggestions for future work

9.1 Conclusions

In this chapter, I summarise my thesis findings and give suggestions for future work in this area of research.

Robustness of PS-converted wave splitting for fracture detection

PS-converted wave splitting analysis is a robust method to detect fractures. The fracture directions and densities can be estimated from the splitting analysis. By compensating for the time delay between split PS-converted waves, the imaging quality can be improved. The splitting analysis was applied to Sanhu 3D3C data. Direct processing of the radial component data degrades imaging quality and seismic resolution. By applying compensation for PS-converted wave splitting, the imaging quality is significantly improved. Fracture properties acquired from the splitting analysis also show good correlation with information on the stress field in the local area.

Azimuthal variations of PS-converted waves in HTI media

Due to shear-wave splitting, both fast P-SV1 and slow P-SV2 waves are recorded on both radial and transverse components in HTI media. The P-SV1 component is polarised in the fracture direction while the P-SV2 component is polarised in the direction perpendicular to the fracture direction. The NMO velocities of both P-SV1 and P-SV2 components can be approximated as velocity ellipses in the azimuthal plane. Velocity ellipses can be used to compensate for azimuthal variation, which is beneficial for imaging quality. Moreover, real processing can be made easier by using a simplified cosine equation instead of the exact elliptical equation. However, the simplified cosine equation is only valid when the seismic anisotropy is weak.

Analysis of the azimuthal variations of velocities in PS-converted wave seismic data

A processing workflow has been developed to compensate for azimuthal variations of PS-converted wave seismic data. It includes the separation of split PS-converted waves, azimuthal binning, azimuthal velocity analysis, velocity ellipse fitting, and applying velocity ellipses to the NMO correction and stack. Azimuthal variations of P-SV1 and P-SV2 waves are complicated by PS-converted wave splitting. It is necessary to separate them from each other before applying any azimuthal analysis. Azimuthal binning, in which a certain azimuth range is regarded as a single common azimuth angle, is also important in azimuthal analysis. The choice of bin size is a compromise between the accuracy of analysis and an adequate signal-to-noise ratio. Velocity models acquired from azimuthal velocity analysis are fitted into velocity ellipses by using a least-square fitting method. The accuracy of this method is affected by velocity errors, which are especially significant for the velocity perturbation parameter. Using synthetic data involving both dry and water-saturated fractures, imaging quality was improved by applying compensation for azimuthal variations. The improvement was found in both NMO-corrected data and the amplitude spectrum of stacked data.

Analysis of azimuthal anisotropy for fracture detection

Azimuthal variations and PS-converted wave splitting can be both studied to determine fracture properties. PS-converted wave splitting analysis is a more robust method to characterise fractures but it is not sensitive to fluid saturation. Azimuthal parameters obtained from the analysis of azimuthal variations can also be related to fracture properties. However, small magnitudes of azimuthal variations can introduce significant errors.

P-wave azimuthal variation is found to be greater for dry fractures than water-saturated fractures, but it is not sufficient to discriminate between fracture saturations. PS-converted waves are sensitive to fluid saturations, and azimuthal variations of both P-SV1 and P-SV2 waves are greater for dry fractures than for water-saturated fractures. More importantly, P-SV1 and P-SV2 waves exhibit in-phase azimuthal variations in dry fractures but out-of-phase azimuthal variations in water-saturated fractures. This important fact could provide a new way of distinguishing between oil-filled and gas-filled fractures using PS-converted wave data.

Layer-stripping method for compensation for azimuthal anisotropy

A layer-stripping method has been developed, to use when multiple HTI layers are involved. The azimuthal anisotropy induced by the lower HTI layers is affected by the upper HTI layers. Direct analysis could introduce inaccurate fracture properties for the lower HTI layers. By applying the layer-stripping algorithm, splitting effects and azimuthal variations are all compensated for. Moreover, the real fracture properties of the lower HTI layers can be successfully obtained.

Field data applications

Analysis azimuthal variations was applied to Daqing 3D3C seismic data. Azimuthal variations of PS-converted waves were found on both radial and transverse components. In particular, the polarisation reversals are clearly shown on the

transverse components. By horizontal rotation, azimuthal variations of individual P-SV1 and P-SV2 components were studied and compensated for. The imaging quality is improved, especially in the anticline area. P-SV2 waves suffer weaker azimuthal variations, and this causes the imaging improvement to be smaller in the P-SV2 component than in the P-SV1 component.

Dominant fracture directions are obtained from the azimuthal analysis, and these are generally aligned in the NE-SW direction. This result is close to the E-ENE direction, which is the maximum stress direction of the local stress field. Velocity perturbations, which are related to fracture densities, have higher values along an approximate NE-NNE direction. This result provides information on the possible extent of the anticline area, where intensive fractures could be developed. Fracture properties obtained from PS-converted wave splitting are well-correlated to the local stress field. This proves that more robust fracture information is obtained by PS-converted wave splitting analysis.

9.2 Suggestions for future work

This thesis analyses the azimuthal variation of PS-converted waves in the presence of azimuthal anisotropy, which can be compensated for and analysed in order to characterise fractured reservoirs. However, there are still a few issues which need to be studied to get a better understanding of azimuthal anisotropy from PS-converted wave seismic data. I give the following suggestions for future work:

- Azimuthal variations of PS-converted wave amplitudes can also be studied to obtain fracture properties. They could provide additional valuable information on fracture characterisation, which can be integrated into a multi-attribute fracture characterisation system.
- Analysis of the azimuthal anisotropy of PS-converted waves can be further extended to orthorhombic media, so using a more realistic anisotropic model for fractured reservoir characterisation.
- Responses of azimuthal variations of PS-converted waves for different fracture saturations can be modelled and studied. This could improve discrimination between different fracture saturations, which is very important in reservoir characterisation and hydrocarbon production.

The layer-stripping method could be carefully implemented into real data studies, although practical issues may arise, which might degrade the imaging quality

References

Alford, R., Shear data in the presence of azimuthal anisotropy: Dilley Texas, *in* Proceedings 1986 SEG Annual Meeting1986, Society of Exploration Geophysicists.

Alkhalifah, T., and Tsvankin, I., 1995, Velocity analysis for transversely isotropic media: Geophysics, v. 60, no. 5, p. 1550-1566.

Bakulin, A., Grechka, V., and Tsvankin, I., 2000, Estimation of fracture parameters from reflection seismic data-Part I: HTI model due to a single fracture set: Geophysics, v. 65, no. 6, p. 1788-1802.

Bale, R., Gratacos, B., Mattocks, B., Roche, S., Poplavskii, K., and Li, X., 2009, Shear wave splitting applications for fracture analysis and improved imaging: Some onshore examples: first break, v. 27, no. 9.

Barkved, O., Bartman, B., Compani, B., Gaiser, J., Van Dok, R., Johns, T., Kristiansen, P., Probert, T., and Thompson, M., 2004, The many facets of multicomponent seismic data: Oilfield Review, v. 5, p. 42-56.

Booth, D. C., and Crampin, S., 1985, Shear-wave polarizations on a curved wavefront at an isotropic free surface: Geophysical Journal International, v. 83, no. 1, p. 31-45.

Burchfiel, B. C., and Wang, E., 2008, Investigations into the tectonics of the Tibetan plateau, GSA Bookstore.

Chapman, M., 2003, Frequency-dependent anisotropy due to meso-scale fractures in the presence of equant porosity: Geophysical Prospecting, v. 51, no. 5, p. 369-379.

Cheng, B., Xu, T., and Tang, J., 2009, Splitting Estimation and Compensation of Converted Wave in Multilayer Fracture Media: A Numerical Modeling Study, Beijing 2009 International Geophysical Conference and Exposition: Beijing, China, p. 159-159.

Chi-Tung, T., Yu-Ming, C., Kwei-Lin, H., and Fu-Tian, F., 1979, On the tectonic stress field in China and its relation to plate movement: Physics of the Earth and planetary Interiors, v. 18, no. 4, p. 257-273.

Corrigan, D., Withers, R., Darnall, J., and Skopinski, T., Fracture mapping from azimuthal velocity analysis using 3D surface seismic data, *in* Proceedings 1996 SEG Annual Meeting1996, Society of Exploration Geophysicists.

Crampin, S., 1984, An introduction to wave propagation in anisotropic media: Geophysical Journal International, v. 76, no. 1, p. 17-28.

-, 1993, A review of the effects of crack geometry on wave propagation through aligned cracks: Can. J. Expl. Geophys, v. 29, p. 3-17.

-, 1994, The fracture criticality of crustal rocks: Geophysical Journal International, v. 118, no. 2, p. 428-438.

Dai, H., and Li, X.-Y., 2010, A practical approach to compensate for diodic effects of PS converted waves: The Leading Edge, v. 29, no. 11, p. 1350-1353.

Dai, H., Li, X., Yu, C., and Wang, J., A Practical Approach to Compensate for the Azimuth Anisotropy in 3D PS Converted Wave Processing, *in* Proceedings 72nd EAGE Conference & Exhibition2010.

Dai, H., Li, X. Y., Ford, R., Yu, C., and Wang, J., Fracture Detection Using PS Converted Waves–A Case Study From Daqing Oil Field, *in* Proceedings 2011 SEG Annual Meeting2011, Society of Exploration Geophysicists.

Desheng, L., 1995, Hydrocarbon habitat in the Songliao rift basin, China: Geological Society, London, Special Publications, v. 80, no. 1, p. 317-329.

Dufour, J., Squires, J., Goodway, W. N., Edmunds, A., and Shook, I., 2002, Integrated geological and geophysical interpretation case study, and Lamé rock parameter extractions using AVO analysis on the Blackfoot 3C-3D seismic data, southern Alberta, Canada: Geophysics, v. 67, no. 1, p. 27-37.

Eaton, D., Slotboom, R., Stewart, R., and Lawton, D., Depth-variant converted-wave stacking, *in* Proceedings 1990 SEG Annual Meeting1990, Society of Exploration Geophysicists.

Eaton, D. W., and Lawton, D. C., 1992, P-SV stacking charts and binning periodicity: Geophysics, v. 57, no. 5, p. 745-748.

Ensley, R. A., 1984, Comparison of P-and S-wave seismic data: A new method for detecting gas reservoirs: Geophysics, v. 49, no. 9, p. 1420-1431.

Frasier, C., and Winterstein, D., 1990, Analysis of conventional and converted mode reflections at Putah sink, California using three-component data: Geophysics, v. 55, no. 6, p. 646-659.

Garotta, R., 1985, Observation of shear waves and correlation with P events: Seismic Shear Waves: Handbook of Geophysical Exploration, v. 15, p. 1-86.

Garotta, R., 1999, Shear Waves from Acquisition to Interpretation: 2000 Distinguished Instructor Short Course, Society of Exploration Geophysicists.

Garotta, R., and Granger, P., 2003, Some requirements for PS-mode acquisition: The Leading Edge, v. 22, no. 2, p. 106-112.

Gibson, J., Burnett, R., Ronen, S., and Watt, H., 2005, MEMS sensors: some issues for consideration: The Leading Edge, v. 24, no. 8, p. 786-790.

Granli, J. R., Arntsen, B., Sollid, A., and Hilde, E., 1999, Imaging through gas-filled sediments using marine shear-wave data: Geophysics, v. 64, no. 3, p. 668-677.

Grechka, V., Contreras, P., and Tsvankin, I., 2000, Inversion of normal moveout for monoclinic media1: Geophysical Prospecting, v. 48, no. 3, p. 577-602.

Guevara, S. E., 2000, Analysis and filtering of near-surface effects in land multicomponent seismic data, University of Calgary.

Hall, S. A., and Kendall, J.-M., 2003, Fracture characterization at Valhall: Application of P-wave amplitude variation with offset and azimuth (AVOA) analysis to a 3D ocean-bottom data set: Geophysics, v. 68, no. 4, p. 1150-1160.

Hardage, B. A., DeAngelo, M. V., Fomel, S., Fouad, K., Murray, P. E., Remington, R., and Sava, D., 2008, Imaging Super-Deep Gas Plays Across the Gulf of Mexico Shelf with Multicomponent Seismic Technology: University Of Texas At Austin.

Hardage, B. A., DeAngelo, M. V., Murray, P. E., and Sava, D., 2011, Multicomponent Seismic Technology, Society of Exploration Geophysicists.

Hardage, B. A., Murray, P. E., and Sava, D. C., 2006, Combining Multicomponent seismic attributes, new rock physics models, and In situ data to estimate gas-hydrate concentrations in Deep-Water, Near-Seafloor Strata of the Gulf of Mexico.

Harrison, M. P., 1992, Processing of P-SV surface-seismic data: Anisotropy analysis, dip moveout, and migration, Geology and Geophysics, University of Calgary.

Heidbach, O., Tingay, M., Barth, A., Reinecker, J., Kurfeß, D., and Müller, B., 2008, The world stress map database release 2008, doi: 10.1594/GFZ: WSM. Rel2008.

Helbig, K., 1983, Elliptical anisotropy-its significance and meaning: Geophysics, v. 48, no. 7, p. 825-832.

Hons, M., Stewart, R., Lawton, D., Bertram, M., and Hauer, G., 2008, Field data comparisons of MEMS accelerometers and analog geophones: The Leading Edge, v. 27, no. 7, p. 896-903.

Horne, S., 2003, Fracture characterization from walkaround VSPs: Geophysical Prospecting, v. 51, no. 6, p. 493-499.

Hudson, J., Overall properties of a cracked solid, *in* Proceedings Mathematical Proceedings of the Cambridge Philosophical Society1980, Volume 88, Cambridge Univ Press, p. 371-384.

-, 1981, Wave speeds and attenuation of elastic waves in material containing cracks: Geophysical Journal of the Royal Astronomical Society, v. 64, no. 1, p. 133-150.

Ikelle, L., 1997, Parametrization of AVAZ (amplitude variations with azimuths) inversion: Journal of Seismic Exploration, v. 6, no. 1, p. 19-34.

Jianming, T., Yue, H., Xiangrong, X., Tinnin, J., and Hallin, J., 2009, Application of converted-wave 3D/3-C data for fracture detectionin a deep tight-gas reservoir: The Leading Edge, v. 28, no. 7, p. 826-837.

Johnstad, S. E., 2008, Geophysical data acquisition system, Google Patents.

Kristiansen, P., 4 years experience with 4C seismic: what we have learned: Presented at the SEG, *in* Proceedings EAGE Summer Research Workshop, Boise, Idaho2000.

Li, X.-Y., Fracture detection using PP and PS waves in multicomponent sea-floor data, *in* Proceedings 1998 SEG Annual Meeting1998, Society of Exploration Geophysicists.

-, 1999, Fracture detection using azimuthal variation of P-wave moveout from orthogonal seismic survey lines: Geophysics, v. 64, no. 4, p. 1193-1201.

Li, X.-Y., and Crampin, S., 1993, Linear-transform techniques for processing shear-wave anisotropy in four-component seismic data: Geophysics, v. 58, no. 2, p. 240-256.

Li, X.-Y., Dai, H., Mueller, M. C., and Barkved, O. I., 2001, Compensating for the effects of gas clouds on C-wave imaging: A case study from Valhall: The Leading Edge, v. 20, no. 9, p. 1022-1028.

Li, X.-Y., Liu, Y.-J., Liu, E., Shen, F., Qi, L., and Shouli, Q., 2003, Fracture detection using land 3D seismic data from the Yellow River Delta, China: The Leading Edge, v. 22, no. 7, p. 680-683.

Li, X.-Y., and Yuan, J., 2003, Converted-wave moveout and conversion-point equations in layered VTI media: theory and applications: Journal of Applied Geophysics, v. 54, no. 3, p. 297-318.

Li, X. Y., 1997, Fractured reservoir delineation using multicomponent seismic data: Geophysical Prospecting, v. 45, no. 1, p. 39-64.

Li, Y., Sun, P., Tang, D., He, Y., Chen, H., and Yue, Y., Imaging through Gas-Filled Sediments with Land 3C Seismic Data, *in* Proceedings 69th EAGE Conference & Exhibition2007.

Li, Z., Cao, X., Chen, J., Liu, J., and Zhang, Z., 1985, Some considerations on the recent tectonic stress field of China: Tectonophysics, v. 117, no. 1, p. 161-176.

Liu, E., Hudson, J. A., and Pointer, T., 2000, Equivalent medium representation of fractured rock: Journal of Geophysical Research: Solid Earth (1978–2012), v. 105, no. B2, p. 2981-3000.

Lynn, H., Stewart, R. R., Garotta, R., and Thomsen, L., 2001, 4C-ing the future—a word from the "gurus": The Leading Edge, v. 20, no. 9, p. 978-982.

Lynn, H. B., Beckham, W. E., Simon, K. M., Bates, C. R., Layman, M., and Jones, M., 1999a, P-wave and S-wave azimuthal anisotropy at a naturally fractured gas reservoir, Bluebell-Altamont field, Utah: Geophysics, v. 64, no. 4, p. 1312-1328.

Lynn, H. B., Campagna, D., Simon, K. M., and Beckham, W. E., 1999b, Relationship of P-wave seismic attributes, azimuthal anisotropy, and commercial gas pay in 3-DP-wave multiazimuth data, Rulison Field, Piceance Basin, Colorado: Geophysics, v. 64, no. 4, p. 1293-1311.

MacBeth, C., 1999, Azimuthal variation in P-wave signatures due to fluid flow: Geophysics, v. 64, no. 4, p. 1181-1192.

-, 2002, Multi-component VSP analysis for applied seismic anisotropy, Gulf Professional Publishing.

Macbeth, C., and Crampin, S., 1991, Comparison of signal processing techniques for estimating the effects of anisotropy: Geophysical Prospecting, v. 39, no. 3, p. 357-385.

MacLeod, M., Hadley, M., Reynolds, K., and Tura, A., Multicomponent analysis of OBC data, *in* Proceedings Offshore Technology Conference1999, Offshore Technology Conference.

Mallick, S., Craft, K. L., Meister, L. J., and Chambers, R. E., 1997, Computation of principal directions of azimuthal anisotropy from P-wave seismic data: Exploration Geophysics, v. 28, no. 4, p. 379-382.

Mattocks, B., Li, J., and Roche, S. L., Converted-wave azimuthal anisotropy in a carbonate foreland basin, *in* Proceedings Proceedings of the 75th Annual International Meeting2005, p. 897-890.

Mavko, G., Mukerji, T., and Dvorkin, J., 2009, The rock physics handbook: Tools for seismic analysis of porous media, Cambridge University Press.

Merks, J., 1992, Geostatistics or voodoo science: Northern Miner, April, v. 20, p. A4.

Milici, R. C., and Swezey, C., 2006, Assessment of appalachian basin oil and gas resources: Devonian shale-middle and upper paleozoic total petroleum system, US Department of the Interior, US Geological Survey.

Mougenot, D., and Thorburn, N., 2004, MEMS-based 3D accelerometers for land seismic acquisition: Is it time?: The Leading Edge, v. 23, no. 3, p. 246-250.

Musgrave, M. J., 1970, Crystal acoustics, Holden-Day San Francisco.

Nelson, R., 2001, Geologic analysis of naturally fractured reservoirs, Gulf Professional Publishing.

Norris, M. W., and Faichney, A. K., 2002, SEG Y rev 1 Data Exchange format: Technical Standards Commitee SEG (Society of Exploration Geophysicists).

Olofsson, B., Probert, T., Kommedal, J. H., and Barkved, O. I., 2003, Azimuthal anisotropy from the Valhall 4C 3D survey: The Leading Edge, v. 22, no. 12, p. 1228-1235.

Ouenes, A., Zellou, A. M., Robinson, G., Balogh, D., and Araktingi, U., Seismically driven improved fractured reservoir characterization, *in* Proceedings SPE International Petroleum Conference in Mexico, Puebla Pue, Mexico, SPE2004, Volume 92031.

Pilant, W. L., 2012, Elastic waves in the earth, Elsevier.

Probert, T., Robinson, J., Ronen, S., Hoare, R., Pope, D., Kommedal, J., Crook, H., and Law, A., Imaging Through Gas Using 4-Component 3D Seismic Data: A Case Study From The Lomond Field, *in* Proceedings Offshore Technology Conference2000, Offshore Technology Conference.

Qian, Z., Li, X., and Chapman, M., 2007a, Azimuthal variations of PP- and PS-wave attributes: A synthetic study, SEG Technical Program Expanded Abstracts 2007, p. 184-188.

Qian, Z., Li, X., and Chapman, M., Effects of Fluid Saturation on Shear-wave Splitting in Multicomponent Seismic Data, *in* Proceedings EAGE/SEG Research Workshop-Fractured Reservoirs, Integrating Geosciences for Fractured Reservoirs Description2007b.

Ren, J., and Xiao, L., 2002, Tectonic settings of petroliferous basins in continental China: Episodes, v. 25, no. 4, p. 227-235.

Rodriguez, C., 2002, Advanced marine seismic methods: PhD thesis.

Rogers, S., Mac Beth, C., Liu, E., and Angerer, E., Constraining models of fractured reservoirs using seismic anisotropy maps, for improved reservoir performance and prediction, *in* Proceedings 2003 SEG Annual Meeting, Dallas2003.

Ronen, S., Comeaux, L., Cartwright, M., Gibson, J., Burnett, R., Roy, J., and Watt, H., Comparison between geophones and two MEMS types and repeatability of land

data, *in* Proceedings 2005 SEG Annual Meeting2005, Society of Exploration Geophysicists.

Rudzki, M. P., 1911, Parametrische Darstellung der elastischen Welle in anisotropen Medien, Imprimerie de l'Universit é.

Rüger, A., 1998, Variation of P-wave reflectivity with offset and azimuth in anisotropic media: Geophysics, v. 63, no. 3, p. 935-947.

-, 2001, Reflection coefficients and azimuthal AVO analysis in anisotropic media, Society of Exploration Geophysicists.

Rüger, A., and Tsvankin, I., 1997, Using AVO for fracture detection: Analytic basis and practical solutions: The Leading Edge, v. 16, no. 10, p. 1429-1434.

Schafer, A. W., 1992, A comparison of converted-wave binning methods using a synthetic model of the Highwood Structure, Alberta: CREWES Research Report, 1992,(4): 1-9.

Schoenberg, M., 1980, Elastic wave behavior across linear slip interfaces: The Journal of the Acoustical Society of America, v. 68, no. 5, p. 1516-1521.

Schoenberg, M., and Douma, J., 1988, Elastic wave propagation in media with parallel fractures and aligned cracks: Geophysical Prospecting, v. 36, no. 6, p. 571-590.

Schoenberg, M., and Sayers, C. M., 1995, Seismic anisotropy of fractured rock: Geophysics, v. 60, no. 1, p. 204-211.

Shearer, P. M., 2009, Introduction to seismology, Cambridge University Press.

Sheriff, R. E., and Geldart, L. P., 1982, Exploration seismology, Cambridge university press Cambridge.

Shuai, Y., Zhang, S., Su, A., Wang, H., Cai, B., and Wang, H., 2010, Geochemical evidence for strong ongoing methanogenesis in Sanhu region of Qaidam Basin: Science in China Series D: Earth Sciences, v. 53, no. 1, p. 84-90.

Simmons Jr, J. L., 2008, Converted-wave splitting estimation and compensation: Geophysics, v. 74, no. 1, p. D37-D48.

Song, T., 1997, Inversion styles in the Songliao basin (northeast China) and estimation of the degree of inversion: Tectonophysics, v. 283, no. 1, p. 173-188.

Stewart, R., Ferguson, R., Miller, S., Gallant, E., and Margrave, G., 1996, The Blackfoot Seismic Experiments: Broad-band, 3C-3D, and 3D VSP surveys: CSEG Recorder (June 1996).

Stewart, R. R., Gaiser, J. E., Brown, R. J., and Lawton, D. C., 2002, Converted-wave seismic exploration: Methods: Geophysics, v. 67, no. 5, p. 1348-1363.

Stotter, C., Angerer, E., and Herndler, E., Comparison of single sensor 3C MEMS and conventional geophone arrays for deep target exploration, *in* Proceedings 2008 SEG Annual Meeting2008, Society of Exploration Geophysicists.

Sutton, G. H., and Duennebier, F. K., 1987, Optimum design of ocean bottom seismometers: Marine geophysical researches, v. 9, no. 1, p. 47-65.

Taner, M. T., and Koehler, F., 1969, Velocity spectra-digital computer derivation applications of velocity functions: Geophysics, v. 34, no. 6, p. 859-881.

Taylor, D., 1990, Aniseis manual: V5, Applied Geophysical Software Inc, Houston.

Tessmer, G., and Behle, A., 1988, Common Reflection Point Data-Stacking Technique for Converted WAVES1: Geophysical Prospecting, v. 36, p. 671-688.

Tessmer, G., Krajewski, P., Fertig, J., and Behle, A., 1990, Processing of PS-reflection data applying a common conversion-point stacking technique: Geophysical Prospecting, v. 38, no. 3, p. 267-268.

Thomsen, L., 1986, Weak elastic anisotropy: Geophysics, v. 51, no. 10, p. 1954-1966.

-, 1988, Reflection seismology over azimuthally anisotropic media: Geophysics, v. 53, no. 3, p. 304-313.

-, 1995, Elastic anisotropy due to aligned cracks in porous rock: Geophysical Prospecting, v. 43, no. 6, p. 805-829.

-, 1999, Converted-wave reflection seismology over inhomogeneous, anisotropic media: Geophysics, v. 64, no. 3, p. 678-690.

-, 2001, Seismic anisotropy: Geophysics, v. 66, no. 1, p. 40-41.

-, 2002, Understanding seismic anisotropy in exploration and exploitation, Society of Exploration Geophysicist.

Tillotson, P., Sothcott, J., Best, A. I., Chapman, M., and Li, X. Y., 2012, Experimental verification of the fracture density and shear-wave splitting relationship using synthetic silica cemented sandstones with a controlled fracture geometry: Geophysical Prospecting, v. 60, no. 3, p. 516-525.

Tod, S., Taylor, B., Johnston, R., and Allen, T., 2007, Fracture prediction from wide-azimuth land seismic data in SE Algeria: The Leading Edge, v. 26, no. 9, p. 1154-1160.

Tsvankin, I., 1997a, Anisotropic parameters and P-wave velocity for orthorhombic media: Geophysics, v. 62, no. 4, p. 1292-1309.

-, 1997b, Reflection moveout and parameter estimation for horizontal transverse isotropy: Geophysics, v. 62, no. 2, p. 614-629.

Tsvankin, I., and Thomsen, L., 1994, Nonhyperbolic reflection moveout in anisotropic media: Geophysics, v. 59, no. 8, p. 1290-1304.

Vermeer, G. J., and Beasley, C. J., 2002, 3-D seismic survey design, Society of Exploration Geophysicists Tulsa.

Vetri, L., Loinger, E., Gaiser, J., Grandi, A., and Lynn, H., 2003, 3D/4C Emilio: Azimuth processing and anisotropy analysis in a fractured carbonate reservoir: The Leading Edge, v. 22, no. 7, p. 675-679.

Wang, S., and Li, X.-Y., 2006, Layer stripping of azimuthal anisotropy from P-wave reflection moveout in orthogonal survey lines: Journal of Geophysics and Engineering, v. 3, no. 1, p. 1.

Wild, P., and Crampin, S., 1991, The range of effects of azimuthal isotropy and EDA anisotropy in sedimentary basins: Geophysical Journal International, v. 107, no. 3, p. 513-529.

Winterstein, D., 1990, Velocity anisotropy terminology for geophysicists: Geophysics, v. 55, no. 8, p. 1070-1088.

Xiyuan, C., Tian-ji, X., Jian-ming, T., Xian-gui, L., Tinnin, J., and Hallin, J., 2009, Research and application of gas detection techniques using full‐wave attributes in southwest China: first break, v. 27.

Xu, S., and King, M., 1989, Shear-wave birefringence and directional permeability in fractured rock: Sci. Drill, v. 1, p. 27-33.

Yuan, J., 2001, Analysis of Four-component Seafloor Seismic Data for Seismic Anisotropy [PhD: University of Edinburgh.

Yue, Y., Li, J., Qian, Z., Sun, P., Cheng, C., and Zhang, X., Converted-wave Splitting Analysis and Application, *in* Proceedings 75th EAGE Conference & Exhibition incorporating SPE EUROPEC 20132013.

Appendix A: Basic reflectivity theory implemented in ANISEIS

ANISEIS is a flexible computer modelling system for calculating synthetic seismograms from point sources in plane-layered anisotropic and cracked models. The methods used in ANISEIS are based on plane-wave analysis and involve use of the reflectivity method and accumulation of plane-waves for different horizontal slownesses and horizontal azimuths.

This Appendix aims to briefly explain the basic algorithms implemented in the ANISEIS package. First, I introduce the basic theory of the reflectivity method for isotropic media. Then I explain how the reflectivity method is extended to anisotropic media and what specific approximations are made in ANISEIS.

The reflectivity method for isotropic media

The reflectivity method was originally developed by Fuchs and Müller (1971). The method was then extended by many different workers (Kennett, 1974, 1975a, b, 1979; Kennett and Clarke, 1983; Kennett and Kerry, 1979; Kind, 1976; Stephen, 1977). The technique was originally developed to guide the interpretation of seismic data but has been widely used to model seismic data to improve the understanding of Earth's structure (Mallick and Frazer, 1987).

The essential theory of the reflectivity method is to study wave propagation in horizontally-layered media, which is bounded above by either a half-space or free

surface and below by a half-space. The theoretical model used in this appendix is built in the cylindrical coordinate system (*r, θ, z*), which is illustrated in Figure A-1. The point source is located at the origin of the cylindrical coordinate system. The receiver may be placed anywhere within the layered model. The vertical plane containing both source and receiver is regarded as the sagittal plane. The transition zone containing layer 1 to layer n and the halfspace form the reflection zone. Each layer is isotropic and is characterised by its individual parameters. P-wave velocity α_n, S-wave velocity β_n and density of the medium ρ_n can be defined for the *n*-th layer.

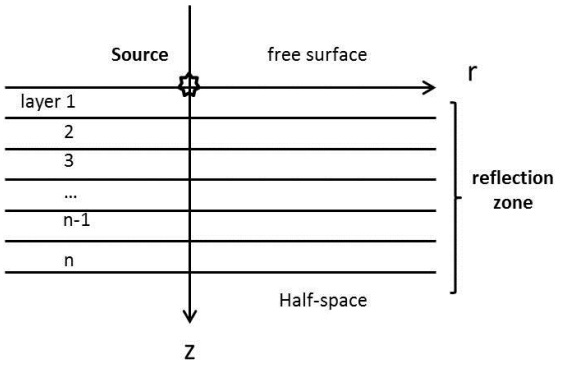

Figure A-1. Illustration of horizontally-layered media

Seismic wave propagation in isotropic medium can be described by the wave equation, which is based on the equation of motion and relation between stress and strain tensors (Kennett, 2009):

$$\left.\begin{aligned} \nabla \bullet \sigma &= \rho \frac{\partial^2 u}{\partial t^2} \\ \sigma &= C\varepsilon \end{aligned}\right\} \tag{A-1}$$

where u is the elastic displacement, ρ is the density of the medium, σ is the stress tensor and ∇ is the Laplace operator. The stress tensor σ, strain tensor ε and stiffness tensor C satisfy Hook's law ($\sigma = C\varepsilon$).

Alternatively, in isotropic media, wave propagation is usually characterised in terms of scalar potentials ϕ, ψ and χ corresponding to P-, SV- and SH-wave propagation. The potentials are solutions of the wave equations (Müller, 1969):

$$\left.\begin{aligned}\nabla^2\phi &= \frac{1}{\alpha^2}\frac{\partial^2\phi}{\partial t^2}\\ \nabla^2\psi &= \frac{1}{\beta^2}\frac{\partial^2\psi}{\partial t^2}\\ \nabla^2\chi &= \frac{1}{\beta^2}\frac{\partial^2\chi}{\partial t^2}\end{aligned}\right\} \tag{A-2}$$

And the displacements in the radial, transverse and vertical directions in cylindrical coordinates are:

$$\left.\begin{aligned}u_r &= \frac{\partial\phi}{\partial r}+\frac{\partial^2\psi}{\partial r\partial z}\\ u_\theta &= -\frac{\partial\chi}{\partial r}\\ u_\theta &= \frac{\partial\phi}{\partial z}+\frac{\partial^2\psi}{\partial z^2}-\frac{1}{\beta^2}\frac{\partial^2\psi}{\partial t^2}\end{aligned}\right\} \tag{A-3}$$

where α and β are the P-wave and S-wave velocities, respectively.

Then a stress-displacement vector can be defined to introduce the propagator matrix:

$$B=\begin{bmatrix}u\\ \sigma\end{bmatrix} \tag{A-4}$$

where *B* is called stress-displacement vector and is continuous across any horizontal interface. The stress-displacement vectors *B* at the top and bottom interfaces z and z_0 of any plane isotropic sequence of layers are related by:

$$B(z)=P(z,z_0)B(z_0) \tag{A-5}$$

where *P* is the 6×6 propagator matrix for the particular sequence (Gilbert and Backus, 1966). B can be also given in terms of the vector of plane wave potentials in layer *z* by:

$$B(z)=T(z)\Gamma(z) \tag{A-6}$$

where $\Gamma(z)$ is the vector of plane wave potentials ($\varphi_j(z,1)$, $\varphi_j(z,2)$ and $\varphi_j(z,1)$) for downward and upward propagating waves. The 6×6 matrix *T* performs differentiation on the potentials to give the displacements and stresses. For example, the displacements are given by equation (A-3).

Appropriate boundary conditions need to be applied in order to solve equations (A-5) and (A-6). The assumption is made that no energy is travelling upwards from the lower half-space, which gives:

$$\varphi_j(4) = \varphi_j(5) = \varphi_j(6) = 0 \ \ (j = 1,2,3) \tag{A-7}$$

where numbers 4, 5 and 6 represent upward propagating P-, SV- and SH-waves. Numbers 1, 2 and 3 represent the corresponding downward propagating waves.

If a plane P-wave incident on the upper boundary of the reflection-zone, the following relation can be made:

$$\varphi_1(2) = \varphi_1(3) = 0 \tag{A-8}$$

Then the plane wave potential vector at the top layer is defined as:

$$\Gamma(0) = (1,0,0,g^0(4),g^0(5),g^0(6))^T \tag{A-9}$$

Its corresponding vector at the lower half-space can be also defined as:

$$\Gamma(z) = (g^z(1),g^z(2),g^z(3),0,0,0)^T \tag{A-10}$$

where $g^n(p)$ $(p = 1,2,3,4,5,6)$ are the potential excitation factors, which are complex functions of layer parameters and the wavenumber *k*.

Equations (A-5), (A-6), (A-9) and (A-10) may be solved to give the excitation factors and wave potentials generated at any point in a layer by the incident plane P-wave. The potentials of SV- and SH-waves may be solved in a similar procedure with appropriate boundary conditions. The potential excitation factors described above correspond to the reflection and transmission coefficients (e.g.Fuchs, 1971; Kennett, 1974).

Finally, with the excitation of seismic waves, using the propagator matrix of seismic waves and appropriate boundary conditions, the numerical calculations for seismograms can be achieved.

Reflectivity method extended into anisotropic media

The reflectivity theory can be extended to model seismic data in anisotropic media by using propagator matrices (Crampin, 1981) to characterise plane wave propagation in a sequence of horizontal layers. Plane wave propagations in each anisotropic layer can be described by applying the propagator matrices with appropriate boundary conditions.

However, there are several special issues regarding implementation of the reflectivity method in anisotropic media, particularly in ANISEIS.

First, the source is required to be in the isotropic layer in ANISEIS. The analytic solutions to the problem of an explosive source in an infinite medium satisfies the radiation criterion given as (Ziolkowski, 1993):

$$\Omega(R,t) = \frac{1}{R} f(t - \frac{R}{c}) \tag{A-11}$$

where Ω (ϕ , ψ and χ) represents the displacement potentials, f is the volume injection function, R is the distance from the source ($R = \sqrt{r^2 + z^2}$) and c is the wavespeed.

If the source is contained in an anisotropic layer, Equation (A-11) will not be valid and the following calculation of plane wave excitation factors for the given reflector will be inaccurate. In ANISEIS, the source should be located in an isotropic layer. This restriction on the source layer is not onerous since the layer can be made very thin and internal reflections within it can be suppressed. If an isotropic source layer is not created, ANISEIS will construct a thin isotropic layer which approximates the material in the user-specified source layer using the vertical wave velocities.

Second, the plane wave solutions in anisotropic media are described in terms of displacements because no convenient potential formula is available. The general form of plane wave solutions for the displacements in anisotropic media is (Booth and Crampin, 1983):

$$u_j = a_j \exp[i\omega(t - q_k x_k)] \tag{A-12}$$

where a is the polarisation vector specifying the polarisation of the particle motion, ω is the angular frequency and q is the slowness vector.

However, the analytic solution to an explosive source in an infinite medium is in a form of potentials rather displacements (Equation A-11) which is different from Equation (A-12). The following discussion focuses on this issue.

Taking the temporal Fourier transform of Equation (A-11):

$$\Omega(R,\omega) = \frac{F(\omega)}{R}\exp(i\omega\frac{R}{c}) \tag{A-13}$$

where $F(\omega)$ is the source spectrum.

The Fourier transformed potential of a spherical wave from a point source may be expressed as integral of cylindrical-wave potentials by the use of Sommerfeld's integral (Aki and Richards, 2002, p.194):

$$\frac{1}{R}\exp(i\omega\frac{R}{c}) = \int_0^\infty \frac{kJ_0(kr)\exp(-\gamma z)}{\gamma}dk \tag{A-14}$$

where $\gamma = \sqrt{(\omega^2 - c^2k^2)/c^2}$, k is the wavenumber and J_0 is the zero-order Bessel function of the first kind. Then equation (A-13) can be written in the following form:

$$\Omega(R,\omega) = F(\omega)\int_0^\infty \frac{kJ_0(kr)\exp(-\gamma z)}{\gamma}dk \tag{A-15}$$

By taking spatial derivatives of equation (A-15), the displacements can be written as:

$$\left.\begin{aligned} u_z(\omega) &= \frac{\partial\Omega}{\partial z} = -F(\omega)\int_0^\infty kJ_0(kr)\exp(-\gamma z)dk \\ u_r(\omega) &= \frac{\partial\Omega}{\partial r} = -F(\omega)\int_0^\infty \frac{k^2J_1(kr)\exp(-\gamma z)dk}{\gamma} \end{aligned}\right\} \tag{A-16}$$

where J_1 is the first-order Bessel function.

If the calculation is limited in the far-field, the following approximation can be obtained (Abramowitz and Stegun, 1972, p.364):

$$\left.\begin{aligned} J_0(kr) &\approx \frac{1}{\sqrt{2\pi kr}}\exp[-i(kr-\frac{\pi}{4})] \quad kr >> 0 \\ J_1(kr) &\approx iJ_0(kr), \quad kr >> 0 \end{aligned}\right\} \tag{A-17}$$

Then the polarisation vector as $(\sin\theta, \cos\theta)$ can be defined:

$$\left.\begin{aligned} \cos\theta &= \frac{v_1}{k_1} \\ \sin\theta &= \frac{k}{k_1} \\ k_1 &= \frac{\omega}{c} \\ v_1 &= i\gamma \end{aligned}\right\} \tag{A-18}$$

Substituting equations (A-17) and (A-18) into (A-16), we have:

$$\left.\begin{aligned} u_z(\omega) &= -F(\omega)\exp(\frac{i\pi}{4})\int_0^\infty \frac{k_1}{v_1}\sqrt{\frac{k}{2\pi r}}\cos\theta\exp(-ikr-\gamma z)dk \\ u_r(\omega) &= F(\omega)\exp(\frac{i\pi}{4})\int_0^\infty \frac{k_1}{v_1}\sqrt{\frac{k}{2\pi r}}\sin\theta\exp(-ikr-\gamma z)dk \end{aligned}\right\} \tag{A-19}$$

By taking the far-field approximation, the displacements have the term "$\exp(-ikr-\gamma z)$", which makes it possible to match the general form of a plane wave (Equation (A-12)).

In ANISEIS, a far-field approximation is made for this purpose. The key theory of ANISEIS is to deal with plane wave solutions in each layer. Specifically, the displacement spectrum at a point (*x*, *y*, *z*) in Cartesian coordinates can be written as:

$$u_i(\omega) = F(\omega)\sum_{p=1}^{6}\int_{-\infty}^{\infty}\int_{-\infty}^{\infty} Sf^m(p)a_i^m(p)\exp[-i\omega q_3^m(z-d_m)]\exp[i(k_x+k_y)] \tag{A-20}$$

where *p* represents six wave types (P, SV, SH, up- and down-going). k_x and k_y are radial and transverse components, respectively, of the horizontal wavenumber vector. $f^m(p)$ is the excitation factor which gives the relative wave displacement amplitude of each wave-type p and in the *m*'th layer in the direction of its unit displacement vector *a*. S is the source term and d_m is the depth of the *m*'th layer.

As discussed before, the source layer is required to be isotropic in ANISEIS to avoid mathematical difficulties in describing the source in anisotropic media. Therefore the source function and zero-order Bessel function remain the same as for isotropic media. Moreover, the far-field approximation can also be applied to equation (A-20). Thus the displacement spectrum has a similar form to equation (A-19) (Ekanem, 2012, Appendix A).

Third, the excitation factors in each anisotropic layer can be described by applications of propagator matrices with appropriate boundary conditions (Crampin, 1981). The displacement-stress vectors B at interfaces z and $(z+1)$ are related by the anisotropic propagator matrix A^z :

$$B^{z+1} = A^z B^{z+1} \tag{A-20}$$

Meanwhile, the excitation factor vector f can be also related to the displacement-stress vector B by matrix E^z :

$$B^z = E^z f^z \tag{A-21}$$

where A^z and E^z are all 6×6 matrices. They are both complex functions of the anisotropic elastic tensors, slowness and polarisation vectors.

Application of the propagator matrices, with the appropriate boundary conditions, permits the plane wave propagation in each layer to be described in terms of displacement excitation factors for each wave-type.

Specifically, the generation of true seismograms in ANISEIS requires the integration of plane waves for different horizontal slownesss and horizontal azimuths. This 2D integration instead of 1D integration is accomplished by Taylor (1990). It is the most important feature of this commercial software.

References

Abramowitz, M., and Stegun, I. A., 1972, Handbook of mathematical functions, Dover New York, v. 5.

Aki, K., and Richards, P. G., 2002, Quantitative seismology.

Booth, D. C., and Crampin, S., 1983, The anisotropic reflectivity technique: theory: Geophysical Journal International, v. 72, no. 3, p. 755-766.

Crampin, S., 1981, A review of wave motion in anisotropic and cracked elastic-media: Wave motion, v. 3, no. 4, p. 343-391.

Ekanem, A. M., 2012, Analysis of P-wave attenuation anisotropy in fractured porous media [PhD thesis]: University of Edinburgh.

Fuchs, K., 1971, The method of stationary phase applied to the reflection of spherical waves from transition zones with arbitrary depth-dependent elastic moduli and density: Geophys, v. 37, p. 89-117.

Fuchs, K., and Müller, G., 1971, Computation of synthetic seismograms with the reflectivity method and comparison with observations: Geophysical Journal International, v. 23, no. 4, p. 417-433.

Gilbert, F., and Backus, G. E., 1966, Propagator matrices in elastic wave and vibration problems: Geophysics, v. 31, no. 2, p. 326-332.

Kennett, B., 1974, Reflections, rays, and reverberations: Bulletin of the Seismological Society of America, v. 64, no. 6, p. 1685-1696.

-, 1975a, The effects of attenuation on seismograms: Bulletin of the Seismological Society of America, v. 65, no. 6, p. 1643-1651.

-, 1975b, Theoretical seismogram calculation for laterally varying crustal structures: Geophysical Journal of the Royal Astronomical Society, v. 42, no. 2, p. 579-589.

-, 1979, Theoretical reflection seismograms for elastic media: Geophysical Prospecting, v. 27, no. 2, p. 301-321.

Kennett, B., 2009, Seismic wave propagation in stratified media, ANU E Press.

Kennett, B., and Clarke, T., 1983, Seismic waves in a stratified half-space—IV: P—SV wave decoupling and surface wave dispersion: Geophysical Journal International, v. 72, no. 3, p. 633-645.

Kennett, B., and Kerry, N., 1979, Seismic waves in a stratified half space: Geophysical Journal International, v. 57, no. 3, p. 557-583.

Kind, R., 1976, Computation of reflection coefficients for layered media: JOURNAL OF GEOPHYSICS-ZEITSCHRIFT FUR GEOPHYSIK, v. 42, no. 3, p. 191-200.

Mallick, S., and Frazer, L. N., 1987, Practical aspects of reflectivity modeling: Geophysics, v. 52, no. 10, p. 1355-1364.

Müller, G., 1969, Theoretical seismograms for some types of point-source in layered media, part III: single force and dipole sources of arbitrary orientation: Journal of Geophysics, no. 35, p. 347-371.

Stephen, R., 1977, Synthetic seismograms for the case of the receiver within the reflectivity zone: Geophysical Journal International, v. 51, no. 1, p. 169-181.

Taylor, D., 1990, Aniseis manual: V5, Applied Geophysical Software Inc, Houston.

Ziolkowski, A., 1993, Determination of the signature of a dynamite source using source scaling, Part 1: Theory: Geophysics, v. 58, no. 8, p. 1174-1182.

Appendix B: Hudson's model for cracked media

Hudson's model (1980, 1981) is based on a scattering theory analysis of the mean wavefield in an elastic solid with thin, penny-shaped ellipsoidal cracks or inclusions. The penny-shaped cracks, which are embedded into the background medium, are illustrated in Figure B-1. Ellipsoidal cracks are used in Hudson's model for two major reasons. First, an ellipsoidal is flexible so that a wide range of shapes can be approximated, such as needle-shaped or spherical pores (Tod, 2002). Second, there is an analytic solution which relates strain in an ellipsoid to an imposed external stress or a strain field (Eshelby, 1957).

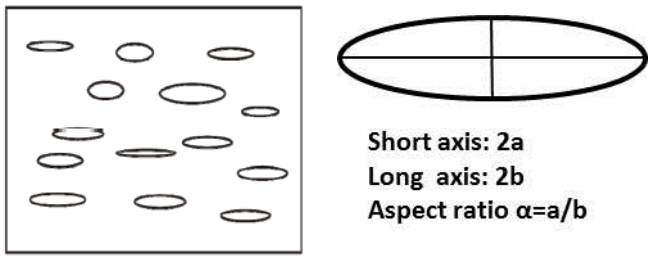

Figure B-1. Illustrations of penny-shaped cracks embedded into the background medium.

Hudson's model of cracked media is built under some assumptions:

(1) A long-wavelength approximation is made.
    Seismic wavelength >> fracture spacing >> fracture radius (aperture)
(2) Cracks and fractures are randomly distributed within a wavelength
(3) Cracks are sparse
(4) Cracks are isolated with respect to fluid flow

With these approximations, the medium containing penny-shaped cracks can be replaced as a homogeneous medium with the same overall properties. To describe the effective medium, specific parameters are required: orientation of aligned cracks, crack density, aspect ratio and modulus of crack filling material. Aligned cracks often give rise to HTI anisotropy. The orientation of aligned cracks determines the direction of the plane of isotropy or the symmetry axis (Figure B-2). The crack density is defined as:

$$e = \frac{Na^3}{V} = \frac{3\phi}{4\pi\alpha} \tag{B-1}$$

where e is the crack density, a is the crack radius and N is the number of such cracks in a volume V. ϕ is the crack porosity. α is the crack aspect ratio, which is illustrated in Figure B-1. The moduli of the crack filling material are required to complete the modelling of cracked media. Usually, the crack filling material is specified by its density (ρ) and Lame constants (λ and μ).

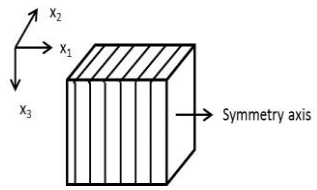

Figure B-2. A HTI medium induced by a set of aligned cracks or fractures

Considering thin and penny-shaped cracks orthogonal to the x_1 axis (Figure B-2), the effective moduli can be given as:

$$C^{eff} = C^0 + C^1 + C^2 \tag{B-2}$$

where C^{eff} is the stiffness tensor of the effective medium. C^0 is the stiffness tensor of the isotropic background medium. C^1 and C^2 are the first- and second-order corrections, respectively. C^1 and C^2 are introduced to describe the overall effect as a result of the cracks, and are dependent on the crack parameters introduced above:

$$\left.\begin{aligned} C_{11}^1 &= -\frac{(\lambda+2\mu)^2}{\mu} eU_3 \\ C_{13}^1 &= -\frac{\lambda(\lambda+2\mu)}{\mu} eU_3 \\ C_{33}^1 &= -\frac{\lambda^2}{\mu} eU_3 \\ C_{44}^1 &= 0 \\ C_{66}^1 &= -\mu e U_1 \end{aligned}\right\} \tag{B-3}$$

$$\left.\begin{aligned} C_{11}^2 &= \frac{q(\lambda+2\mu)}{15}(eU_3)^2 \\ C_{13}^2 &= \frac{q\lambda}{15}(eU_3)^2 \\ C_{33}^2 &= \frac{q\lambda^2}{15(\lambda+2\mu)}(eU_3)^2 \\ C_{44}^2 &= 0 \\ C_{66}^2 &= \frac{\mu(3\lambda+8\mu)}{15(\lambda+2\mu)}(eU_1)^2 \\ q &= 15\frac{\lambda^2}{\mu^2} + 28\frac{\lambda}{\mu} + 28 \end{aligned}\right\} \tag{B-4}$$

The terms U_1 and U_3 depend on the crack conditions. For weak inclusions (i.e., when $\mu\alpha/(K^I + 4\mu^I/3)$ is of the order of 1 and is not small enough to be neglected):

$$\left.\begin{aligned} U_1 &= \frac{16(\lambda+2\mu)}{3(3\lambda+4\mu)(1+M)} \\ U_3 &= \frac{4(\lambda+2\mu)}{3(\lambda+\mu)(1+\kappa)} \\ M &= \frac{4\mu^I(\lambda+2\mu)}{\pi\alpha\mu(3\lambda+4\mu)} \\ \kappa &= \frac{(K^I + \frac{4}{3}\mu^I)(\lambda+2\mu)}{\pi\alpha\mu(\lambda+\mu)} \end{aligned}\right\} \tag{B-5}$$

where K^I and μ^I are the bulk and shear moduli of the inclusion material. The criteria for an inclusion to be 'weak' depend on its shape or aspect ratio α as well as on the relative moduli of the inclusion and matrix material. Dry cavities can be modelled by setting the inclusion moduli to zero. Fluid-saturated cavities are simulated by setting the inclusion shear modulus to zero.

However, the second-order correction C^2 is not a uniformly converging series and predicts increasing moduli with crack density beyond the formal limit (Cheng, 1993). Better results will be obtained by using just the first-order correction rather than inappropriately using the second-order correction (Mavko *et al*., 2009).

For an aligned set of cracks, crack filling materials have influences on the final effective moduli. I perform a numerical study to verify the influence of water-saturation on anisotropic parameters of cracked media with different values of aspect ratio. A set of aligned cracks are built based on Hudson's model. The parameters are listed in Table B-1. The bulk (K) and shear (μ) moduli of the isotropic background medium are 12.29 GPa and 3.72 GPa, respectively. The density of the background medium is 2.2 g/cm^3.

e	K(GPa)	μ (GPa)	ρ (g/cm^3)	α
0.08	12.29	3.72	2.2	$1\times10^{-2},5\times10^{-3},1\times10^{-3},5\times10^{-3},1\times10^{-4}$

Table B-1. Parameters of a set of aligned cracks

If dry cracks are assumed, the effective stiffness tensor of the crack medium can be calculated according to Equations (B-2) to (B-5). Note that only the first-order correction is used in this study. Then the Thomsen's parameters can be computed using Equation (2-18).

For gas-filled cracks, the modulus of gas can be calculated according to the relation between natural gas and air density at 15.6 ^oC and atmospheric pressure (Batzle and Wang, 1992). Methane is selected to fill the cracks in this numerical study. Its density at 15.6 ^oC and atmospheric pressure is 0.00068 g/cm^3 and its calculated bulk modulus is 0.0001 GPa. For water-saturated cracks, the density of water is 1.0 g/cm^3 and the bulk modulus of water is 2.2 GPa (Mavko *et al*., 2009).

When the crack filling material is a mixture of gas and water, the Reuss average bulk modulus of the inclusion is given as (Wood, 1955):

$$K_{Reuss} = \left(\frac{sw}{K_{water}} + \frac{1-sw}{K_{gas}}\right) \tag{B-6}$$

where K_{water} and K_{gas} are bulk moduli of water and gas, respectively. sw is the percentage water saturation, which ranges from 0% to 100%. The average density can also be defined as (Wood, 1955):

$$\rho = \rho_{water} sw + \rho_{gas}(1 - sw) \tag{B-7}$$

Then the moduli of inclusions with different sw can be calculated. Finally, the effective stiffness tensor and Thomsen's parameters can be computed.

The result of the Reuss average bulk modulus is shown in Figure B-2. It is nearly equal to zero even when sw is as large as 0.9. It implies that the bulk modulus of the fracture filling material is close to zero when $sw < 0.9$.

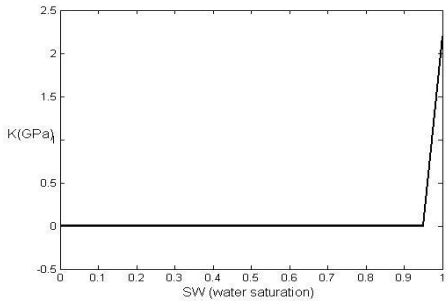

Figure B-2. Reuss bulk modulus with different sw

The results for Thomsen's parameters with different aspect ratios and different water saturation percentages are shown in Figure B-3 to B-5. Thomsen's parameters of a cracked medium with different sw are represented by solid lines. Different colours represent different aspect ratios. As dry fractures are not affected by aspect ratio, Thomsen's parameters calculated from dry fractures are marked as black dashed lines to allow comparisons to be made.

For all different aspect ratios, significant changes in parameter ε can be observed when sw is greater than 0.9. Moreover, as aspect ratio decreases, ε of fluid-filled cracks deviates from ε of dry cracks. When the aspect ratio is as small as 0.0001, there is a significant difference in parameter ε between fluid-filled cracks and dry cracks. For both dry and fluid-filled cracks, the parameter γ is nearly the same. Different aspect ratios and different water-saturation

percentages have no significant influences on parameter γ. Parameter δ also shows significant changes when sw is greater 0.9. Meanwhile, aspect ratio has an influence on parameter δ, which is similar to parameter ε. δ of fluid-filled cracks deviates from δ of dry cracks, as aspect ratio decreases.

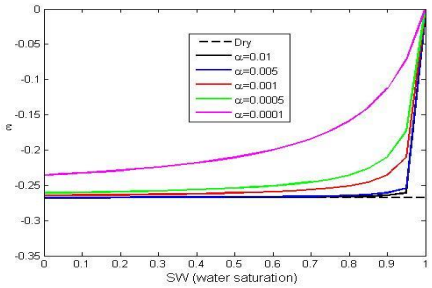

Figure B-3. Parameter ε with different sw (ε of dry cracks is marked by the red dashed line)

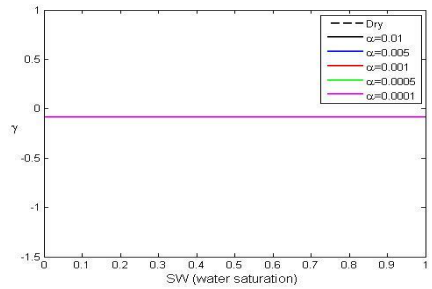

Figure B-4. Parameter γ with different sw (γ of dry cracks is marked by the red dashed line)

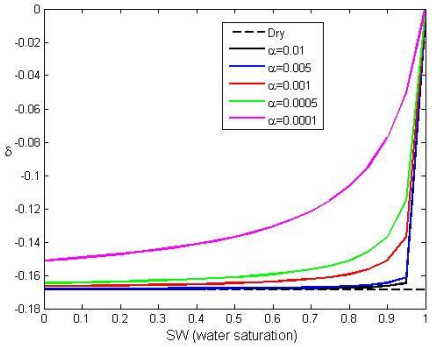

Figure B-5. Parameter δ with different sw (δ of dry cracks is marked by the red dashed line)

In conclusion, a mathematical complication arises for very thin cracks (where aspect ratio is very small). As the aspect ratio tends to zero, for any fixed (but small) value of the fluid modulus, the stiffness tensor approaches the "stiff crack" limit. However, as the fluid modulus tends to zero for any fixed (but small) value of the aspect ratio, the elastic constants tend to the dry crack limit. This complication places a limit on our ability to reliably model the case we are interested in: thin cracks filled by a weak fluid. It also has limited the application of Hudson's theory to quantitative fluid identification.

Nevertheless, there are clearly physical limitations to how small the crack aspect ratio can be. With this in mind, the model for a crack which we propose in this thesis with the aspect ratio range between 0.01 and 0.0005, for which the gas saturation is larger than 0.1, can be considered as a dry crack.

Much work is underway on trying to understand the elastic effects of penny-shaped cracks through laboratory tests on synthetic rocks with controlled fracture geometry (e.g. Tillotson *et al*, 2012; Amalokwu, 2014). We expect that future work may be guided more by these studies than by simplified mathematical models.

References

Amalokwu K, Best A I, Sothcott J, et al. 2014. Water saturation effects on elastic wave attenuation in porous rocks with aligned fractures[J]. Geophysical Journal International, 2014: ggu076.

Batzle, M. and Wang, Z., 1992. Seismic properties of pore fluids. Geophysics., 57, 1396-1408.

Cheng, C.H., 1993. Crack models for a transversely anisotropic medium. J. Geophys. Res., 98, 675-684.

Eshelby, J.D., 1957. The determination of the elastic field of an ellipsoidal inclusion and related problem. Proceeding of Royal Society of London A241, 376-396.

Hudson, J., 1980. Overall properties of a cracked solid, in Proceedings Mathematical Proceedings of the Cambridge Philosophical Society, Volume 88, Cambridge Univ Press, p. 371-384.

-, 1981, Wave speeds and attenuation of elastic waves in material containing cracks: Geophysical Journal of the Royal Astronomical Society, v. 64, no. 1, p. 133-150.

Mavko, G. and Mukerji, T. and Dvorkin, J., 2009. The Rock Physics Handbook, Cambridge University Press, New York.

Tillotson, P., Sothcott, J. Best, A, Chapman, M., and Li, X.-Y., 2012, Experimental verification of the fracture density and shear-wave splitting relationship using synthetic silica cemented sandstone with a controlled fracture geometry, Geophysical Prospecting, 60 (3), 515-525.

Tod, S.R., 2002. The effects of stress and fluid pressure on the anisotropy of interconnected cracks. Geophysical Journal International 149, 149-156.

Wood, A. W., 1955. A Textbook of Sound. New York: McMillan Co.

Appendix C: Derivation of the simplified cosine function

The P-wave NMO velocity follows an elliptical variation and can be written as:

$$v_{p2}{}^{2}(\theta)=\frac{v_{p2-0^o}^2 v_{p2-90^o}^2}{v_{p2-0^o}^2\sin^2(\theta-\beta)+v_{p2-90^o}^2\cos^2(\theta-\beta)} \tag{C- 1}$$

Where θ is the azimuth angle. β represents the isotropy plane direction, which is fracture direction. v_{p2-0^o} and v_{p2-90^o} are P-wave NMO velocity along directions parallel and perpendicular to the fracture direction, respectively.

Reform Equation (C- 1) in the following steps:

$$\begin{aligned}
v^2_{p2}(\theta) &= \frac{v_{p2-0^o}^2 v_{p2-90^o}^2}{v_{p2-0^o}^2\sin^2(\theta-\beta)+v_{p2-90^o}^2\cos^2(\theta-\beta)} \\
&= \frac{2v_{p2-0^o}^2 v_{p2-90^o}^2}{v_{p2-0^o}^2[1-\cos 2(\theta-\beta)]+v_{p2-90^o}^2[1+\cos 2(\theta-\beta)]} \\
&= \frac{2v_{p2-0^o}^2 v_{p2-90^o}^2/(v_{p2-0^o}^2+v_{p2-90^o}^2)}{1-[(v_{p2-0^o}^2-v_{p2-90^o}^2)/(v_{p2-0^o}^2+v_{p2-90^o}^2)]\cos 2(\theta-\beta)} \\
&= \frac{[(v_{p2-0^o}^2+v_{p2-90^o}^2)^2-(v_{p2-0^o}^2-v_{p2-90^o}^2)^2]/2(v_{p2-0^o}^2+v_{p2-90^o}^2)}{1-[(v_{p2-0^o}^2-v_{p2-90^o}^2)/(v_{p2-0^o}^2+v_{p2-90^o}^2)]\cos 2(\theta-\beta)} \\
&= \frac{(v_{p2-0^o}^2+v_{p2-90^o}^2)/2-(v_{p2-0^o}^2-v_{p2-90^o}^2)^2/2(v_{p2-0^o}^2+v_{p2-90^o}^2)}{1-[(v_{p2-0^o}^2-v_{p2-90^o}^2)/(v_{p2-0^o}^2+v_{p2-90^o}^2)]\cos 2(\theta-\beta)} \\
&= \frac{v_p^2(1-\frac{\Delta_p^4}{v_p^4})}{[1-\frac{\Delta_p^2}{v_p^2}\cos 2(\theta-\beta)]}
\end{aligned} \tag{C- 2}$$

where $v_p^2 = \frac{v_{p2-0^o}^2 + v_{p2-90^o}^2}{2}$ and $\Delta_p^2 = \frac{v_{p2-0^o}^2 - v_{p2-90^o}^2}{2}$.

Using Taylor series expansion:

$$v_{p2}^2(\theta) \approx v_p^2 + \Delta_p^2 \cos 2(\theta - \beta) \qquad \text{(C- 3)}$$

Appendix D: Derivation of PS-converted wave azimuthal NMO velocity

Take the P-SV1 wave as an example, the NMO velocity of the P-SV1 wave can be written as:

$$v_{psv_1}^2(\theta) = \frac{1}{1+R_0} v_{P2}^2(\theta) + \frac{R_0}{1+R_0} v_{S_1 2}^2(\theta) \tag{D- 1}$$

where R_0 is the vertical velocity ratio. $v_{P2}^2(\theta)$ and $v_{S_1 2}^2(\theta)$ are NMO velocities of the P- and S1-wave, respectively. They both suffer from elliptical azimuthal variations.

Substituting Equations (5- 47) and (5- 50) and into Equation (D- 1):

$$v_{psv_1 2}^2(\theta) \approx \frac{1}{1+R_0}(v_p^2 + \Delta_p^2 \cos 2\theta) + \frac{R_0}{1+R_0}(v_{s_1}^2 + \Delta_{s_1}^2 \cos 2\theta) \tag{D- 2}$$

Reform Equation (D- 2) as:

$$v_{psv_1 2}^2(\theta) \approx (\frac{1}{1+R_0} v_p^2 + \frac{R_0}{1+R_0} v_{s_1}^2) + (\frac{1}{1+R_0} \Delta_p^2 + \frac{R_0}{1+R_0} \Delta_{s_1}^2) \cos 2\theta \tag{D- 3}$$

Defining Δ_{psv1}^2 and v_{psv1}^2 as:

$$v_{psv_1}^2 = (\frac{1}{1+R_0} v_p^2 + \frac{R_0}{1+R_0} v_{s_1}^2) \tag{D- 4}$$

$$\Delta_{psv_1}^2 = (\frac{1}{1+R_0} \Delta_p^2 + \frac{R_0}{1+R_0} \Delta_{s_1}^2) \tag{D- 5}$$

The azimuthal variation of P-SV1 wave NMO velocity can be described as:

$$v^2_{psv_1 2}(\theta) \approx v^2_{psv_1} + \Delta^2_{psv_1} \cos 2\theta \tag{D- 6}$$

The azimuthal variation of P-SV2 wave NMO velocity can be similarly derived.

Appendix E: Derivation of the least-square algorithm for ellipse fitting

The elliptical equation of the NMO velocity can be approximated into:

$$v\ (\theta) = v_0 + \Delta \cos 2(\theta - \beta) \tag{E- 1}$$

where $v\ (\theta)$ is the NMO velocity at azimuth angle θ, v_0 is the base velocity, Δ is the velocity perturbation and β represents the fracture direction.

Theoretically, knowing NMO velocity values at three different azimuth angles could solve the equation and obtain v_0, Δ and β. However in the real data processing, more than three azimuth angles are available. Equation is reformed into:

$$v_i(\theta) = v_0 + \Delta \cos 2(\theta_i - \beta) \quad (i = 1, 2, 3 \cdots N) \tag{E- 2}$$

An error function is defined as:

$$e = \sum_{i=1}^{N} [v(\theta_i) - v_0 - \Delta \cos 2(\theta_i - \beta)]^2 \quad (i = 1, 2, 3 \cdots N) \tag{E- 3}$$

Apply the least-square algorithm and take the partial differential:

$$\left.\begin{aligned}
&\frac{\partial e}{\partial v_0} = 2\sum[v_i - v_0 - \alpha\cdot\cos 2(\theta_i-\beta)]^2 = 0\\
&\frac{\partial e}{\partial \alpha} = -2\sum[v_i - v_0 - \alpha\cdot\cos 2(\theta_i-\beta)]\cos 2(\theta_i-\beta) = 0\\
&\frac{\partial e}{\partial \beta} = 4\sum[v_i - v_0 - \alpha\cdot\cos 2(\theta_i-\beta)]\alpha\sin 2(\theta_i-\beta) = 0
\end{aligned}\right\} \quad \text{(E- 4)}$$

Solve the equation set and get:

$$\left.\begin{aligned}
\tan 2\beta == &\frac{\begin{aligned}&n\sum v_i\cos 2\theta_i\sum\cos 2\theta_i\sin 2\theta_i - n\sum(\cos 2\theta_i)^2\sum v_i\sin 2\theta_i\\&+\sum v_i\sin 2\theta_i(\sum\cos 2\theta_i)^2 - \sum v_i\cos 2\theta_i\sum\cos 2\theta_i\sum\sin 2\theta_i\\&+\sum v_i\sum(\cos 2\theta_i)^2\sum\sin 2\theta_i - \sum v_i\sum\cos 2\theta_i\sin 2\theta_i\sum\cos 2\theta_i\end{aligned}}{\begin{aligned}&n\sum v_i\sin 2\theta_i\sum\cos 2\theta_i\sin 2\theta_i - n\sum v_i\cos 2\theta_i\sum(\sin 2\theta_i)^2\\&+\sum v_i\cos 2\theta_i(\sum\sin 2\theta_i)^2 - \sum v_i\sin 2\theta_i\sum\cos 2\theta_i\sum\sin 2\theta_i\\&+\sum v_i\sum(\sin 2\theta_i)^2\sum\cos 2\theta_i - \sum v_i\sum\cos 2\theta_i\sin 2\theta_i\sum\sin 2\theta_i\end{aligned}}\\
\alpha = &\frac{n\sum v_i\cos 2(\theta_i-\beta) - \sum v_i\sum\cos 2(\theta_i-\beta)}{n\sum[\cos 2(\theta_i-\beta)^2] - [\sum\cos 2(\theta_i-\beta)]^2}\\
v_0 = &\frac{\sum v_i - \alpha\sum\cos 2(\theta_i-\beta)}{n}
\end{aligned}\right\} \quad \text{(E- 5)}$$

Appendix F: Publications

Liu, W., Dai, H. and Li, X-Y, 2013, The Feasibility of Compensation for the Azimuthal Anisotropy of PS-converted Waves in HTI Media: 75th EAGE Conference, Expanded Abstracts, TH P03-02.

Liu, W., Dai, H. and Li, X-Y, 2012, The analysis of the azimuthal variation of PS converted waves in HTI media: A synthetic study: 82nd SEG Annual Meeting., Expanded Abstracts, pp. 1-5.

Liu, W., Dai, H., Li, X-Y, 2011, Compensation for the Azimuthal Anisotropy of PS-converted Waves in HTI Media, 74th EAGE Conference, Expanded Abstracts, P136.

Liu, W., Dai, H., Li, X-Y, 2010, Azimuthal variation of the velocity and moveout of PS converted waves in HTI media, 73rd EAGE Annual Meeting, Expanded Abstracts, P071.